

ISSN 1980-9743

# Soils and Rocks

An International Journal of Geotechnical  
and Geoenvironmental Engineering

$\frac{\Delta B}{MS}$



Volume 41, N. 3  
September-December 2018

# **SOILS and ROCKS**

An International Journal of Geotechnical and Geoenvironmental Engineering

**Editor** Paulo Scarano Hemsí - Aeronautics Institute of Technology, Brazil

**Co-editor** José Couto Marques - University of Porto, Portugal

## **Executive Board**

Waldemar Coelho Hachich  
*University of São Paulo, Brazil*  
António Topa Gomes  
*University of Porto, Portugal*

Gustavo Ferreira Simões  
*Federal University of Minas Gerais, Brazil*  
Rafaela Cardoso  
*University of Lisbon, Portugal*

## **Associate Editors**

H. Einstein  
*MIT, USA*  
John A. Hudson  
*Imperial College, UK*  
Kenji Ishihara  
*University of Tokyo, Japan*  
Michele Jamiolkowski  
*Studio Geotecnico Italiano, Italy*  
Willy A. Lacerda  
*COPPE/UFRJ, Brazil*

E. Maranha das Neves  
*Lisbon Technical University, Portugal*  
Nielen van der Merve  
*University of Pretoria, South Africa*  
Paul Marinos  
*NTUA, Greece*  
James K. Mitchell  
*Virginia Tech., USA*  
Lars Persson  
*SGU, Sweden*

Harry G. Poulos  
*University of Sidney, Australia*  
Niek Rengers  
*ITC, The Netherlands*  
Fumio Tatsuoka  
*Tokyo University of Science, Japan*  
Luiz González de Vallejo  
*UCM, Spain*  
Roger Frank  
*ENPC-Cermes, France*

## **Editorial Board Members**

Roberto F. Azevedo  
*Federal University of Viçosa, Brazil*  
Milton Kanji  
*University of São Paulo, Brazil*  
Kátia Vanessa Bicalho  
*Federal University of Espírito Santo, Brazil*  
Omar Y. Bitar  
*IPT, Brazil*  
Lázaro V. Zuquette  
*University of São Paulo at São Carlos, Brazil*  
Fabio Taioli  
*University of São Paulo, Brazil*  
Tarcisio Celestino  
*University of São Paulo at São Carlos, Brazil*  
Edmundo Rogério Esquivel  
*University of São Paulo at São Carlos, Brazil*  
Nilo C. Consoli  
*Federal Univ. Rio Grande do Sul, Brazil*  
Sandro S. Sandroni  
*Consultant, Brazil*  
Sérgio A.B. Fontoura  
*Pontifical Catholic University, Brazil*  
Ennio M. Palmeira  
*University of Brasília, Brazil*  
Luciano Décourt  
*Consultant, Brazil*  
Faïçal Massad  
*University of São Paulo, Brazil*  
Marcus Pacheco  
*University of the State of Rio de Janeiro, Brazil*  
Paulo Maia  
*University of Northern Rio de Janeiro, Brazil*  
Renato Cunha  
*University of Brasília, Brazil*

Orencio Monje Vilar  
*University of São Paulo at São Carlos, Brazil*  
Maria Eugenia Boscov  
*University of São Paulo, Brazil*  
Eda Freitas de Quadros  
*BGTECH, Brazil*  
Tácio de Campos  
*Pontifical Catholic University of Rio de Janeiro, Brazil*  
Richard J. Bathurst  
*Royal Military College of Canada*  
Robert Mair  
*University of Cambridge, UK*  
Serge Leroueil  
*University of Laval, Canada*  
Mario Manassero  
*Politécnico di Torino, Italy*  
Luis Valenzuela  
*Consultant, Chile*  
Jorge G. Zornberg  
*University of Texas/Austin, USA*  
Andrew Whittle  
*MIT, USA*  
Pierre Bérest  
*LCPC, France*  
Peter Kaiser  
*Laurentian University, Canada*  
He Manchao  
*CUMT, China*  
Teruo Nakai  
*Nagoya Inst. Technology, Japan*  
Claudio Olalla  
*CEDEX, Spain*  
Frederick Baynes  
*Baynes Geologic Ltd., Australia*

R. Kerry Rowe  
*Queen's University, Canada*  
R. Jonathan Fannin  
*University of British Columbia, Canada*  
Laura Caldeira  
*LNEC, Portugal*  
António S. Cardoso  
*University of Porto, Portugal*  
José D. Rodrigues  
*Consultant, Portugal*  
António G. Coelho  
*Consultant, Portugal*  
Luís R. Sousa  
*University of Porto, Portugal*  
Rui M. Correia  
*LNEC, Portugal*  
João Marcelino  
*LNEC, Portugal*  
António C. Mineiro  
*University of Lisbon, Portugal*  
António P. Cunha  
*LNEC, Portugal New*  
António G. Correia  
*University of Minho, Portugal*  
Carlos D. Gama  
*Lisbon Technical University, Portugal*  
José V. Lemos  
*LNEC, Portugal*  
Nuno Grossmann  
*LNEC, Portugal*  
Luís L. Lemos  
*University of Coimbra, Portugal*  
Ricardo Oliveira  
*COBA, Portugal*

## “Ad hoc” Reviewers (2018)

Ana Cristina Sieira <i>UERJ, Brazil</i>	Gustavo Rocha Vianna <i>Novasolo, Brazil</i>	Maurício M. Sales <i>UFG, Brazil</i>
André Luís Brasil Cavalcante <i>UnB, Brazil</i>	Harry Poulos <i>Coffey, Australia</i>	Miriam Gonçalves Miguel <i>Unicamp, Brazil</i>
Antônio Alberto Correia <i>Univ. Coimbra, Portugal</i>	Indiara Giugni <i>Consultant, Brazil</i>	Nilo Cesar Consoli <i>UFRGS, Brazil</i>
Antônio Topa Gomes <i>FEUP, Portugal</i>	Isabel Lopes <i>TPF, Portugal</i>	Nuno M. da Costa Guerra <i>Univ. Nova de Lisboa, Portugal</i>
Arsenio Negro Jr. <i>Bureau, Brazil</i>	João Marcos Vaillant <i>CEFET-MG, Brazil</i>	Olavo Francisco dos Santos Jr. <i>UFRN, Brazil</i>
Carlos Emmanuel Ribeiro Lautenschläger <i>PUC-RJ, Brazil</i>	Jorge Carvalho <i>FEUP, Portugal</i>	Orencio Monje Vilar <i>USP-S.Carlos, Brazil</i>
Caroline Tomazoni Santos <i>UFPR, Brazil</i>	José Eduardo Quintanilha Menezes <i>FEUP, Portugal</i>	Otávio Coaracy Brasil Gandolfo <i>IPT, Brazil</i>
Castorina Vieira <i>FEUP, Portugal</i>	José Maria de Barros <i>IPT, Brazil</i>	Paulo César Lodi <i>UNESP, Brazil</i>
Celeste Jorge <i>LNEC, Portugal</i>	José Muralha <i>LNEC, Portugal</i>	Paulo Ivo Braga de Queiroz <i>ITA, Brazil</i>
Celso Lima <i>FEUP, Portugal</i>	José Tadeu Balbo <i>USP-Poli, Brazil</i>	Paulo José Brugger <i>Brugger Eng., Brazil</i>
Celso Romanel <i>PUC-RJ, Brazil</i>	Kátia Vanessa Bicalho <i>UFES, Brazil</i>	Paulo José Rocha Albuquerque <i>Unicamp, Brazil</i>
Claudio Michael Wolle <i>USP-Poli, Brazil</i>	Larissa de Brum Passini <i>UFPR, Brazil</i>	Paul W. Mayne <i>GA Tech, USA</i>
Cristina de Hollanda Cavalcanti Tsuha <i>USP-S.Carlos, Brazil</i>	Lucas Festugato <i>UFRGS, Brazil</i>	Pérsio Leister de Almeida Barros <i>Unicamp, Brazil</i>
Eda Quadros <i>BGTECH, Brazil</i>	Luísa Braga <i>LNEC, Portugal</i>	Rafaela Cardoso <i>IST, Portugal</i>
Eduardo Fortunato <i>LNEC, Portugal</i>	Luís Lemos <i>Univ. Coimbra, Portugal</i>	Renato Pinto da Cunha <i>UnB, Brazil</i>
Elisabete Esteves <i>ISEP, Portugal</i>	Luís Ribeiro e Souza <i>FEUP, Portugal</i>	Ricardo Correia dos Santos <i>LNEC, Portugal</i>
Elisabeth Ritter <i>UERJ, Brazil</i>	Luiz Guilherme F.S. de Mello <i>Vector, Brazil</i>	Roberto Quental Coutinho <i>UFPE, Brazil</i>
Ennio Marques Palmeira <i>UnB, Brazil</i>	Mafalda Laranjo <i>Inst. Politécnico de Viana do Castelo, Portugal</i>	Ronaldo Luis dos Santos Izzo <i>UFTPR, Brazil</i>
Fernando Saboya Albuquerque Jr. <i>UENF, Brazil</i>	Marcia Maria dos Anjos Mascarenhas <i>UFG, Brazil</i>	Rogério Mota <i>LNEC, Portugal</i>
Filipe Telmo Jeremias <i>LNEC, Portugal</i>	Maria das Graças Gardoni Almeida <i>UFMG, Brazil</i>	Sara Rios <i>FEUP, Portugal</i>
Francisco Rezende Lopes <i>UFRJ, Brazil</i>	Maria de Lurdes Lopes <i>FEUP, Portugal</i>	Tallyta da Silva Curado <i>IFG, Brazil</i>
Gemmina Di Emidio <i>U. Gent, Belgium</i>	Maria Eugenia G. Boscov <i>USP-Poli, Brazil</i>	Werner Bilfinger <i>Vector, Brazil</i>
Gisleine Coelho de Campos <i>IPT, Brazil</i>	Marcus Pacheco <i>UERJ, Brazil</i>	

**Soils and Rocks** publishes papers in English in the broad fields of Geotechnical Engineering, Engineering Geology and Geoenvironmental Engineering. The Journal is published in April, August and December. Subscription price is US\$ 90.00 per year. The journal, with the name “Solos e Rochas”, was first published in 1978 by the Graduate School of Engineering, Federal University of Rio de Janeiro (COPPE-UFRJ). In 1980 it became the official magazine of the Brazilian Association for Soil Mechanics and Geotechnical Engineering (ABMS), acquiring the national character that had been the intention of its founders. In 1986 it also became the official Journal of the Brazilian Association for Engineering Geology and the Environment (ABGE) and in 1999 became the Latin American Geotechnical Journal, following the support of Latin-American representatives gathered for the Pan-American Conference of Guadalajara (1996). In 2007 the journal acquired the status of an international journal under the name of Soils and Rocks, published by the Brazilian Association for Soil Mechanics and Geotechnical Engineering (ABMS), Brazilian Association for Engineering Geology and the Environment (ABGE) and Portuguese Geotechnical Society (SPG). In 2010, ABGE decided to publish its own journal and left the partnership.

### **Soils and Rocks**

1978,	1 (1, 2)
1979,	1 (3), 2 (1,2)
1980-1983,	3-6 (1, 2, 3)
1984,	7 (single number)
1985-1987,	8-10 (1, 2, 3)
1988-1990,	11-13 (single number)
1991-1992,	14-15 (1, 2)
1993,	16 (1, 2, 3, 4)
1994-2010,	17-33 (1, 2, 3)
2011,	34 (1, 2, 3, 4)
2012-2017,	35-40 (1, 2, 3)
<b>2018,</b>	<b>41 (1, 2, 3)</b>

ISSN 1980-9743

CDU 624.131.1

**SOILS and ROCKS**

An International Journal of Geotechnical and Geoenvironmental Engineering

**Publication of****ABMS - Brazilian Association for Soil Mechanics and Geotechnical Engineering****SPG - Portuguese Geotechnical Society****Volume 41, N. 3, September-December 2018****Table of Contents***XXXV MANUEL ROCHA LECTURE**Internal Erosion in Dams*

L. Caldeira

237

*ARTICLES**Some Case Histories with Lessons to Learn in Dam Engineering (2<sup>nd</sup> Dr. Victor de Mello Goa Lecture)*

L.G.F.S. de Mello

267

*A Method for Designing Finger Drains and Assessing Phreatic Lines for Dams*

M.C.N. Araújo, T.F. de Souza Júnior, M.N.B. Trevizolli, C.A. Teixeira, S.H.C. Teixeira, V.P. Faro

309

*Assessment of Rate Effects in Piezocone Tests from Poroelastic Cavity Expansion Analysis*

G. Dienstmann, S. Maghous, F. Schnaid

319

*Behavior of Geosynthetic-Encased Stone Columns in Soft Clay: Numerical and Analytical Evaluations*

N.R. Alkhorshid, G.L.S. Araújo, E.M. Palmeira

333

*On the Compatibility and Theoretical Equations for Mixtures of Tropical Soils and Bentonite for Barrier Purposes*

T.L.C. Morandini, A.L. Leite

345

*TECHNICAL NOTES**The Performance of a Sand Reinforced with Coconut Fibers Through Plate Load Tests on a True Scale Physical Model*

J.M.G. Sotomayor, M.D.T. Casagrande

361

*Porosity Changes of Compacted Soil Percolated with Acidic Leachate*

E.P. Korf, P.D.M. Prietto, A.A. Silveira, C. Ulsen, L. Bragagnolo

369

*CASE STUDY**Effects of Spatial Variability on Slope Reliability: A Hypothetical Case Study*

E. Muñoz, M.P. Cordão Neto, A. Ochoa

381



## **Manuel Rocha Lecture**



**Manuel Rocha** (1913-1981) was honoured by the Portuguese Geotechnical Society with the establishment of the Lecture Series bearing his name in 1984.

Having completed the Civil Engineering Degree at the Technical University of Lisbon (1938) he did post-graduate training at MIT. He was the driving force behind the creation of the research team in Civil Engineering that would lead to the foundation of the National Laboratory for Civil Engineering (LNEC), in Lisbon. He was Head of LNEC from 1954 to 1974 and led it to the cutting edge of research in Civil Engineering.

His research work had great impact in the area of concrete dams and rock mechanics. He was the 1<sup>st</sup> President of the International Society for Rock Mechanics and organized its 1<sup>st</sup> Congress in Lisbon (1966). He did consultancy work in numerous countries. He was Honorary President of the Portuguese Geotechnical Society, having promoted with great commitment the cooperation between Portugal and Brazil in the area of Civil Engineering, and member of the National Academy of Sciences of the USA. Recognized as a brilliant researcher, scientist and professor, with a sharp, discerning intellect allied to a prodigious capacity for work and management, he was truly a man of many talents.



The 2018 Manuel Rocha Lecture was presented by Prof. Dr. **Laura Caldeira**, Head of the Geotechnics Department of LNEC, the National Laboratory for Civil Engineering in Lisbon, Portugal. She is a former professor of Universidade do Porto and Universidade Nova de Lisboa and, between 2008 and 2016, of Instituto Superior Técnico. Dr. Caldeira graduated in Civil Engineering with honours in 1981 from Universidade do Porto, having obtained a Ph.D. degree from the same institution in 1994. Her Ph.D. research focused on the dynamic analysis of embankment dams, including studies conducted at University of Princeton (USA) of strain localization in particulate media and liquefaction of the alluvial foundation of embankment dams. In 1998, Dr. Caldeira became a researcher at LNEC, and, in the following year, head of the Foundations Division. In 2006 she obtained her Habilitation, presenting a research program on Risk Analyses in Geotechnics and Application to Embankment Dams. Dr. Caldeira has also been involved in consulting, including a number of large dams, tunnels, and the Lisbon Docks, and has authored or co-authored more than 40 journal and 140 congress publications, one book and 15 book chapters, and more than 260 technical reports. Dr. Caldeira delivered more than 40 invited lectures in Portugal and elsewhere, and was president of the Portuguese Geotechnical Society from 2008 to 2012. She has integrated several committees, namely at the Science and Technology Foundation, the Engineering Academy, and the Dam Safety Commission in Portugal, and the European Large Geotechnical Institutes Platform.

**Soils and Rocks**  
**v. 41, n. 3**



# Internal Erosion in Dams

L. Caldeira

**Abstract.** In embankment dams and dam foundations, internal erosion is the major cause of structural dam failures and incidents. Internal erosion develops locally along concentrated leaks or in the largest flow velocity zones, where the permeability is high, and at the interface between coarse and fine materials, where the flow velocity in coarse material may be high compared to the adjacent fine material. The mechanics of the equilibrium of the particle governs the initiation of the internal erosion. Filter and drain systems constitute a first line of defense against the phase of continuation of erosion. It is assumed by several authors that the continuation of internal erosion can be prevented by using adequate granular filters in areas where important hydraulic gradients may develop. This lecture addresses the most important and frequent of those internal erosion mechanisms in dams - induced by concentrated leaks or by backward erosion piping, presenting event trees for estimating the resultant probabilities of failure. To assist in the determination of the range of probabilities of their branches, a set of laboratory tests is described. In complement, some knowledge gaps related to the described mechanisms are identified, where future research efforts are directed at LNEC. Two case studies of dams and one case study of a cofferdam with internal erosion problems are described. The first is an embankment dam, Lapão dam, where due to design and construction problems an internal erosion process was developed. The other is Crestuma dam, a gated structure type. Since the dam started operating, the riverbed near the dam has been subject to frequent monitoring that showed progressive scour of the protective rockfill layer. This lecture presents the results of the studies undertaken in relation to the hydraulic stability of the alluvial foundation of the dam stilling basins and of the downstream rockfill, and the main features of the implemented repairing solutions. The last case is a cofferdam constituted by natural decomposed granite rock mass and a water tightness solution with jet grouting columns and grouting. The problems of internal erosion related to this type of formation are described, as well as the interventions adopted to overcome their effects.

**Keywords:** backward erosion piping, case studies, concentrated leaks, laboratory tests.

## 1. Introduction

Internal erosion is a major cause of structural dam failures and of incidents on embankment dams and on foundations of concrete or masonry dams. The statistics of embankment dam failures shows that internal erosion is responsible for 46%, overtopping for 48%, and sliding for only 6% (4% in static conditions and 2% in seismic conditions) of the failures with known failure mode.

Most of these failures occurred on the first filling, but they also can happen after this period due to cracking (more likely to occur in the upper part of the dam), deterioration of the conduits through embankments and adjacent structures confining with embankments or the ground, and non-existent or deficient filter systems. Incidents include excessive, new or increased seepage and leakage, sinkholes, sand boils, and fast settlements of the dam. Sinkholes may be present in all types of internal erosion, and if they are observed, the erosion has already progressed and time to failure may be small.

In recent years, two lines of investigation of internal erosion have been addressed: the application of risk assessment methods in the estimation of the probability of failure of dams due to internal erosion phenomena, and the improvement of the knowledge about the mechanisms that

can result in dam failure by internal erosion (ICOLD, 2017).

Internal erosion develops locally along concentrated leaks or in the largest flow velocity zones, where the permeability is high, and at the interface between coarse and fine materials, where the flow velocity in coarse material may be high compared to the adjacent fine material. The mechanics of the equilibrium of the particle governs the initiation of the internal erosion, and five main mechanisms can be distinguished: concentrated leaks along flaws, backward erosion, contact erosion, suffusion and suffosion.

This lecture addresses the most important and frequent failure mechanisms in dams: those induced by concentrated leaks and backward erosion piping. It describes in detail the internal erosion process necessary to evaluate the probability of dam failure, based on event tree analyses, and including the purpose and functions of filters. It also presents the tests that assist the assessment of some of the probabilities of the branches. Some of the gaps of knowledge that require further investigation are also identified.

Case studies of two dams and a cofferdam with internal erosion problems are presented. The first is an embankment dam, Lapão dam, where due to design and construction problems internal erosion processes were developed

through concentrated leaks. The other is a large gated concrete structure type where the riverbed near the dam had been subject to frequent monitoring that showed progressive scour of the protective layer. With this scour, the foundation of the dam was no longer protected against backward erosion piping. Finally, it is presented a cofferdam, with internal erosion initiation and progression in natural decomposed granite, and the evidences of their occurrence are described.

## 2. Failure Probability Due to Internal Erosion Induced by Concentrated Leaks

A methodology for estimating probabilities of failure of embankment dams by internal erosion and to investigate aspects related with internal erosion in embankment dams and their foundations is being developed, which involves the decomposition of the internal erosion failure process into a sequence of steps (Fell *et al.*, 2008). Generally, the steps considered are the following: (1) loading conditions assessment; (2) identification of the location where the internal erosion can start, and of its paths; (3) initiation of erosion; (4) filtration or continuation of erosion; (5) progression; (6) detection; (7) intervention and repair; (8) and formation of a breach mechanism. This sequence can be interrupted if there are zones capable of stopping the erosion process once initiated, or if it is detected and inhibited during the erosion phases prior to the formation of the breach.

In terms of loading conditions, the historic cases showed that nearly all internal erosion failures in the embankment took place when the reservoir was at the highest level ever, or within one meter of that level, while in the foundation the reservoir level was not as determinant (ICOLD, 2017). However, Engemoen & Redlinger (2009) and Engemoen (2011), based on a detailed analysis of internal erosion incidents of 220 embankment dams, concluded that they can occur at any time in the dam life, when the reservoir level is close to normal high water level.

Figure 1 presents the event tree developed for the estimation of the probability of failure induced by a concen-

trated leak due to the presence of a transverse crack in the embankment, caused by differential settlement. To evaluate the probability of failure, one must assess the probability of the initial event (the assumed reservoir loading) and the probability of each branch of the event tree that leads to the breach formation, *i.e.*, the failure of the dam, in Fig. 1 represented by the red triangular shape.

Internal erosion may initiate in the embankment due to a concentrated leak in transverse cracks, poorly compacted or high permeability zones, a gap at the interface with concrete structures formed due to differential settlement between the embankment and the structure, or due to the collapse settlement of poorly compacted fill in the embankment around conduits and adjacent to walls.

Cracking in embankment dams can be induced by vertical stress release caused by arching between two or more locations that do not settle as much as the location between them, by hydraulic fracturing, and by seismic action. Most of hydraulic fracturing occurs during the first filling of the reservoir as a wetting front passes through the dam. Nevertheless, water penetrating the sides of a crack may produce some swelling in unsaturated soils that can close the crack before erosion begins to make it wider, the behaviour of the dam being dependent on which process progresses faster (swelling or erosion).

If the gradient is sufficient to detach particles by slaking along the walls of the crack or flaw, the soil is subsequently eroded by water flowing at relatively high velocity, and the erosion or scour process initiates.

If there is a proper filter, the eroded particles are then carried out through the preferential flow path to the filter face, and the filter will stop particle erosion through the crack by a self-healing process presented in Fig. 2.

In an initial stage (Fig. 2a), the soil eroded from a crack is caught at the filter face, forming a cake (a material with high solids content and low permeability), by a penetration mechanism. The eroded particles progressively fill the voids with a velocity that decreases with increasing head loss, until equilibrium between driving forces and

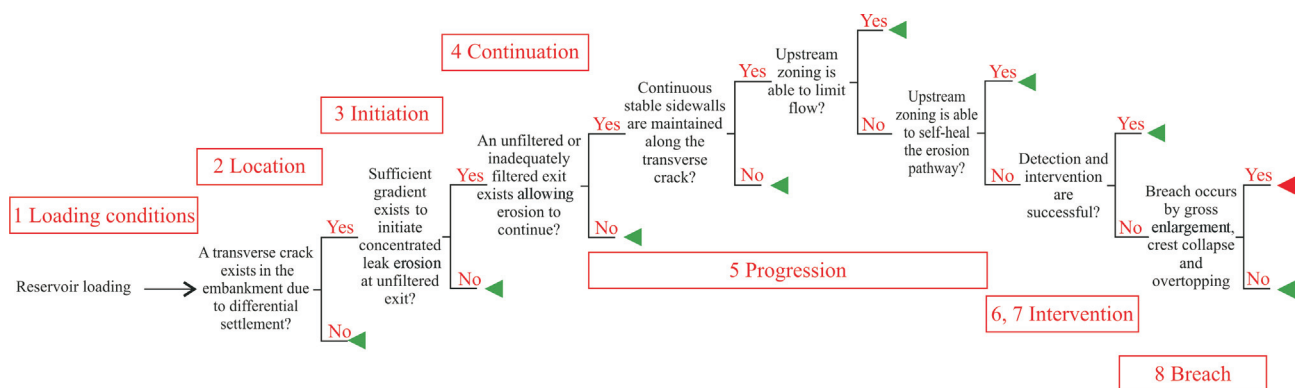


**Figure 1** - Event tree for estimation of the probability of failure by internal erosion induced by concentrated leaks (adapted from Shewbridge, 2014).

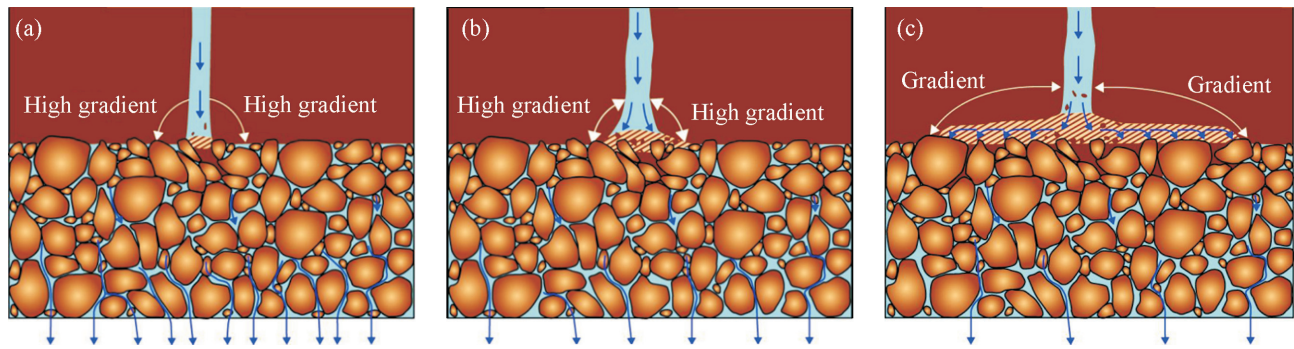


**Figure 2** - Self-healing process at the end of a crack: a) initial stage; b) intermediate stage; c) final stage (adapted from Redlinger, 2014).

friction forces stops the flow. The depth of penetration of the eroded particles into the confining filter is governed by the hydraulic gradient and the geometrical characteristics of the pore system. The high gradient between water in the crack and the adjacent filter causes some widening of the filter cake near the crack. Further widening of the filter cake is induced in the next stages (Fig. 2b), until the local hydraulic gradient is reduced. At the final stage (Fig. 2c) the low permeability filter cake covers the opening and the adjacent zones on each side of the crack. The remaining filter adequately collects seepage flow through the pores of the soil.

Once the internal erosion process starts, for a given load condition, and there are no effective filters stopping eroded particles along the erosion path, the continuation and progression of internal erosion are governed by the mechanics of grain transport and shall be assessed. Mechanical and hydraulic conditions must take place simultaneously (ICOLD, 2017), namely cracks, pipes, or other defects must be sustained, and the drag force by seepage flow must be sufficient to continue the particle transport. The erosion will progress unless an equilibrium situation develops and the eroding forces become equal to or less than the resisting forces.

Soils capable of holding a crack or pipe, either fully or partially saturated, are: well compacted soils containing more than 5% plastic fines, poorly compacted soils containing more than 15% plastic fines, and soils containing more than 30% non-plastic fines. Non-plastic silts, sands, and gravels will not in general hold a roof as the roof will collapse when they become saturated. However, partially saturated and non-plastic soils with high fines content may hold a roof along the phreatic surface, for example, but the roof, which in this situation is sustained by the negative pore water pressure, *i.e.*, by suction, may collapse when saturated.

As the flaw enlarges, the hydraulic shear stresses increase, and the erosion will progress unless the reservoir is drawn down to reduce the gradient. In general, this enlargement is rapid, leading to the dam breach, usually within few hours. However, in some cases, even though initially concentrated leaks had rapidly been developed in the embankment, the flow stopped or tended to stabilize. The most

relevant issue in zoned dams appears to be related to the types of material upstream of the cracked core (Fell *et al.*, 2003). In the described scenarios, the limitation of erosion progression may be attributed to the flow restriction and/or crack-filling actions. Therefore, it is necessary to evaluate the possible contribution of those materials in the internal erosion process.

The flow restriction action is in place when the upstream shell or an upstream transition zone in a zoned dam is able to restrict the flow that can pass through a concentrated leak in the core. An example of an accident where the flow appears to have been restricted has occurred in the Balderhead dam.

Balderhead dam is 48 m high earth-rockfill dam, built in England in 1961-1965, where transverse cracks were detected in the thin central clayey core, likely due to hydraulic fracture (Sherard, 1973). Compacted schist materials constituted the upstream shell. A transition zone was adopted immediately upstream of the core, using fine schist material. The flow restriction action was partially imputed to the relatively low permeability of the upstream transition zone.

The upstream crack-filling action involves the washing in of particles of the upstream material into core cracks. These particles are transported by seepage flow from the interface with the cracked core up to the downstream material. The upstream material from higher levels may fall down into the empty space created by the particles dislocated at the crack level, and then carried away downstream. This continuous process can fill up the crack and stop the concentrated leakage, and eventually may lead to the development of a sinkhole at the crest or at the upstream slope.

This concept has been incorporated into embankment dam design for some decades, by the use of upstream sandy zones as crack stoppers (Sherard & Dunnigan, 1985), a redundant measure that takes into account the possible presence of a deficiently designed or constructed filter. The filter might not properly hold the eroded particles from the cracked core, but it can retain the particles washed from the upstream material.

Foster *et al.* (1998) identified several case studies with evidences of the washing in of materials into cracks (shown by sinkhole formation), and of the decrease of leak-

age flow rates. Examples include Balderhead dam in England, Matahina dam in New Zealand, Viddalsvatn dam in Norway, Wreck Cove dam in Canada, Uljua dam in Finland, and St. Stephen Powerhouse dam in USA. They noticed the following common characteristics of those dams: a downstream filter or permeable zone, which enables the filtering of particles washed from upstream materials, and a coarse granular material constituting the upstream zone.

When the upstream material is unable to provide flow limitation or a crack filling action and if the internal erosion phenomenon is not detected, or proper mitigation measures are not implemented, the crack tends to enlarge very quickly, the crack walls become very unstable, collapsing into the flow, and a breach is formed.

### 3. Failure Probability Due to Backward Erosion Piping

The detachment of particles at the exit of the leakage path characterizes the initiation of a backward erosion mechanism. Along any given seepage flow path through the pore space, each soil will have a critical gradient based on its properties. If this gradient is exceeded at the discharge point, soil particles will be eroded away with the flow water. For silts and clays ( $IP > 7$ ), very high gradients are required to initiate backward erosion piping, but for non-clayey soils ( $IP < 7$ ) and particularly non-plastic soils, much lower gradients will initiate it.

The critical gradient depends on the uniformity of particle size distribution, the mass and size of particles, and soil density. High susceptibility to detachment is present in soils with particles of fine uniformly graded sand with no clay (SP or SP-SM according to the Unified Soil Classification System), low particle mass, and lack of inter-particle attraction. More resistant are large sand particles and gravels, due to their large mass, well-graded sands, where small particles are blocked by larger particles in the mass, and compacted or dense soils. According to Schmertmann (2001), the minimum hydraulic gradient that leads to material movement is only 0.08 and the velocity required for scour along a concentrated leak is 40 to 90 times that required for piping (a quick condition resulting in localized

sloughing and transport under essentially zero effective stress).

When a filter does not support the discharge face and the critical gradient is exceeded, soil particles are eroded from that discharge face. A cavity or a pipe is formed and it progresses from downstream to upstream at a faster and faster rate, as the gradient and the flow increase with the loss of soil.

If the soil is capable of supporting the cavity, failure follows as the cavity enlarges rapidly due to the intense erosive forces. This type of occurrence is called backward erosion piping, and its onset at the foundation is often detected by the presence of sand boils at the downstream side of the dam.

If the soil is unable to hold the cavity, the pipes collapse, resulting in the movement of the soil above, and unravelling if it occurs on the downstream slope of an embankment. In this case, the phenomenon is called global backward erosion.

To protect against backward erosion piping, a granular filter is placed in contact with a surface of the soil (herein called base soil), properly confined by a downstream zone such that positive pressure is ensured. Filters support the discharge face with points of contact spaced at some distance as determined by the gradation of the filter. Figure 3 shows the interface between the base soil and the filter, where after stabilization, the coarse particles of the soil base ( $D_{85}$ ) are retained by the fine particles of the filter ( $D_{15}$ ), creating a bridging effect between contact points, which prevents any particle movement (including colloidal particles).

Filters are granular soils, cleaned of fine particles, manufactured from natural earth materials by grading, screening, washing and/or crushing. The fines content must be insufficient to bind the granular particles together (no cohesion criterion) and to prevent free flow of water. It consists of an internally stable granular porous medium (self-filtration or stability and segregation criteria) with pore size openings small enough to prevent migration of the base soil through which the water is flowing into the filter (retention

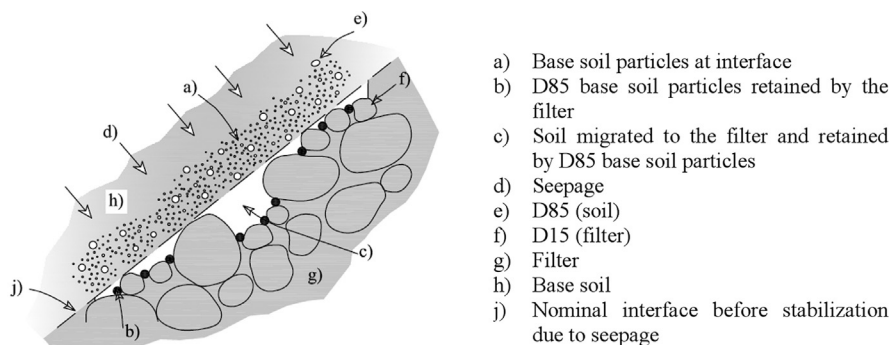


**Figure 3** - Bridging effect at the interface between the base soil and the filter (adapted from Cedergren, 1977).

criterion) and sufficiently pervious to offer little resistance to water flow (drainage criterion).

They serve to accommodate high gradients through a dam by intercepting the seepage flow from the zone containing high gradients and reducing them to near zero in the internal drainage system. The filter materials must be of sufficiently high quality (strength criterion) so that the filter will not be able to sustain a crack. The compaction characteristic must also be controlled, because there is some evidence that very dense compacted filters, namely gravels, may hold a crack (Redlinger *et al.*, 2011).

In the past and presently, the development of filter criteria for soils has been centred on empirical relationships based on laboratory testing, focused on determining the grain size of a filter required to protect a base soil, which limited the fines content and precluded the use of materials with plasticity or any type of binders or cementing agents.

However, analysing the results of tests, Foster and Fell verified that filters which were too coarse to satisfy the usual design criteria could eventually seal after retaining a certain quantity of eroded material. The coarser particles from the base soil may become retained at the surface of the filter forming a finer filter, which in turn may stop the erosion process. Therefore, they considered three filter erosion boundaries, namely: no erosion, excessive erosion, and continuing erosion boundaries (Fig. 4). These boundaries allow to define when the filter works with practically no erosion, after “some” erosion of the base material and after “excessive” erosion of the base material, and when the filter is too coarse to retain the eroded base materials, *i.e.*, is prone to continuing erosion. Based on test results, they proposed the criteria for these boundaries that can be found in Foster & Fell (2000, 2001).

The criteria for excessive and continuing erosion boundaries are particularly useful when assessing existing dams with a filter or transition zone which is coarser than required by current filter design criteria. ICOLD (2017), based on the information about case histories, suggests the following categories for filters as a function of the maxi-

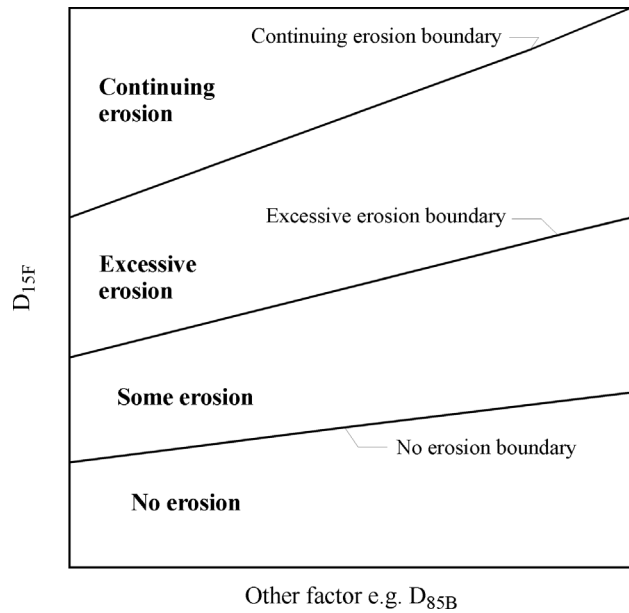


Figure 4 - Conceptual filter erosion boundaries (Foster & Fell, 2000, 2001).

imum leakage flow that could develop due to piping: up to 100 L/s, filters with some erosion; between 100 and 1,000 L/s, filters with excessive erosion; and more than 1,000 L/s, filters with continuing erosion.

Figure 5 presents the event tree developed for the estimation of the probability of failure induced by backward erosion piping due to the presence of an unfiltered exit associated to a continuous layer of sandy soil. As explained before, the internal erosion starts when the critical gradient is exceeded at the exit point (internal erosion initiation). Whether the erosion progresses upstream towards the reservoir depends on the seepage gradient within the erosion pipe. There is a critical gradient above which the soil particles will be detached and a critical flow velocity above which the particles will be transported in the erosion pipe. For reaching dam failure, it is essential that no filter exists

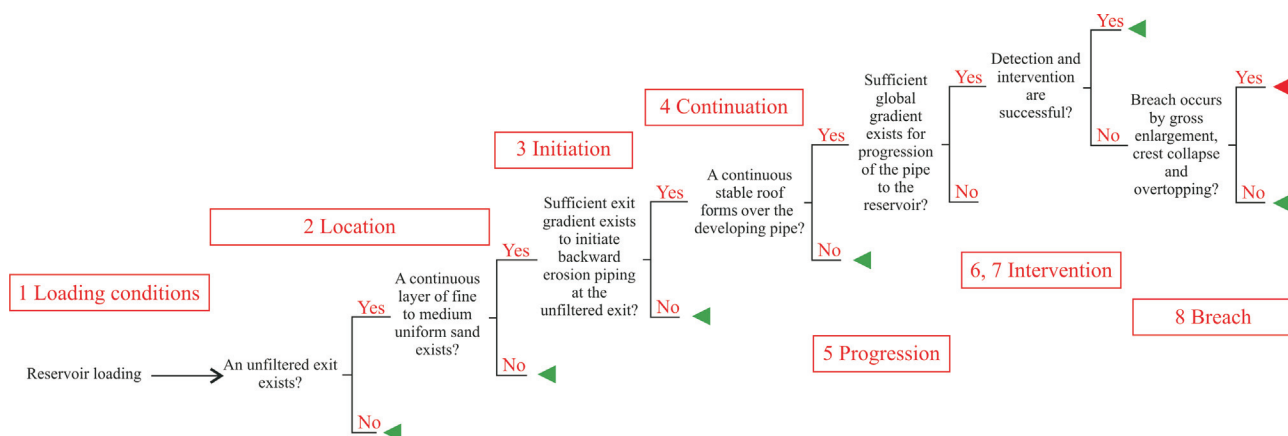


Figure 5 - Event tree for estimation of the probability of failure by backward erosion piping (adapted from Shewbridge, 2014).

or filters with continuing erosion be present along the seepage path ending in the formed pipe, that the pipe is stable, and that the reservoir level is sufficient high to continue the detachment and transport of the particles from the pipe surface (internal erosion progression). Breach initiation is less likely if some or excessive erosion are expected. Additionally, it is necessary that no detection or no timely intervention take place.

There are two basic approaches to make dams capable of resisting internal erosion: barriers, to prevent seepage from passing through the dam or foundation, and filters to trap any particles eroded by seepage, while allowing the water to drain away downstream.

In general, filters are associated to drains, which are a second stage to the first stage filter, and are used to convey larger amounts of seepage flow, in order to control the saturation level and the seepage pressure in the downstream section of the dam, and to carry the water to a safe and controlled exit. The filter and drains must have sufficient capacity to carry the volume of seepage water, and a permeability larger than any of the layers of the dam or foundation that encounters the filter. Otherwise, the pressure will build up in the layers with higher permeability.

#### 4. Tests to Assist the Assessment of Failure Probability Due to Internal Erosion

Some of the probability ranges associated to some of the branches of the event trees presented can be estimated through laboratory testing, namely, the dispersion of clayey soils, the soil erodibility, as well as the flow restriction and the crack filling actions. In the following, this section de-

scribes some of the tests used for those purposes, and presents their results.

##### 4.1. Pinhole test

For evaluating the adequacy of a filter, it is necessary to characterize the soil to be protected in terms of its dispersion. The pinhole test is possibly the most used direct and qualitative measurement of the dispersibility and colloidal erodibility of clayey soils.

Figure 6 shows the setup of the pinhole test, which models the action of water flowing along a flaw. The test starts with distilled water flowing horizontally under a hydraulic head of 50 mm through a 1 mm diameter pipe punched in a nominal 38 mm long specimen of clay. During the test, it is appreciated the cloudiness of the flowing solution emerging from the specimen, and evaluated the flow rate and the final size of the pipe through the specimen. The first measurement of discharge corresponds to the time, in seconds, required to collect 10 mL, and the following to the time interval required to collect 25, 50 or 100 mL of effluent. Normally, the duration of the test is 5 or 10 min (see Table 1). It is important to observe and record the characteristics of the pipe at the end of the test. Due to the heterogeneous nature of the soil, it is possible to have all the colloidal erosion develop in one or more small areas along the pipe through an undisturbed sample.

Flow from dispersive clay is dark, and the specimen pipe enlarges rapidly with an increase of the flow rate. Flow from slightly to moderately dispersive clay is slightly dark, but the pipe diameter and the flow rate remain constant dur-

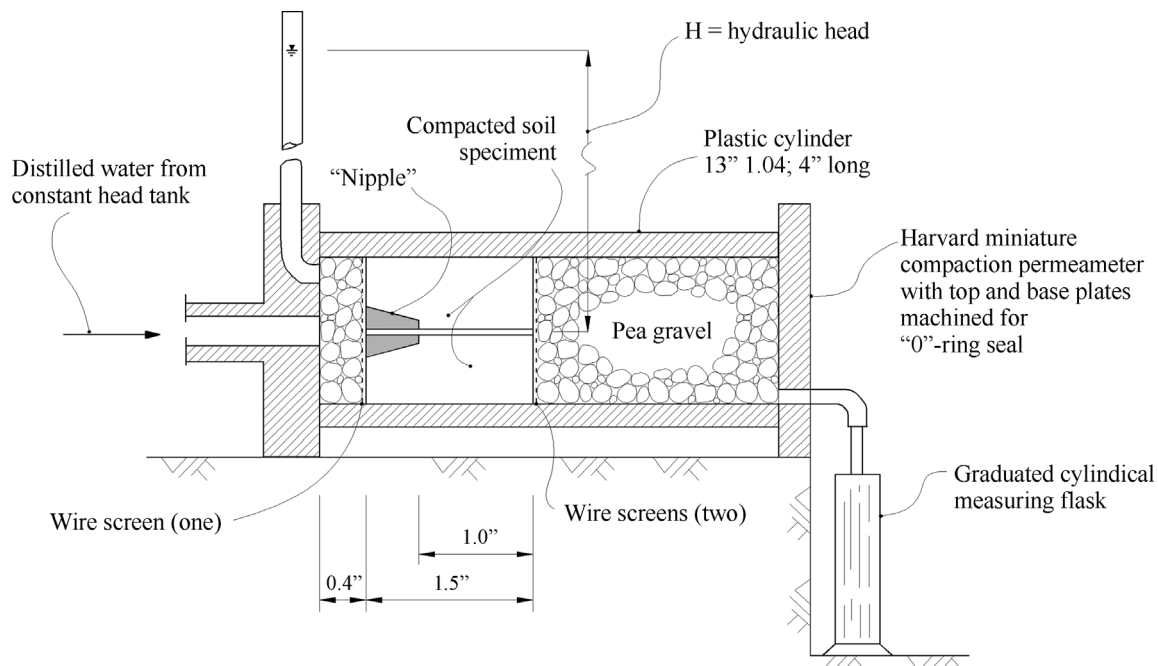


Figure 6 - Pinhole test apparatus (Sherard *et al.*, 1976).

**Table 1** - Summary of criteria for evaluating results of pinhole test (ASTM D4647 / D4647M, 2013).

Dispersive classification	Head (mm)	Test time for given head (min)	Final flow through specimen (mL/s)	Cloudiness flow at end of test		Hole size after test (mm)
				From side	From top	
D1	50	5	1.0-1.4	Dark	Very dark	≥ 2.0
D2	50	10	1.0-1.4	Moderately dark	Dark	> 1.5
ND4	50	10	0.8-1.0	Slightly dark	Moderately dark	≤ 1.5
ND3	180	5	1.4-2.7	Barely visible	Slightly dark	≥ 1.5
	380	5	1.8-3.2			
ND2	1020	5	> 3.0	Clear	Barely visible	< 1.5
ND1	1020	5	≤ 3.0	Perfectly clear	Perfectly clear	1.0

ing the test. In nondispersive clay, the flow is clear with no measurable increase in the pipe size.

Table 1 shows the criteria for evaluating the results of pinhole tests. Soils that fall into the categories D1 and D2 are dispersive. Soils that fall into the categories ND1, ND2, ND3 and ND4 are considered non-dispersive.

#### 4.2. Hole erosion test

For evaluating the probability of initiation of internal erosion induced by concentrated leaks, it is necessary to compare the applied hydraulic shear stress with the critical shear stress that will initiate erosion at the degree of saturation of the soil on the sidewalls of the flaw. For this purpose, it is necessary to carry a series of Hole Erosion Tests (HET) at varying heads.

This type of tests has been conducted in the laboratory to simulate erosion through a concentrated leak in an undisturbed cylindrical specimen or in an unsaturated soil specimen compacted into a mould. It is suitable for soils containing plastic or non-plastic fines, which will sustain an opening when wetted during the test.

Figure 7 shows a schematic diagram of the HET apparatus used at LNEC. The soil specimen can be compacted inside a standard Proctor mould, a 6 mm diameter hole is drilled along the centreline axis, and the mould with the specimen is assembled between two chambers made of acrylic glass. The monitoring devices of the HET are an electromagnetic flow meter, located upstream of the test cell, and two standpipe piezometers installed on the acrylic chambers near the ends of the test specimen. A control valve is installed upstream of the test cell, to assist in the test procedures.

The test starts imposing a selected head loss, by fully opening the control valve. During the test, the flow rate and the piezometric levels are recorded at regular intervals. The test ends when one of the following criteria is attained: 3 h of test duration; 1,000 L/h of flow rate; 25 mm of diameter of the pipe eroded; blocking or collapse of the erosion pipe.

After dismantling the test apparatus, the compaction mould is placed vertically, and the pipe filled in with melted paraffin wax. After cooling of the paraffin wax, the specimen is extracted from the compaction mould, and the soil surrounding the paraffin mould is carefully removed. The equivalent diameter of the resulting erosion pipe is estimated by measuring the paraffin mould volume. The paraffin mould also gives an indication about the shape of the erosion pipe at the end of the test, and the roughness of the surface along its length.

In order to have a successful test, a condition of progressive erosion must be achieved, where the enlargement of the pipe leads to further increase in shear stress and higher rates of erosion. When both the rate of erosion,  $\dot{\epsilon}$ , and the applied hydraulic shear stress,  $\tau$ , increase, they usually have an approximately linear relationship, given by

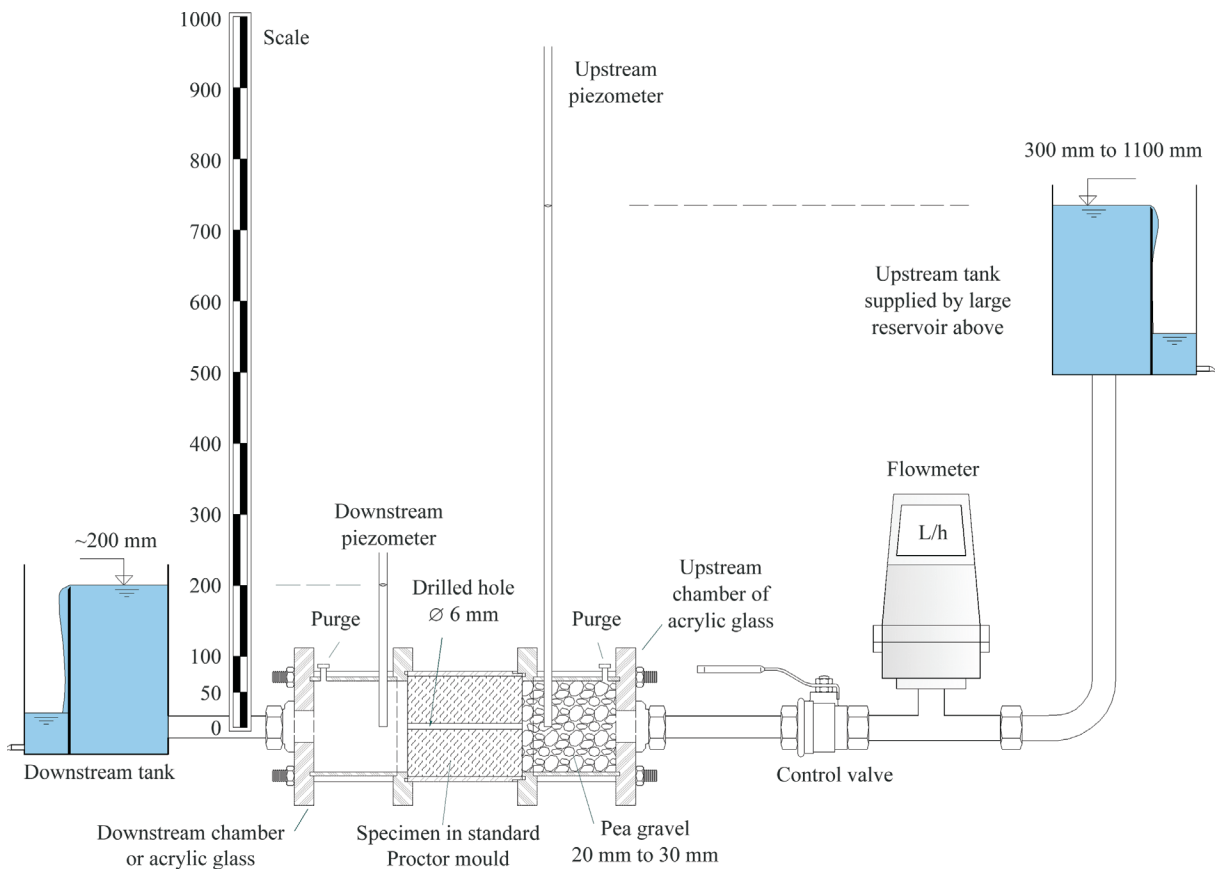


Figure 7 - Schematic diagram of the Hole Erosion Test (HET) setup used at LNEC (Santos, 2014).

$$\dot{\epsilon} = C_e (\tau - \tau_c)$$

(1) Fell (2002, 2004) have found it convenient to define the erosion rate index,  $I$ , as

$$I = -\log C_e \tag{2}$$

where  $C_e$  ( $\text{kg}\cdot\text{N}^{-1}\cdot\text{s}^{-1}$ ) is the coefficient of soil erosion, and  $\tau_c$  (Pa) the critical shear stress for soil detachment, which corresponds to the intersection of the straight line with the horizontal axis. This equation is valid only for  $\tau > \tau_c$ . Wan &

Figure 8 shows the results of a HET, with the evolution of the erosion pipe diameter and its time derivative

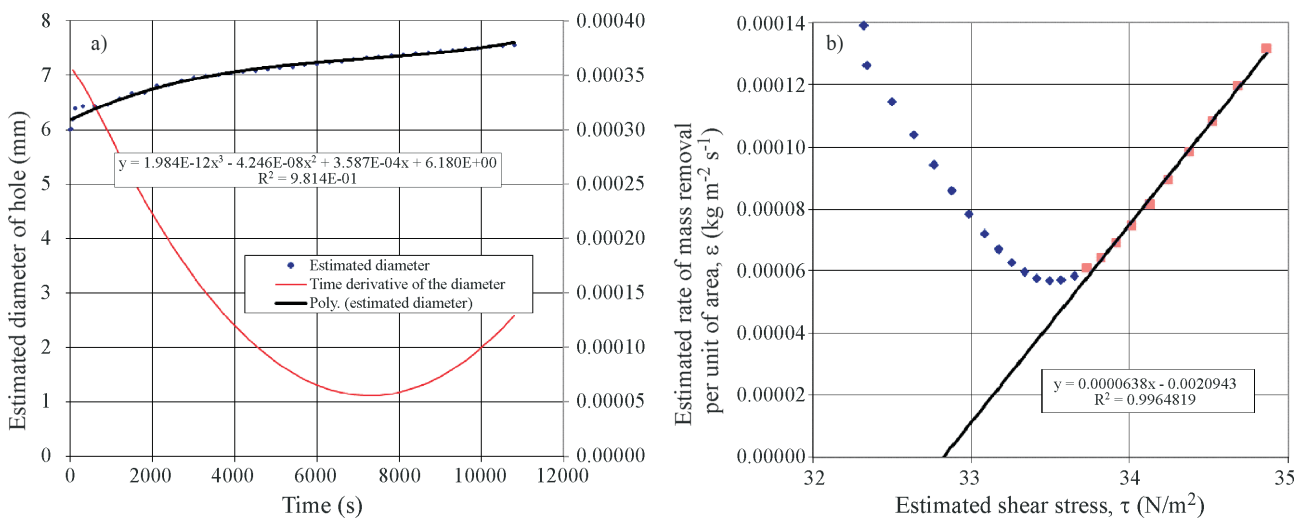


Figure 8 - Estimation of the diameter of the pipe and of the erodibility parameters: a) evolution of the erosion pipe diameter and its time derivative; b) erosion rate vs. applied shear stresses.

(Fig. 8a), used to estimate the erosion rate and shear stresses applied in the pipe walls along the test (Fig. 8b). Based on those results, the erodibility parameters are:  $C_e = 6.38 \times 10^{-5}$  s/m,  $\tau_c = 32.8$  Pa and  $I = 4.2$ .

Soils with erosion rate index lower than 2 are usually so erodible that they cannot be successfully tested in HET devices. Since erodibility is strongly influenced by the compaction characteristics, the authors have defined a representative erosion rate index,  $\tilde{I}$ , determined for soils compacted to 95% standard Proctor maximum dry unit weight at optimum water content, and the classification system is shown in Table 2. The time for erosion to progress is very dependent on the erosion properties expressed by the erosion rate index.

Most clayey soils tested have significantly higher erosion rate indices (slower erosion) and higher critical shear stresses when saturated than at the partially saturated compaction condition. This is an important finding because it means that once the core of a dam built of clayey soil is saturated and consolidated, it may have a slower rate of erosion, and a higher critical shear stress.

Intact samples, with in-place soil structure, are preferred to remoulded samples. Large differences of critical shear stresses are often noticed between them.

#### 4.3. Flow limiting erosion test

Fry (2007) states that an upstream shell of a relatively fine-grained material can generate such relevant head loss that it can stop the erosion in a crack passing through the core. The author considers that crack erosion is mainly dependent on the relation between the critical shear stress of the core and the permeability of the shell. Cyganiewicz *et al.* (2007) suggest that the likelihood of upstream soil cracking should also be considered, since the ability of an upstream material in limiting the flows may be substantial reduced if it can sustain the crack.

To study the flow restriction action, a new test apparatus and its setup procedures have been developed by Santos *et al.* (2014), aiming at the assessment of vulnerability to internal erosion progression of the cracked core of a zoned dam, taking into account the presence of a shell or transition zone upstream of the damaged core.

**Table 2** - Qualitative classification of erodibility of soils based on the representative erosion rate index (Wan & Fell, 2002).

Group	Representative erosion rate index	Classification
1	< 2	Extremely rapid
2	2-3	Very rapid
3	3-4	Moderately rapid
4	4-5	Moderately slow
5	5-6	Very slow
6	> 6	Extremely slow



**Figure 9** - LNEC test cell used in the flow limiting erosion test (Santos *et al.*, 2014).

Figure 9 shows the new test cell designed. It is composed of three aluminium plates, three aligned aluminium rings (with an inner diameter of 280 mm) and a circular cover plate of acrylic glass. The different pieces are sequentially assembled, as the core and the upstream material are being compacted, using threaded steel rods and nuts. The test cell allows the compaction of a specimen composed of a 170 mm long core, and an upstream material up to 250 mm long. The cell has a water inlet chamber, where, to ensure lateral support for the upstream material, two concentric springs of similar stiffness and a rigid annular or a porous plate are installed. At the downstream side, an outlet chamber collects the eroded material from the pipe in the core. The acrylic glass plate allows direct visualization into this chamber. The inlet and outlet chambers have purge valves used for air release/entrance during the filling/emptying of the test cell.

Figure 10 shows a schematic diagram of the setup of the flow limiting erosion test (FLET). A pipe is drilled in the centre of the core to model a concentrated leak. In some tests, to take into account the observation by Cyganiewicz *et al.* (2007), the pipe is also drilled in the upstream material. The specimen is subjected to water flow imposed through a constant hydraulic head loss. The measurements made during the tests include piezometric heads, flow rate, and visual observations through the downstream acrylic glass cover plate. The particle transportation and the turbidity of the effluent observed through the acrylic cover plate are recorded using a digital camera. Detailed information about the test cell, specimen preparation, test concept, test setup, and test procedures can be found in Santos *et al.* (2014).

The FLET results allow the identification of four types of behaviour: flow stopping or decreasing greatly due to upstream pipe collapse (type F1), flow limitation to a threshold value (type F2), slowing down of core erosion (type F3), and progression of severe erosion (type F4). Figure 11 shows the trend of the flow rate for each behaviour

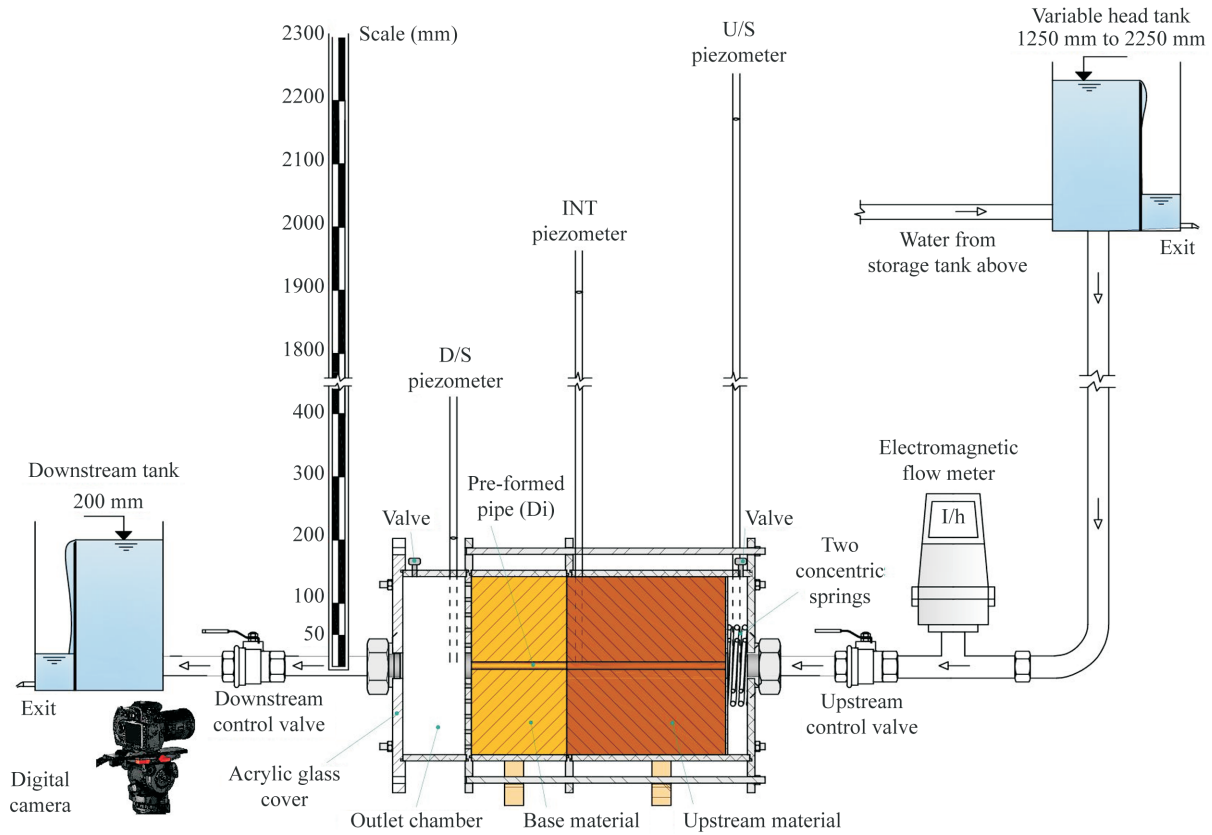


Figure 10 - Setup of the FLET (Santos, 2014).

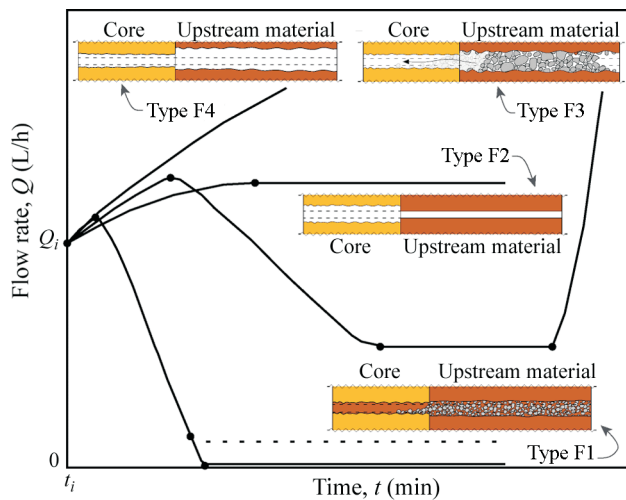


Figure 11 - Behaviour types observed in the FLET (Santos *et al.*, 2014).

type, and illustrates the typical layout of the specimen at the end of the tests.

An extremely rapid erosion of the fines in the inner surface of the erosion pipe in the upstream material, followed by the release of the surrounding coarser particles with fast increasing flow rate, characterize the behaviour type F1. After a short time, some of those coarser eroded

particles are trapped inside the core pipe, which has no erosion, since the core material has considerably higher resistance than the upstream material. The flow rate starts to diminish while the upstream material continues to erode, filling the voids between the trapped particles with even smaller particles. This results in the progressive limitation of the water flow, and the collapse of the pipe in the upstream material, due to prolonged soaking.

Type F2 occurs when the upstream soil is non-erodible for the applied hydraulic load. The initial increase of the flow rate is mostly due to the erosion of the pipe in the core. In general, this occurs with the drop of the hydraulic head loss in the core and with a slight increase of the hydraulic head loss in the upstream material. Consequently, the shear stress, due to the eroding fluid on the pipe surface in the core, decreases below its critical value. The erosion process in the core slows down substantially, or even stops, resulting in a constant flow rate.

In type F3, after the initial increase of the flow rate, the fines of the upstream material erode at a faster rate than the core. This results in release of the coarse particles of the upstream material, whose maximum dimension is higher than the diameter of the pipe in the core. These particles become trapped at the interface with the core, resulting in near-stabilization of the flow rate. Nevertheless, this rate is sufficiently high to continue to erode the core, and those

coarse particles end up being transported from the interface downstream, with the flow rate increasing with no marked restriction.

In type F4, the flow rate increases continually at a very fast rate, mainly because of the high erosion rate of the upstream material. Despite the low erosion resistance of the upstream soil, the developing erosion pipe sustains its roof during the progression of erosion.

Soils exhibiting behaviour type F1 are considered highly capable of stopping the leak along the flaw. Soils with behaviour type F2 are effective at limiting the increase of the flow and thus controlling the progression of the internal erosion along a flaw in the core. Upstream soils showing type F3 and type F4 cannot be relied upon for providing limitation to the progression of internal erosion.

#### 4.4. Crack filling erosion test

There are very few laboratory experiments focused on this topic. The exceptions are the laboratory tests carried out by Maranhã das Neves (1989, 1991), at LNEC, with the Crack Erosion Test (CET). The CET allowed, for the first time, the direct observation of the transport of eroded materials, from a crack wall to the filter face, as well as the assessment of the filtering mechanism at the filter layer. Using a uniform layer located upstream of the core (which acted as a crack stopper), the tests performed also enabled the visualization of the crack filling action. Figure 12 shows the setup of the CET. This apparatus allows to test any crack orientation (horizontal, vertical or inclined), by setting the position of the test cell, and a range of applied hydraulic gradients and crack apertures. The original test setup, represented in Fig. 12, was slightly changed by replacing the pea gravel layer enwrapped with an upstream soil acting as crack filler.

Instead of simulating a crack, the crack filling erosion test (CFET), designed by Santos *et al.* (2015) to study the crack filling action, uses the test apparatus and cell developed for the FLET. For establishing the setup procedures,

the authors assumed the following basic assumptions: there is a downstream filter that may not properly filter the particles eroded from the core, but can retain some of the particles that are washed from the upstream material. Consequently, this test aims to assess the vulnerability to internal erosion progression of the cracked core of a zoned dam, taking into account the presence of a shell or transition zone upstream, and an inadequate filter.

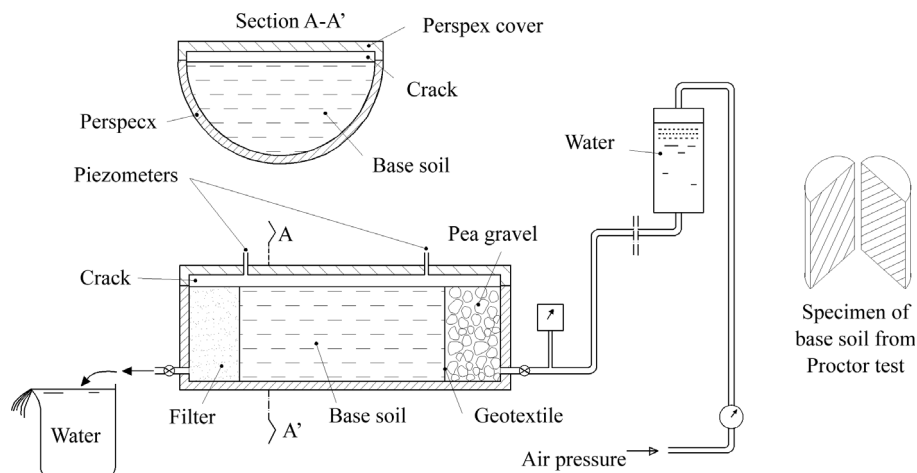
As in the previous type of test, the different pieces of the test cell are sequentially assembled, as the core, the upstream material, and the filter are being compacted. The downstream filter is compacted within the outlet chamber, which allows the compaction of a specimen with a 120 mm long filter. A pipe is drilled in the centreline of the core to model the concentrated leak.

Figure 13 shows a schematic diagram of the specimen used in a CFET. The hydraulic loading conditions, measurements and observations made during the tests are those described for the FLET. Detailed information about the specimen preparation, test concept, test setup, and test procedures can be found in Santos *et al.* (2015).

The CFET results allow the identification of three main types of behaviour: rapid crack filling with almost no



**Figure 13** - Longitudinal section of specimen in a typical CFET (Santos, 2014).



**Figure 12** - Setup of the Crack Erosion Test (Maranhã das Neves, 1989).

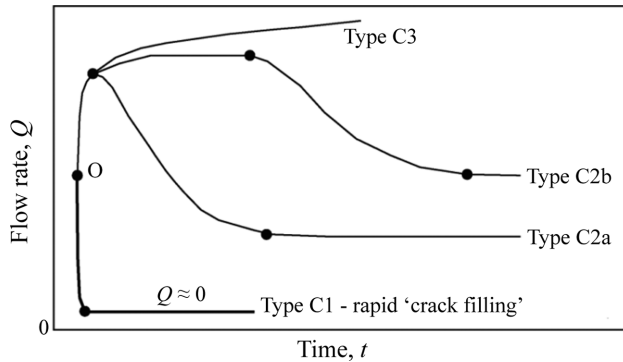


**Figure 14** - Behaviour types observed in the CFET (Santos *et al.*, 2015).

erosion of the core (type C1), filtering and stabilization after erosion of the core and/or upstream material (type C2), and continuing erosion of the core and upstream material (type C3). Type C2 behaviour can be divided into two groups: after some erosion (type C2a), and after excessive erosion (type C2b). Figure 14 shows the trend of the flow rate for each behaviour type and Fig. 15 displays the typical layout of the specimen at the end of the tests.

An extremely rapid transport of a considerable amount of particles of the upstream material at the interface with the core, along the pipe (forming a 'sand jet') up to the downstream filter face, characterizes the behaviour type C1. The flow rate falls abruptly at an earlier stage of the test.

In tests of type C2, the flow rate increases rapidly due to the development of suffusion in the upstream material. The downstream filter is unable to retain this fine material coming from the upstream material. At a given time, the hydraulic shear stresses, applied to the inner surface of the pipe, reach values high enough to detach the sand-size particles, which are retained at the downstream filter face. This filtering mechanism leads to a progressive decrease of the flow, even to its stabilization. The eroded particles are transported by flow up to the filter face, and, then, slowly seep into the filter. This leads to two opposite effects on the flow rate. On the one hand, the widening of the pipe diameter tends to increase the flow, and, on the other hand, the decrease of the filter permeability causes the decrease of the seepage flow. This balance may result in an increase or stabilization of the flow for a period.

In tests of type C3, the flow rate increases rapidly. There is a fast progression of suffusion in the upstream material, and the filter is too coarse to retain those particles.

Upstream soils showing behaviour type C1 in the CFET are considered highly capable of rapidly filling cracks in the core, and are effective in limiting the progression of internal erosion. Upstream soils exhibiting behaviour type C2 can stop the progression of the internal erosion process by providing the filtering mechanism, which will occur after some erosion or after excessive erosion. Upstream soils showing behaviour type C3 cannot be relied upon for providing any effect on the progression of internal erosion caused by a crack-filling action.

## 5. Knowledge Gaps in the Internal Erosion Failure Process

There are some topics in the methodology and tests presented that need further investigation in theoretical and experimental terms, namely the following are recognised as very important:

- the conditions required for the stability of the walls of cracks or the roof of pipes during and after the erosion process;
- the influence of the seepage forces in the stability conditions in both types of internal erosion mechanisms (along concentrated leaks or backward erosion piping);
- the representativeness of the laboratory tests, mostly performed on pipes, for the evaluation of erodibility conditions along cracks.

The concern about the structural behaviour of a dam has always been to try to ensure a ductile, thus more stable, structural behaviour, for which conditions of placement and construction should be established so as to locate the soil on the wet side of the critical state line (CSL), exhibiting a contractile behaviour. According to the critical states concepts, the soil must be in a state of optimal compaction when subjected to the service loads. Over-compaction has the risk of cracking the soil body in blocks, presenting a permeable to highly permeable behaviour as a whole.

An element of the core after compaction is characterized by its non-saturated state and some overconsolidation, that is, the value of  $\eta = q/p'$  is less than  $M$ . The stresses in the element will proportionally increase due to the weight of the overlying embankment. The mean stress increment

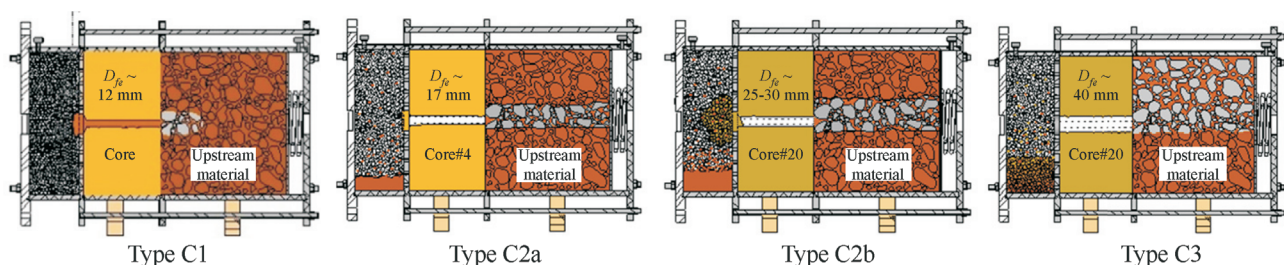


**Figure 15** - Typical layout of the specimen at the end of the tests (Santos, 2014).

determines a reduction in void ratio, and if the initial saturation degree is relatively high (80 to 90%), the soil becomes saturated. Nevertheless, at the end of construction, the stress state will remain slightly OC (point A in Fig. 16). The soil will then exhibit a stable contractive behaviour.

When the dam is in operation, the total stresses before and after reservoir filling are practically constant, and the rise of the water level in the reservoir will induce saturation in most of the core. However, it will also increase the pore water pressure,  $u_w$ , decreasing the effective stress, and the soil becomes progressively OC ( $p'$  decreases and  $q$  remains, from a practical point of view, constant). The corresponding stress path is represented in Fig. 16 by the arrow  $AB$ . Depending on the value of  $u_w$  and the depth of the element, the soil can reach a highly OC state (point B in Fig. 16). Figure 16 also shows that, the larger the value of  $\eta$  (represented, for example, by point  $B_1$ ), the larger the increase in the specific volume needed to reach failure, *i.e.*, the critical state.

Independently of some precisions relative to the above (total pressure increase with soil saturation, flow effect, etc.), in general terms, a core transition effect is plausible from slightly OC to strongly OC, associated with the filling of the reservoir, especially at dam lower levels (Maranha das Neves, 2018).

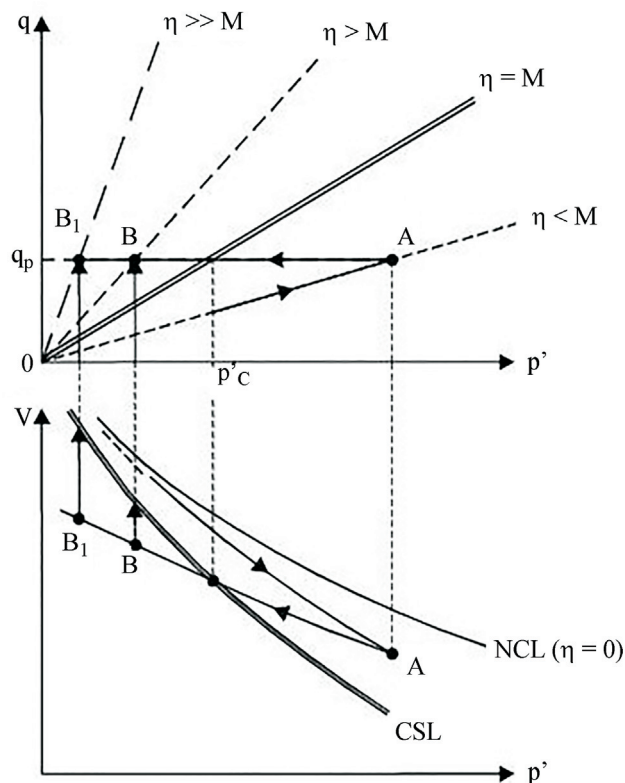


**Figure 16** - Decrease of  $p'$  due to the increase of  $u_w$ , bringing the soil from a slightly OC state to very OC states (passage of a contractile behaviour to a dilative behaviour) (Maranha das Neves, 2018).

The mechanical (and hydraulic) behaviour of a saturated highly OC soil is very different from that of a NC soil or slightly OC. This contrast is well identified in the behaviour map of a saturated remoulded soil (Fig. 17) presented by Schofield (2005). In this figure,  $v_\lambda$  is a measure of the liquidity and degree of compaction of a set of stressed soil particles, and  $\eta = q/p'$  is a measure of the stress obliquity. The left part of the map is of major interest as it concerns heavily OC soils. The contrast of the soil behaviour in this area with that of the area on the right is flagrant. In the latter, the soil behaviour (NC or slightly OC, that is, with OCR of the order of 2.5) is the most well known and, in terms of the stability of most geotechnical structures, the desired one.

In the leftmost part of the map ( $\eta = 3$  in compression), the action of  $q$  can originate several types of possible mechanical and hydromechanical behaviour, such as cracking, generation of fluidized soil blocks (rubbles), hydraulic fracturing and internal erosion (piping). They all are situations difficult to model, barely known in their characteristics. For  $M_c < \eta < 3$  (in compression), the action of  $q$  gives rise to impervious sliding planes (in the sense that the water pressure on a slip surface does not transmit to that of the neighbouring soil).

It should be noted that the stress-strain behaviour of highly OC soils is far from having been as well studied as that of the NC or slightly OC soils. In the former, the occurrence of shear bands, despite the many difficulties that the subject raises, has been widely studied. In the evaluation of the localization, it is legitimately assumed that the soil is uniform, since the shear bands corresponds to a plastic flow. But, once critical situations are established regarding the obliquity of stresses, such legitimacy is indeed dubious (Gudehus, 2011).

On the other hand, a prolonged major drawdown of the reservoir will substantially increase effective stress and the undrained strength. With the refilling of the reservoir, the water content will be increased but it will not reach the values before the lowering of the water level in the reservoir, resulting in an increase of the undrained strength and the resistance to hydraulic fracture (Atkinson *et al.*, 1994). This helps to explain why hydraulic fracture, in undrained conditions, is more likely to occur during the first impounding of the reservoir.

Consider, now, a longitudinal or transversal vertical crack developed during construction or induced by hydraulic fracture after or during reservoir filling, and filled with water. Knowing that saturated soils do not exhibit effective cohesion, what must be analysed is if there is a justification, based on the high OC generated by the increase in pore water pressure, for crack sidewalls to be stable. This must consider the equilibrium of the flat face of the soil element where the effective normal stress is zero. Up to now, there is no knowledge of studies that meet all of these conditions (of experimental nature or based on the study of mechanical

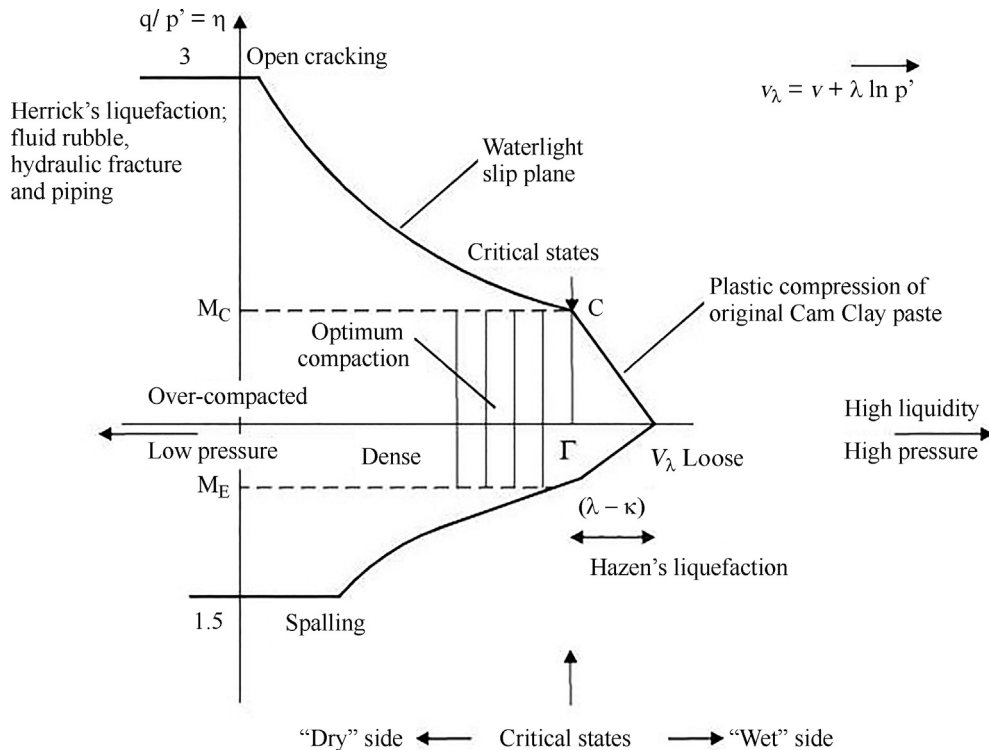


Figure 17 - Map of disturbed saturated soil behaviour (Schofield, 2005).

behaviour), as well as the stability condition of cracks in unsaturated soils. In addition, the mechanism of hydraulic fracture in dam cores remains to be fully resolved (Atkinson *et al.*, 1994).

There is no doubt that cracks decisively influence the mechanical behaviour of the soil, but it is very difficult that the occurrence of cracks can be detected using constitutive relations. The transport of pore water and air becomes chaotic due to cracks, which can lead to a deterioration of the soil skeleton and internal erosion (Gudehus, 2011).

The study of the stress-strain behaviour of highly OC soils at low effective stress will be carried out at LNEC, using triaxial tests. The stress path of a soil element of the core during construction, first filling and operation of a dam will be simulated, in order to assess the failure mechanism and configuration, and the strength of the soil in those conditions.

Another question is the contribution of the seepage forces to the stability of the walls of cracks or the roof of the pipes originated by both internal erosion mechanisms (concentrated leakage and backward erosion piping). An example of a flow net induced in the cracked core of a dam is presented in Figure 18. Around the crack, the flow lines diverge from the crack and the seepage forces are directed into the core, having a stabilizing effect on the crack walls.

Figure 19, on other hand, represents the flow nets of an incipient pipe and of a developed backward erosion pipe. Based on this figure, it can be concluded that the erosive capacity of the erosion pipe increases as its length, as well as

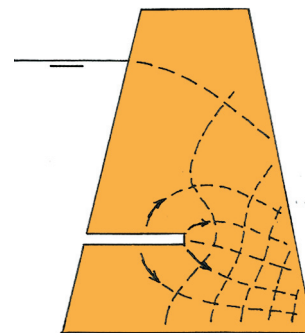
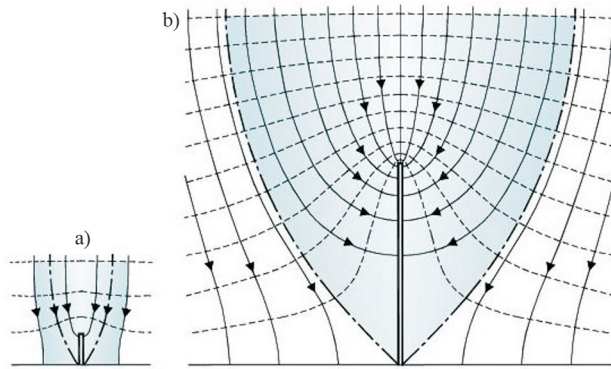


Figure 18 - Flow net in a homogeneous core with a crack (Löfquist, 1992).

the intake area (in blue), increase. The seepage forces originated by the flow in the soil are directed towards the pipe, having therefore a diminishing (or negative) effect on the pipe stability.

These opposite effects of seepage forces on these mechanisms may help to justify the fact that the hydraulic gradient needed to induce backward erosion piping is much lower than that required for erosion along concentrated leaks. Nevertheless, this subject requires further and systematic investigation.

As described in the previous section, the most commonly used tests involving internal erosion mechanisms rely on pipes in cylindrical specimens, which are easier to prepare. However, their results are used to evaluate the soil erodibility along cracks and the flow restriction and crack



**Figure 19** - Flow nets illustrating increase of flow intake area as length of erosion pipe increases: a) incipient state; b) after backward erosion piping has proceeded to a considerable distance from the exit point (Terzaghi *et al.*, 1996).

filling actions, which have very distinctive geometry, boundary conditions and stress state around the crack. Moreover, the tests are generally performed on unsaturated soils, imposing hydraulic gradients much higher than those present in dams.

Carrying out HETs, FLETs and CFETs, using cracks with different orientations to model a concentrated leak in the core, can be helpful for the research on the differences in terms of stability, erodibility, flow limitation and crack filling actions between cracks and pipes. Presently, these tests are being performed and their results compared with those of pipes, to establish correlations or correction factors between both flaw geometries.

Nevertheless, the relationship between dam internal erosion and the laboratory tests is less certain, and the results must be carefully calibrated with data from real case studies.

## 6. Case Studies

### 6.1. Lapão dam

Lapão dam is located in the central part of Portugal, with a total reservoir volume of  $1.26 \times 10^6 \text{ m}^3$ , and was built for water supply and irrigation purposes. The dam, with a maximum height of 39 m, is constituted of clayey and silty materials in the upstream shell and core, and materials re-

jected from Mortágua and Gândara ceramic industries in the downstream shell, essentially composed of clayey sands and gravels (Fig. 20). An internal drainage system, with a vertical filter, a horizontal drainage blanket over the riverbed and a downstream toe drain, was designed to control the seepage through the dam body and its foundation. The downstream shell also contains several horizontal drains to help the dissipation of pore water pressures resulting from the construction process. The upstream and downstream slopes are, respectively, 1(V):4(H) and 1(V):2.9(H). The normal water level (NWL) is 217 m, the maximum water level is 218.6 m, and the crest elevation is 220 m. The downstream slope includes an access road to the bottom outlet exit. The dam is inserted in a narrow valley, with very steep slopes (1(V):1.39(H), at the left riverbank, and 1(V):1.32(H), at the right riverbank), especially at the bottom, where the slope reaches 1(V):0.32(H) (Fig. 21).

The rock foundation is constituted by schistose rocks, highly fractured superficially. From the hydraulic conductivity point of view, a series of Lugeon tests was executed, in which very high absorptions were recorded down to 15 m depth. Nevertheless, during construction, the foundation treatment was limited to a restricted zone in the right riverbank, discarding the bottom valley and the left riverbank.

During the first filling of the dam, in 2002, only 2 months after the beginning of the reservoir filling, when the water level was 211 m, it was detected an extensive cracking and settlements at the crest, mainly at the interface with the spillway structure (Fig. 22). As a precautionary measure, it was decided to lower the reservoir level, to open the bottom outlet valve, to carry out a proper field and laboratory investigation, and to install additional monitoring devices to identify the causes of such anomalous behaviour of the dam.

In January 2003, after an intense rainfall in the catchment area, the reservoir level exceeded the NWL. It was recorded a large increase of seepage at the downstream toe drain exit with cloudy water, as well as the formation of sinkholes in the berm over the toe drain (Fig. 23) and in the access to the bottom outlet valve (Fig. 24). These cavities were promptly filled with sand bags to reduce the rate of progression of internal erosion (Fig. 25), and the labyrinth weir of the spillway was partial demolished to lower the

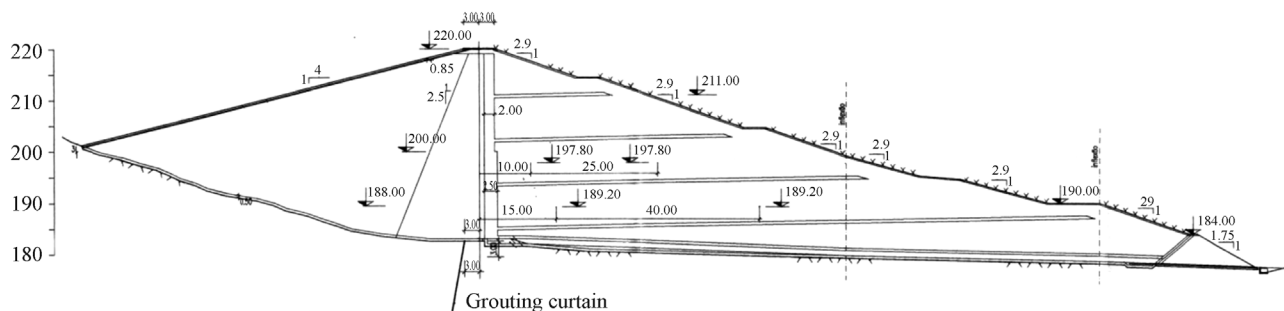


**Figure 20** - Typical cross section of Lapão dam.



**Figure 21** - General view of the bottom valley before construction and during the placement of the drainage blanket.



**Figure 22** - Extensive cracking and settlements at the crest.

water level in the reservoir (Fig. 26). During and after emptying of the reservoir, two upstream sinkholes were noticed at the spillway wall vicinity (Fig. 27).

The analysis of the design and construction available elements, field and laboratory tests results, monitoring data, and results from the visual inspections (Marcelino *et al.*, 2003) led to the following conclusions.



**Figure 23** - Sinkhole in the berm over the toe drain.

Based on the valley shape and rock mass characteristics at the foundation and abutments, the design should include transition zones composed of plastic materials compacted on the wet side in contact with the rock formation and the spillway structure, as well as, in the lower part of the dam, where the arching effects could be significant.

Lefranc and Lugeon tests carried out at the foundation and foundation-embankment interface allowed to detect several high permeability zones. The drainage blanket dimensions seemed to be insufficient to catch and safely carry the seepage water downstream.

The records of the compaction control tests revealed that the embankment was compacted with water contents lower than the optimum, which could result in an excessive stiffness and high susceptibility to cracking induced by wetting collapse or differential settlement. They also showed that the average thickness of lifts was excessive for the vibrating rollers adopted.



**Figure 24** - Sinkhole in the access to the bottom outlet valve.



**Figure 25** - Sand bags placed inside the sinkholes.

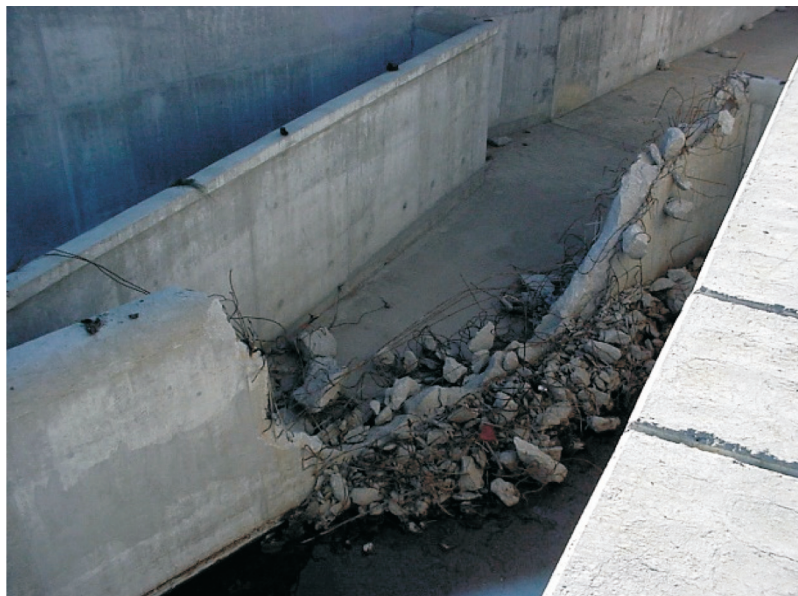


**Figure 26** - View of the spillway after partial demolition of the labyrinth weir.



**Figure 27** - Upstream sinkhole in the spillway vicinity.

The *in situ* investigation confirmed that the embankment was poorly compacted, especially in the upper part of the dam.

The monitoring data indicated a deferred increase of the settlement rates with the increase of the water level in

the reservoir, and horizontal displacements towards upstream and in the valley direction, during the first filling (Marcelino, 2004, 2008). The results of two groups of total cell pressures showed very pronounced arching effects at the bottom of the dam, with the vertical stress of the group at elevation 187.7 m (32 m deep) reaching the minimum value of 100 kPa (Fig. 28). It is apparent in this figure that, especially during the first filling, the embankment experienced significant changes in the stress field, capable of causing hydraulic fracturing.

The above description of the dam and of its behaviour allows to conclude that internal erosion processes have occurred in Lapão dam, initiated by two simultaneous mechanisms, both induced by concentrated leaks. The first was caused by arching in the lower part of the dam, which resulted in hydraulic fracture during the filling of the reservoir. The cracks remained open until pore water pressure dropped because of the lowering of the reservoir water levels. The cracks that closed, probably, re-opened when the reservoir water level raised during the intense rainfall event of January 2003, producing the downstream toe sinkhole.

These arching effects are due to the very narrow shape of the bottom valley and the very difficult compaction conditions in the lower part of the dam, and have been confirmed by the total pressure cell data. The materials of the core and shells, being unsaturated clayey materials, could easily sustain the crack, so the internal erosion process could continue as long as the hydraulic gradient was enough to erode the walls of the crack, leading to the formation of the sinkhole over the downstream toe drain.

The other mechanism is associated to the interface between the embankment and the spillway wall, and the con-

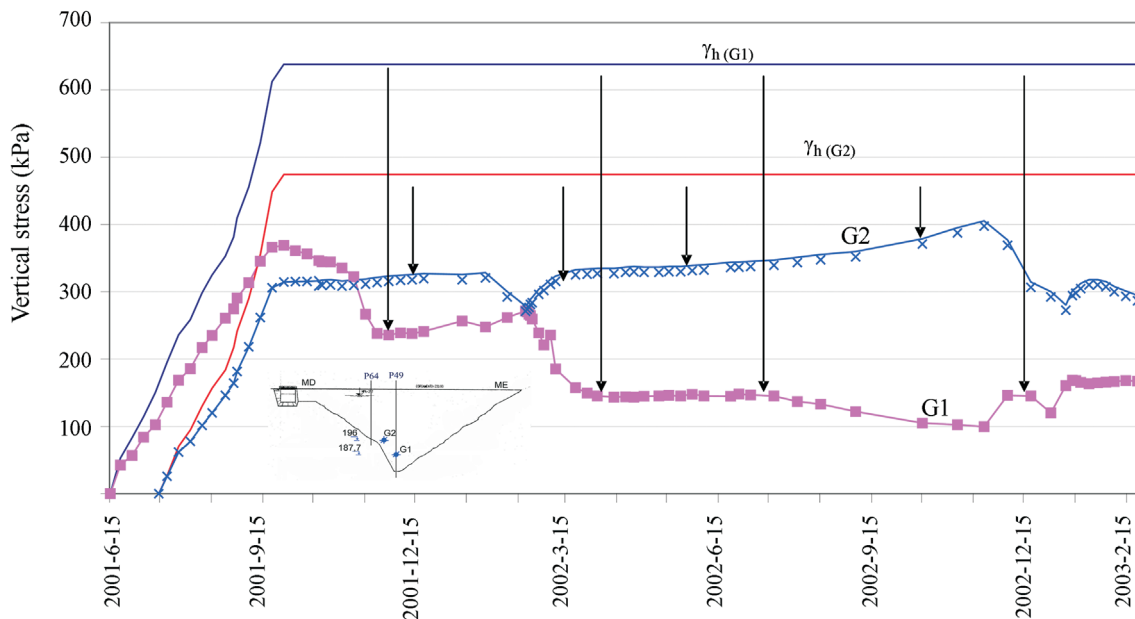


**Figure 28** - Vertical stress recorded in the cell groups G1 (at elevation 187.7 m) and G2 (at elevation 196 m) and corresponding overburden stresses.

ditions of the (poorly compacted) upper part of the dam. Vertical walls are likely to have gaps, where the soil collapses on saturation, forming a flaw (an open pathway) in which water flows. The upper parts are also more likely to be affected by cracking and hydraulic fracture due to differential settlements within the dam and its foundation during and after construction. The effects of this mechanism are the upstream sinkholes and the various downstream sinkholes near the spillway wall.

Additionally, the internal drainage system was not properly designed or built to protect the dam given that cloudy water flowed downstream.

## 6.2. Crestuma-Lever dam

Crestuma-Lever dam (Fig. 29), located 13 km upstream from Porto, is the last downstream hydropower scheme of a dam cascade system in the Douro River, which comprises 6 Spanish and 8 Portuguese dams. The catchment covers 97,603 km<sup>2</sup>. The dam was designed and built by Electricity of Portugal (EDP) (completed in 1985) for hydropower purposes (105 MW), water supply and river navigation. The dam safety control has been followed-up closely by EDP, with technical support from the National Laboratory for Civil Engineering (LNEC).

Crestuma-Lever dam must cope with a very wide range of flow discharges (the maximum flood discharge is 26,000 m<sup>3</sup>/s) and a considerable variation of water depths downstream (from a few meters to over 20 m), involving tidal effects. To deal with these hydraulic constraints, a gated dam was designed, composed of 8 concrete stilling basins (56 m long), equipped with double leaf vertical roller gates (28 m wide, 13.8 m high - Fig. 30), supported by seven concrete piers, discharging floods by the crest and bottom. These piers reach the schist bedrock, and cross 40 m of sandy soils. The stilling basins rest in the alluvial riverbed. To reduce the seepage flow and hydraulic gradi-

ents, upstream and downstream partial concrete cut-off walls were adopted, reaching elevation -17.50 m.

For the construction of the dam, two cofferdams were used in each riverbank (Fig. 31), essentially formed by the natural sand of the river bed as shells and a central concrete diaphragm wall, properly sealed to the bedrock. In the central part of the river (stilling basins 1E and 3E), two plastic self-hardening slurry walls (constituted of bentonite and cement, represented in Fig. 31 in red) were executed upstream and downstream down to the bedrock, at a distance of around 1 m from stilling basins 1E and 3E.

This solution is particularly sensitive to any abnormal scouring of the riverbed downstream, and its foundation to backward erosion piping, especially stilling basins 1E and 3E. To prevent uncontrolled scouring, the riverbed has been protected with rockfill extending 80 m downstream of the spillway (Fig. 32), placed over filter layers to inhibit the initiation of backward erosion piping.

From the records of the spillway operation, it was concluded that the most severe conditions concerning energy dissipation are those involving flow passing under the gates. In fact, in special conditions, the hydraulic jump can be pushed downstream of the stilling basin end sill, or even worse, the outflow can be, in essence, a high energy horizontal jet (Melo *et al.*, 2014).

Regular surveying of the downstream rockfill stability has been carried out. Particular attention has been given after the occurrence of significant flood discharges. The survey completed after the first significant flood (13,000 m<sup>3</sup>/s), in the 1989/90 winter, detected a 4 m deep scour cavity in the initial 10 to 20 m of rockfill, and a 1 to 2 m high bar around 30 m downstream of the spillway end sill in three out of the four basins surveyed. The following surveys showed a general scour of the rockfill protection close to the downstream concrete cut-off wall (Fig. 33). Three-dimensional bathymetry surveys performed from



**Figure 29** - Crestuma-Lever dam aerial view.

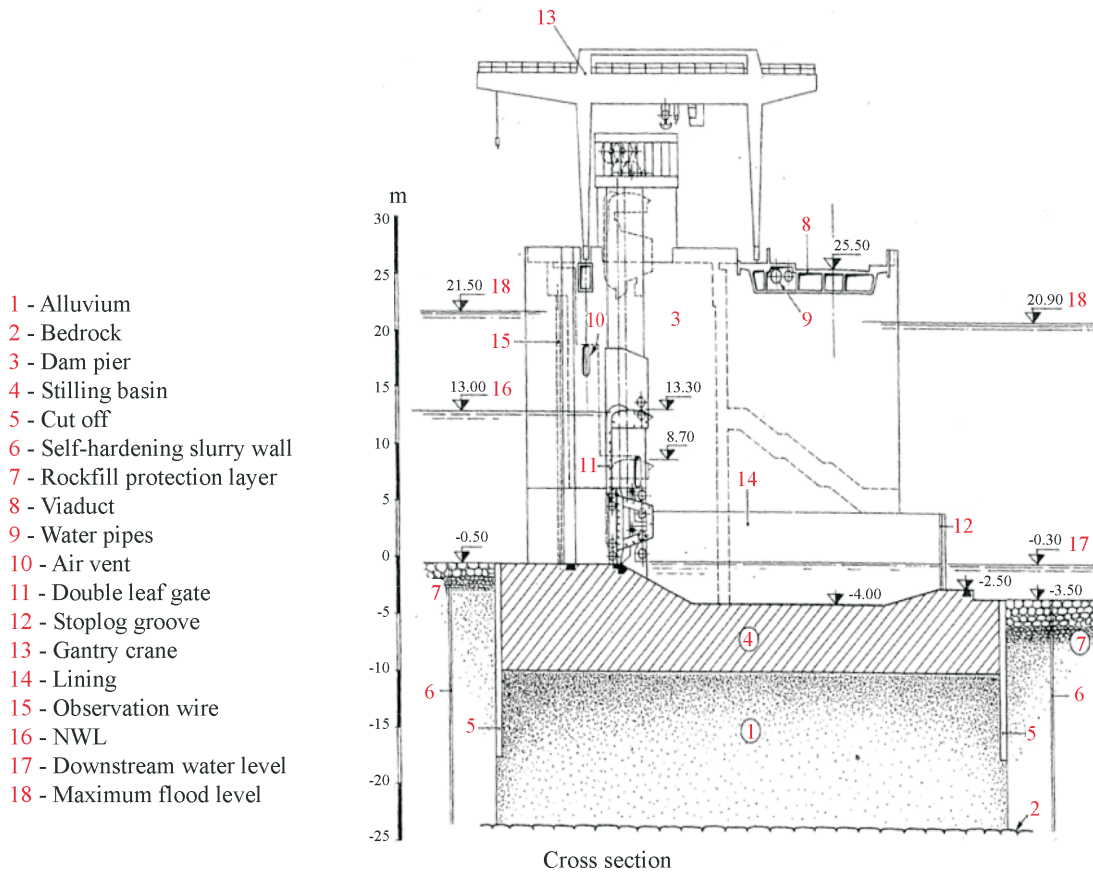


Figure 30 - Crestuma-Lever cross section (Álvares Ribeiro *et al.*, 1982).

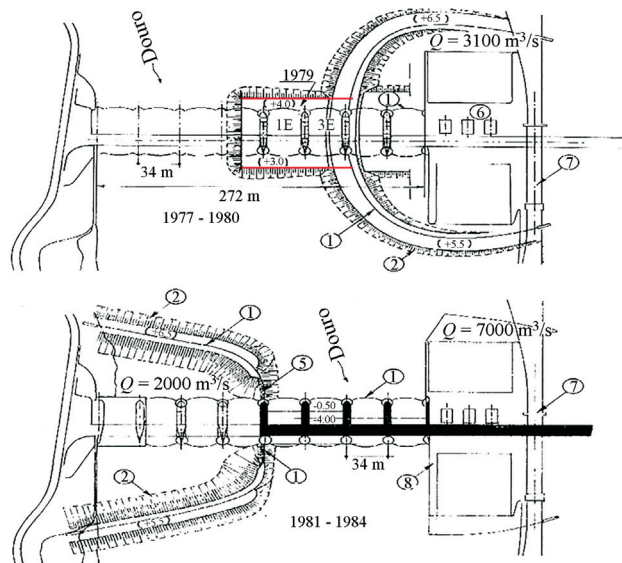


Figure 31 - Crestuma-Lever cofferdams and plastic self-hardening slurry walls, in red (Álvares Ribeiro, 1991).

October 2007 onwards confirmed the previous general scour near the stilling basins. Also visual inspections performed by divers showed that most material in the scour depression was formed by sediments and that the protective

rockfill and underlying filter layers, adjacent to the downstream cut-off wall zone, were severely damaged.

In these circumstances, unprotected exits of the seepage flow in the downstream foundation existed, as well as a continuous layer of fine to medium uniform sand in contact with the stilling basins. Therefore, there were conditions for the initiation of backward erosion piping if a sufficient hydraulic gradient was induced at the exit point. If initiated, this phenomenon would tend to progress and continue, given that the overlying concrete structures constitutes an artificial roof, which could allow the enlargement of the formed pipes.

In 2012, after 27 years of systematic observation of the rockfill, it was decided to perform a detailed analysis of the causes for the unexpected rockfill scour, and an assessment of the risk of backward erosion piping in the alluvial foundation.

A seepage study through the foundation of stilling basins 1E and 3E was carried out by LNEC (Caldeira *et al.*, 2012). For that purpose, a 2D numerical model was developed using the PlaxisFlow 1.1 software. The main goals of the model were to assess the conditions for initiation of downstream backward erosion piping and hydraulic heave. The model allowed a comparison of foundation behaviour considering the design assumptions and the scouring condi-

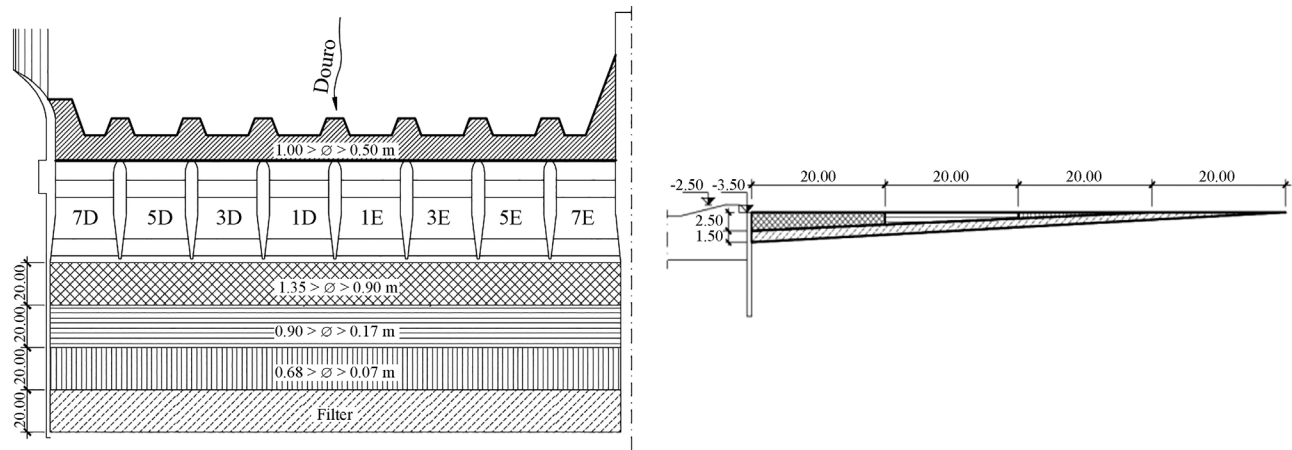


Figure 32 - Rockfill downstream protection (Caldeira *et al.*, 2013).

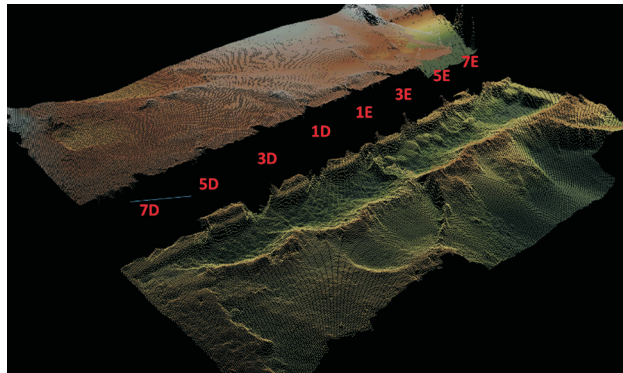


Figure 33 - Downstream rockfill scour (Caldeira *et al.*, 2013).

tions observed in 2012. Geotechnical investigation data, dating back to May 1972, was used to estimate the foundation hydraulic conductivity and the critical hydraulic gradient of the superficial alluvial formation. Data from piezometer readings provided information on pore water pressures of the foundation to calibrate the main parameters of the model. The finite element model reproduced the ge-

ometry of the stilling basin, concrete cut-off walls and self-hardening slurry walls. The riverbed was modelled considering a 32.5 m thick alluvium layer, over a 4.0 m thick layer of slightly weathered rock on top of an 8.0 m thick layer of moderately weathered rock. Figure 34 shows that, in stilling basins 1E and 3E, the flow is concentrated in the upstream and downstream zones between the basin and cut-off walls and self-hardening slurry walls, increasing the exit hydraulic gradients, and decreasing the safety conditions in terms of backward erosion piping and heaving. More pronounced effects exist when the downstream scour depression is considered, associated to a partial loss of confinement of the downstream cut-off wall.

The numerical modeling of the foundation provided helpful information regarding its safety and the effect of the erosion of bed material immediately downstream of the stilling basin cut-off wall. It evidenced that any further development of the erosion would result in reduction of the foundation safety margin comparing to the designed solution, namely if erosion went below elevation -8.0 m near the downstream cut-off walls.

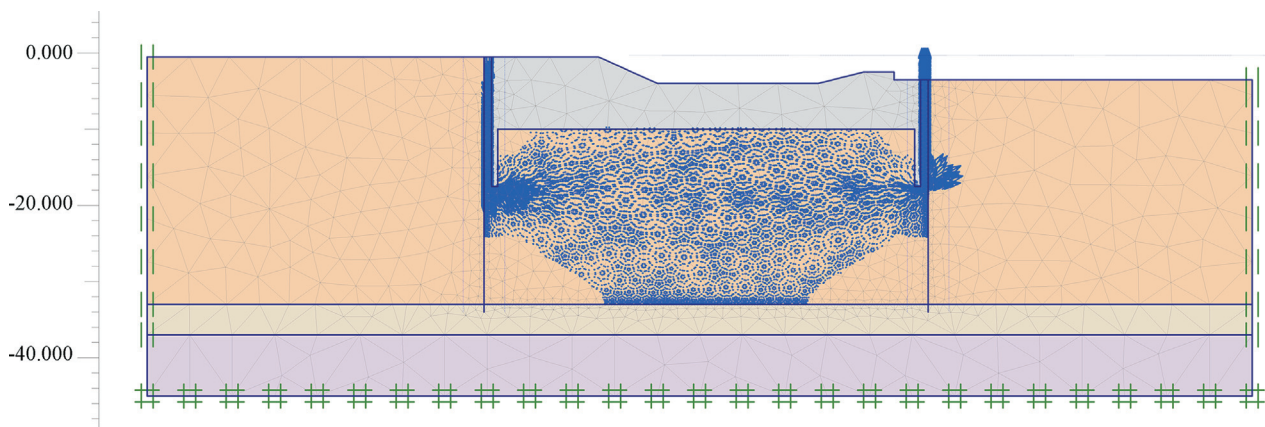


Figure 34 - Foundation 2D model of stilling basins 1E and 3E with the flow velocity vectors (Caldeira *et al.*, 2012).

Additionally, a physical hydraulic model was developed by LNEC, to study the causes of the scour and a corrective solution capable of resisting the hydrodynamic actions imposed by spillway operation (Melo *et al.*, 2014). If the gate operation rules were followed or slightly violated, the model tests showed that no scour would be observed. Based on operational data, a new rating curve was derived and applied in new tests. Then, the rockfill scour developed in accordance with the monitored pattern of erosion, indicating that the unfavorable evolution of the river natural rating curve was a major factor leading to the experienced scour.

Tests with rockfill involving larger blocks were then carried out to assess the size capable of withstanding the hydrodynamic actions of the flood discharges considering the revised downstream rating curve of the river. A considerable increase of block dimensions was necessary. The average size increased from a range of 0.9 to 1.35 m, considered in the design, to a range of 1.0 to 2.2 m.

These studies made clear that the phenomenon of backward erosion piping could be initiated and that remedial measures should be implemented for inhibiting its continuation and progression. Quoting Victor de Mello, in his Rankine Lecture (de Mello, 1977): “Engineering involves action based on decision despite uncertainty. Prediction is one necessary vehicle for adequate decision; but, most often an engineer’s capacity at predicting is disparately poor regarding what will happen, and quite competent, in comparison, at predicting what will not happen”.

In order to guarantee the non-occurrence of failure by piping, the corrective measures found to address foundation safety of stilling basins 1E and 3E were the construction of an upstream solution completely watertight and new filters beneath the rockfill protective layer (Caldeira *et al.*, 2012). These measures greatly decreased the hydraulic gradients in the active seepage zone of the dam, protected the

downstream flow exit points, avoiding the development or progression of backward erosion piping, minimized the thickness of alluvium material removal, limited the intervention area to the zone adjoining the stilling basins, and its functioning is virtually independent of the downstream scour conditions. The upstream watertight intervention consisted of a secant pile wall, embedded, at least, 1 m in the bedrock formation, sealed at the top by a jet grout slab and laterally by grouting (Fig. 35).

Based on hydraulic test results, which required larger rockfill blocks than those of the original design, new particle size curves and layer thicknesses were prescribed for rockfill and underlying filter layers, taking into account up-to-date filter criteria.

In order to ensure the global homogeneous behaviour of the new rockfill protection, the removal of the damaged rockfill was carried out, from the stilling basins end sill up to the existing bar (formed approximately 40 m downstream, with crest approximately at elevation -2.0 m). Excavation near the downstream cut-off wall of the stilling basins was foreseen until the original riverbed was attained, and down to elevation -8.0 m, allowing to accommodate the required thickness for the filter and rockfill layers (Fig. 36).

### 6.3. Caniçada cofferdam

Figure 37 presents the plan view and a cross section of the cofferdam, excavation slopes and zone of the inlet structure of the complementary spillway of Caniçada dam. The proposed solution (MotaEngil, 2014; JetSJ, 2015) consists of a concrete gravity retaining wall, resting on a curtain with two rows of jet grout columns (with 1.0 m diameter) and on vertical and inclined steel profiles, complemented with micro piles and grouting executed between the jet grout column rows. Therefore, the cofferdam is made of the natural ground and the described ground reinforcement. The final geometry is achieved through the

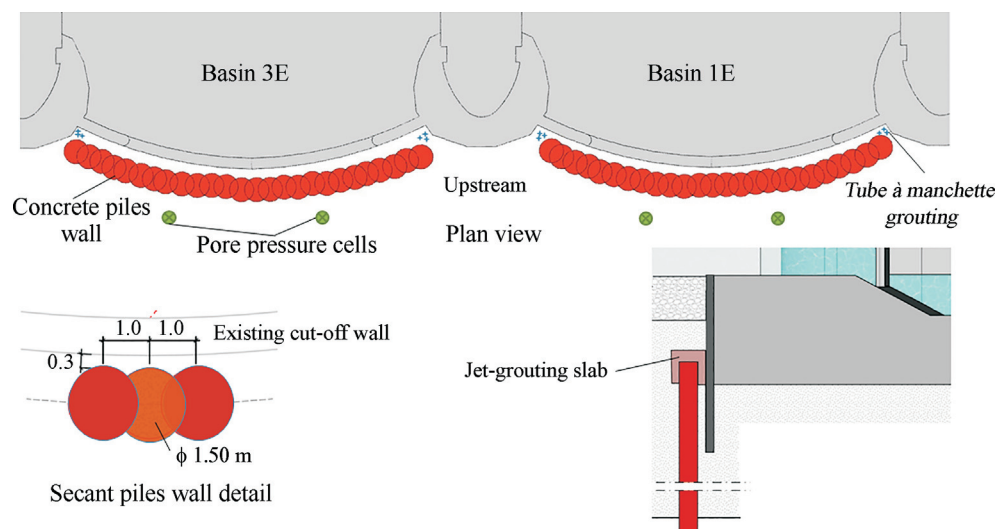


Figure 35 - Upstream watertight intervention (Caldeira *et al.*, 2013).

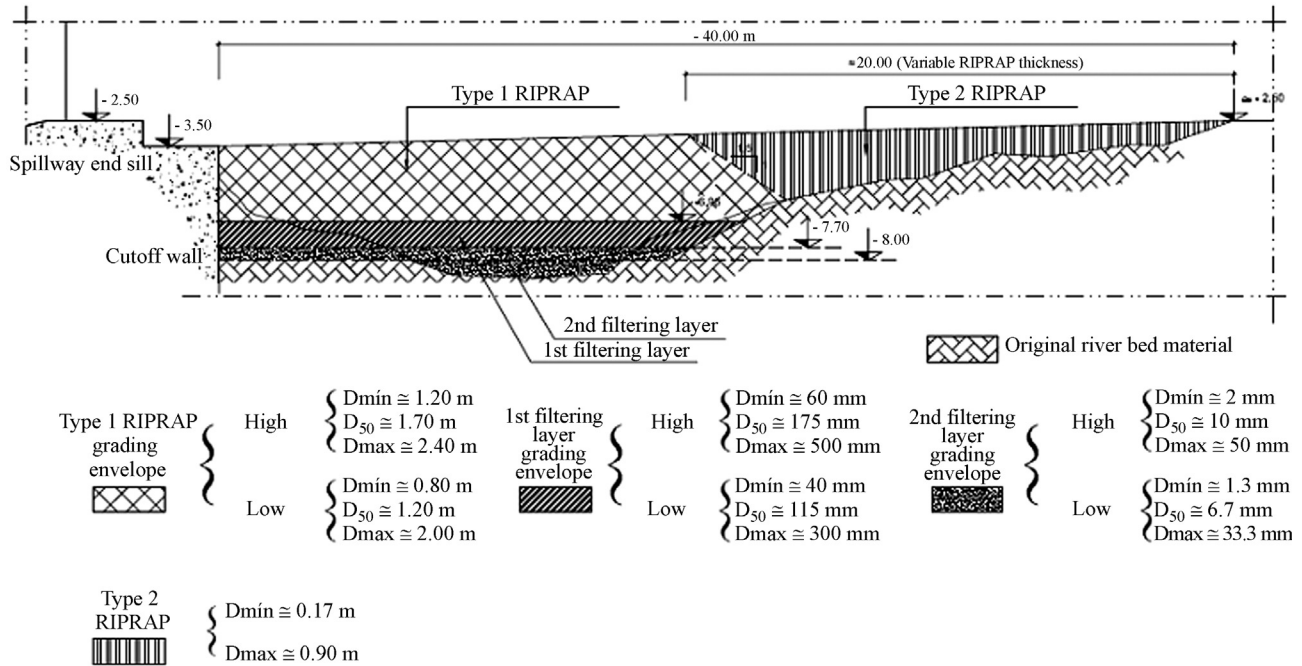


Figure 36 - Schematic representation of the filters and rockfill replacement in the damaged zone (Caldeira *et al.*, 2013).

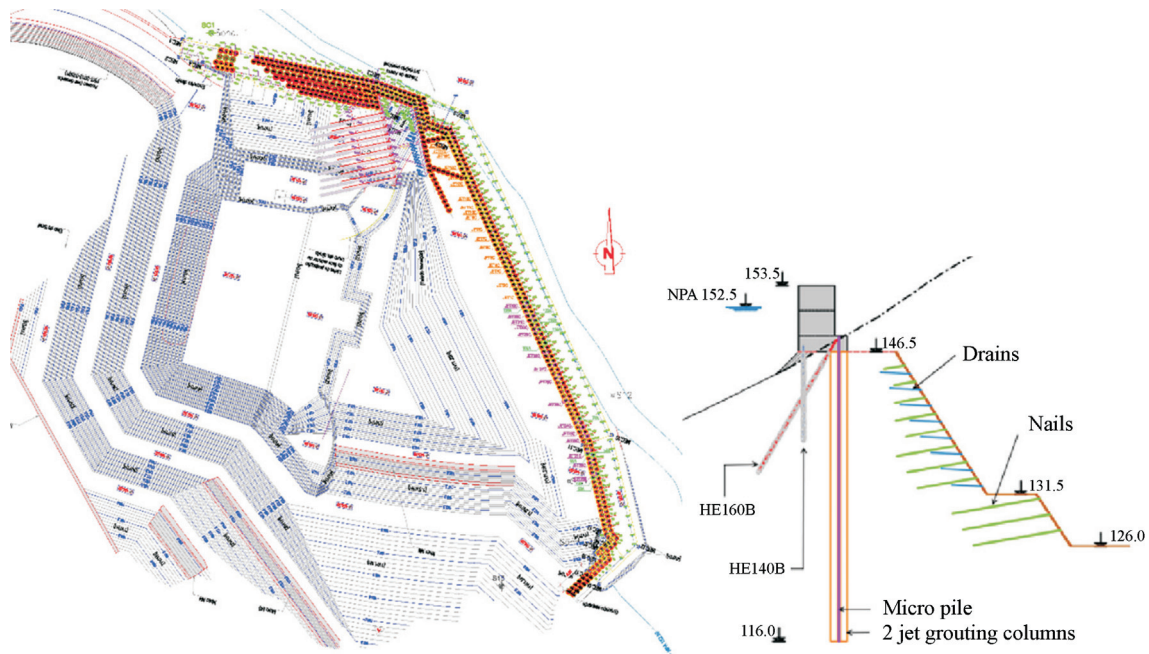


Figure 37 - Plant and a cross section of the cofferdam, excavation slopes and zone of the inlet structure of the complementary spillway of Caniçada dam (MotaEngil, 2014).

excavation of the ground and the application of nails and drains at slope inner faces.

The ground is essentially a granite rock mass, very decomposed superficially, but in depth formed by mixtures of residual soils and granite blocks, and finally by sound granite. In this type of ground, it was very difficult to materialize properly the jet grout columns, and it was necessary

to complement the ground treatment with grouting, executed with *tube à manchette*.

The weathering process produced a wide range of soil types within the weathered soil profile. This includes silty sand residual soils, which are easily eroded, gap-graded soils, which may be suffusive, zones of contrasting grading, where contact erosion may initiate on the interface, and

hard rock-like soil or granite blocks, which can provide a roof below which backward erosion piping can occur, if the hydraulic gradients are sufficient.

At the left abutment of the cofferdam, the curtain of jet grout columns and grouting was too short and its extent was not sufficient to prevent the described internal erosion phenomena, and some signs of their occurrence began to be observed during the ground excavation, such as sinkholes (Fig. 38) and cloudy water exiting at some points.

To control seepage through the left abutment of the cofferdam and adjacent excavation slopes, it was decided to extend and deepen the water tightness curtain in order to decrease the hydraulic gradient, installed in the decomposed granite rock mass, below the critical value, and to reduce the probability of occurrence of internal erosion. Figure 39 shows the initial position of the jet grout columns at the left abutment of the cofferdam and a secant pile wall constructed for that purpose. After the pile wall execution, the seepage flow from Caniçada reservoir had to skirt this pile wall before reaching the definitive slopes contiguous to the entrance structure of the spillway.

Nevertheless, due to the high susceptibility of the solution and of the decomposed granite rock mass to internal erosion, other effects were observed during the construction of the spillway. Figure 40 shows an exit point of flow with a pipe already formed, and water with fines entrainment (cloudy water). These effects, as well the seepage flow inside of the cofferdam, worsened with the rise of the Caniçada reservoir water level up to 151.7 m, in November of 2016, as required for testing the hydraulic circuit of the harnessing of Salomonde II. To stop the progression of the internal erosion process, the downstream area of the cofferdam was inundated (Fig. 41). The works were resumed with no major effects when the reservoir water level decreased, and the water downstream of the cofferdam was pumped. Nevertheless, during the final excavation, sand boiling was detected at several points (Fig. 42), which pro-

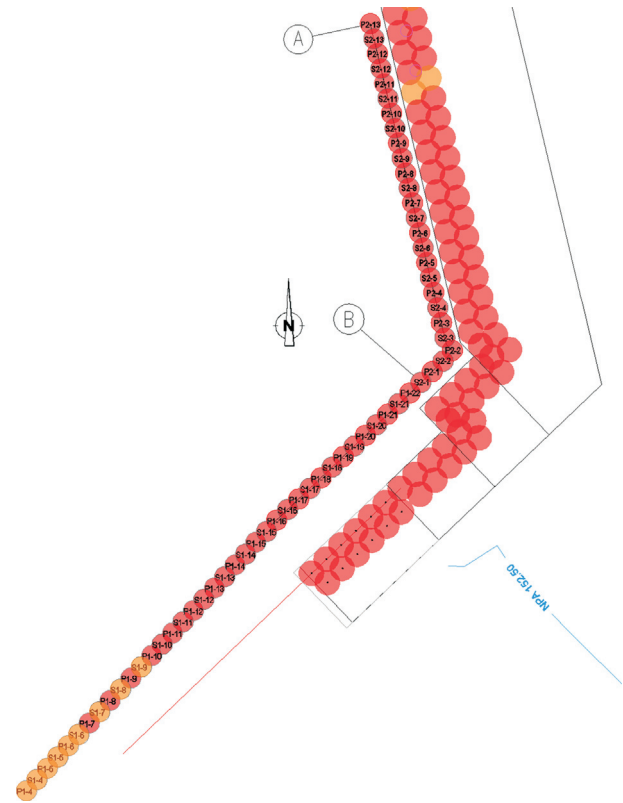


**Figure 39** - Jet grout columns at the left abutment of the cofferdam and secant pile wall built to decrease the internal erosion effects (Caldeira *et al.*, 2016a).

gressively disappeared with the drainage of the rock mass at the slope.

## 7. Conclusions

In embankment dams and dam foundations, filters and drainage systems constitute a first line of defence against the phase of continuation of erosion. There is evi-



**Figure 38** - a) Location of a sinkhole; b) aspect of the sinkhole (Caldeira & Santos, 2015).



**Figure 40** - Exit point of the flow with the formation of a pipe and fines entrainment (Caldeira *et al.*, 2016b).



**Figure 41** - Inundation of the cofferdam interior up to elevation 138.0 m in November 2016 (Caldeira *et al.*, 2017a).



**Figure 42** - Soil boiling at the slope toe (Caldeira *et al.*, 2017b).

dence from failure statistics (Foster *et al.*, 1998) that since the improvement of filter design and construction methods, there was a reduction of the ratio of failures due to internal erosion to the number of dams. However, such ratio has not

been reduced drastically (FEMA, 2011), due to the fact that dams deteriorate with ageing due to undetected internal erosion, and small embankments and dikes continue to be built without adequate filter protection, and fail upon first filling.

The filters are means of controlling and directing the seepage flow. They also prevent movement of soil particles from or between various zones of the dam and its foundation. Even in dams designed with adequate hydraulic gradients, they are needed when dams present cracks, are poorly constructed and are built with highly erodible materials, or their foundation conditions allow large amounts of under seepage. Therefore, filters constitute a defensive measure to protect the dams from the less than desirable conditions.

Existing dams may not comply with the up-to-date filter criteria or have deficient filters. In these cases, it is necessary to assess the probability of failure by internal erosion. Event tree analyses and laboratory tests were developed and are herein described to assist that purpose case by case, thus supporting the judgement of the dam engineers.

In addition, new lines of research are needed to overcome some knowledge gaps regarding the behaviour of saturated and unsaturated soils under reduced effective stresses, the stability conditions of cracks and pipes taking into account the soil state and seepage conditions, and soil erodibility characteristics, namely, flow limiting and crack filling actions, along cracks based on laboratory tests.

As case studies, two dams with internal erosion evidences - in Lapão dam induced by concentrated leaks, and the Crestuma-Lever dam affected by backward erosion piping - were presented in this lecture. The first is an embankment dam where during a flood several sinkholes were detected. The causes of the anomalous behaviour are related to a deficient design that neglected the possible arching effects associated to the shape of the valley, and to the compaction conditions, namely, at the interface with the spillway structure. During construction, the compaction control was ineffective and the foundation treatment was limited to the right riverbank, despite the identification of high permeability zones.

The second dam is a gated structure built in alluvial foundation, where an abnormal rockfill scour was observed. Given that this solution is very prone to occurrence of internal erosion, it was assessed its safety against backward erosion piping. Geotechnical analysis allowed the definition of corrective measures for increasing the foundation safety and the downstream protective rockfill stability. These measures involved the definition of an upstream water tightness solution and the redesign of geometry and grading curves for rockfill and filters layers.

Finally, attention was focused on a cofferdam composed of a weathered soil profile, very susceptible to internal erosion phenomena. The evidences observed and the

mitigation measures that allowed the conclusion of a spillway structure in safety conditions were described.

## Acknowledgments

The author wishes to express her gratitude to Electricity of Portugal (EDP) for the permission to publish the data contained in the lecture and to emphasize that the work presented in this paper was only possible with the essential advice and main collaboration of Prof. E. Maranha das Neves, and also Dr. Ricardo Santos and Dr. João Marcelino.

## References

- Álvares Ribeiro, A.; Ferreira Lemos, J.; Moutinho Cardoso, M. & Maranha das Neves, E. (1982). The exceptional foundations of the gated dams of Crestuma and Coimbra. Proc. 14<sup>th</sup> International Congress on Large Dams, Rio de Janeiro, v. II, pp. 387-404.
- Álvares Ribeiro, A. (1991). Douro River. Overtopped cofferdams. Proc. 17<sup>th</sup> International Congress on Large Dams, Vienna, v. IV, pp. 489-495.
- ASTM D4647 / D4647M-13 (2013). Standard Test Methods for Identification and Classification of Dispersive Clay Soils by the Pinhole Test. ASTM International, West Conshohocken, PA, 9 p.
- Atkinson, J.; Charles, J. & Mhach, H. (1994). Undrained hydraulic fracture in cavity expansion tests. Proc. XIII ICSMFE, New Delhi, India, pp. 1009-1012.
- Caldeira, L.; Miranda, L. & Brito, A. (2012). Crestuma-Lever Dam. Solution for the Internal Erosion Control. Report 155/2012, LNEC, Lisboa (in Portuguese).
- Caldeira, L.; Miranda, L. & Melo, J. (2013). Crestuma-Lever Dam. Follow-up of the Works for Implementation of the Solution to Guarantee the Stability of the Stilling Basins and Downstream Rockfill Apron. Report 456/2013, LNEC, Lisboa (in Portuguese).
- Caldeira, L. & Santos, R. (2015). Cofferdam at Caniçada Dam for the execution of the Complementary Spillway. Site Inspection on November 19<sup>th</sup> 2015 and Performance Evaluation. Technical Note 199/2017, DG-Chefia, LNEC, Lisboa (in Portuguese).
- Caldeira, L.; Santos, R. & Serra, J. (2016a). Cofferdam at Caniçada Dam for the Execution of the Complementary Spillway. Site Inspection on February 29<sup>th</sup> 2016 and Execution Conditions of the Piles and Anchors and Performance Evaluation. Report 150/2016, LNEC, Lisboa (in Portuguese).
- Caldeira, L.; Santos, R. & Serra, J. (2016b). Cofferdam at Caniçada Dam for the Execution of the Complementary Spillway. Site Inspection on November 21<sup>st</sup> 2016, Present Phase of the Works and Performance Evaluation. Report 355/2016, LNEC, Lisboa (in Portuguese).
- Caldeira, L.; Santos, R. & Serra, J. (2017a). Cofferdam at Caniçada Dam for the Execution of the Complementary Spillway. Site Inspection on December 20<sup>th</sup> 2016, Present Phase of the Works and Performance Evaluation. Report 33/2017, LNEC, Lisboa (in Portuguese).
- Caldeira, L.; Santos, R. & Serra, J. (2017b). Cofferdam at Caniçada Dam for the Execution of the Complementary Spillway. Site Inspection on July 7<sup>th</sup> 2017, Present Phase of the Works and Performance Evaluation. Report 289/2017, LNEC, Lisboa (in Portuguese).
- Cedergren, H.R. (1977). Seepage, Drainage and Flow Nets. John Wiley & Sons, New York, 2<sup>nd</sup> ed.
- Cyganiewicz, J.; Engemoen, W.O. & Redlinger, C.G. (2007). Bureau of reclamation experience with evaluating internal erosion of embankment Dams. In: Internal Erosion of Dams and Their Foundations. Fell, R. & Fry, J.-J. (eds). Taylor and Francis, Aussois, pp. 55-64.
- De Mello, V. (1977). Reflections on design decisions of practical significance to embankment dams. The Rankine Lecture. Geotécnique, 27(3):79-355.
- Engemoen, W.O. & Redlinger, C.G. (2009). Internal erosion incidents at Bureau of Reclamation dams. Proc. 29<sup>th</sup> USSD Annual Meeting and Conference, United States Society on Dams, Nashville, pp. 731-745.
- Engemoen, W.O. (2011). Bureau of reclamation experiences with internal erosion incidents. Proc. Internal Erosion in Embankment Dams and Their Foundations, European Working Group of ICOLD, Brno, Czech Republic, p. 11-18.
- Fell, R.; Foster, M.; Davidson, R.; Cyganiewicz, J.; Sills, G. & Vroman, N. (2008). A Unified Method for Estimating Probabilities of Failure of Embankment Dams by Internal Erosion and Piping. UNICIV Report R446, The School of Civil and Environmental Engineering, University of New South Wales, Sydney, Australia, [www.engineering.unsw.edu.au/civil-engineering/uniciv-reports](http://www.engineering.unsw.edu.au/civil-engineering/uniciv-reports).
- Fell, R.; Wan, C.F.; Cyganiewicz, J. & Foster, M. (2003). Time for development of internal erosion and piping in embankment dams. Journal of Geotechnical and Geoenvironmental Engineering, 129(4):307-314.
- FEMA (2011). Filters for Embankment Dams. Best Practices for Design and Construction. Federal Emergency Management Agency, USA.
- Foster, M.; Fell, R. & Spannagle, M. (1998). Analysis of Embankment Dam Incidents. Report UNICIV No. R-374, School of Civil and Environmental Engineering, The University of New South Wales, Sydney, Australia.
- Foster, M. & Fell, R. (2000). Assessing Embankment Dam Filters which do not Satisfy Design Criteria. Report UNICIV No.R-376, School of Civil and Environmental Engineering, The University of New South Wales, Sydney, Australia.
- Foster, M. & Fell, R. (2001). Assessing embankment dam filters that do not satisfy design criteria. Journal of Geotechnical and Geoenvironmental Engineering, 127(5):398-407.

- Fry, J.J. (2007). Current practice and new view on granular filters. In: *Assessment of the Risk of Internal Erosion of Water Retaining Structures: Dams, Dykes and Levees*. Intermediate Report of the European Working Group of ICOLD. Contributions to the Symposium on 17-19 September 2007 in Freising, Germany. German National Committee on Large Dams (Deutsches TalsperrenKomitee e.V.), Freising.
- Gudehus, G. (2011). *Physical Soil Mechanics, Advances in Geophysical and Environmental and Mathematics*. Springer-Verlag Berlin, Heidelberg.
- ICOLD (2017). Internal erosion of existing dams, levees and dikes, and their foundations. Bulletin n. 164, v 1: Internal Erosion Processes and Engineering Assessment, International Commission on Large Dams.
- JetSJ (2015). Caniçada Dam - Cofferdam. Final Design. Review D. Supporting Documents, JetSJ, Lisbon.
- Löfquist, B. (1992). Hydraulic Penetration in Embankment Dams. *Ground Engineering*, London, pp. 40-43.
- Maranha das Neves, E. (1989). Analysis of crack erosion in dam cores: The crack erosion test. In: *De Mello Volume: A Tribute to Prof. Dr. Victor F.B. de Mello*. Editora Edgard Blucher Ltda, São Paulo, pp. 284-298.
- Maranha das Neves, E. (1991). Behaviour of Earth-Rockfill Dams. Ph.D. Thesis, Universidade Nova de Lisboa, Faculdade de Ciências e Tecnologia, Lisboa, Portugal (in Portuguese).
- Maranha das Neves, E. (2018). Personal Communication.
- Marcelino, J.; Caldeira, L. & Silva Gomes, A. (2003). Lapão Dam. Analysis of the Causes of the Accident and Evaluation of the Safety Conditions of the Dam. Report 56/2003. LNEC, Lisboa (in Portuguese).
- Marcelino, J. (2004). Observation of Lapão Dam. Its importance in the detection of the accident of January 2003. Proc. II Congresso Luso-Brasileiro de Geotecnia, Aveiro (in Portuguese).
- Marcelino, J. (2008). The importance of the observation in the safety control. Lapão Dam example. Proc. 5º Congresso Luso-Moçambicano de Engenharia, Maputo (in Portuguese).
- Melo, J.; Dias da Silva, J.; Fernandes, I.; Caldeira, L. & Miranda, L. (2014). Corrective measures of the River Bed protection downstream of a dam founded in deep alluvia. The case of Crestuma-Lever Dam. Proc. 3rd IAHR Europe Congress, Porto, Portugal, 14-16 April, 13 p.
- Mota-Engil (2014). Caniçada Dam. Complementary Spillway. Final Design. Outline Drawings.
- Redlinger, C.G.; O'Leary, T.M.; Henn, K.H. & Scott, G.A. (2011). Current methodology and research at the Corps of Engineers for assessing internal erosion risks of dams. Proc. Internal Erosion in Embankment Dams and Their Foundations, European Working Group of ICOLD, Brno, pp. 123-130.
- Redlinger, C.G. (2014). Potential failure modes related to internal erosion (periodic assessment). Dam Safety Workshop N. 2, Aracaju, Sergipe, Brazil, 19-23 May.
- Santos, R. (2014). Experimental Investigation on Limitation of the Progression of Internal Erosion in Zoned Dams. Ph.D. Thesis, Instituto Superior Técnico, Lisbon, Portugal.
- Santos, R.; Caldeira, L. & Maranhã das Neves, E. (2014). Laboratory test for evaluating limitation of flow during internal erosion. *Geotechnical Testing Journal*, 37(3):463-476.
- Santos, R.; Caldeira, L. & Maranhã das Neves, E. (2015). Laboratory test for evaluating crack filling during internal erosion in zoned dams. *Geotechnical Testing Journal*, 38(6):915-928.
- Schmertmann, J.H. (2001). The no-filter factor of safety against piping through sands. In: *Judgement and Innovation*. Geotechnical Special Publication N. 111, ASCE, pp. 63-133.
- Schofield, A.N. (2005). *Disturbed Soil Properties and Geotechnical Design*. Thomas Telford, London.
- Sherard, J.L. (1973). Embankment dam cracking. In: *Embankment Dam Engineering*. Hirschfeld and Poulos (eds). John Wiley & Sons, New York.
- Sherard, J.L.; Dunnigan, L.P.; Decker, R. & Steele, E.F. (1976). Pinhole test for identifying dispersive soils. *Journal of Geotechnical Engineering*, ASCE, 102(1):69-85.
- Sherard, J.L. & Dunnigan, L.P. (1985). Filters and leakage control in embankment dams. In: *Symposium on Seepage and Leakage from Dams and Impoundments*, ASCE, pp. 1-30.
- Shewbridge, S.E. (2014). Introduction to mechanics of internal erosion. In: *Dam Safety Workshop N. 2, Aracaju, Sergipe, Brazil, 19-23 May*.
- Terzaghi, K.; Peck, R. & Mesri, G. (1996). *Soil Mechanics in Engineering Practice*. Third Edition. John Wiley & Sons, Inc., New York.
- Wan, C.F. & Fell, R. (2002). Investigation of Internal Erosion and Piping of the Slot Erosion Test and the Hole Erosion Test. Report UNICIV No. R-412, School of Civil and Environmental Engineering, The University of New South Wales, Sydney, Australia.
- Wan, C.F. & Fell, R. (2004). Investigation of rate of erosion of soils in embankment dams. *Journal of Geotechnical and Geoenvironmental Engineering*, 130(4):373-380.



## ***Articles***

***Soils and Rocks***  
**v. 41, n. 3**



# Some Case Histories with Lessons to Learn in Dam Engineering

(2<sup>nd</sup> Dr. Victor de Mello Goa Lecture, presented on October 15<sup>th</sup>, 2018, in Farmagudi, Goa, India)

L.G.F.S. de Mello

**Abstract.** Three case histories of dam engineering related topics are presented as previous knowledge and experience would not have led to predict their impact on dam design. The Lecture honours Prof. Victor de Mello by discussing the Balbina HPP where Prof. de Mello led the saprolite foundation design when ancient termite canaliculae were found, imposing the need to control seepage through the dam's foundation. The remote location of the dam site associated to its meteorological characteristics did not allow for conventional earthmoving or plastic diaphragm solutions to be used, and special pressure grouting was studied and successfully applied. Details of the field studies to allow pressure grouting in saprolite soils as well as to define the grout mixtures are presented. Two other very interesting case histories are presented, one being the Teles Pires HPP. In this project thrust faulting generated unforeseen persistent sub-horizontal joints to depths not associated to the common pattern of stress relief joints in granitic rock masses, with presence of preserved slickensides and estriae. Stability considerations for the Intake Structure lead to the need of excavating shear keys consisting of tunnels filled with concrete, drainage tunnels and installation of passive anchors. Finally, the Chaglla HPP head race tunnel case history is presented. This tunnel 9 km long tunnel excavated through limestones previously investigated did not intersect any karstic feature. During commissioning turbine tests, with the tunnel pressurized, a small magnitude shallow earthquake occurred very close to the site, and muddy water was seen outcropping in a small creek valley in the side slope of the mountain where the tunnel was excavated. Detailed investigation lead to postulate a mode of failure in which the earthquake generated the disarticulation of a very fractured and saturated stratigraphic fault, leading to the retrogressive erosion developing from a distant karstic feature till the vicinity of the tunnel's shotcrete, drastically reducing its passive support, leading to the failure inside out of the tunnel lining and support. The importance of sound geological models is emphasized by these case histories, as always strongly argued by Prof. de Mello.

**Keywords:** case histories, embankment dams, forensic investigations, foundations, geological model, head race tunnel, karstic behaviour, shear keys, termite canaliculae.

## 1. Introduction

Honouring Prof. Victor de Mello is a very hard task; doing it in his hometown raises the responsibility many steps higher.

I have decided to look into one of his loved fields of expertise, sharing with a broad community a less known but important contribution he has conceived, coordinated design and tests, and led throughout the implementation in the field, following its success through monitoring results. This contribution is not as well-known as his discussion and proposal of understanding compacted fine grained / clayey fills as pre-consolidated materials, of using an inclined upstream stepped chimney filter in different earth fill dams, and the optimization of the wrap-around interface between concrete structures and the adjacent compacted earth fill in dams, as illustrated in Figs. 1-4, and discussed in detail in his Rankine Lecture - de Mello, V.F.B. (1977).

It was a pioneering solution at the time it was conceived, impacted positively the dam where it was implemented, and was used in other situations of my knowledge.

This technical paper presents other two case histories focusing on particular geological situations faced during dam construction or final stages of commissioning, both also in the tropical environment of Brazil's Amazon region. One led to the need of completely changing the geological / geomechanical model for the stability calculations of its intake structure, and the other led to the failure of a headrace tunnel following a mechanism not previously reported in the specialized literature. Geological particularities of the three sites are described in detail for two of the sites, with contribution from the geologists involved, endorsing many other authors (for example Fookes *et al.*, 2000) on the need of having a sound geological model to work with.

The idea of discussing geotechnical challenges, either in time to make the best decisions possible or after a failure happens and repair is to be discussed, comes from the valid-

---

Luiz Guilherme F.S. de Mello, M.Sc., Assistant Professor, Escola Politécnica, Universidade de São Paulo, and Geotechnical Consultant – Vector Projetos, São Paulo, SP, Brazil. e-mail: lgmello@vector.com.br.

Submitted on October 15, 2018; Final Acceptance on October 30, 2018; Discussion open until April 30, 2019

DOI: 10.28927/SR.413267

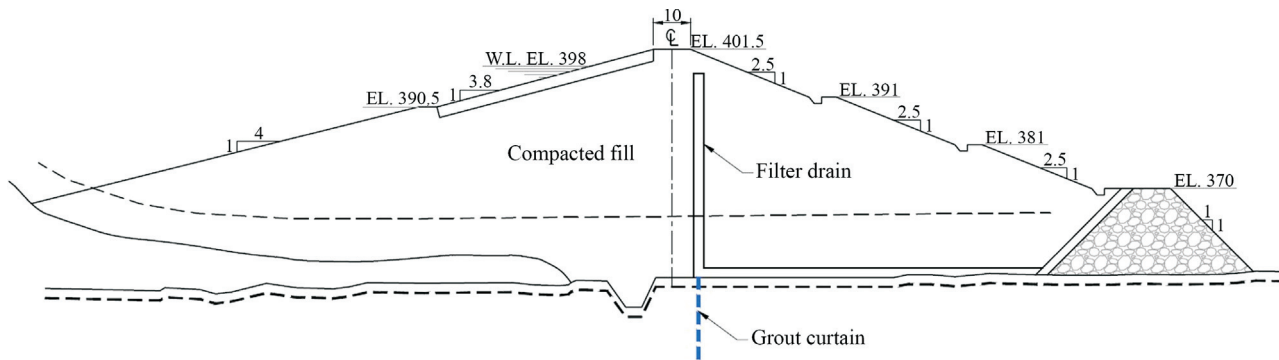


Figure 1 - Traditional earthfill cross section in Brazil attributed to Terzaghi.

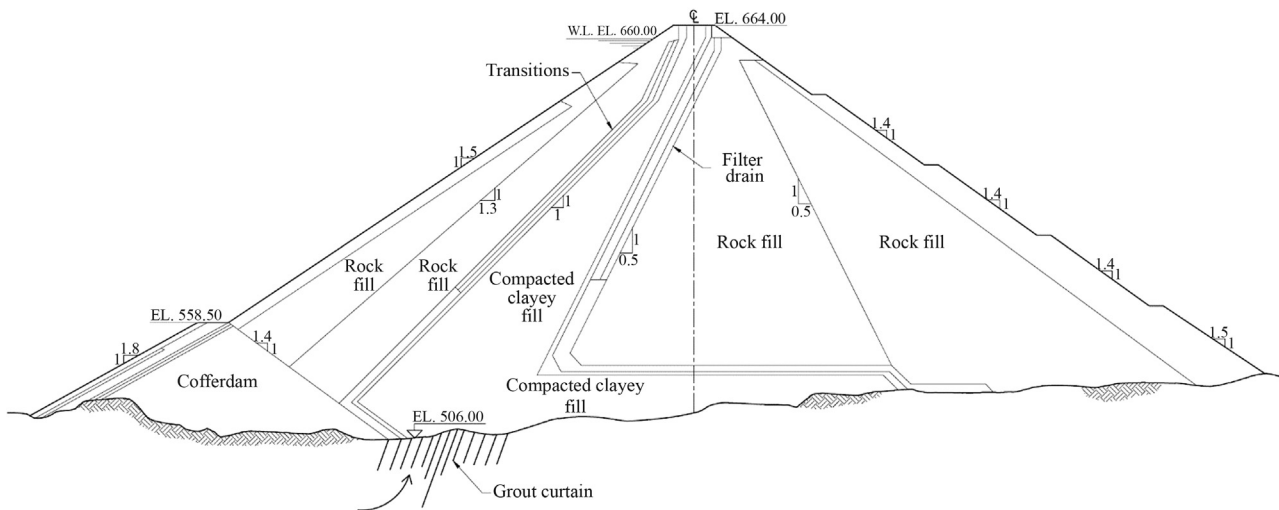


Figure 2 - Cross section optimized by Victor de Mello with upstream inclined impervious core and internal impervious blanket.

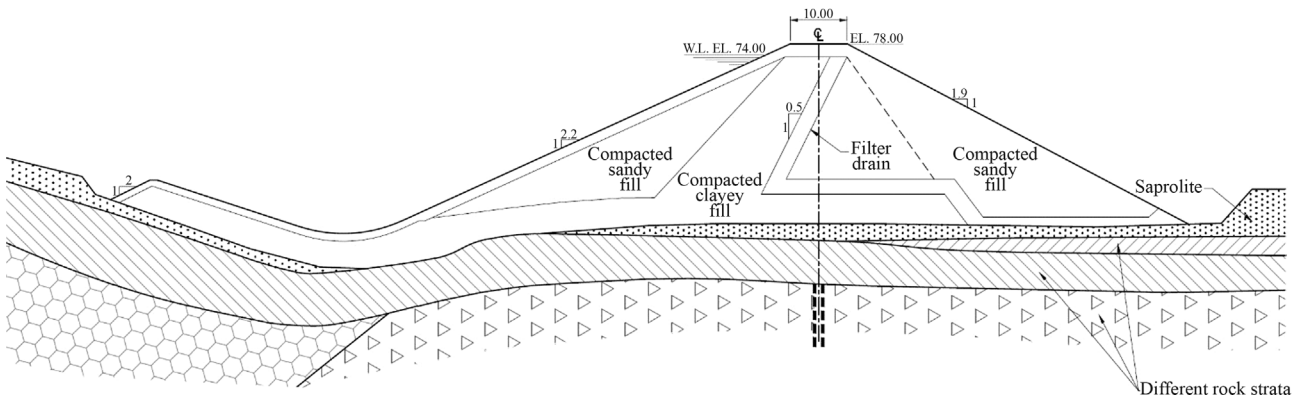
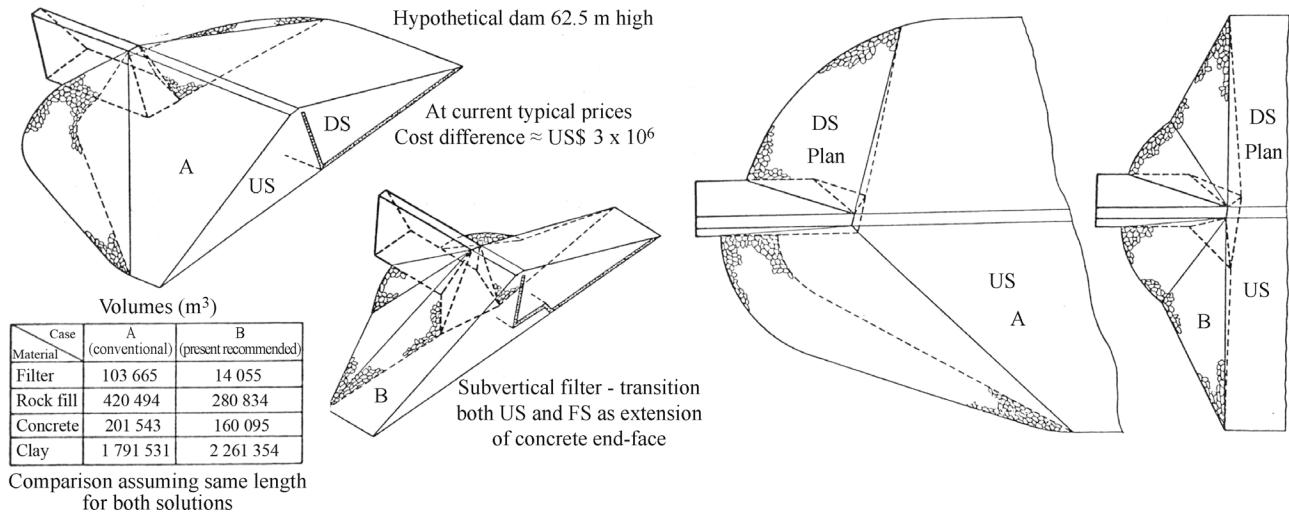


Figure 3 - Cross section optimized by Victor de Mello with upstream inclined impervious core and internal impervious blanket.

ity of sharing the experience gained when unforeseeable situations arise, so that equivalent future cases are prevented. Case histories add an important source of information for practitioners and even researchers when reporting situations properly documented. In all these cases a clear understanding of both the geological and physical model,

leading to identifying the prevailing and conditioning behaviour(s), is fundamental. It is understood that case histories are an important tool to disseminate gained experience; in a previous lecture the author has shared some other situations of failures, discussing his views on this important source of knowledge (de Mello, L.G., 2005).



**Figure 4** - From V. de Mello's Rankine Lecture - optimizations proposed and routinely used in South America for the wrap around interface of concrete structure and earthfill dam.

## 2. Balbina Hydroelectric Power Plant

The Balbina Hydroelectric Scheme is located 170 km north of Manaus, in the Uatumã River, left side contributor of the Amazon River. Its embankment dam is a homogeneous earth fill with average height of 30 m, having as foundation silty-clayey residual and saprolitic soils generated by the weathering of volcanic rocks, called volcanites to keep the same simplified terminology used during the works. The main features associated to the plant are: installed capacity 250 MW, generating since 1989; concrete volume  $350,000 m^3$ ; volume of the compacted soil  $5,000,000 m^3$ ; total length of dam 3,300 m, 330 m of which correspond to the concrete structure; maximum height of the structures 34 m and 33 m for the earth fill dam.

### 2.1. Local geology

The volcanic rocks present at the site show all features of a theoretical weathering profile. The main characteristic of the materials is the relatively low thickness of the weathered rock (usually fractured), being about 2 m thick. The saprolite and residual soils capping the rock present typical thickness greater than 10 m; the saprolite and saprolitic soil predominate in 80% of the strata, the mature residual soil being often eroded, remaining only the saprolitic soil. Another important aspect is the extremely irregular topography of the interface with the volcanic rock top, as well as the absence of boulders or core stones in the soil mass, which is very favorable to investigation and/or soil grouting.

Among the geotechnical-geological features conditioning the design of the embankment dam, the existence of regions points with permeability higher than  $10^{-3} cm/s$  needs to be emphasized. These high values of permeability were measured in constant level in situ permeability tests

carried out in the clayey and silty saprolitic soil, as well as in in situ tests performed in trenches.

This layer of low density (dry density between 5 and  $10 kN/m^3$ ) saprolitic soil showed areas with high occurrence of tubular cavities denominated "canaliculi", with typical diameters of a few millimetres to 2 cm, and, in exceptional cases, of 2 to 10 cm.

Figure 5 presents the distribution of the measured permeability values in the saprolitic soil; it can be seen that 38% of the values are higher than  $10^{-4} cm/s$ , and 10% are higher than  $10^{-3} cm/s$ , values which are not compatible with the existing experience in saprolitic soils. No sample from the SPT tests recovered every meter exhibited any feature that could justify the high permeability values encountered, such as sand or gravel.

On this basis, the high permeability values were put under suspicion; in early stages of design, the saprolitic soil was treated as a low permeability soil, consistently with its grain size curve and plasticity characteristics. Basic design conceived foundation treatment with a shallow cut off down to the bottom of the alluvial layer, associated

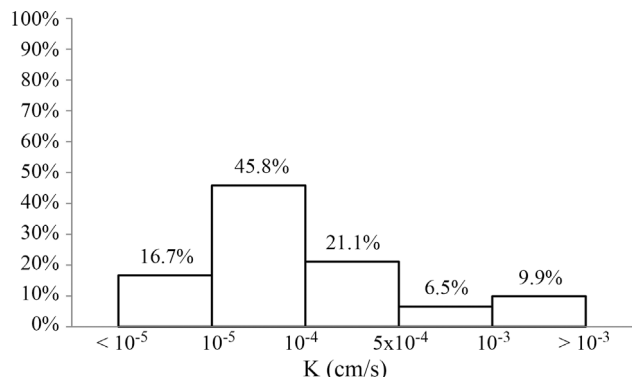


**Figure 5** - Distribution of measured permeability values.

with an upstream impervious blanket and relief wells downstream.

Different phases and sophisticated subsoil investigation associated the high permeabilities to the presence of tubular cavities, canaliculi, in the saprolitic soil profile, with diameters varying from millimetric to centimetric (2 to 3 cm), intercommunicating—and with an erratic geometric pattern. They were detected in most trenches, with a frequency, which would vary grossly between one or two per square meter for the largest diameters, and one per square decimeter (100 per m<sup>2</sup>) for the canaliculi of 2 mm diameter. This frequency varied along the foundation, and some trenches did not detect any canaliculi at all.

The previously described sequence of in situ investigations and observations led to the following conclusions:

- the saprolitic soil underlying the alluvium and overlying the highly fractured weathered rock consists mainly of a silty matrix. This matrix has a typical permeability of 10<sup>-5</sup> cm/s, in tune with Brazilian experience.
- criss-crossing the soil matrix, tubular cavities/canaliculi ranging in diameter from 2 to 30 mm are present, conditioning the flow of water and giving the soil mass an equivalent permeability which can locally reach values as high as 10<sup>-2</sup> to 10<sup>-1</sup> cm/s.

Since it was found impossible to follow the canaliculi into the soil mass, no determination of their length, continuity, interconnections and preferential direction could be made. Visually they seemed to be distributed in all directions with their diameter varying along their course by a factor of approximately two. The interconnection between the canaliculi was demonstrated by the excavation and dewatering of adjacent trenches; the addition of a tracer in a trench lead to its surge in the other in only 20 s. These investigations led to the conclusion that the canaliculi needed to be considered continuous at least over a distance of the order of 5 m.

Another very important question was associated with the stability of the canaliculi's walls when submitted to a continuous flow of water.

These canaliculi were interpreted as being generated by intense termite activity linked with the last glacial period and the associated lowering of the water table linked to the ocean regression (de Mello, L.G. *et al.*, 1987). The action of termites was proposed by the Portuguese biologist A. B. Machado (1983), confirming the activity of these insects in all the samples, through traces, essentially composed of faecal and oral pellets, found inside the canaliculi. According to Machado, the canaliculi developed probably in the last glacial quaternary era (12,000 to 18,000 years ago), when the region had relatively dry climatic conditions, decisive for the existence of vegetation formations designated as "credo" and "caatinga", propitious for the proliferation of termites. These insects became rare after the formation of the Amazon forest and were not found inside the canaliculi studied. Machado also suggested that the canaliculi of

higher diameters should correspond to ramifications of roots, which the termites had eaten, and that those with diameter smaller than 0.8 millimetres would have their origin associated with the disintegration of thin roots, still partially preserved in the regional soils. Figures 6-8 illustrate said canaliculi in inspection trenches just excavated.

## 2.2. Foundation treatment

Many different alternatives were evaluated prior to the definition of the foundation treatment to be used in the dam (Sathler & Camargo, 1985; Remy *et al.*, 1985), including conventional cut-offs, use of diaphragm walls to implement a cut-off, use of impervious blankets, etc. Grouting of the saprolitic soils at high pressure, generating hydraulic fracturing using the tube a manchette technique and thus intercepting the net of canaliculi was proved to be the best cost-effective alternative, when proper consideration of logistic and climatic peculiarities of the Amazon Region were included in the analysis.

The essence of the concept behind treating the foundation by grouting, aimed at creating a zone under the embankment's core in which all localized permeability singu-



**Figure 6** - Canaliculi at Balbina hydroelectric power plant dam foundations.



**Figure 7** - Canaliculi at Balbina hydroelectric power plant dam foundations.

larities were eliminated, allowing all foundation studies to treat it as homogeneous, in terms of statistics of averages, in tune with the de Mello, V.F.B. (1977) Rankine Lecture.



**Figure 8** - Canaliculi at Balbina hydroelectric power plant dam foundations.

The same grout holes were used to extend and grout through the weathered and fractured rock beneath the saprolitic soils. The self-testing characteristics of the treatment methodology by grouting were also valued, leading to the concentration of treatment where specifically required. Figure 9 illustrates a typical cross section for the proposed hydraulic fracturing grouting foundation treatment. The goal of grouting was defined as creating, by grout pressure fracturing, a net of grout planes which would intercept each other and the canaliculi, filling them with grout over part of their length, in order to create a zone 5 m to 6 m wide with reduced and homogenised permeability. A maximum value of permeability of  $10^{-4}$  cm/s was expected after treatment.

Using the tube a manchette technique, grouting in phases and localized was performed, applying pressures high enough to generate hydraulic fracturing of the soil, to allow penetration, interception and filling of the canaliculi and voids by the lenses of grout. The tube a manchette grouting apparatus used in Balbina is shown schematically in Fig. 10.

The advantages of this concept of treatment are:

- a) grouting can be intensified in regions where intake was higher;
- b) treatment can be done all year round, despite the climatic changes that are drastically conditioning in the Amazon Region;
- c) use of conventional equipment;
- d) the same boreholes can be used to treat the weathered and sound rock underneath the saprolitic soil.

An in situ inspection trench of a grouted borehole is shown in Fig. 11.

### 2.3. Grouting experimental stretch

The pioneering characteristics of the proposed foundation treatment in saprolitic soils led to scheduling and

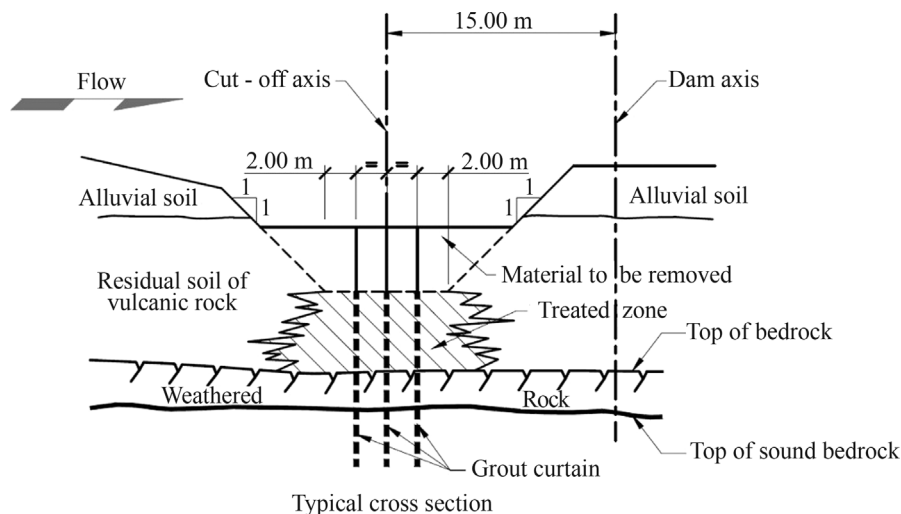


**Figure 9** - Balbina Dam foundation treatment typical cross section.

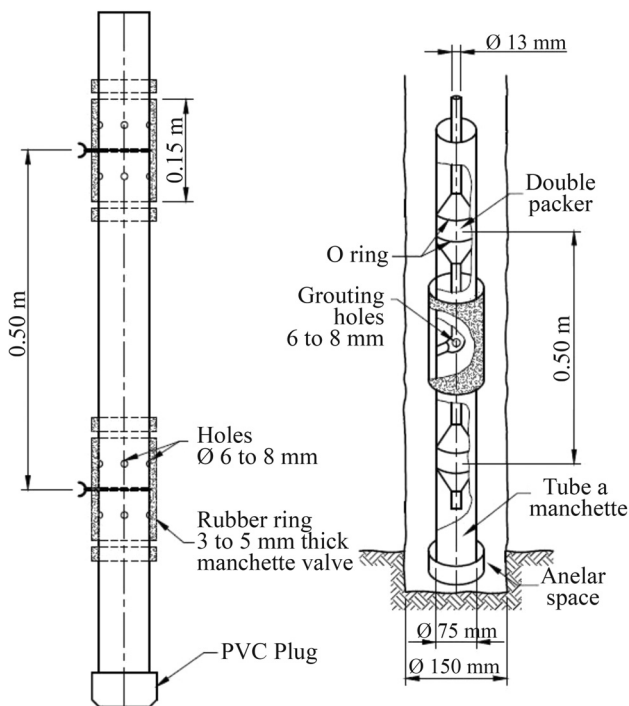


Figure 10 - Tube with manchette valve and grouting packers.

performing an experimental grouting stretch about 180 m long to allow selection of the criteria and methodology for the abovementioned treatment. This grouting test was carried out in the dam foundation area so as to be a part of the whole treatment of the dam's foundations.

The main aspects considered in the experimental stretch are summarized in Table 1, as well as the variables, which were analyzed on each of the four sub-segments grouted, as presented by Santos *et al.* (1985).

2.4. Treatment methodology

At the beginning of the treatment, special tests and a experimental stretch of work were performed to supply the engineers involved with data, which, in turn, helped optimize the treatment specifications. The special tests included:



Figure 11 - Inspection trench - Tube a manchette in grouted borehole, with grout planes generated by hydraulic fracturing.

- carefully performed water loss tests in drained and in un-drained conditions. Figure 12 presents two of the referred tests, from which the pressure causing hydraulic fracturing and the minor principal total stress  $\sigma_3$ , were interpreted. Following Bjerrum and Andersen (1972) discussions, the coefficient of earth pressure at rest  $K_0$  was estimated, provided that  $\sigma_3$  is assumed to be horizontal. This value was estimated to vary between  $0.21 \leq K_0 \leq 0.36$ .

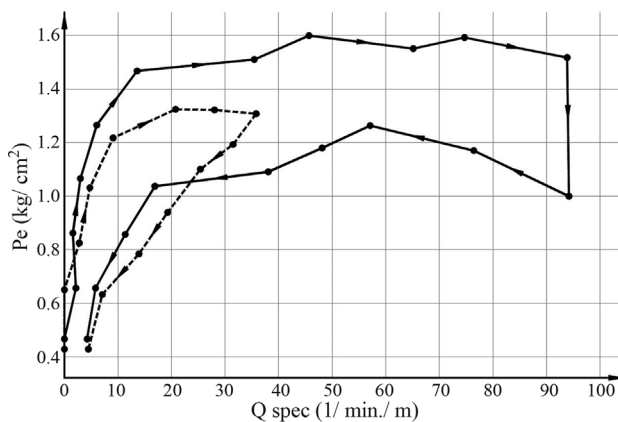


Figure 12 - Groutability test example – Hydraulic fracturing of the saprolitic soil.

Table 1 - Balbina Dam foundation grouting experimental stretch main aspects and analyzed variables.

Characteristics	Parts of the experimental grouting line			
	I	II	III	IV
Length (m)	40	24	50	68
Borehole disposition (m)	2 x 4	2 x 2	2 x 4	2 x 2
Phases of grouting (un.)	3	2	1	1
Volume grout per phase (L)	333	125	1000	300
Total grout vol. per valve (L)	1000	250	1000	300
Order of execution	Soil/rock	Rock/soil	Soil/rock	Soil/rock

- after grouting with different colored cement pigments added to each grouting phase, inspection trenches showed valid the assumption of the orientation of  $\sigma_3$ .

Once the value of  $K_0$  is known with some degree of confidence, many theories exist which enable the pressure of hydraulic fracturing of a massif to be estimated (Bjerrum *et al.*, 1972; Kennard, 1970; Haimsom and Fairhurst, 1967; Morgenstern and Vaughan, 1963).

The data collected allowed the following relation to be established between the formulation proposed by Bjerrum and the observed values:

$$\Delta\mu_{obs} = 78.3 + 1.02 \Delta\mu_{Bjerrum} \text{ (kPa)} \quad (1)$$

The grouting methodology used in the treatment resulted from the experience of the professional team involved and was optimized many times as a function of the results and data collected. The methodology used during the major part of the work can be summarized as:

- Double packers developed at the site were used for testing and for grouting, which sealed through O-rings against a PVC tube left in each grouting borehole, weakly grouted in its external side to develop close contact with the saprolitic soil (as shown in Fig. 11).
- initially, water loss tests were done in the saprolitic soils with pressure stages of 20; 40; 60... kPa until hydraulic fracturing occurred. Through this testing the determination of the coefficient of permeability prior to treatment and relevant indications of the pressures with which treatment was to be performed were gathered. Figure 13 presents some of the results obtained. Special techniques to ensure perfect contact of the expandible packers with the walls of the boreholes were developed in order to avoid preferential vertical seepage

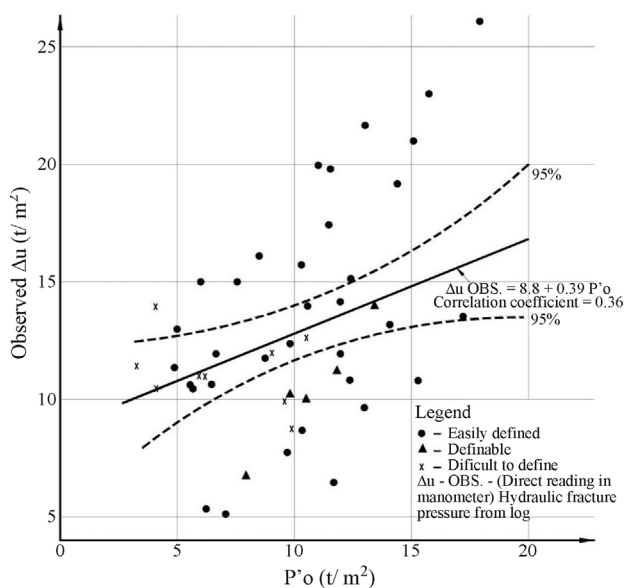


**Figure 13** - Relationship between the increase of pressure to generate hydraulic fracturing and effective stresses in water loss tests.

due to deformation of the saprolitic soil when submitted to the packer pressure, which would invalidate all the testing. Spacing between valves was defined as 0.5 m.

- three lines of grouting holes were planned – central/upstream/downstream - with grouting starting from the external lines in order to confine and improve treatment through the central holes.
- the soil-cement grouts postulated to treat the soil were different from those used to fix and seal the PVC grouting tube. Both used as much as possible the local clayey saprolitic soils in order to reduce costs of treatment, due to the difficulties in hauling bentonite to the site. The physical characteristics of the grout necessary to fix and seal the PVC tube needed to be carefully evaluated so that they would not condition the pressure values required for its rupture when grouting the foundation soil. Several grouts were prepared in PVC pipe molds, with variable thickness and grout resistance. Tests simulated rupture processes of the annular seal grout, as a function of its thickness, grout strength and confining pressure. The results of these tests showed that the increments of the seal grout rupture pressure, as a function of the three variables tested, were higher with the confinement pressure and with the seal thickness, for rupture pressure values within the same order of magnitude, as shown in Fig. 14. Based on these results, a grout mixture for the annular seal was defined as cement: 285 kg / soil: 290 kg / water: 805 L. The specification of the soil-cement foundation grout asked for:

- uniaxial compressive strength at 28 days of 1.5 kg/cm<sup>2</sup>;
- viscosity ≤ 50 cP;
- sedimentation factor ≤ 5%;
- fluidity in Marsh cone of 40 s to 45 s;
- yield limits ≤ 0.1 g/cm<sup>2</sup>, which was achieved with the following mixture: cement: 73 kg / soil: 310 kg / water: 860 kg.

It is worth noting that the initial amount of cement considered was 375 kg in the proportion above and was reduced substantially during the tests.

- grouting of the saprolitic soils was undertaken bottom-up, from the lowest manchette valve towards the top under a 3 m high compacted earth fill, at pressures compatible with the hydraulic fracturing pressures as a function of depth previously determined. Tests were also performed to investigate if the ideal grouting sequence was to initially grout the saprolitic soils, and then to grout the underlying weathered rock horizon, or to invert this sequence. Water loss tests were made in the contact zone between saprolitic soil and weathered rock horizons, showing that foundation treatment was more efficient when the weathered rock was grouted first. The possible explanation for the lower

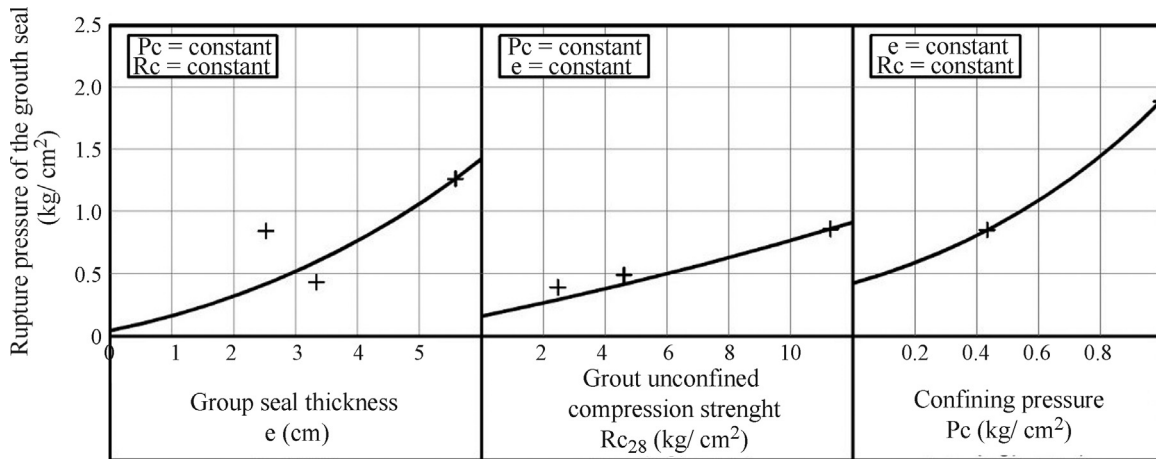


Figure 14 - Results of tests with grout seal models.

effectiveness of grouting close to the horizons interface in a top-down sequence was interpreted as probably associated to soil-cement grout migration to the untreated weathered rock fractures. As grouting of the higher depths of saprolitic soils was implemented with constant grout volumes, such migration would reduce grout quantity at the bottom of the saprolitic soil, consequently reducing the effectiveness of treatment in this interface.

- f) grout flow was usually 60 L/min, and this value was sporadically reduced to control and reduce occasional grout surge at the surface.
- g) grouting, in stages, until the postulated volume per manchette is completed, was conceived to create hydraulic fracturing planes in several directions, associated to each grouting stage. Initially, a 1,000 L grout volume per manchette was postulated in analogy with permeation grouting in sands, estimated as a function of the soil porosity. Tests showed this volume to be excessive, due to the long reach of the hydraulic fracturing planes as inspected in trenches, often at points over 10 m away from the grout hole. Treatment was defined to stop when 300 L of grout were absorbed by the soil or after 10 min of no intake of grout. Inspection trenches were opened and visual inspection showed that grouting planes of different stages generally formed parallel planes, often overlapping. These observations led to defining grouting in a single stage per manchette.
- h) water loss tests were performed in specially located additional boreholes to document the benefit of the treatment, limiting the maximum pressure of the test to 1.0 kg/cm<sup>2</sup> not to hydraulically fracture the soil.

Grout pressures suffer loss of applied head pressure during grouting, at the manchette borehole seal and at the hydraulic fracturing planes. This head loss depends on the physical characteristics of the rupture planes in the bore-

hole seal as well as in the hydraulic fracture planes, not allowing an effective control of the grouting process.

During the works, the control of the grout flow, by recording the manometric pressure resulting from the process, was pursued. It was postulated that the resulting manometric pressure, as read at gauges immediately at the surface, did not exceed in more than 50% the pressure recorded immediately after hole seal rupture.

Such control parameter derived from the relation between initial and final manometric pressure recorded during the execution of the experimental stretch. It was also observed that the occurrence of cracks at the surface followed by surge of grout, generally happened when this relation was greater than 1.5.

## 2.5. Evaluation of the subsoil treatment

The evaluation of the improvement of the saprolitic soil of the foundation of Balbina Dam with respect to its permeability was done through water loss tests carefully performed after the treatment, having as target the value of permeability of 10<sup>-4</sup> cm/s.

In Fig. 15 some test results are presented in relation to the information collected before grouting. The benefit of the treatment is obvious. In the mentioned figure, the interpretation of the water loss tests following Babouchkine's (1965) formulation is presented. The control tests indicated that after grouting there was considerable reduction in permeability coefficients, especially with the elimination of coefficients above 5.10<sup>-3</sup> cm/s.

An analysis of the data demonstrated the success of the treatment applied considering the elimination of high permeability zones and the consequent foundation homogenization with respect to its permeability.

Figures 16 to 19 were taken at the inspection trenches, depicting the successful treatment of the canaliculi.

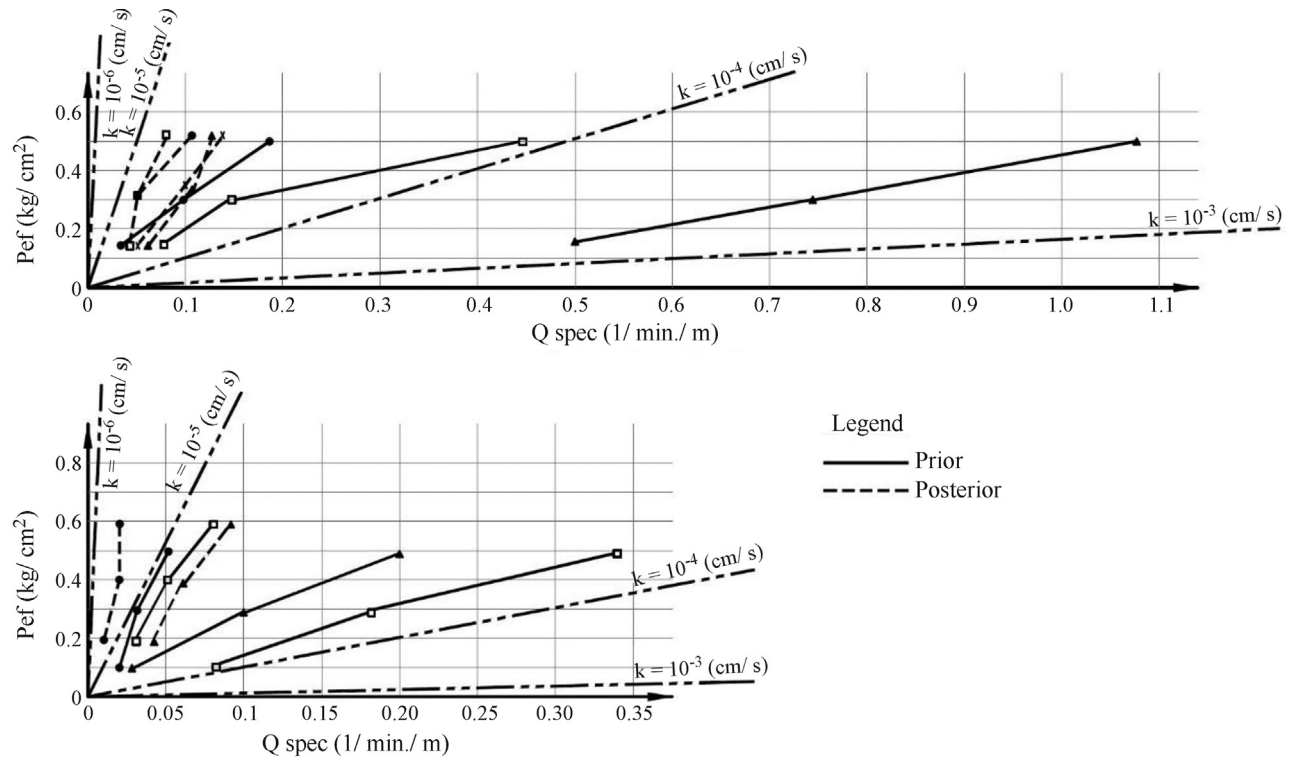


Figure 15 - Comparison of water loss tests prior and posterior to treatment.



Figure 16 - Inspection trench – clacage planes intersecting and treating canaliculi.



Figure 17 - Inspection trench – clacage planes intersecting and treating canaliculi.



Figure 18 - Inspection trench – clacage planes intersecting and treating canaliculi.



Figure 19 - Inspection trench – treated canaliculi.

### 2.6. Filling of the reservoir

Two different embankment cross sections were used during construction in order to separate the activities of foundation treatment from the earthmoving and compacting of embankment raising, which had to be done in a very defined time of the year due to the heavy rains that affect the Amazon Region. For this reason, in a region the grout buffer was positioned in the upstream of the dam and linked to the impervious core of the dam by a compacted berm,

while in other region the grout buffer was positioned just underneath the core of the dam, where the applied stresses are higher.

Monitored filling of the reservoir started in mid-1987; the first rainy season was not able to fill the reservoir, and data during partial filling is available. It documents the benefit of the treatment.

Figures 20 to 23 present cross sections of the dam in the described situations with plots of the water level in the

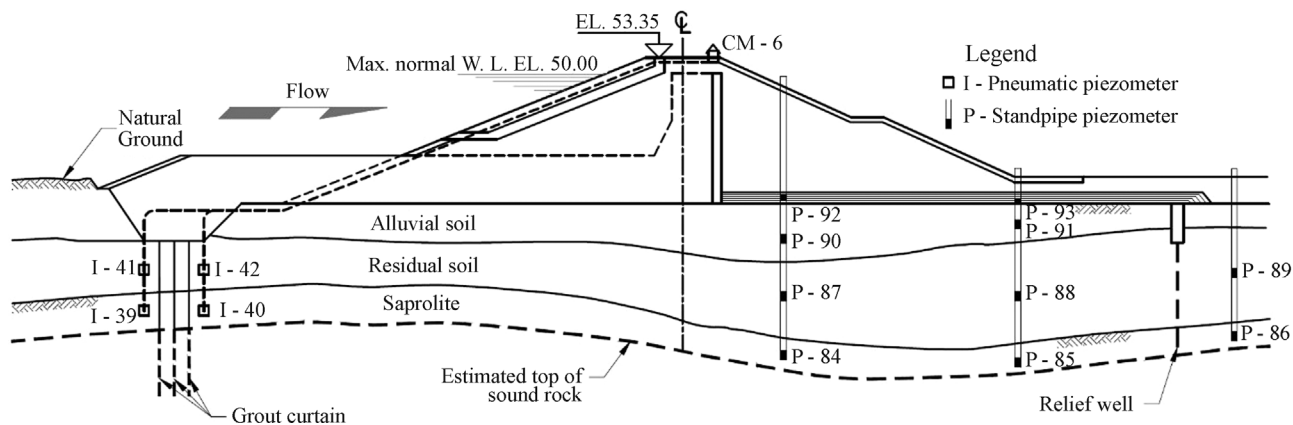


Figure 20 - Typical instrumentation in the right abutment.

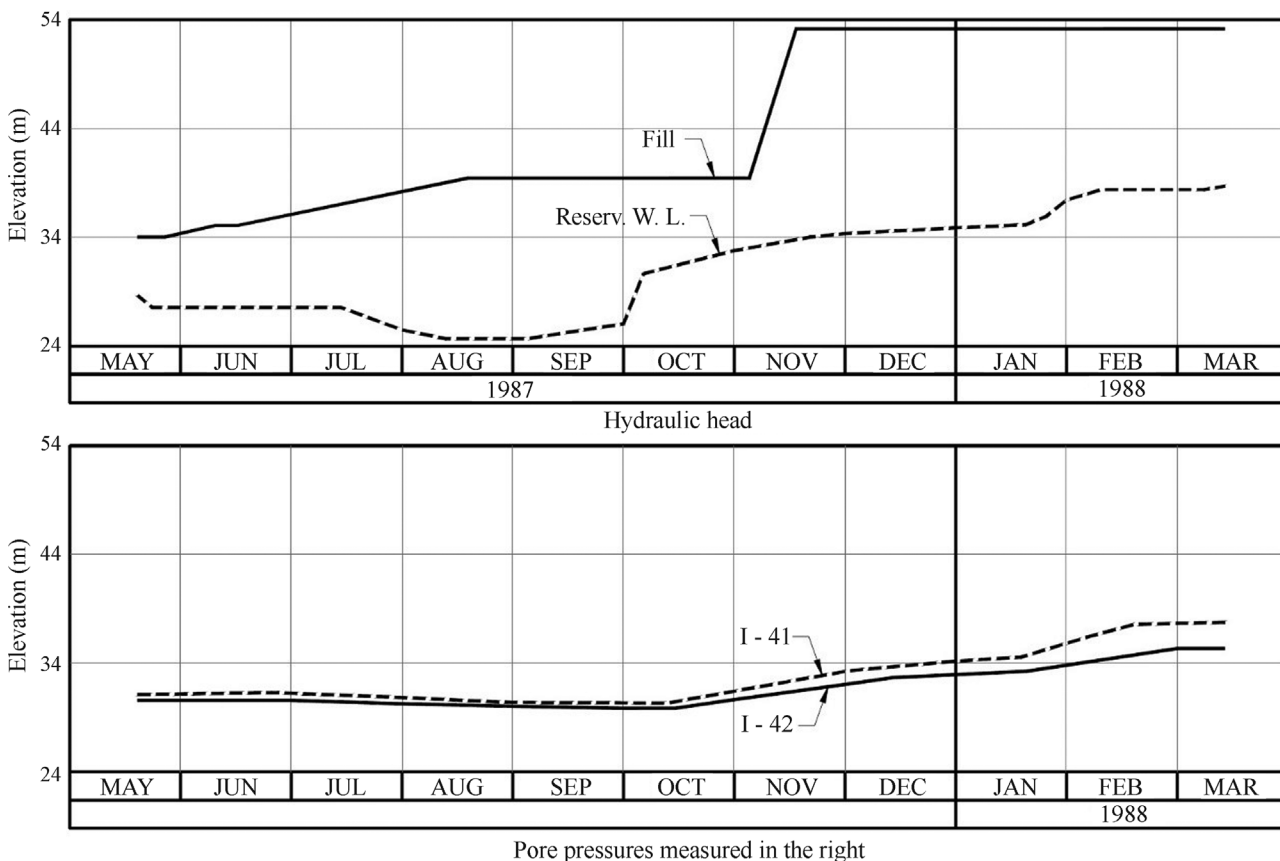


Figure 21 - Hydraulic head and pore pressure monitoring data for the right abutment.

reservoir and measured pore pressures in hydraulic piezometers.

The data collected as well as situ inspections demonstrated the validity of the use of the discussed treatment to homogenize and diminish the permeability of a saprolitic soil with a net of open canaliculi. Prof. Victor F.B. de Mello and Eng. Joaquim Franco were of crucial importance in conceiving and implementing this solution for Balbina HPP.

### 3. Teles Pires Hydroelectric Power Plant

The Teles Pires HPP is located in the Teles Pires River, contributor of the Tapajós River in the Amazon Basin at the border of Mato Grosso and Pará States. The main features associated to this power plant are: installed capacity 1,820 MW, generating since 2015; its structure includes a section in roller compacted concrete (RCC) and an embankment dam of rock fill with impervious earth fill core with maximum height of 80 m, and total crest length of

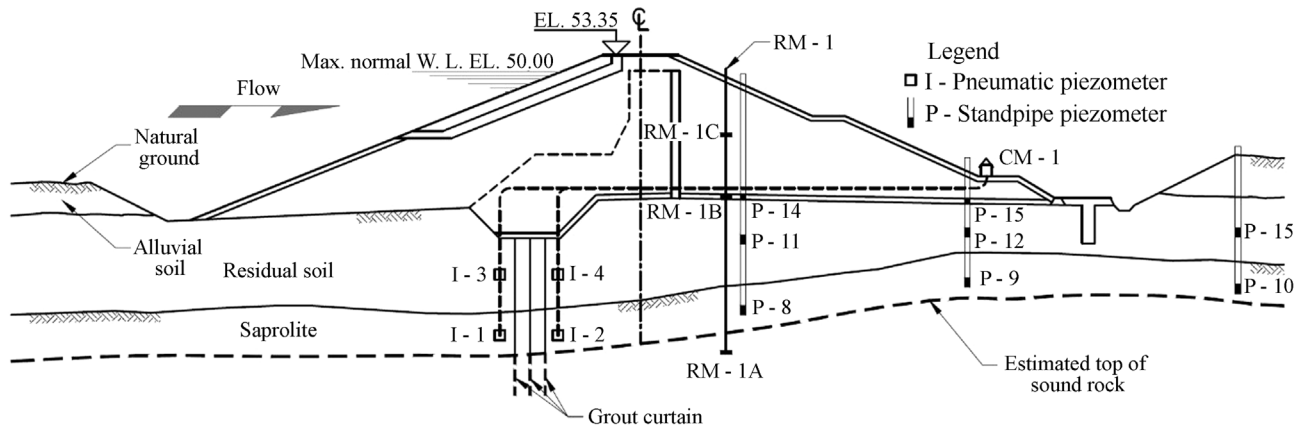


Figure 22 - Typical instrumentation on the left abutment.

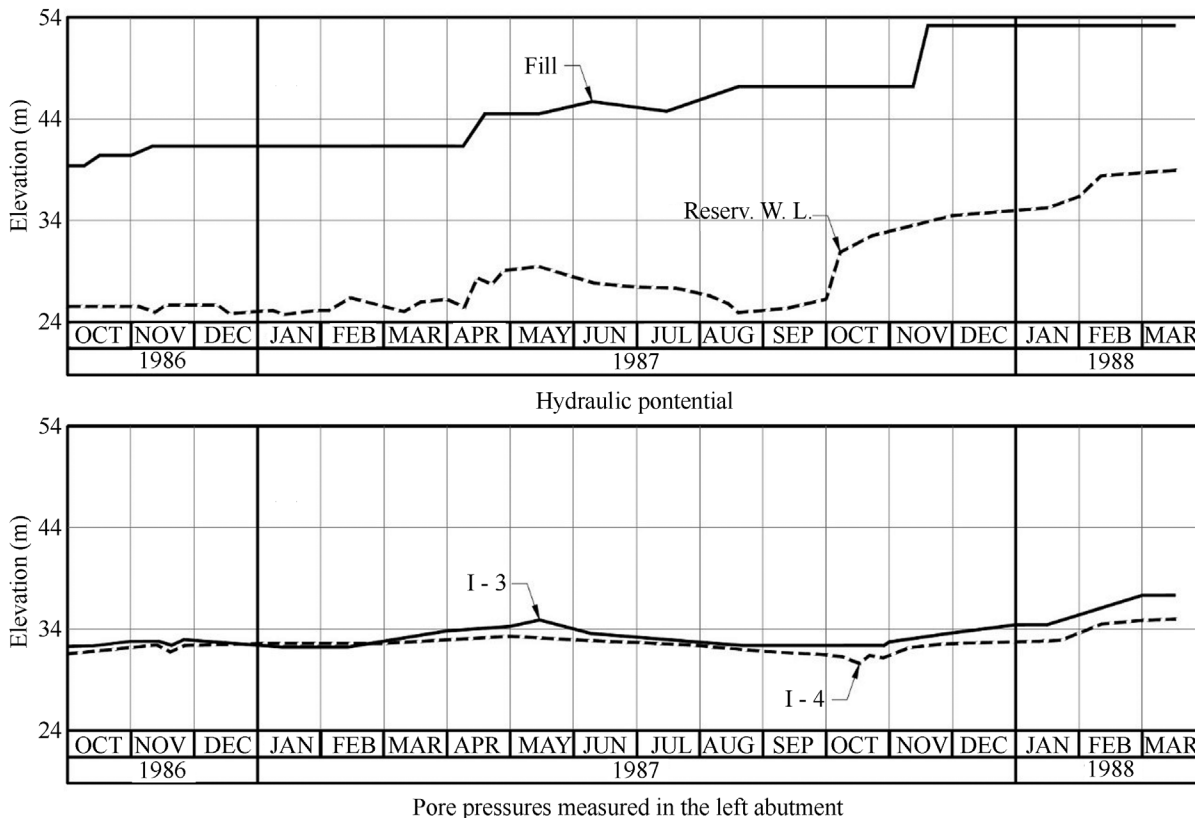


Figure 23 - Hydraulic head and pore pressure monitoring data for the left abutment.

1,650 m, 330 m of which correspond to the concrete structure; volume of the compacted soil 5,000,000 m<sup>3</sup>, maximum height of the structures 34 m and 33 m for the earth fill dam.

### 3.1. Local geology

The site is located in the north portion of the Teles Pires granitic batholite, not far away from its contact with the Colider volcanites. The most recent rocks found in this igneous body are basic dikes sheared by posterior events.

Two large sinistral wrench faults striking N40W generated an important tectonic binary responsible for a system of subvertical joints that affected the Teles Pires granite (Fig. 24). Other important vertical EW faults present a component of sinistral slip and cut the region together with extensive NE linears of an assumed gravitational distensive character.

As the mentioned faults are superimposed to the Teles Pires intrusion, the initial geologic model of the project was based on the presence on brittle tectonic features. These features are represented by subvertical and inclined shear fractures with slickensides, which could be identified in drill cores and excavation cuts. Such features are common in the transcurrent regime (Fig. 25).

In Riedel's model for conjugate fault systems (Fig. 26) the NW and sub EW subvertical and inclined striking fractures are of a typically dominant left lateral strike slip dynamics, while the NE fractures should be essentially of distensive character. In conclusion, the tectonic environment should be essentially transcurrent compressive represented by subvertical and inclined discontinuities.

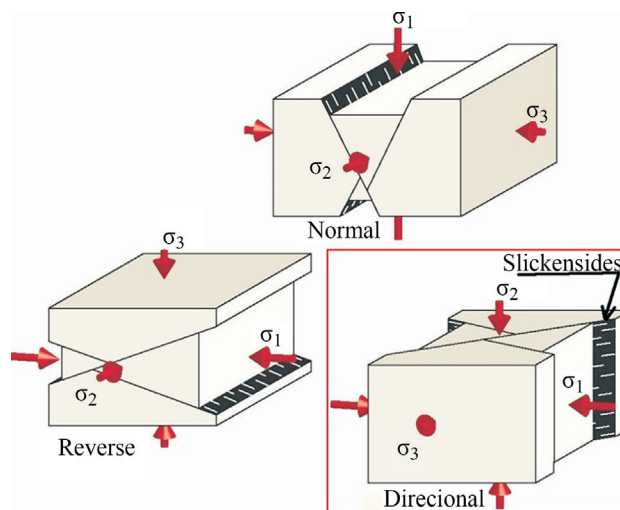


**Figure 25** - Illustration of the dominant transcurrent and reverse type of faulting (adapted from Fossen, 2010).

Additionally, the whole region was subjected to an intense hydrothermal activity along the different faults and shear zones. Therefore, the presence of caolinized zones, fillings of white and green clay minerals and even, locally, sulphides, are expected to mingle together with evidences of brittle tectonism such as gouges and slickensides.

During the initial design studies for this power plant, the geologic model assumed also incorporated the presence of relatively shallow sub-horizontal stress relief joints that would gradually vanish with depth. This common pattern of relief joints attenuating with depth is established in geological literature and also clearly exposed along several Brazilian dam foundations (Santa Clara, Santo Antônio and

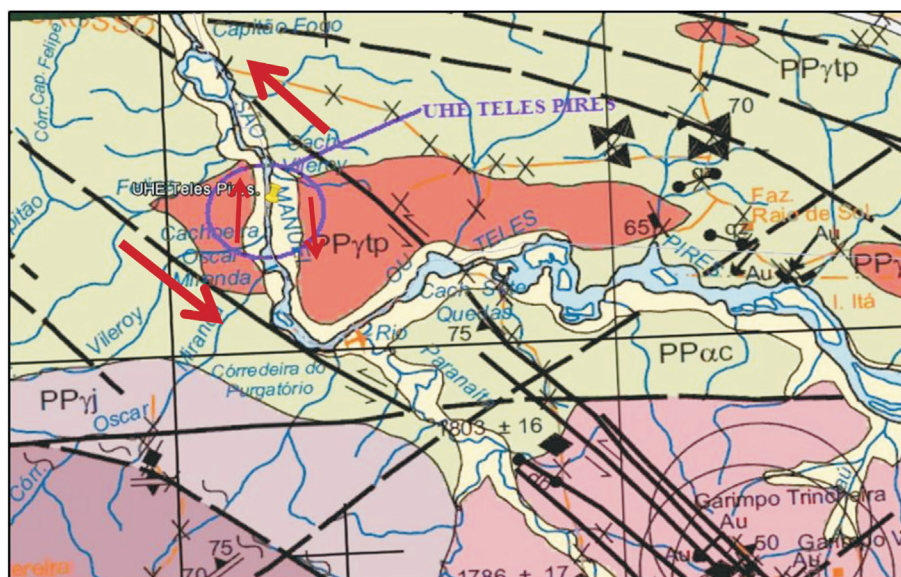


**Figure 24** - Detail of the official geological map of the Alta Floresta mineral province. The Teles Pires granite (PPγtp) intruded the Colider Group (in green). Both are cut by large strike slip component subvertical faults (thick black lines). Relative binary dynamics is expressed through the red arrows as also the slip component of the NS fault along the Teles Pires River.

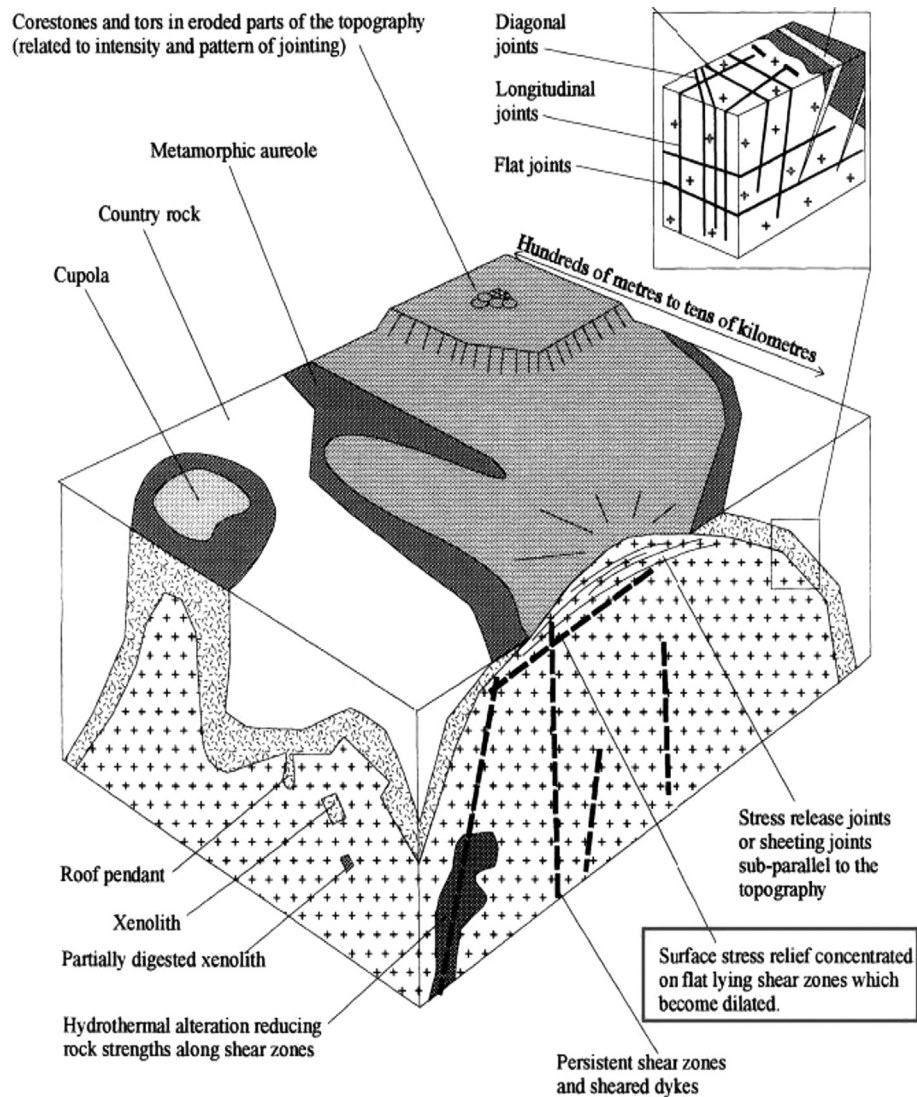


**Figure 26** - Stress relief sub-horizontal discontinuities and sub-horizontal shear zones dilated due to the vertical stress relief in granites.

Jirau dams, for example) as also internationally in some important engineering geological texts, such as the classic paper of Terzaghi and several other authors (Dale, 1923; Carlsson and Olsson, 1977; Holzhausen, 1989; Fookes *et al.*, 2000; Hencher *et al.*, 2011).

### 3.2. Update of the geologic model and of design

For detailed design, local difficulties prevented that detailed investigations were performed before beginning of the excavations in some regions, principally at the dam right abutment, where the intake and the powerhouse structures are located. As soon as access was permitted, 38 additional rotary borings were initially done, 4 with optical imaging, which allowed the visualization of the spatial position of the weathered zones. This allowed the separation of the horizontal from the inclined or vertical discontinuities, which is difficult and very debatable when the correct control of the discontinuities strike is not known due to the

mechanical fragmentation of the rock cores during drilling and core recovery. A high frequency of weathered sub-horizontal discontinuities was observed but the difficulty of correlating its continuity inhibited its extrapolation in the design cross sections used for design decisions and calculations, as shown Fig. 27.

The gradual increase in data acquisition clearly showed that the necessary revision of the geological model previously conceived had a major impact in the project structures stability. The incidence of weathered sub-horizontal discontinuities (Fig. 28) combined with the joints pattern had direct practical implications in the excavations design, leading to the need to lower the foundation of the water intake structure.

A comprehensive investigation program based on a dense array of rotoperussive borings, described by qualified geologists, was performed to better and quickly map the substrata underneath this structure, leading to the prop-

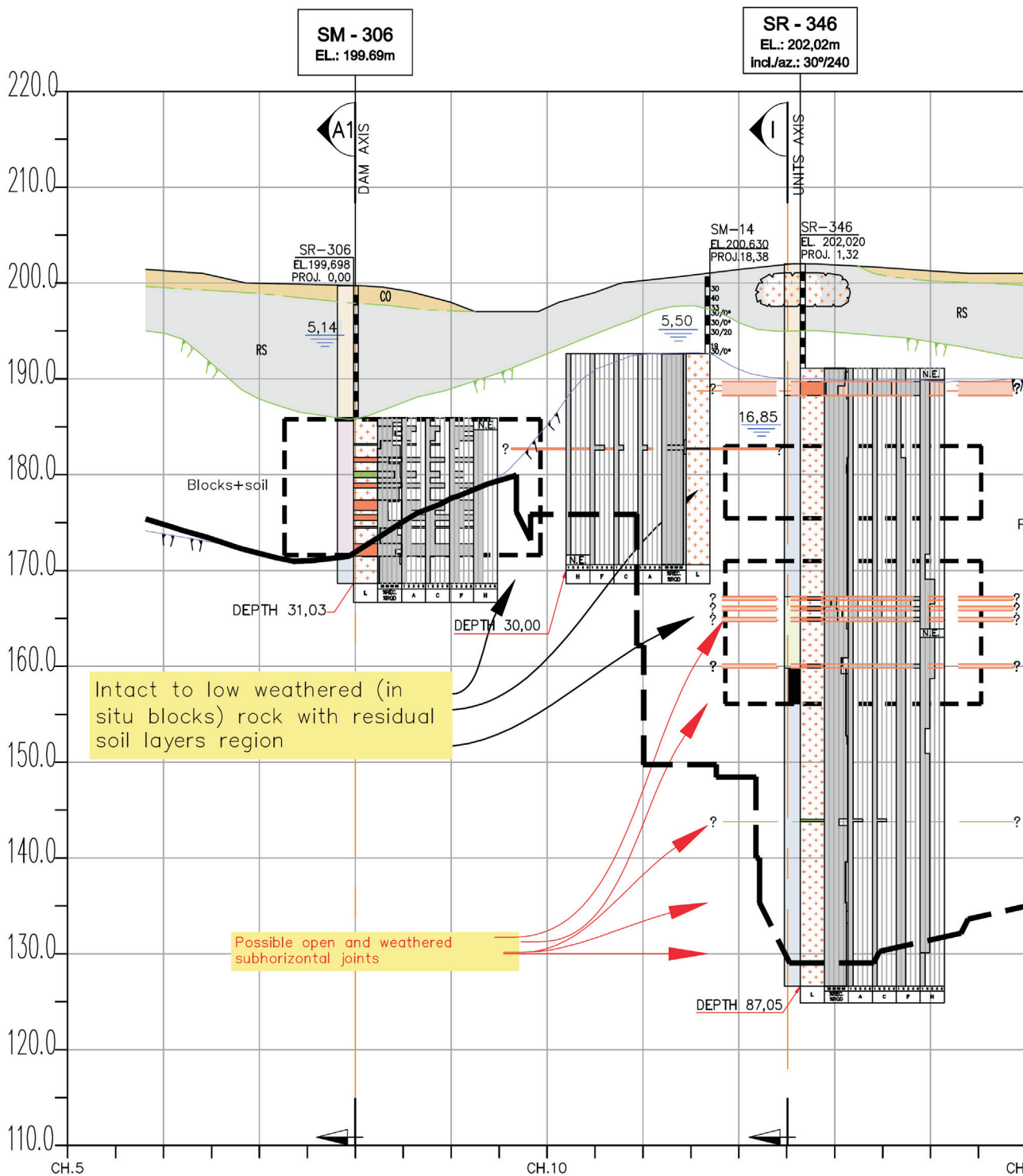
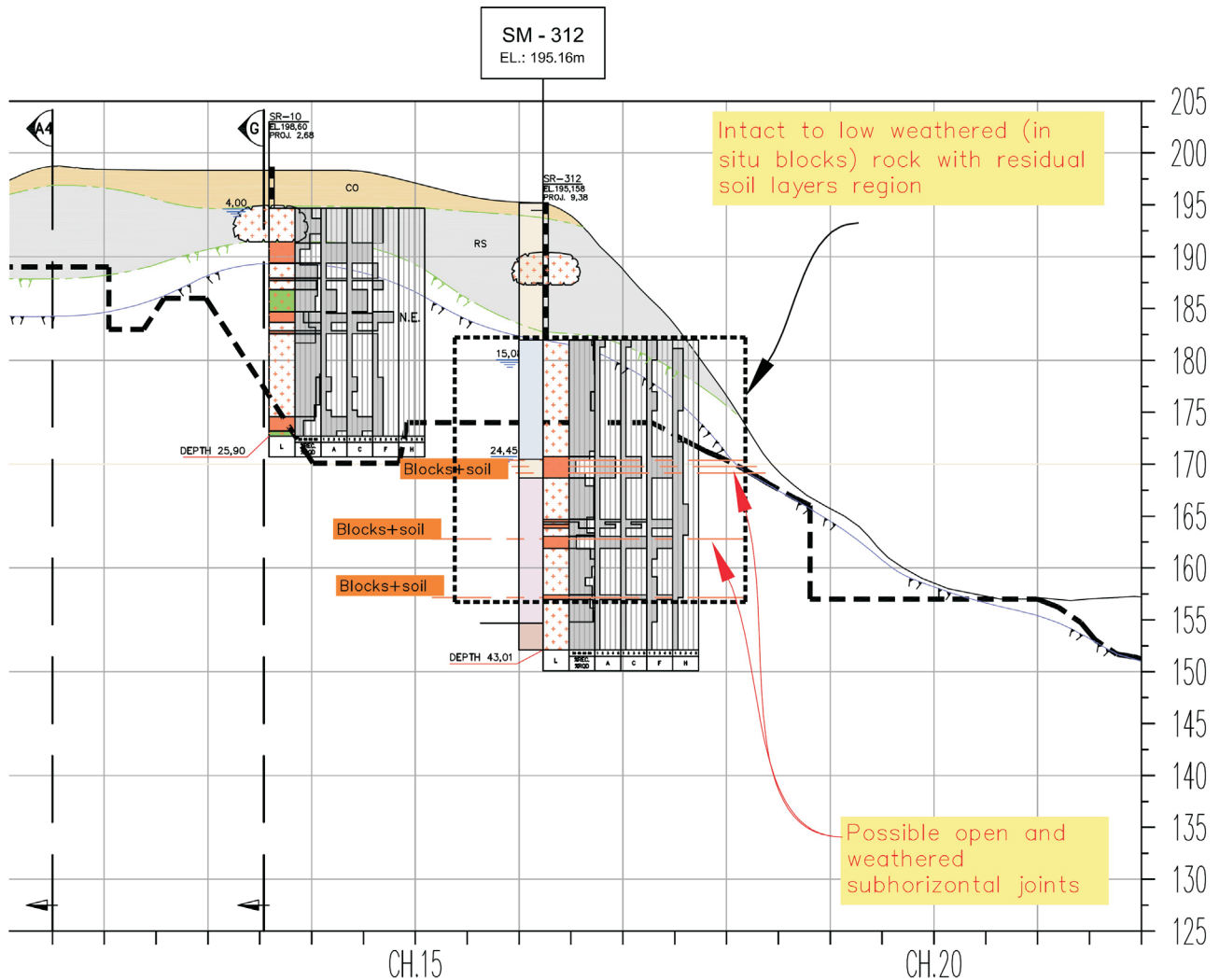


Figure 27 - Teles Pires intake structure foundation geological cross section after initial additional investigations for detailed design.

osition of a much more complex discontinuities pattern than initially predicted (Figs. 29 and 30). It clearly indicated the presence of thick discontinuities with soil filling concentrated between elevations 155 m and 170 m.

Later, during excavations, geological mapping confirmed that numerous of the sub-horizontal discon-

tinuities presented decametric extension with weathered soils filling frequently laminated and pre-sheared, with presence of estriae and slickensides. This characterized a sub-horizontal shear zone with indication of displacements accompanied by its sub-parallel secondary joints.



**Figure 28** - Teles Pires intake structure foundation geological cross section after further investigations, showing denser pattern of weathered subhorizontal joints.

This shear zone, identified as master joint, has its trace clearly visible on all walls of the excavation, dipping downstream with local components towards the river as shown in Figs. 31 and 32.

Features of the tectonic of displacements between the rock strata were gradually determined allowing to characterize a particular situation, distinct from the usual stress relief joints common in granites. A package of various subhorizontal shear zones with different indications of thrust in the NS direction was identified, in a non-previously described pattern for the region.

Figure 33 (a) to (e) and Fig. 34 (a) to (e) illustrate the typical characteristics and the variability of these characteristics in the master joint and its secondary structures.

The indications of thrust tectonism along extensive sub-horizontal discontinuities confirm the presence of pre-shearing, including in the rock / rock surfaces as observed in different locations of the excavated face, as well as, later,

in the stabilizing structures excavated in the area (Fig. 34 (a) to (e)).

Based on this revised geological model the stability of the intake structure with relation to its sliding became intrinsically conditioned by the master joint, requiring special attention. Figure 35 presents the discontinuity pattern mapped at the water intake structure foundation as seen on the penstock excavation face, and Fig. 36 displays a cross section for the water intake structure, presenting the identified discontinuity pattern as used in the geomechanical model proposed.

### 3.3. Laboratory tests

In order to characterize the geomechanical properties of the more intensively weathered material present in the master joint, a series of laboratory tests were performed in samples prepared from undisturbed blocks. Full characterization of the material and shear strength determination were pursued, through direct shear and triaxial tests. In or-

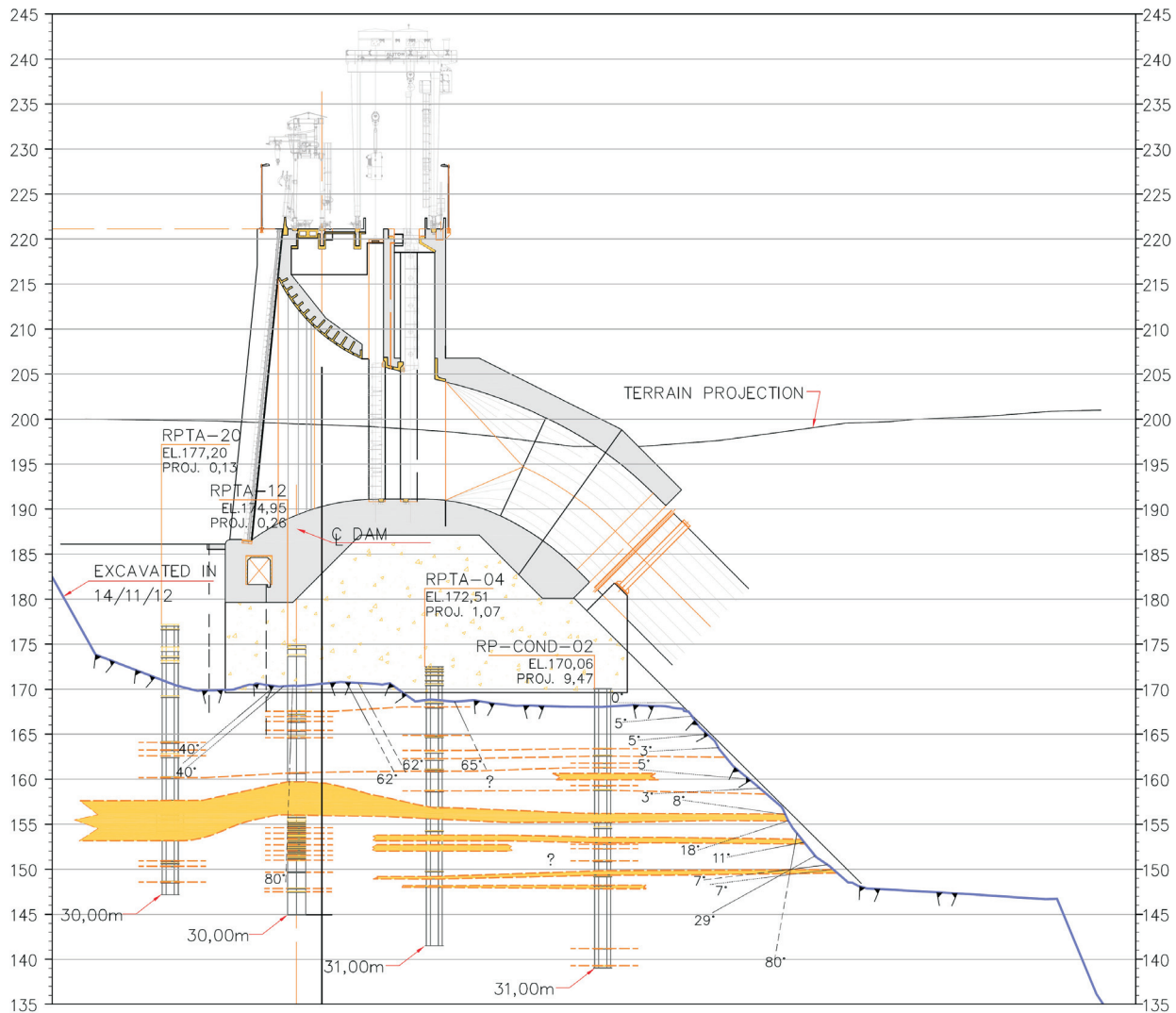


Figure 29 - Updated discontinuity pattern at the water intake structure foundation – Cross section after rotoperussive dense array investigations.

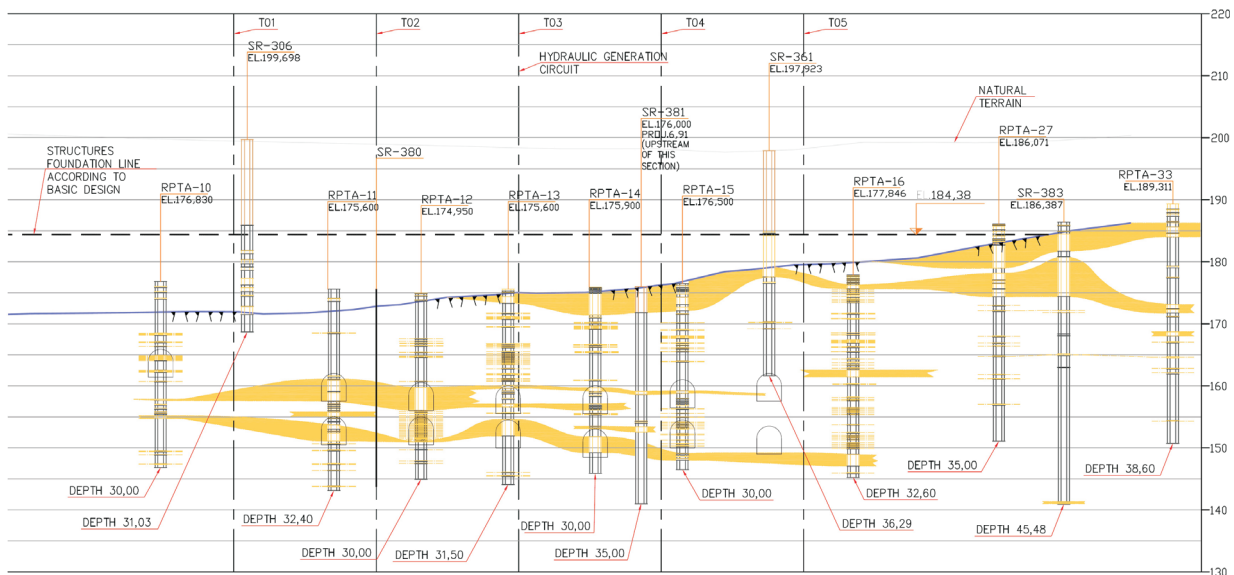


Figure 30 - Updated discontinuity pattern at the water intake structure foundation – Longitudinal section.

Intake structure

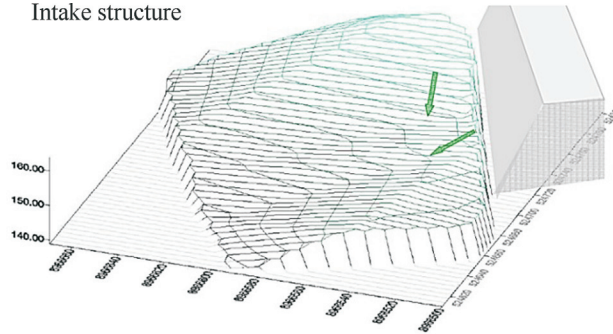


Figure 31 - Master joint 3 D surface model.



Figure 32 - Master joint trace emphasized in yellow, as visible at the excavation walls.

der to try to bypass the problem of sample heterogeneity, step incremental stress tests on the same samples were performed, with partial success.

The interpretation of the test results was done trying to postulate the shear strength available at strains of 0.5% in the triaxial tests and displacements of 0.5 mm in the shear box, of 1.0%/1.0 mm, and 2.0%/2.0 mm, as well as at peak values.

Figures 37 to 40 plot the laboratory shear strength test results and proposed envelope. The results are presented plotting the normal and shear stresses acting at the oriented plane; a Mohr-Coulomb failure envelope with null cohe-

sion tangent to the Mohr's Circle is proposed for each hypothesis of strain at failure.

Fixing a null cohesion intercept, the range of values of friction angle,  $\phi'$ , obtained vary between: 10° and 27° for strains / displacements of 0.5% / 0.5 mm; 16° and 40° for strains / displacements of 1.0% / 1.0 mm; 18° and 40° for strains / displacements of 2.0% / 2.0 mm; and 20° and 42° for peak stress-strain values.

Additionally to the shear strength parameters of the more intensively weathered material present in the master joint, parameters for the secondary features associated to the master joint were also necessary. Considering that these

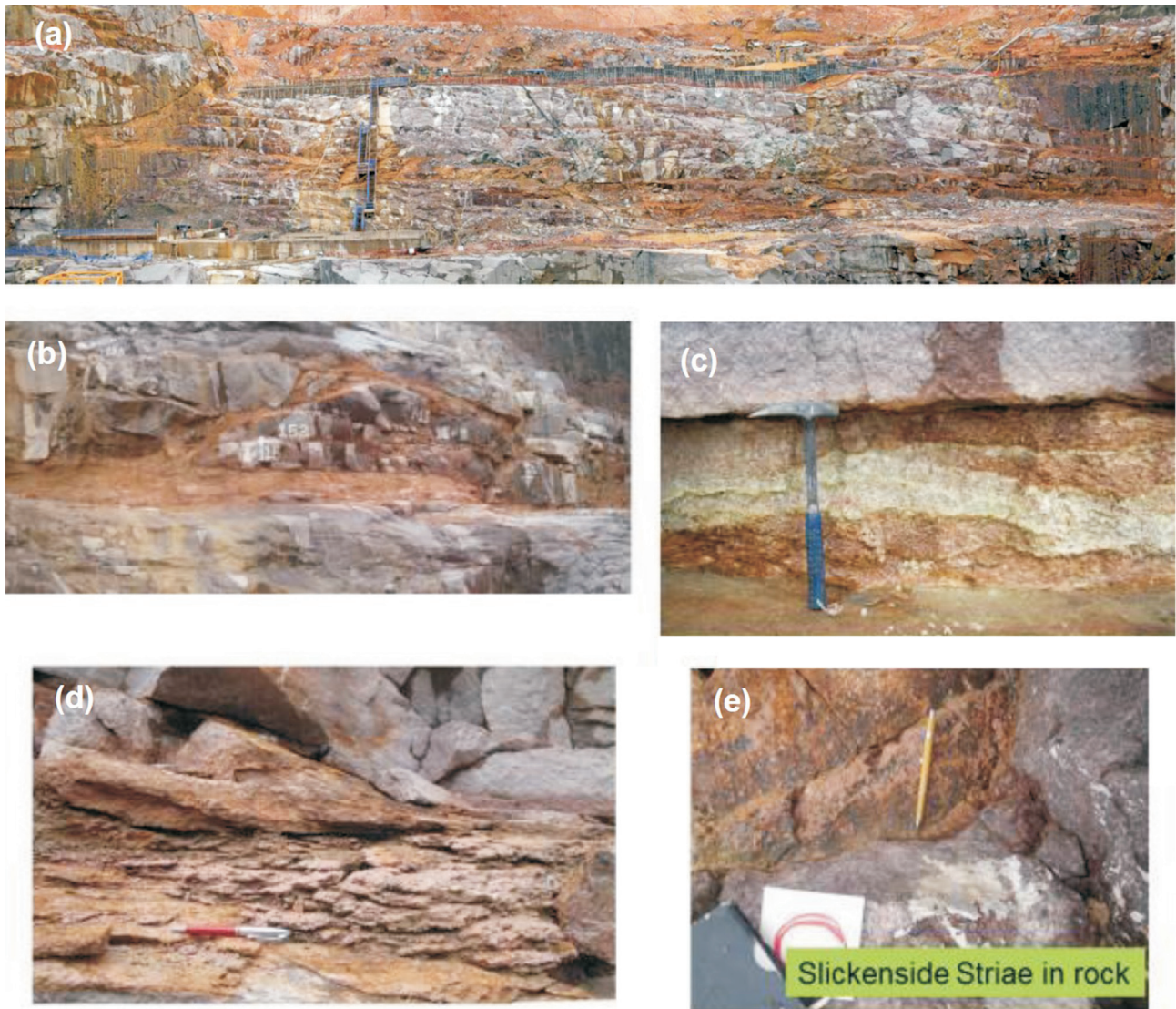


**Figure 33** - Typical shear features in the master joint: (a) General view of excavation wall; (b) Isolated shear lens; (c) Clayey zone in a lens; (d) Lenticular lamination; (e) rock-rock displacement estriae.

secondary features present less weathered to rocky characteristics in some regions, associated to difficulties of obtaining undisturbed samples of these materials to fit in a shear box, estimates of the shear strength available in these locations was pursued from Barton's classification parameters  $J_r$  (joint roughness number) and  $J_a$  (joint alteration number). For regions where these structures present themselves associating soil-like material with saprolites/slightly weathered rock with lateral continuity, this procedure led to postulating values of angle of friction,  $\phi'$ , varying between  $7^\circ$  and  $11^\circ$ ; and finally, in locations where less weathered rock dominates, a friction angle,  $\phi'$ , of  $20^\circ$  was postulated.

Difficulty remained in interpreting and postulating an average shear strength value representative of the master joint as a whole.

### 3.4. Design of the stabilizing structure

Safety of the water intake structure was verified against sliding, overturning, flotation and maximum stresses at its base, for different loading hypotheses, as routinely done in design procedures. Specifically, the sliding verifications were performed following the basic equation:

$$FSD = \frac{\sum N_i \tan(\phi_i) + \sum C_i A_i}{\sum T_i} \geq 1.0 \quad (2)$$

where  $FSD$  = Factor of safety against sliding;  $CSD\phi$  = Reduction factor on the friction angle  $\phi'$ ;  $CSDc$  = Reduction factor on the cohesion  $c'$ ;  $N_i$  = Resultant of normal forces to the sliding surface being analysed;  $\phi_i$  = Characteristic fric-

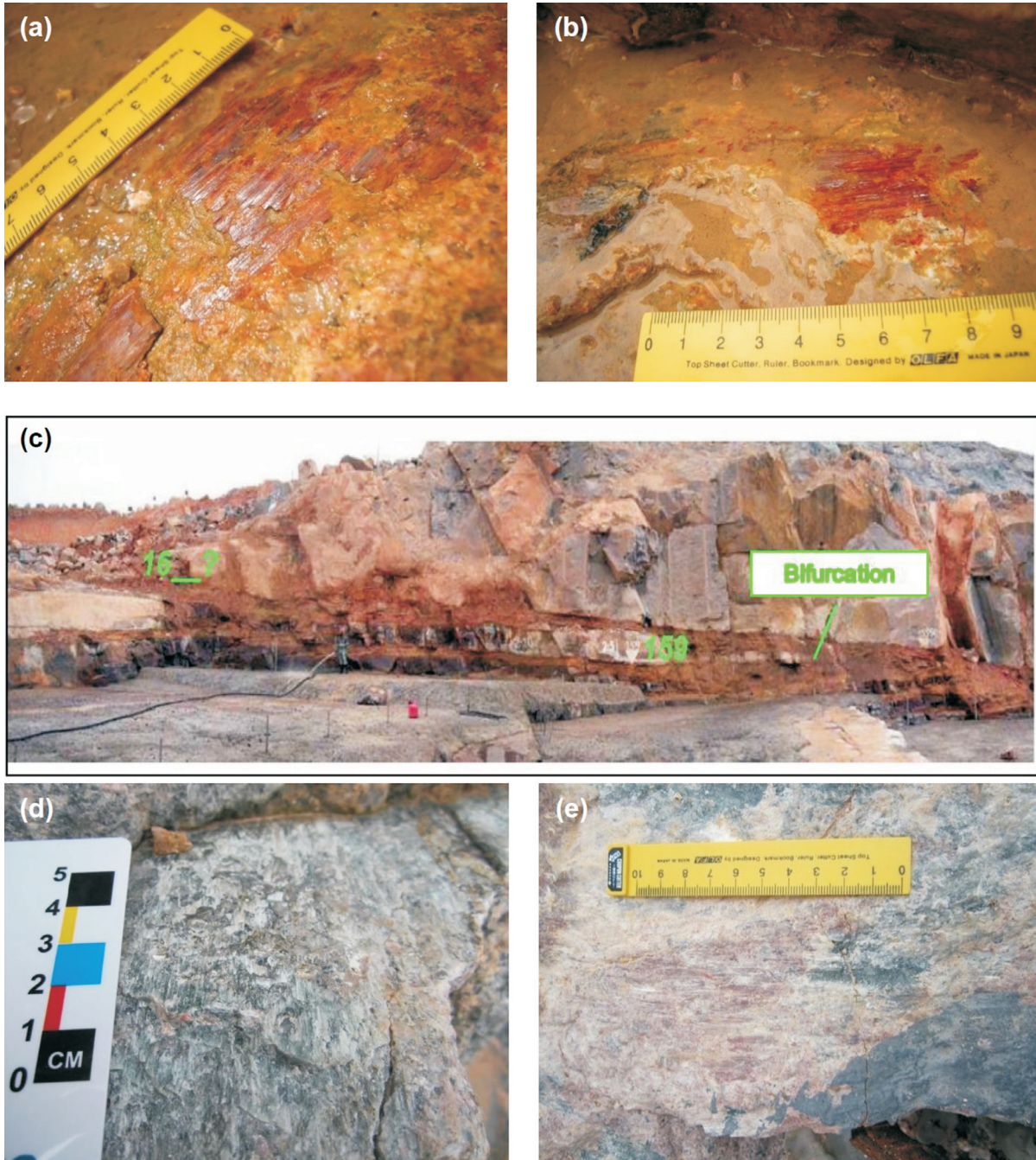


**Figure 34** - Typical shear features in the master joint: (a) (b) Slickensides; (c) Bifurcation at master joint; (d) and (e) Estriae in non-weathered rock / rock interface.

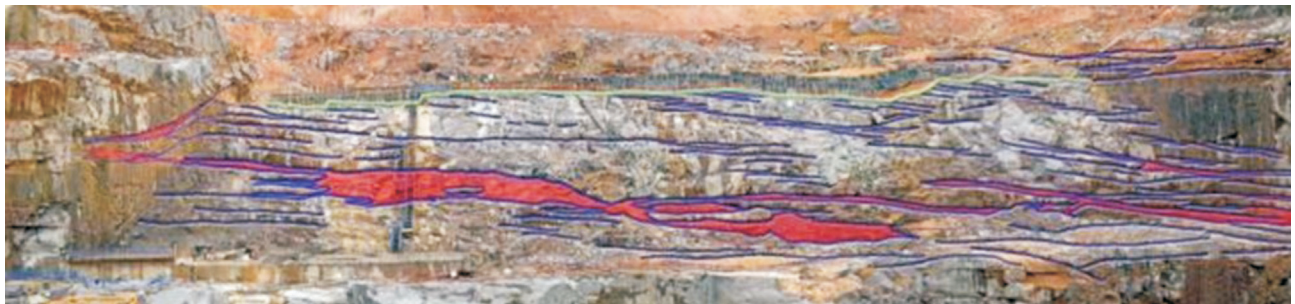


**Figure 35** - Master joint and discontinuity pattern at water intake structure foundations.

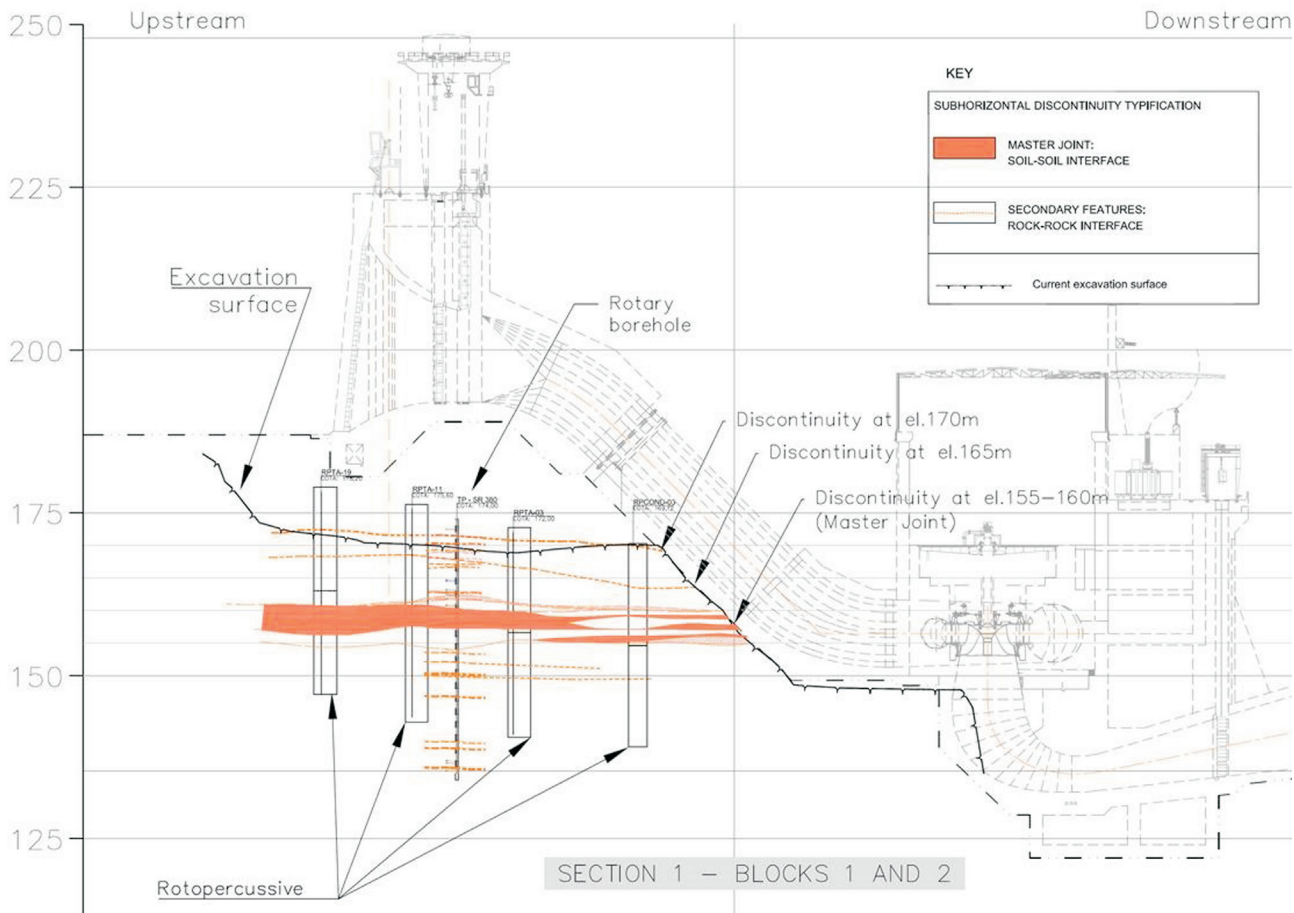


Figure 36 - Water intake structure cross section with discontinuity pattern in tune with proposed updated geological model.

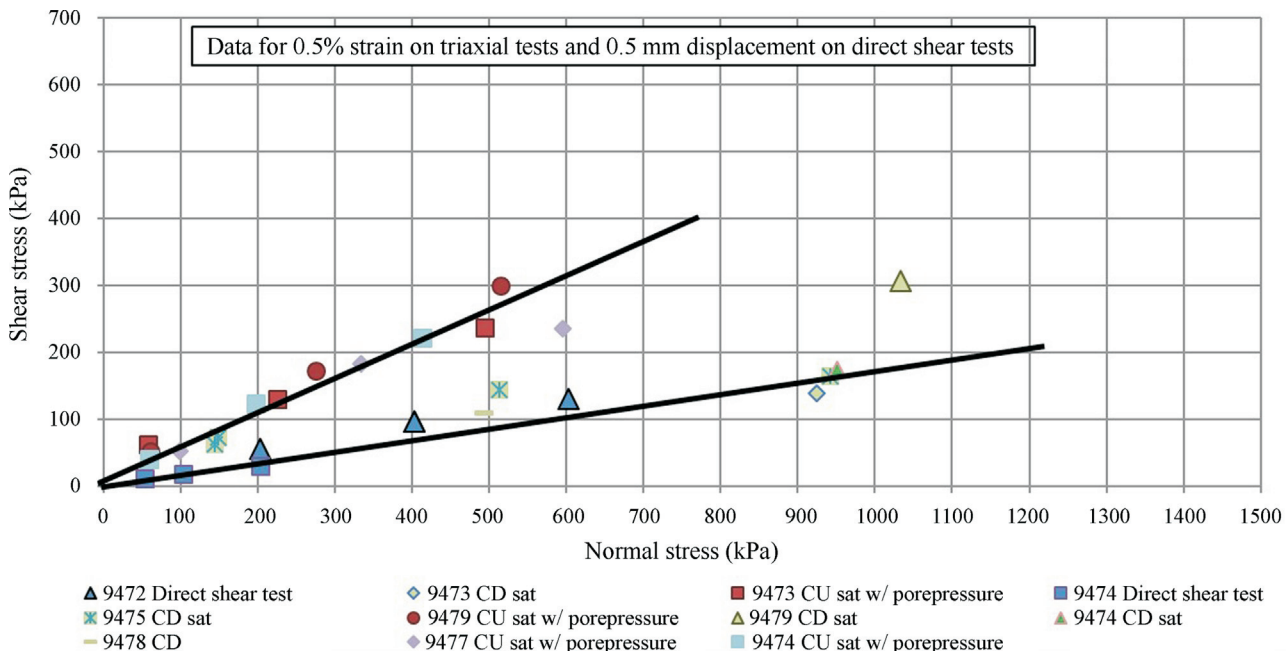


Figure 37 - Triaxial tests and direct shear tests results for 0.5% strain / 0.5 mm displacement.

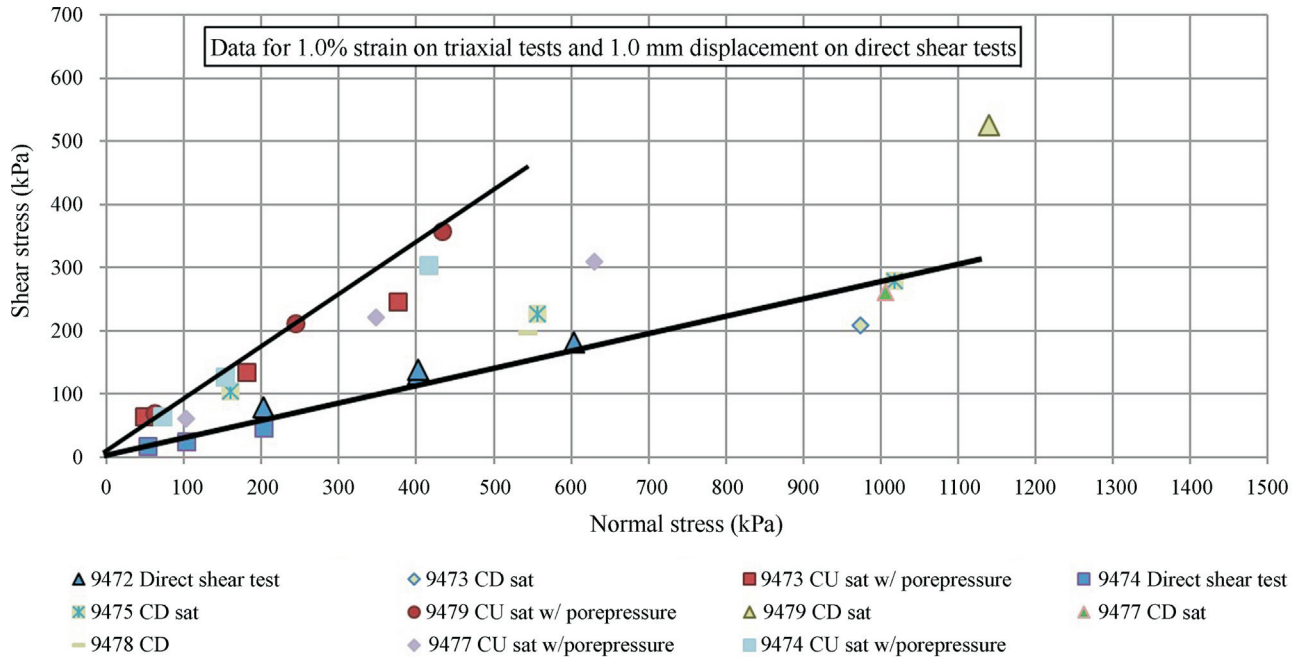


Figure 38 - Triaxial tests and direct shear tests results for 1.0% strain / 1.0 mm displacement.

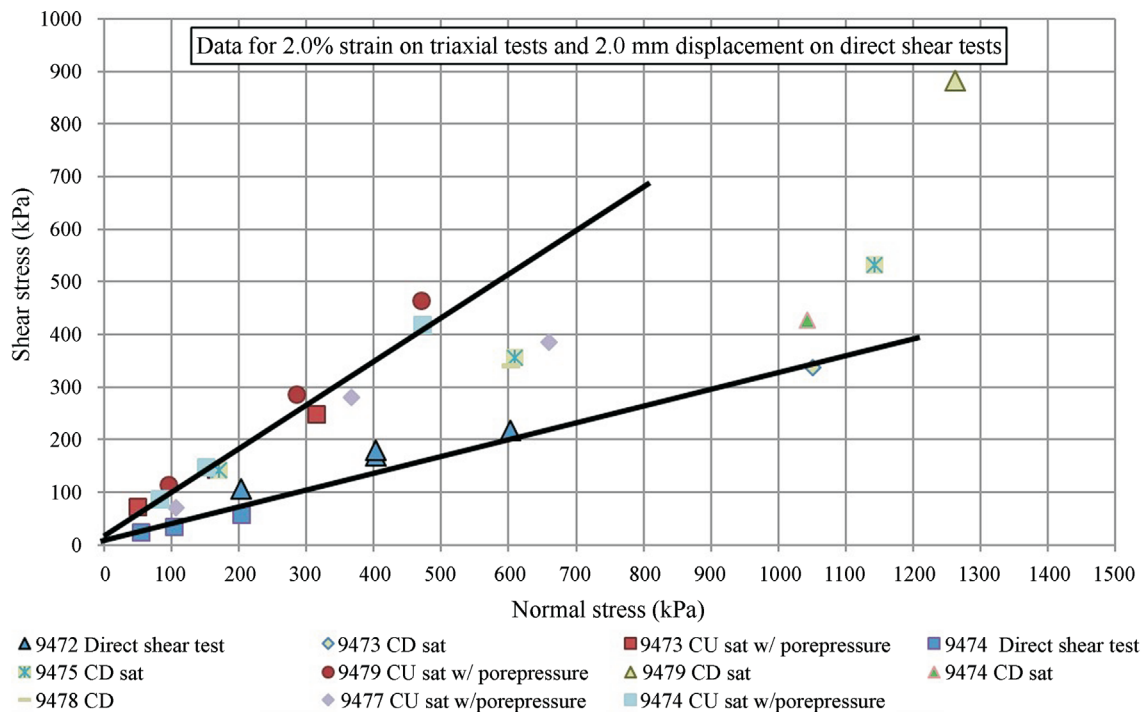


Figure 39 - Triaxial tests and direct shear tests results for 2.0% strain / 2.0 mm displacement.

tion angle of the sliding surface being analysed;  $C_i$  = Characteristic cohesion along the surface being analysed;  $A_i$  = Structure contact effective area in the plane being analysed;  $T_i$  = Resultant of the forces parallel to the sliding surface.

The Brazilian codes require values of partial factors of safety  $CSD\phi$  and  $CSDc$  of 1.3 and 1.5, respectively for

the angle of friction and the cohesion, for normal loading conditions.

Initially, reverse calculations were performed to check what values of shear strength parameters were necessary to comply with the safety requirements. With zero cohesion intercept, as associated to surfaces with pre-existing slickensides, a value of  $34.9^\circ$  was shown to be required to

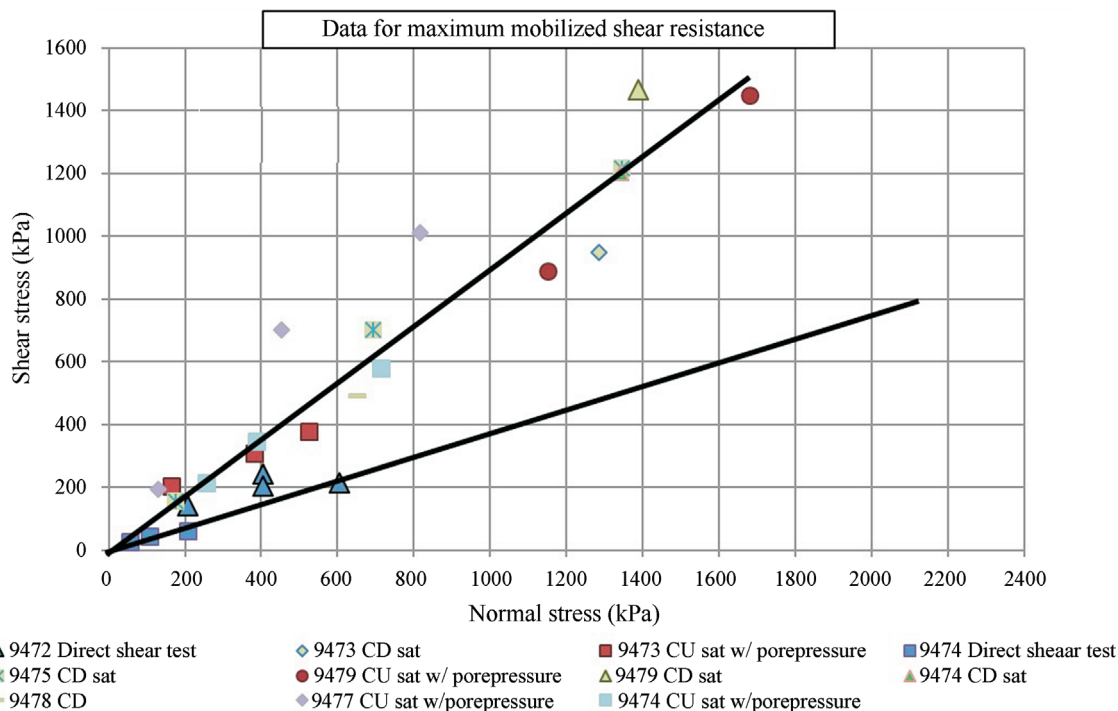


**Figure 40** - Triaxial tests and direct shear tests results for peak values.

comply with stability safety factors. As this value of shear strength could not be anticipated to prevail in the master joint or any other discontinuity with slickensides, a drainage gallery was conceived and designed at elevation 140 m linked to the water intake structure gallery by a series of vertical drains. The reduction of water pressure in the base of the intake structure led to a reduction of the required shear strength of the conditioning discontinuities, which under this hypothesis resulted in  $29.5^\circ$ .

Again, this value of shear strength could not be anticipated to prevail in the master joint or any other persistent discontinuity with slickensides, leading to the decision to design underground galleries filled with concrete to contribute as shear keys, increasing the safety factors to sliding to the required value. Having in consideration the distinct stress-strain behaviour of the concrete in the shear keys with relation to the soil filling of the discontinuities, it was decided that the shear keys should sustain all the horizontal stresses applied at the elevations where discontinuities prevailed, with no load being transmitted through the rock mass. Two longitudinal shear keys linked by five transversal shear keys were designed. The geometry of these galleries was not rigidly fixed in design, the specifications being that the galleries should follow the master joint (Fig. 41), excavating an additional 2.5 m of the rock mass above its crown and 1 m below its invert.

An international Board of Consultants was invited to contribute in the difficult decision of postulating a representative value of average operating shear strength in the master joint; the results of the shear strength tests per-

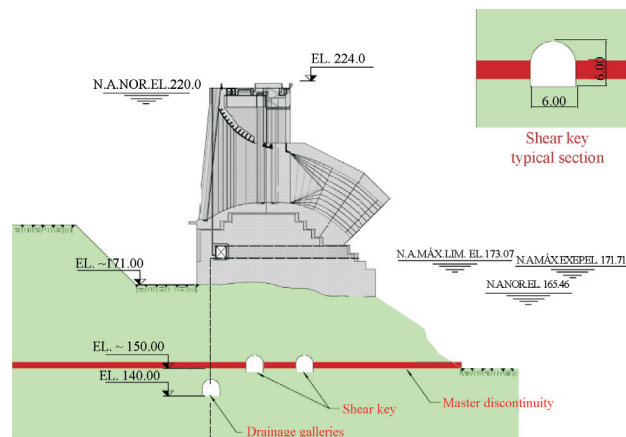


**Figure 41** - Modeled shear key geometry.

formed were used to help in the postulation of the average representative values to be used in stability analysis. The estimative of an angle of friction for the master joint postulated by the BoC was between  $25^\circ$  and  $28^\circ$ , with worst-case scenarios to be verified with  $22^\circ$ .

Stabilizing shear keys were designed to guarantee safety of the structure from sliding as conditioned by the master joint (Figs. 42 to 45), associated to a drainage gallery previously conceived, also at the foundation of the intake structure, at elevation 140 m, and relieving the water pressure as drained by a battery of vertical drains (Figs. 42 to 47).

Secondary parallel joints above the master joint were also identified and mapped during excavation (Fig. 48);

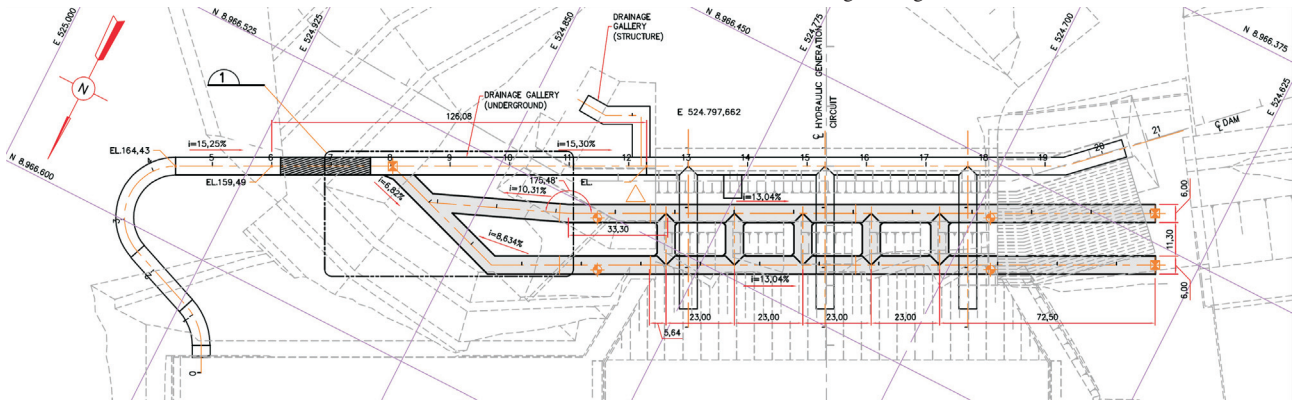


Figure 42 - Shear keys and drainage galleries – Plan view.

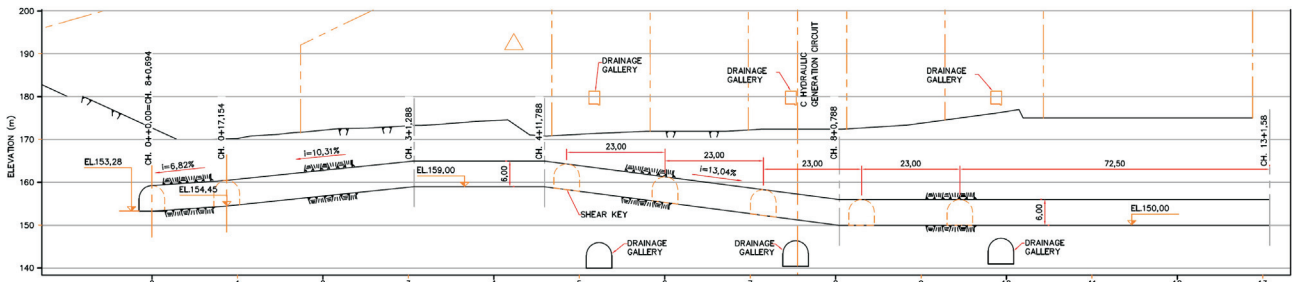


Figure 43 - Shear keys and drainage galleries – Longitudinal profile – Access to shear keys.

their influence on the stability of the intake structure had to be discussed and evaluated together with that of the master joint itself, taking in consideration their spatial random variation.

Further sliding stability verifications were performed, leading to the decision to install an upstream impervious blanket with two HDPE layers (Fig. 49) to reduce the water pressures in the intake structure foundation, as well as 55 passive subvertical anchors of 57 mm diameter, working in shear. These additional stabilizing details increased the factor of safety by 12% to 18%, depending on the loading case and depth of the discontinuity, also guaranteeing the stability of all secondary sub-horizontal planes/features existing between the foundation of the water intake structure and the master joint.

### 3.5. Monitored behaviour of the dam during initial filling and subsequent period

Reservoir filling began in December 2014 and was very fast, with 85% filling happening in only 8 days; after all environmental issues were properly dealt with, the last 1.8 m of the reservoir was filled after 1 month. Readings of the extensive monitoring program after 8 months of maximum reservoir level are summarized below.

Among many instruments installed in the water intake structure, the behaviour of this structure can be represented by the behaviour of extensometers and piezometers installed in the structure foundation underneath one of its concrete blocks.

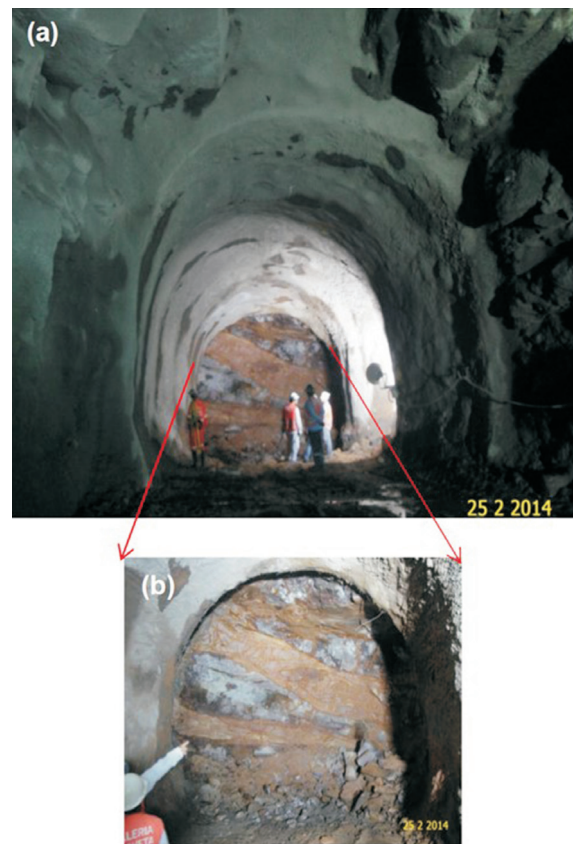


Figure 44 - Front view of the downstream shear key. Note the gallery overbreak above the steel ribs (a), and the detail of the downstream dipping of the weathered master joint (b).



Figure 45 - Detail of the weathering pattern in the master joint.

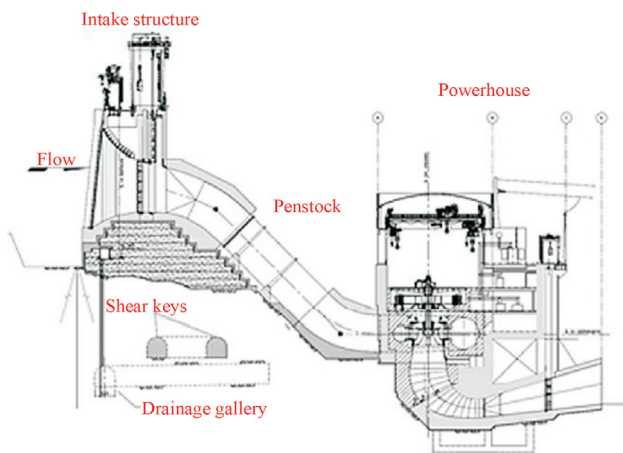


Figure 46 - Cross section of the intake structure foundation shear keys, drainage galleries and drainage curtain.

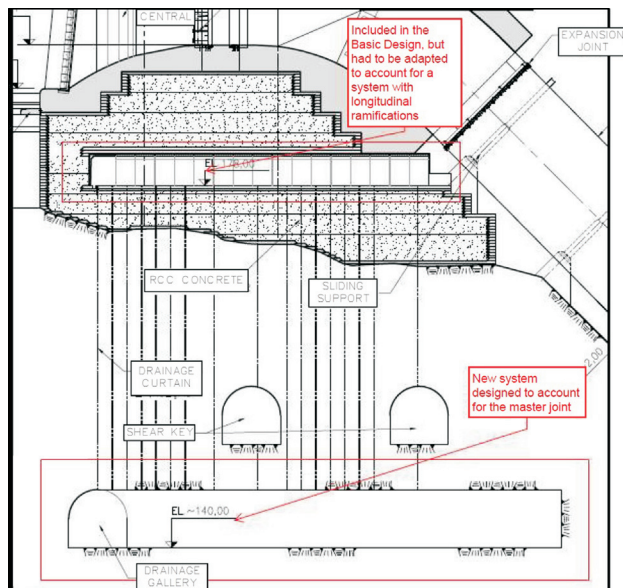


Figure 47 - Detail of the cross section of the water intake structure foundation showing the shear keys, drainage galleries and drainage curtain.

The extensometer measurement results presented in Fig. 50 are representative of the behaviour shown by all such instruments.

Readings show that deformations of approximately 10 mm happened when the galleries were being excavated in the region of influence of the instrument, especially as tunnel excavation suffered important overbreak in following the master joint within the design criteria, leading this excavation to being only 4 m to 5 m from the foundation of the intake structure. Additionally, the load imposed by the concrete around the penstocks before filling the shear keys with concrete is considered to have influenced the behaviour monitored. Soon after concrete filling of each gallery/shear key, deformations stopped completely, and were not affected or mobilized by the reservoir filling at all.

Standpipe and electric piezometers were installed from the intake structure drainage and monitoring gallery, inclined  $10^\circ$  upstream and  $15^\circ$  downstream in order to check the real hydrostatic thrust acting on the structure foundation and compare it to the design hypothesis. The comparison of the hydraulic head measured with that used in design verifications is an important parameter to judge the efficiency of drainage on the thrust diagram acting on the structure foundation. Two distinct water thrust diagrams were used in these verifications: one suggested by the international BoC (Fig. 51 (a)), and another that does not include the contributing efficiency of the HDPE impervious upstream blanket (Fig. 51 (b)).

The measured piezometric values (Fig. 52) led to conclude that the diagram of water thrust suggested by the BoC for the structure foundation was surpassed in some of the intake blocks, while all readings were lower than the piezometric levels associated to the hypothesis of a non-efficient HDPE upstream impervious blanket in the foundation.

Having in consideration that no incremental deformations were measured by the extensometers when the water thrust diagram started to be imposed by reservoir filling, the fact that some readings were higher than those postulated by the BoC did not raise any further concerns.

The piezometers also allow the verification of the efficiency of the grouting curtain. The measured values allow to interpret that this efficiency is on average associated to a reduction of 60% of the measured upstream water pressure.

All readings stabilized soon after reservoir filling and are considered to be in compliance with design predictions and criteria.

#### 4. Chaglla Hydroelectric Power Plant

The Chaglla Hydroelectric Power Plant is located on the Huallaga River in the Chaglla and Chinchao districts, department of Huánuco, Peru. The dam axis is located downstream from the confluence of the Panao River and the Huallaga River and the total catchment area is around  $7,150 \text{ km}^2$ . It comprises a 202 m high concrete face rockfill dam (CFRD) with a crest length of 274 m, three tunnel

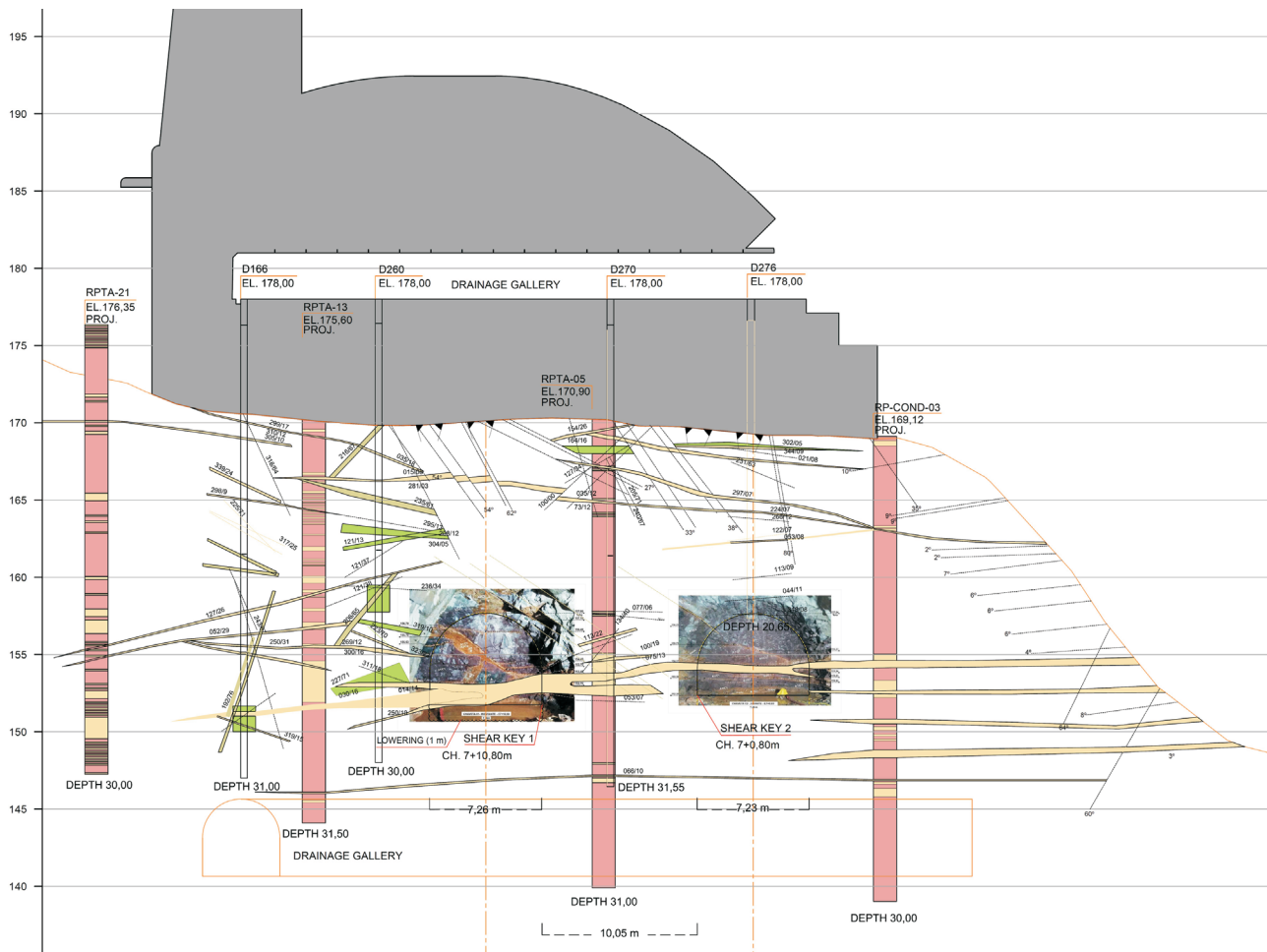


Figure 48 - Water intake structure foundation cross section with master joint and secondary parallel joints.

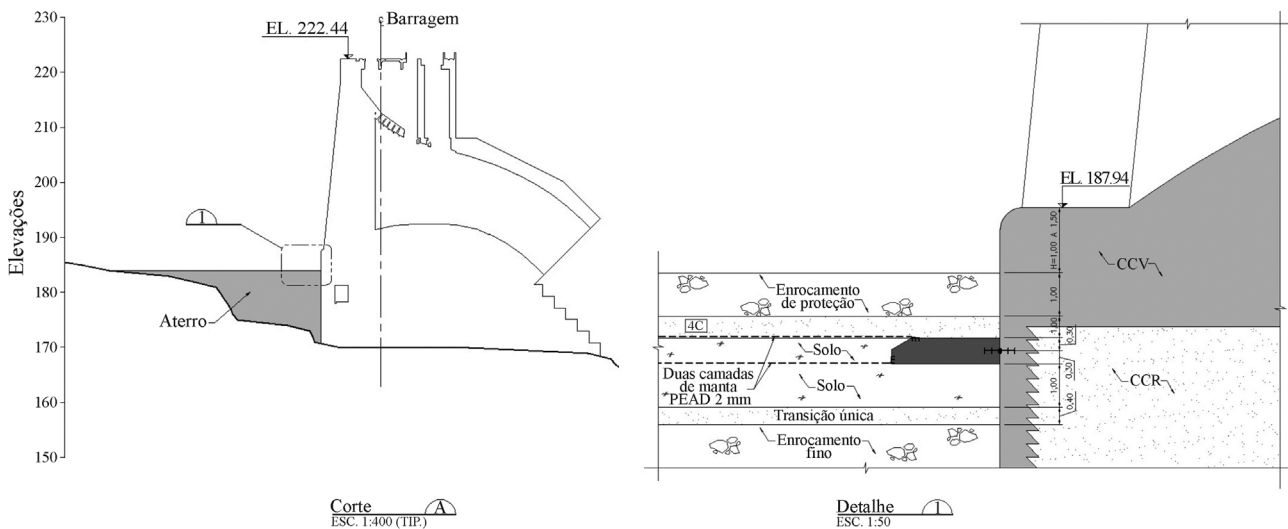


Figure 49 - Upstream impervious blanket – Detail showing fill and HDPE layers.

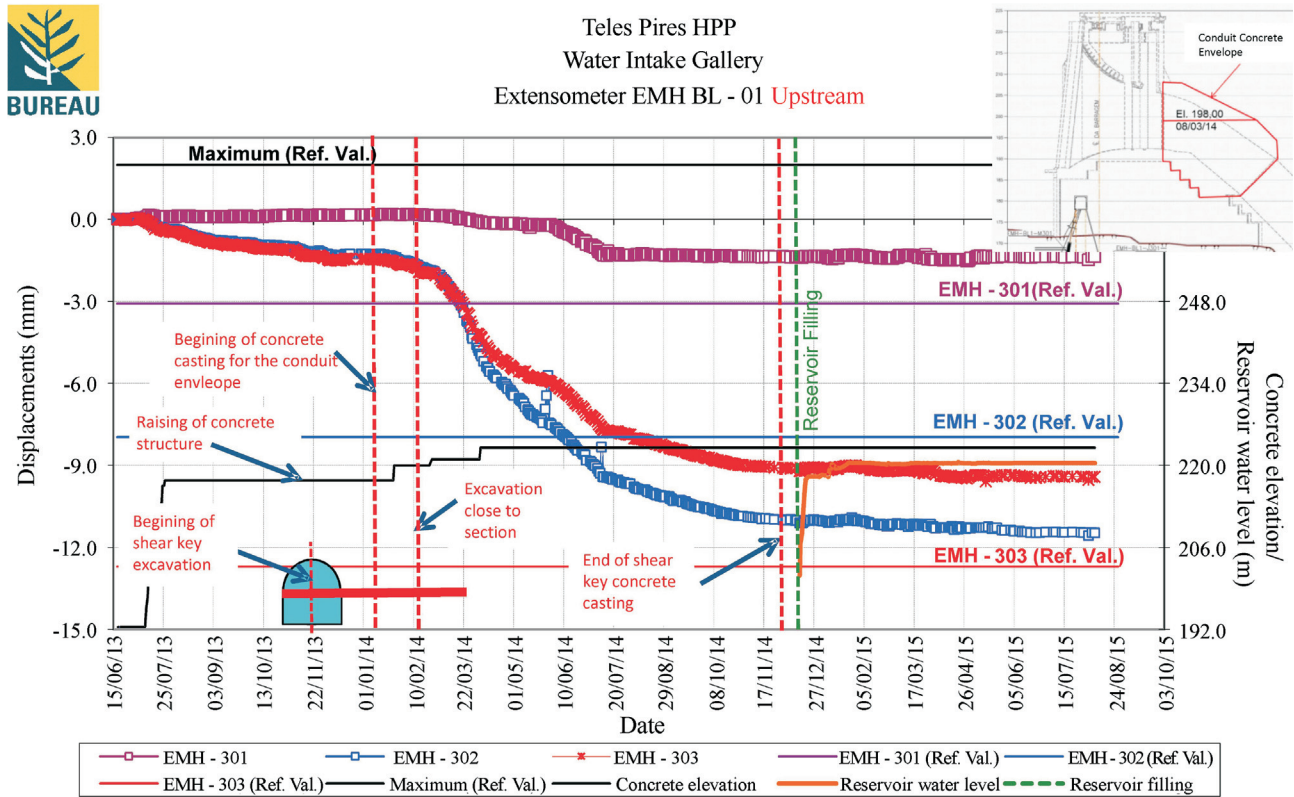


Figure 50 - Typical data for extensometer installed in the water intake structure foundation underneath one of its concrete blocks.

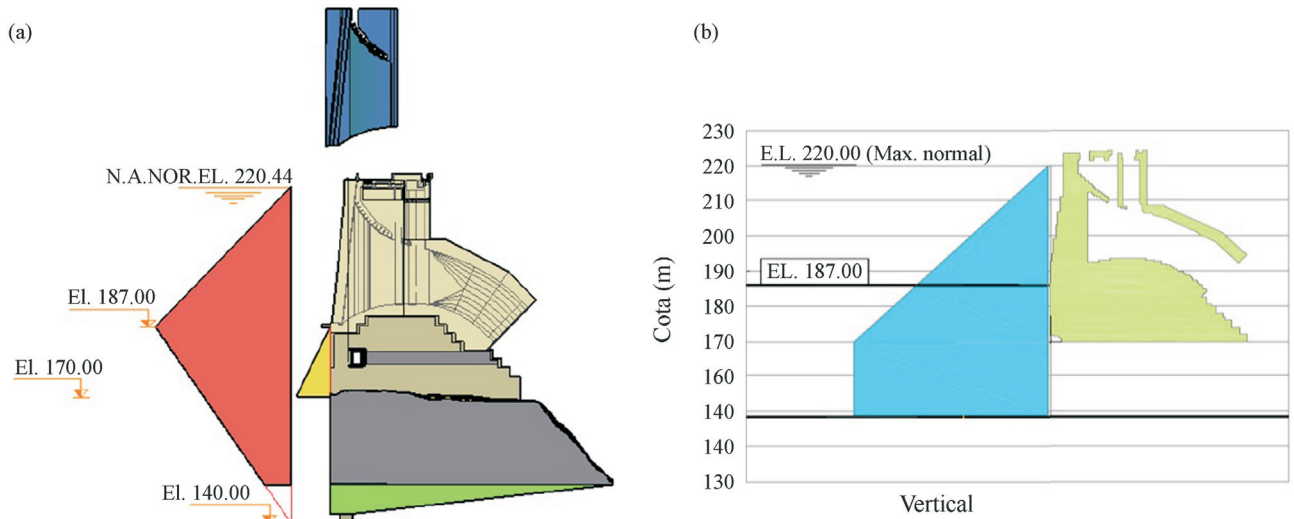
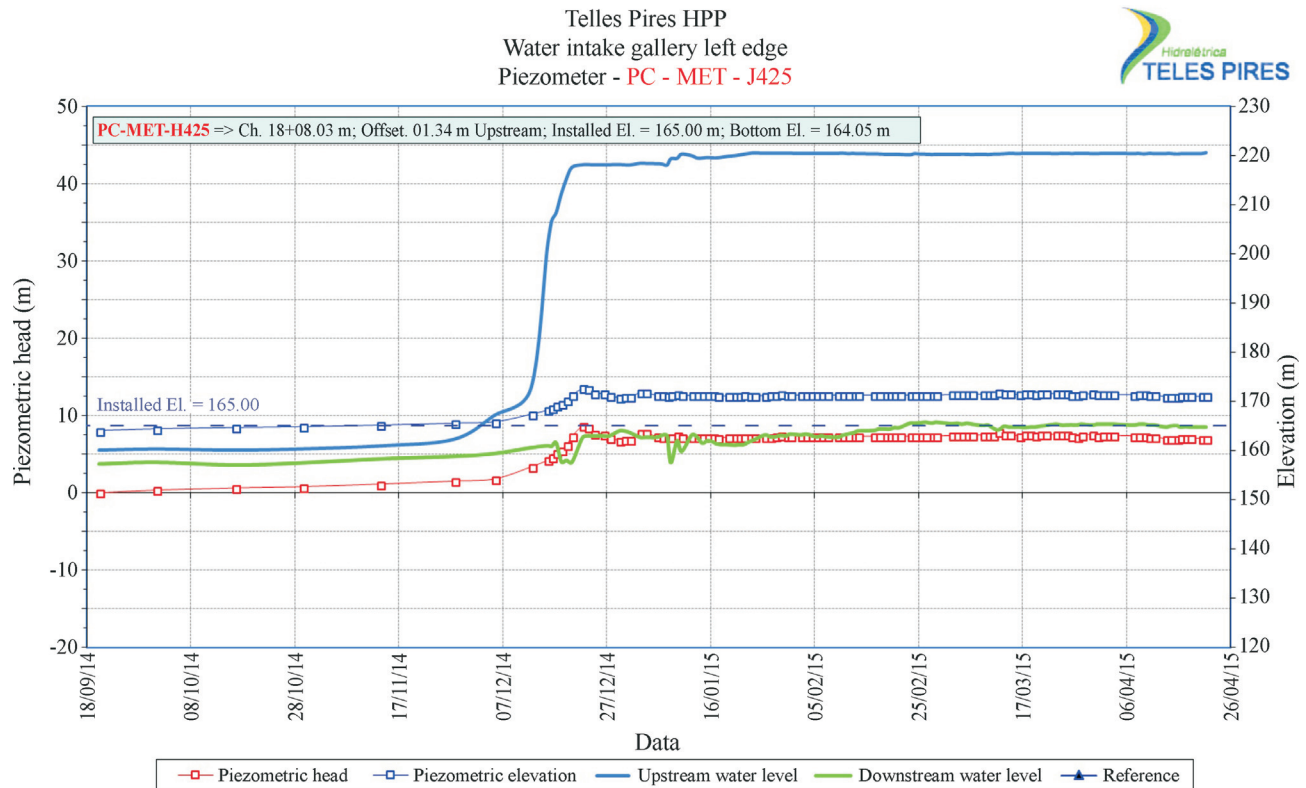


Figure 51 - Water thrust diagrams: (a) Diagram 1 - Proposed by the BoC; (b) Diagram 2 - Without HDPE.

spillways for a design flow of 3620 m<sup>3</sup>/s, a headrace tunnel 14.4 km long, excavated by drill and blast in an 8 m span horse-shoe shaped cross section, feeding two vertical axis Francis turbines, each of 225 MW capacity. The discussion below refers to the headrace tunnel.

#### 4.1. Local geology

The rocks in the region of the project are of sedimentary origin, ranging in age from Permian to Mesozoic periods, 350 to 65 Mya ago. The project area is located within the calcareous rocks of the Pucará Group.



**Figure 52** - Piezometer and reservoir level data.

This geological group is of marine origin and forms a fringe in an NNW-SSE direction, usually subdivided into three formations, which, in a simplified description can be described:

- its base consists of dolomitic, bituminous and limestones with medium to thick stratification;
- in the middle lutite and limestone intercalations occur; the lutites are stratified, forming medium-sized layers, and dark gray to black in color; the limestones are dark gray to black, well stratified in thin to medium-sized layers, somewhat bituminous and occasionally clayey silty, with chert nodules;
- the top of the sequence consists of light-gray limestones in thin to very thick layers.

The carbonate rocks present some karstic action, as discussed below.

The headrace tunnel is located on the left bank of the Huallaga River, on the east flank of a large anticlinal structure trending NW-SE with layers that always dip between 40° and 80° towards NE. The carbonate rocks are characterized by ductile structures with broad folds oriented mainly in a NE-SW direction, these being the features that impact the project structures, particularly the headrace tunnel, as it runs at right angles to these geological structures and, therefore, intersects them in some stretches, such as the Lluto and Chimao creeks.

The main discontinuities in these rock masses are the bedding planes, which are very persistent with thin to medium layers, 20 cm to 60 cm thick. Other discontinuities correspond to two families of tension fractures caused by folding, as well as systems resulting from the shear stresses to which these rocks were subjected.

Thrust faults in a NW-SE direction were mapped on the left bank of the Huallaga River. Various strike-slip faults in a NE-SW direction with regional dimensions that leave deep slopes on the creeks coming down from the mountains were also observed.

In summary, the headrace tunnel is intercepted by beddings and faults, of which only two are effectively major pressure-relief zones (Lluto and Chimao creeks). Most of these beddings have a general NE-SW orientation, corroborating the regional structural characteristics.

#### 4.1.1. Geological-geotechnical investigations

To assess the geological characteristics of the project structures area, dipole-dipole array, vertical electrical sounding, seismic refraction and MASW (Multichannel Analysis of Surface Waves) geophysical methods were used. The local topography of high and steep slopes impacted the performance of the geophysical surveys, especially in matching the most appropriate lines.

Due to the difficult access in virtue of the steep slopes in the project region as well as the dense vegetation, in

some cases field geological surveys were made in locations near to or parallel to the project axis and structures. Along the headrace tunnel axis, 22 surface geomechanical stations conveniently located were defined and used to determine the structural characteristics of the rock mass.

Boreholes were drilled at the tunnel portals, at the adits entrance and at locations of lower massif cover, like the creeks mentioned.

#### 4.1.2. Hydrogeological model

The hydrogeological model developed during the design studies concluded that the supply to the aquifer was the result of:

- infiltration of rainwater and water from tributary creeks or water from remote areas seeping through the longitudinal and transverse fault planes that affect the zone;
- the flow of underground water through the limestone rock mass as a result of its secondary permeability, the final direction of the water flow being the banks of the Huallaga River, which acts as an important natural drain;
- eventual perched aquifers in the limestone rock mass.

Considering that the bedding planes are subvertical, incursions into the caves in the region detected that the main karst access points (sinkholes and dolines) could be investigated to depths of 80 m to 100 m or even more, down to locations where the presence of fallen blocks hindered further access.

#### 4.2. Description of the headrace tunnel

The headrace tunnel horizontal and vertical alignments were selected in order to ensure adequate rock cover in the left-bank side valleys, while minimizing the maximum rock cover and the length of the intermediate construction adits. It has a total length of 14.38 km and a 7.85 m

high, 8.5 m wide horse-shoe shaped cross section. It was excavated by the drill and blast method with full face blasting for each round, using five intermediate adits. Figure 53 illustrates the headrace tunnel alignment and the location of the adits.

The maximum cover above the tunnel is around 880 m. The average unconfined compressive strength (UCS) of the rock is about 100 MPa for the massive gray limestone and about 85 MPa for the bituminous limestone. Thus, considering an average specific weight of the rock of around  $2.6 \text{ tf/m}^3$ , the maximum in situ geostatic stresses are in the range of 23 MPa, or about 25% of the intact rock UCS.

The tunnel alignment crosses two main side valleys at distances of about 2.3 km (Lluto creek) and 12.2 km (Chimao creek) from the intake.

Considering that a maximum hydraulic head of 313 m is imposed at the Chimao creek crossing, hydro-jacking tests were performed from the surface, as well as from inside the tunnel itself, to check the minimum in situ stresses and adjust the lining design. A reinforced concrete lining was used in the low-cover section of the tunnel, about 200 m and 180 m long immediately upstream and downstream, respectively, of the steel lined siphon used to pass underneath the side valley, with length of 323 m to guarantee safe hydraulic gradients during operation in this specific location.

#### 4.3. Geological and geomechanical characteristics of the rock mass along the tunnel

During construction of the headrace tunnel, a very detailed geological mapping was obtained as the excavations progressed. The data collected from this survey included: geological formation, rock mass description, hydrogeological aspects, estimation of Barton's  $Q$  index, including

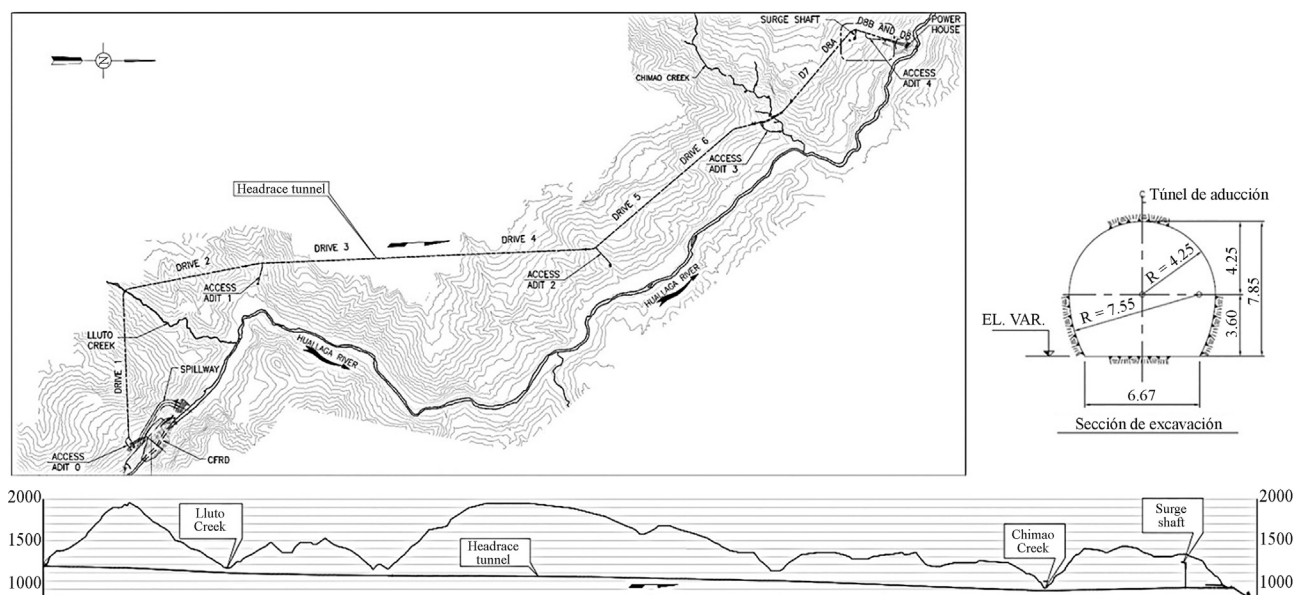


Figure 53 - Plan view, cross section and longitudinal section of the headrace tunnel.

the rock mass class and quality. Photographs showing the rock type, discontinuities, presence of water and other items of interest on the tunnel face at each excavation round were also produced. Figure 54 presents an example of one such document.

Geological/geotechnical maps of 50 m sections along the tunnel were prepared, presenting the different lithological types, the orientation of the bedding planes and other important geological structures. Stereograms showing the orientation of the bedding planes were included as this is the most persistent structure.

Barton's rock mass classification was done methodically at each excavation advance, showing the value attributed to each of the parameters from which it is derived, the GSI punctuation, alteration/consistency/jointing degrees and the features of the main discontinuities. Definition and adjustment of the tunnel support at each excavation round was postulated based on this data.

During excavation of the tunnel, various lithological types were crossed: gray and/or banded limestones, bituminous limestones, breccia and andesitic dykes. At some chainages shearing developed along the bedding planes was observed, which at these locations presented a clayey, silty or crushed rock filling. These particular features were named "stratigraphic fault"; Figs. 55 and 56 illustrate these features in the excavation front.

No karstic cavities were found along the alignment of the headrace tunnel during excavation. The only cavity of karstic origin was intersected at chainage 0+234 of adit 3. At this spot, a cavern filled with clay approximately 6 m wide and 8 m high was found at the adit tunnel crown. It was interpreted to be related to a karstic duct which started at a doline placed about 100 m higher than the level of the adit and ended in a cavity on the right bank of the Chimao

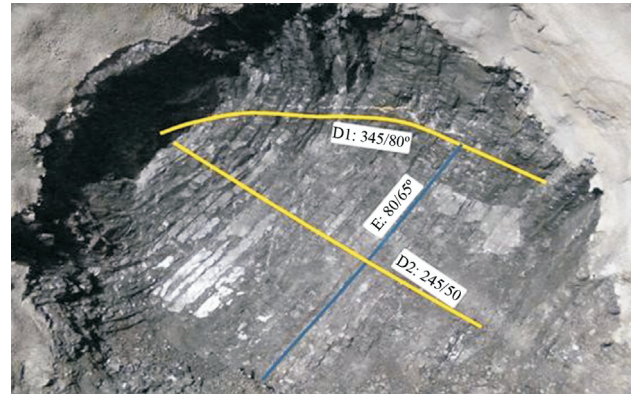


Figure 55 - View of the thinly stratified gray limestone at the excavation front.

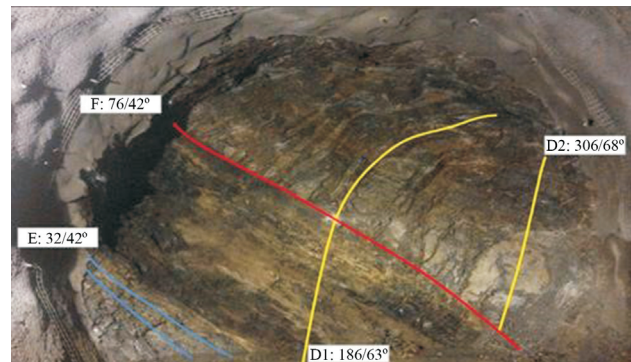


Figure 56 - View of the "stratigraphic faults" in the gray limestones at the excavation front.

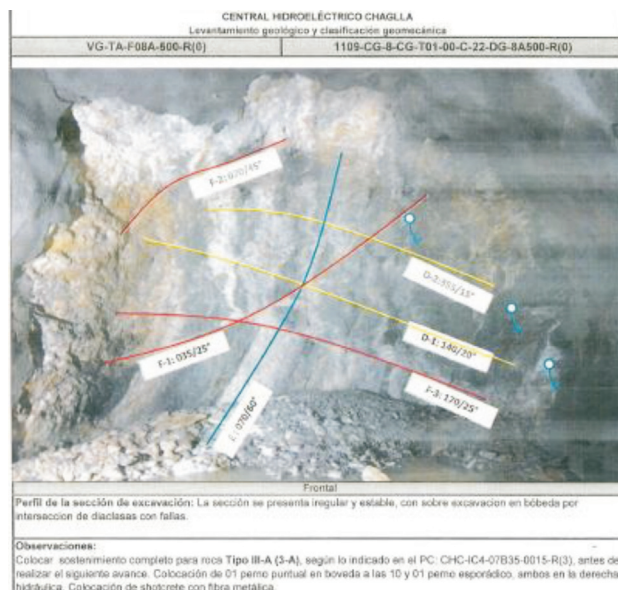
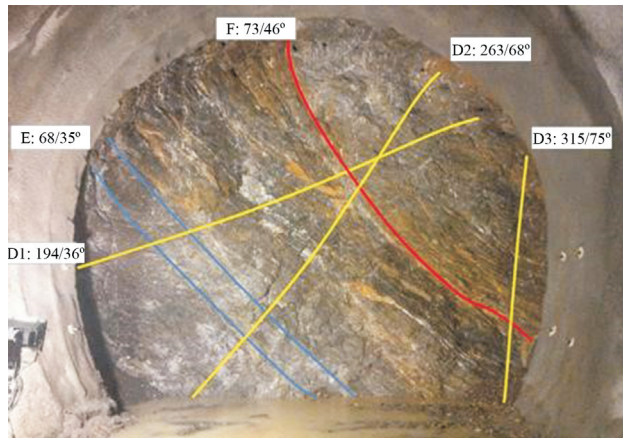


Figure 54 - Tunnel face geological mapping.

creek. The cavity was backfilled with concrete and the infiltration water flowing through the karstic duct was conveyed through pipes to the portal of the adit 3 to allow the excavation to proceed.

The banded limestones described were continuously and irregularly interbedded with the gray limestones and could, therefore, be grouped with them as they have similar geotechnical behaviour. The rock is dark gray with light bands with moderate degree of jointing and alteration, medium to low strength, thin to moderate bedding layers and three joint systems (Fig. 57).

The bituminous limestones are part of the middle member of the Pucará Group and were found overlying the banded gray limestones. This lithological type is black and dark gray with moderate to intense degree of jointing and alteration, low to medium strength, thin to moderate bedding layers and three joint systems, with clayey silt or crushed rock fillings in some bedding planes, as well as thin layers of carbonaceous lutites (Fig. 58).



**Figure 57** - View of the thinly stratified banded limestone at the excavation front.

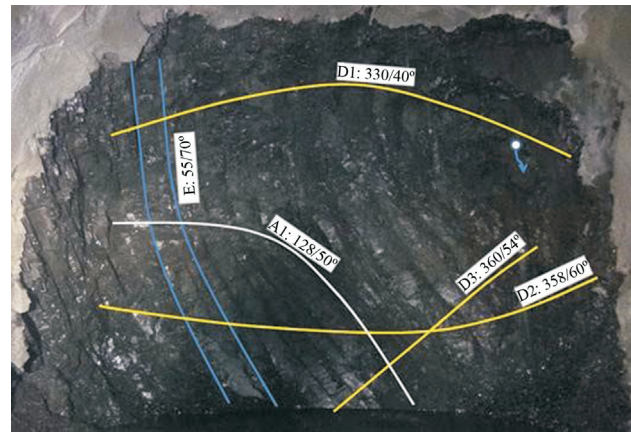


**Figure 58** - View of the bituminous limestone at the excavation front.

#### 4.4. Tunnel lining design

##### 4.4.1. Design assumptions and excavation support

The tunnel support was defined according to the Q-System (Barton, Lien and Lunde, 1974; NGI, 2013). In the crossings under the Lluto and Chimao creeks, where the conventional empirical cover criteria were not met, steel and reinforced concrete linings were used and auxiliary measures taken to ensure safe operation of the tunnel in terms of water losses and the stability of the adjacent slopes.

The final lining for the operation phase in most of the headrace tunnel consisted of shotcrete applied systematically as a permanent excavation support on the crown and sidewalls with a thickness varying between 7 cm and 20 cm according to the rock mass class, and a plain 25 cm thick concrete slab on the tunnel floor poured over a layer of compacted muck. The systematic installation of a secondary lining of cast-in-situ concrete was discarded because

the calcareous rocks encountered along the tunnel were considered durable under the foreseen operating conditions, and the 2.8 m/s flow velocity in the tunnel was compatible with a shotcrete lining.

Table 2 summarizes the tunnel support as a function of Barton's Q value:

##### 4.4.2. Reinforced concrete and steel lining under the Chimao creek

At the location where the tunnel passes under the Chimao creek, at a tunnel chainage of around 12+340, the rock cover is approximately 20 m with an applied hydraulic head reaching 313 m at elevation 883 m above sea level (m.a.s.l.). Steel lining was designed for this section of the tunnel, 322.8 m long and extending to both sides of the Chimao valley. Confinement of the rock mass in the tunnel sections adjacent to the steel lining was checked by means of several hydro-jacking tests; the results showed a minimum safety factor against jacking of the rock of around

**Table 2** - Summary of tunnel lining design as a function of Barton's Q value.

Q	Rock mass class	Description of the tunnel support treatment
$Q > 60$	I (very good rock)	7 cm thick fiber reinforced shotcrete (crown and sidewalls)
$7 < Q \leq 60$	II (good rock)	7 cm thick fiber reinforced shotcrete (crown and sidewalls); spot bolting where required
$0.64 < Q \leq 7$	III (moderately good rock)	10 cm thick fiber reinforced shotcrete (crown and sidewalls); 3 m long passive bolt ( $\phi = 25$ mm) at 2 m spacing in the crown; spot bolting where required
$0.08 < Q \leq 0.64$	IV (poor rock)	15 cm thick fiber or steel mesh reinforced shotcrete (crown and sidewalls); 4 m long passive bolt ( $\phi = 25$ mm) at 2 m centers in the crown and sidewalls
$Q \leq 0.08$	V-A (very poor weathered rock)	20 cm thick steel mesh reinforced shotcrete (crown and sidewalls); steel rib or lattice girder spaced at 1 m centers; forepoles if necessary (crown)
	V-B (very poor altered rock)	20 cm thick steel mesh reinforced shotcrete (crown and sidewalls); steel rib or lattice girder spaced at 1 m centers; forepoles (crown); reinforced invert if necessary

1.10. To ensure a safety factor of 1.30 and to avoid potential leakage from the tunnel, a hybrid impervious lining, extending to the points where the rock cover is sufficient according to conventional empirical cover criteria, was implemented on both sides of the valley. The hybrid lining is composed of the following elements:

- an outer ring of reinforced shotcrete applied over the existing tunnel support with a minimum thickness of 20 cm and a circular inner profile;
- a sprayed 3 mm thick waterproof membrane applied on the inner surface of the shotcrete ring (this membrane was considered an additional measure whose effect was disregarded in the dimensioning of the reinforced concrete);
- a 40 cm thick inner ring of reinforced concrete poured over the waterproof membrane.

Additional grouting of the rock around the tunnel at pressures of up to 30 bar (equivalent to the operating pressure of the tunnel in this section) was performed to further reduce the permeability of the rock mass and also to pre-compress the concrete lining.

The hybrid lining was applied along a 181.0 m length of the tunnel downstream of the steel lining and a 201.0 m length upstream of the lining. Thus, the lined section of the headrace tunnel in the region of the Chimao creek had a total length of about 704.8 m.

#### 4.5. Procedures for filling the headrace tunnel

Special procedures for filling the headrace tunnel were defined in design, considering flow from the gates at the water intake and from the natural water table of the rock

mass into the tunnel, this infiltration being estimated to be around  $2 \text{ m}^3/\text{s}$ . The water intake structure is divided into two bays, each equipped with a fixed-wheel gate. Each gate is divided into three panels; the lower two are rigidly coupled, while the middle and upper panels are linked with a special tie, forming a 50 mm space between them. Opening the middle and upper panels without raising the whole gate is called a “cracking” operation.

Filling of the tunnel started on November 17<sup>th</sup>, 2015, using only the inflow in the tunnel provided by the natural water table. Figure 59 shows that from the beginning the water level inside the headrace tunnel rose at a rate of approximately 0.4 m/h with the infiltration flow alone, well below the maximum recommended rate of 2 m/h (Benson, 1988).

On November 26<sup>th</sup> the level in the reservoir reached the intake structure, allowing crack opening of the gates to start, with the water level inside the tunnel at elevation 975 m.a.s.l.

Filling continued at approximately 0.4 m/h for the next seven days, when the water level inside the tunnel was observed to be stabilizing at approximately at elevation 1,050 m.a.s.l. As the water level inside the tunnel rose, at this moment the exfiltration flow from the tunnel exceeded the infiltration rate.

Throughout this period, the site was inspected to check if water was daylighting and appearing anywhere or if there were any related surface changes, particularly inside the construction adits and respective concrete plugs. No significant changes were detected.

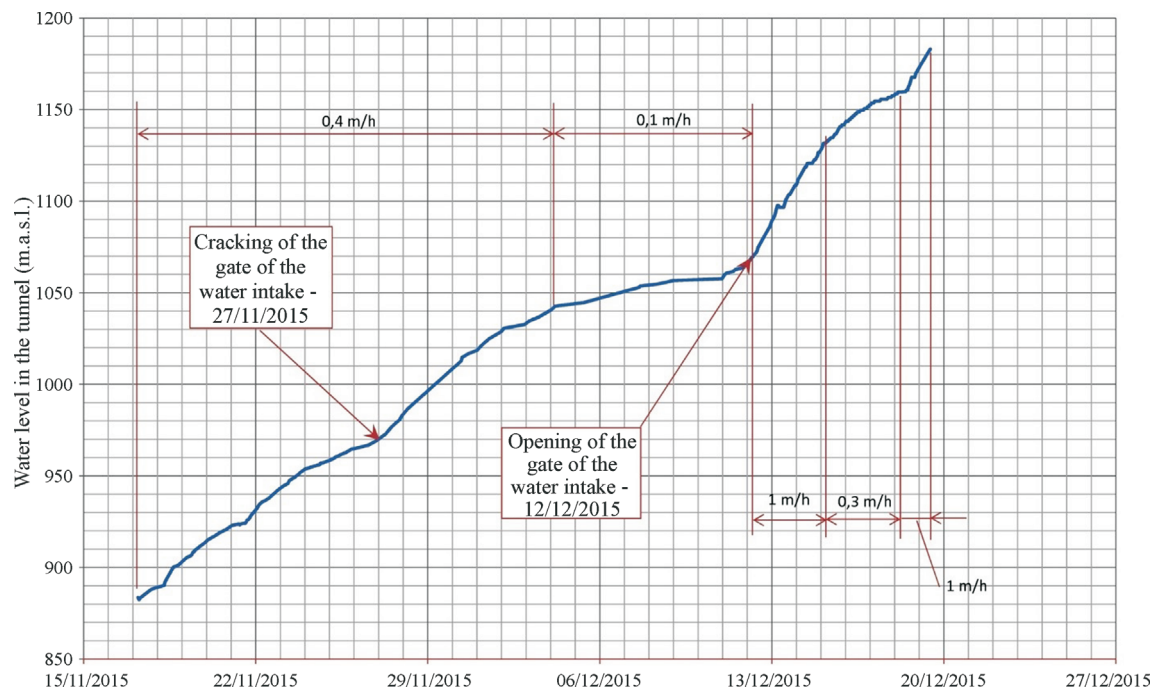


Figure 59 - Tunnel filling.

The maximum normal water level in the reservoir (elevation 1,196 m.a.s.l.) was reached on December 4<sup>th</sup>, and one of the spillway gates was opened to control the level.

As the filling rate fell to 0.1 m/h, it was decided to lower the reservoir level so that one of the gates at the water intake could be opened with a low head. In this way the inflow and water velocities could be controlled, avoiding damage to the concrete floor of the tunnel. Lowering of the water level in the reservoir to elevation 1,182.2 m.a.s.l. (just 0.7 m above the gate sill) began on December 9<sup>th</sup>, and the reservoir level was kept at this elevation, corresponding to an inflow of 4.0 m<sup>3</sup>/s.

With this procedure, the filling rate of the tunnel was increased to 1 m/h for the next three days and dropped again to 0.3 m/h, reaching elevation 1,160 m.a.s.l. around noon on December 18<sup>th</sup>. As the last stretch of the tunnel would be less affected by the filling flow (the floor is less inclined), it was decided to raise the reservoir level again to finish filling the tunnel. This was done on December 19<sup>th</sup> in the morning. The filling rate during this last day was 1 m/h.

The following changes were observed during the first half of December:

- low seepage at the concrete plug in adit 4; complementary grout injections were performed.
- no change at adit 3.
- increased seepage into a drainage gallery excavated under Chimao creek to control uplift water pressure in the siphon.
- significant seepage in the lower half of adit 2.

#### 4.6. Headrace tunnel incident on February 17<sup>th</sup>, 2016

##### 4.6.1. Description of the incident

Filling of the headrace tunnel happened between November 17<sup>th</sup> and December 19<sup>th</sup>, 2015. The tunnel remained pressurized with its normal operating pressure from that date till February 17<sup>th</sup>, 2016, a period of 61 days, without any record of abnormalities. During this period three crude measurements of overall tunnel leakage were performed, by closing the gates at the tunnel intake structure and measuring the drop in the water level in the adjacent adit 0 after a given time interval. The measurements indicated an exfiltration/leakage of around 2.5 m<sup>3</sup>/s.

On February 17<sup>th</sup>, 2016, at 1:03 PM, a load rejection test was performed on one of the generating units with 80% of the maximum generating flow. At 6:57 PM, an earthquake of magnitude 4.2 on the Richter scale was recorded. The epicenter was very close to the dam site, and the earthquake was perceived by the site personnel as an intense, very short shake.

On February 18<sup>th</sup>, 2016, a significant leakage of dirty water on the left bank of Chimao creek was observed and adit 3 flooded. On the same day, a load rejection in the second generating unit with the same 80% of the maximum generating flow was performed. The leakage increased fur-

ther the next day, turning into a very intense surge of water. On February 20<sup>th</sup>, 2016, another general leakage measurement was carried out in the headrace tunnel in the same way as previously. The results indicated a leakage of approximately 11.4 m<sup>3</sup>/s, an increase of about 4.5 times over the previous measurements in the tunnel.

This led to the decision to dewater the tunnel in order to investigate the causes of the problem.

##### 4.6.2. Seismic data recorded on the day

On February 17<sup>th</sup>, 2016, at 6:57 PM an earthquake of magnitude 4.2 on the Richter scale struck at a distance of approximately 3 km from the Chaglla Hydroelectric Power Plant Dam and 13 km from the powerhouse.

The location of the earthquake was initially determined by the Geophysical Institute of Peru (IGP). Figure 60 (a) shows the location of the earthquake on a Google map of Peru (taken from an IGP web page) and Fig. 60 (b) presents a larger scale image showing the locations of the earthquake (SISMO) and the Chaglla Dam (PRESA).

Three accelerographs had been installed on the site to record movements generated by seismic activity. Two were installed at the dam: at the dam's crest, and at its base. The third was installed in the powerhouse structure. At the time of the earthquake, the accelerograph at the base of the dam was out of service because of vandalism, and readings were only available for the crest of the dam and the powerhouse.

##### 4.6.2.1. Earthquake records

Figure 61 shows the recordings of the three earthquake acceleration components over time at the dam. The estimated distances from the epicenter of the earthquake to the dam and power house (other recordings) are 3 km and 13 km, respectively.

##### 4.6.2.2. Seismic interpretation of the records

Table 3 shows a list of the main parameters for recordings on the crest of the dam.

The most remarkable result is the high value of peak acceleration (1.5 g) for the 01-02 (NS) component at the crest of the dam, approximately 150 times greater than the largest component (NS) for the powerhouse. The short distance between the epicenter and the dam would suggest that the peaks are the product of some near-fault effects, such as directivity or the hanging-wall effect.

All the values of the parameters recorded at the powerhouse are very small and of no significance from an engineering point of view, this fact being interpreted as being associated to the installation of the accelerograph in this structure.

As already mentioned, the location of the earthquake was determined by the IGP as latitude 9°42'36" S and longitude 75°51'36" W (-9.71° N, -75.86° E) at a depth of



**Figure 60** - Earthquake location: (a) Location (determined by the IGP) of the 4.2 magnitude earthquake that occurred on February 17<sup>th</sup>, 2016; (b) Close-up showing the location of the Chaglla Dam (PRESA), of the village of the same name and of the earthquake (SISMO).

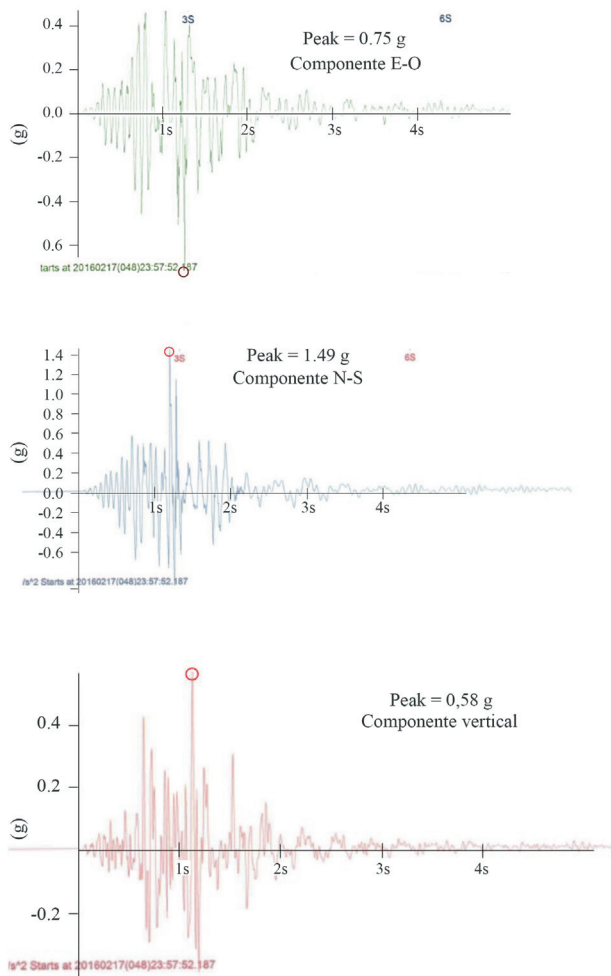


**Figure 61** - Crest of the dam: Recording of the three acceleration components.

26 km; different calculations estimated the depth as being between 1.3 to 4 km.

While further investigation would be required to confirm this calculation, it is interesting to note the association between a shallow earthquake and the characteristics of the three components measured at the crest of the dam: very high peak accelerations and very high frequencies (predominantly very small periods).

The possible peak acceleration and velocity at the opening of the cavity detected in the hydraulic left sidewall of the headrace tunnel, distant 10.8 km from the epicenter, were also estimated. It can be observed that, at the position where the opening in the left sidewall of the headrace was estimated to be, the mean PGA could have reached 0.06 g and around 0.12 g for the mean value plus one standard deviation.

#### 4.6.3. Effects observed on the project structures

Localized damage was observed after the earthquake on February 17<sup>th</sup> and was a result of the seismic event.

##### 4.6.3.1. Dam area

A small shallow landslide was observed on the hillside on the right abutment near the dam, and a metric size rock rolled from the slope, as shown in Fig. 62 (a) and (b).

##### 4.6.3.2. Region near the adit 2

After the earthquake, a shallow landslide was observed near the entrance portal to the adit 2, distant approximately 8 km from the epicenter (Fig. 63).

**Table 3** - Parameters measured by the accelerographs.

Component	Recording rest of the dam		
	01-01 (vertical)	01-02 (NS)	01-03 (EW)
Peak acceleration (g)	0.588	1.491	0.766
Spectral intensity (cm)	0.0929	0.2122	0.1906
Predominant period (s)	0.1009	0.0714	0.0819
Mean period (s)	0.0967	0.1030	0.1277
Peak velocity (m/s)	0.0631	0.1553	0.1556
Peak displacement (mm)	3.584	6.862	5.482
Cumulative absolute velocity (m/s)	2.0725	5.4117	3.4846
Arias intensity (m/s)	0.4813	2.6155	0.9995
Arias duration (5-95) (s)	1.26	1.46	1.45

**Figure 62** - Right bank – landslide downstream of the dam.

#### 4.6.3.3. Chimao creek area

After the earthquake, the following events were observed in the Chimao creek area:

- Small shallow landslide on the left bank of the creek (Fig. 64 (a) and (b));
- An area with a high volume flow of dirty water from the headrace tunnel outcropping on the left bank of the creek (Fig. 65 (a) and (b)).

#### 4.6.4. General considerations on the earthquake

The earthquake recorded on February 17<sup>th</sup>, 2016 was felt as a short duration impulse by personnel in the offices on the site, which is approximately 2 km from Chimao creek. This would indicate that the earthquake had a Modified Mercalli (MM) intensity of between III and IV in the area where the offices are located.

The seismic records from the accelerographs show that the earthquake was of very short duration, of the order of 1.5 s at the dam site. The high peak accelerations of the three components recorded at the crest of the dam are substantially higher than expected, even when an amplification

**Figure 63** - Adit 2 – landslide near the entrance portal.

factor of 2 to 2.5 due to the structural behavior is taken into account. The velocities recorded are within the normal ranges.

In particular, the recordings show very high frequency components. Calculations to determine the location of the earthquake using the three components of the accelerogram recorded at the dam appear to indicate that the earthquake was very close to the surface, at a depth of less than 4 km.

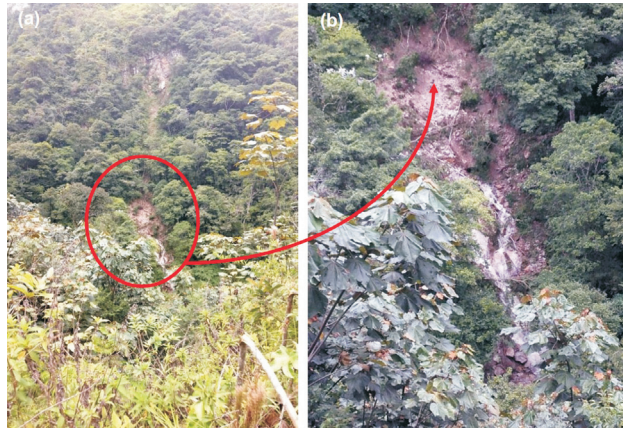


**Figure 64** - Chimao creek – left bank – landslide around 100 m upstream of the access bridge for adit 3.

In a number of localized areas near the dam and the adit 2, small landslides and some minor damage were observed after the earthquake. Using the NGA attenuation formulae (Power *et al.*, 2006), the possible values of peak acceleration and peak velocity at the dam (at the rock base) and powerhouse were estimated. The possible peak acceleration and peak velocity at the opening of the cavity detected in the hydraulic left sidewall of the headrace tunnel were estimated; it is estimated that the horizontal acceleration could have reached between 0.06 g and 0.12 g.

Because of the high volume flow of water outcropping in the region of Chimao creek and the considerable increase in the amount of water pumped out of adit 3, together with the almost 4.5-fold increase in the amount of water exfiltration from the headrace tunnel, it was decided to dewater the headrace tunnel.

#### 4.7. Headrace tunnel dewatering procedure

The dewatering procedure of the headrace tunnel was carefully thought and implemented, as not to further damage the tunnel.

The gates at the water intake structure were closed on February 20<sup>th</sup> in the morning. The water level inside the tunnel was carefully monitored with three manometers installed in adit 3, in adit 4 and in the lower end of the headrace tunnel.

Due to the water leakage in the tunnel, and the lack of infiltration from the rock mass in the upstream section of the tunnel, the initial dewatering rate was very high - 65 m in the first hour. To reduce the dewatering rate, one of the gates at the water intake was cracked and the dewatering rate dropped to 11 m in the second hour, and 8 m in the third.

A special device was installed to crack open the second gate in an attempt to further reduce the dewatering rate. Additionally, to gain better control of the dewatering rate, five pumps were installed close to the water intake. These pumps operated from the night of February 20<sup>th</sup> to the morn-



**Figure 65** - Chimao creek – left bank – high-volume flow of dirty water was observed (later known as coming from the headrace tunnel) about 100 m upstream of the access bridge for adit 3 the day after the earthquake. Water can be seen with important amount of solids in suspension.

ing of February 23<sup>rd</sup>, and the average dewatering rate during these three days was around 1.2 m/h, corresponding to a drop in the water level from about elevation 1,090 m.a.s.l. to 1,005 m.a.s.l. if the first two hours of dewatering are ignored. This corresponded roughly to the prescribed dewatering rate of 1.0 m/h.

On February 23<sup>rd</sup> in the afternoon, a few hours after the pumps had been shut down, one of the gates was completely closed. As a result, the water level in the tunnel dropped quite fast, and the gate had to be crack opened again. In five hours, the level inside the tunnel dropped 43 m, reaching elevation 967 m.a.s.l. During the following three days, the gates were successfully operated until they were finally closed and dewatering could be started from the drainage valve at the bifurcation downstream of the headrace tunnel in the spherical valve room. The average dewatering rate during these three days was approximately 0.3 m/h, and the water level in the tunnel was at elevation 946 m.a.s.l.

On February 25<sup>th</sup> in the afternoon, a site inspection showed that the surge of water at the left bank of the Chimao creek had ceased as the water level inside the tunnel reached elevation 950 m.a.s.l., approximately. On the same day, the tunnel was accessed through adit 0 and a partial inspection was carried out down to adit 2. The water level inside the tunnel had stabilized at elevation 948 m.a.s.l., which meant that the drainage valve capacity was approximately equal to the infiltration flow. On March 1<sup>st</sup> the drainage valves in the powerhouse used to drain the spiral casing could be operated, and dewatering was resumed slowly at around 0.15 m/h until the dewatering valves at adit 3 were operated on March 6<sup>th</sup>.

Dewatering through adit 3 required that several drainage pumps were operated. These were operated for 3 days until the water level reached 920 m.a.s.l., which corresponds to the tunnel floor under the surge chamber at chainage 14+000 approximately, being the highest point in the tunnel downstream of the siphon at Chimao creek. Dewa-

tering through the bypass valves in the powerhouse is not possible from this elevation downwards.

Further lowering of the water level in the tunnel below elevation 920 m.a.s.l. was not possible because of the high infiltration flows, particularly from the upstream stretch of the tunnel. Two boreholes were, therefore, drilled in adits 1 and 2 to install the ventilation system and construct small cofferdams so that the infiltration flows could be diverted to these holes and drained out of the adits.

On March 15<sup>th</sup> the water level inside the tunnel reached elevation 898 m.a.s.l. At this point, as foreseen in the dewatering procedure, a floating movable pumping system was installed inside the tunnel, allowing to dry the siphon at Chimao creek.

Figure 66 shows the dewatering curve and the main events registered during the dewatering procedure.

#### 4.8. Cavity detected at chainage 12+740

##### 4.8.1. Initial site investigations by speleologists

On March 17<sup>th</sup>, 2016, after most of the tunnel had been dewatered, a local failure of the shotcrete lining could be observed in the lower part of the hydraulic left sidewall of the tunnel at chainage 12+740, measuring roughly 1.5 x 1.5 m and triangular in shape.

This cavity was inspected by a team of geo-speleologists and called El Hoyo de la Beba; its internal topogra-

phy was mapped to collect all possible data that could help establishing its possible origin. Additionally, the geo-speleologists inspected and mapped the cavity at the left bank of Chimao creek where the outcrop of water was detected, this cavity being called El Suspiro de la Frescia.

El Hoyo de la Beba cavity is 1.50 m wide and 1.50 m high at the entrance (Fig. 67), subparallel to the rock mass bedding layers, with an average dip/dip direction of 310/76 and extends more than 5 m (the real depth could not be measured due to safety requirements) below the floor of the tunnel in the location where it intersects the tunnel. The roof and walls consist of jointed, stable, gray to black rough limestone rock with layers up to 1.50 m thick, with some indications of slickensides in the rock walls, and without any signs of dissolution.

El Hoyo de la Beba continues approximately 80 m upstream of the point where it starts at chainage 12+740, reaching a maximum width in one of the sections of 8.6 m and a height of 3 m. It runs diagonally to the headrace tunnel and after 80 m turns upward along an axis like a chimney rising more than 30 m above the crown of the tunnel. The end of this chimney was not reachable due to the presence of many unstable blocks, which would put at risk the safety of the personnel involved in the activity.

No stalactites or stalagmites or other characteristic morphological features were found in the area inspected. Vertical rock bolts were observed on the floor of the cavity

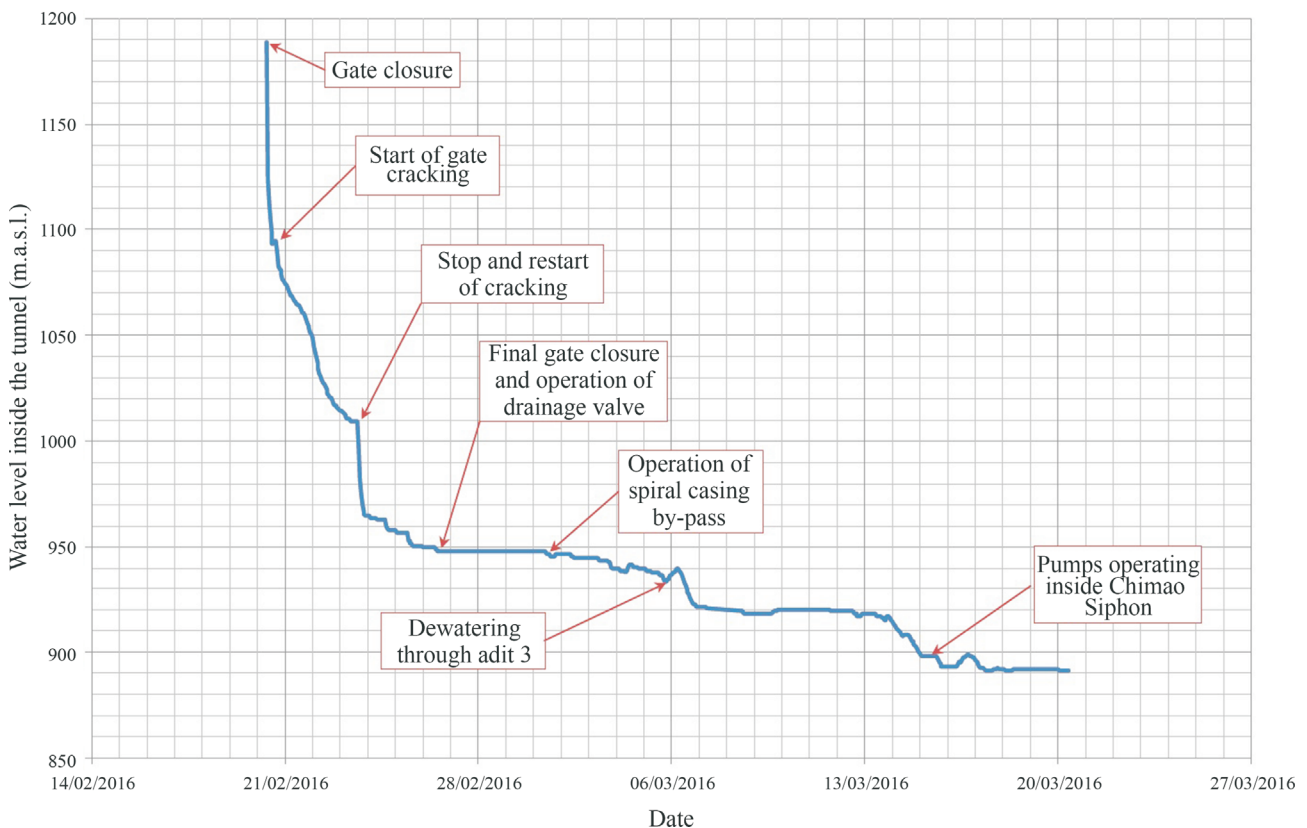


**Figure 66** - Dewatering curve of the headrace tunnel and main events.



**Figure 67** - View of the entrance to the cavity on the hydraulic left sidewall of the headrace tunnel at chainage 12+740.

(Fig. 68), suggesting that the area being inspected was immediately above the crown of the tunnel.

Based on the site inspection, the geo-speleologists concluded that the El Hoyo de la Beba cavity did not exist previously and that it established itself in a “stratigraphic fault” filled with friable intensively fractured material that became erodible when disarticulated and submitted to high flows and water pressures after the earthquake.

The cavity El Suspiro de la Fresca is located in the hydraulic right side of the headrace tunnel approximately



**Figure 68** - View of a headrace tunnel rock bolt. The fact that the bolt is vertical suggests that the area being inspected is above the roof of the tunnel.

subparallel to the axis and to the rock mass bedding layers. The inspection carried out by the geo-speleologists extended around 120 m into the cavity, which is 1.5 m to 10.7 m wide and, on average, 3 m high. Although in the inspection period the cavity was dry, a karstic process was associated to its origin, as well-developed stalactites and stalagmites were documented by the geo-speleologists (Fig. 69).

#### 4.8.2. Internal survey of the cavity

A topographical survey of the El Hoyo de la Beba cavity was carried out with a portable laser scanner. Figures 70 and 71 show isometric side and front views produced as part of this survey, and Fig. 72 shows cross-sections indicating the position of the cavity in relation to the headrace tunnel.

Analysis of Fig. 70 indicates that the cavity extends along a “stratigraphic fault”, that is, a fault developed along the orientation of the limestone bedding, slightly diagonal to the axis of the headrace tunnel between chainages 12+740, where it enters the tunnel, and approximately



**Figure 69** - View of El Suspiro de Fresca cavity with stalactites and stalagmites.

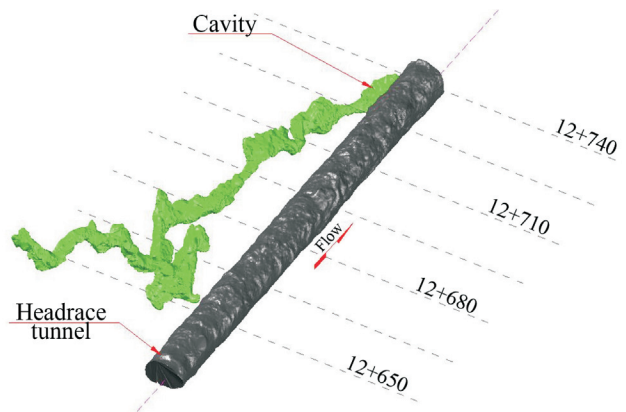


**Figure 70** - Isometric side view of the El Hoyo de la Beba cavity.

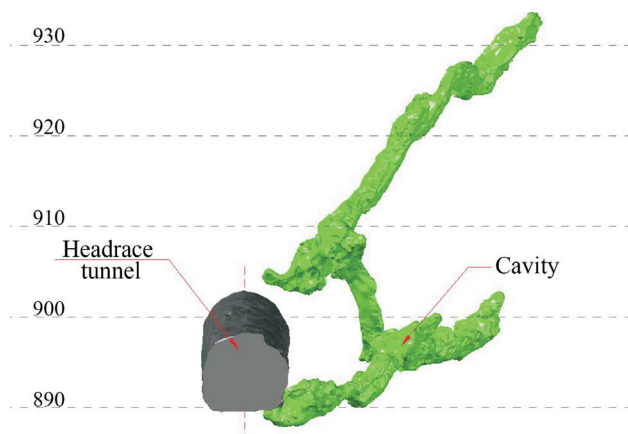


**Figure 71** - Isometric view towards upstream of the El Hoyo de la Beba cavity.

12+680. From this point on, because of joints and / or sinistral faults, the cavity joined a karst conduit, approximately 110 m upstream of chainage 12+740.

It is speculated that approximately around elevation 950 m.a.s.l. this cavity meets the karstic cavity El Suspiro de Frescia, which would have caused the surge of water in the left bank of Chimao creek. This probable connection between the two karstic conduits around the mentioned elevation is interpreted due to the fact that, during the dewatering process, at this water level in the headrace tunnel, the surge of water in the Chimao creek stopped completely.

#### 4.9. Mechanisms involved in the formation of the cavity

The inspections and investigations performed at the site of the incident revealed a large cavity in the rock mass adjacent to the headrace tunnel that could be accessed from the opening in the lining resulting from the failure. According to the geological survey described, the cavity extended about 80 m upstream from the opening in the lining with an

alignment almost parallel to the tunnel axis and then turned upwards into a chimney-like shaft rising more than 30 m above the tunnel crown (see Figs. 70 and 71). At this point access to the cavity was blocked by accumulated debris (mostly rounded boulders) that could not be safely removed to allow further exploration. The initial 140 m of the cavern had rough walls, indicating that no karstic phenomena ever acted in this location; on the contrary the transition to smooth walls was generated by dissolution which was clearly seen and mapped.

The interpretation for the formation of this cavity is that it originated from the erosion of material that filled a stratigraphic fault. This fault was aligned with the bedding of the calcareous rock and was the result of differential movement along the bedding of the rock that occurred during the tectonic history of the area. Its filling material was composed of sheared and crushed rock, originally in a very compact state, but which constituted a preferential seepage path. This fault zone had been intersected during excavation of the tunnel and had been defined as a Class V zone (according to Barton's Q index) for about 12 m long. However, at the chainage where the failed lining was found, the rock mass had been classified as Class III during tunnel excavation and no weak or erodible materials were observed on the tunnel face, walls or crown. The support measures applied in this tunnel section were, therefore, those corresponding to Class III rock mass, and consisted of 10 cm thick fiber reinforced shotcrete on the crown and sidewalls and 3 m long, 25 mm diameter, passive bolts at 2 m intervals in the crown. The tunnel floor was lined with a 25 cm thick plain concrete slab poured over the compacted muck. No abnormalities were recorded when this section of the tunnel was excavated and the support measures were applied.

After filling and pressurization of the tunnel, which at this point had an internal pressure of 31 bar, the water satu-

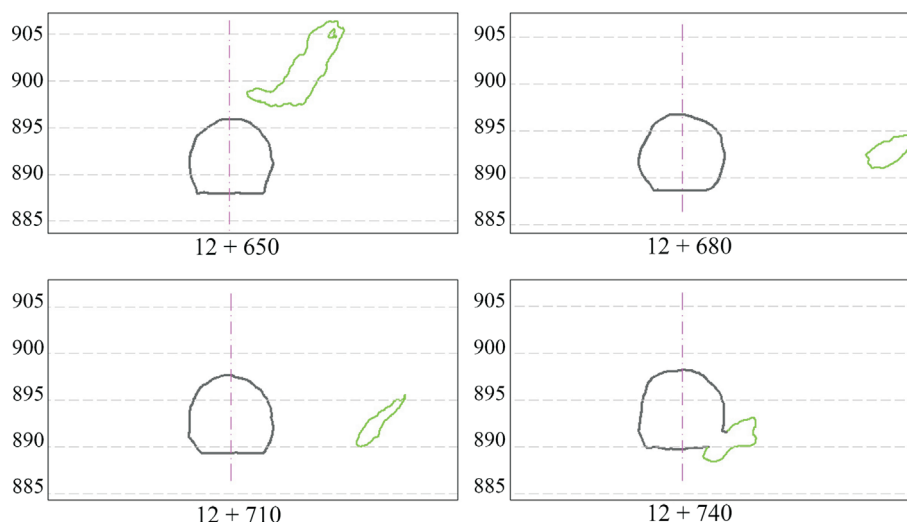


**Figure 72** - Cross-sections of the headrace tunnel showing the position of the El Hoyo de la Beba cavity.

rated the infilling material in the fault zone. It is interpreted that the earthquake acted as a trigger in the disarticulation of the infilling material, which when subjected to the high pressure of approximately 31 bar, suffered a retrogressive erosion process starting from its interface with the karstic feature in the rock mass. This erosion retrogressed until it reached the location where it caused a loss of the passive support of the tunnel wall, leading to the localized failure of the lining. This karstic cavity was connected with an existing cavity that daylighted on the left bank of Chimao creek and constituted the duct through which the observed large flow of dirty water outcropped.

It is important to mention that the installation records of all rock anchors in the region, as well as their quality control load test, were analyzed, and showed no indication of the rock mass in the area being of weaker competence.

#### 4.10. Design solution to the problem

Prior to the implementation of the necessary remedial works, an intense investigation of the tunnel, along all its alignment, was performed using different geophysics processes and direct borings, in order to guarantee that no similar feature existed and could fail in the future pressurizing of the tunnel. Some regions where there were indications of possible presence of cavities were grouted.

The solution for the collapsed region was traditional, simple and quick to implement. The erosion cavity Hoyo de la Beba was filled with concrete until it became distant transversely to the tunnel – a transversal distance of 30 m was postulated as the criterion for concrete filling. The concrete lining previously installed at the Chimao creek was prolonged to a tunnel chainage where the design hydraulic gradient criteria was met in rock mass with reliable geo-mechanical characteristics.

#### 4.11. Conclusions

The Chaglla HPP has been in successful operation since mid 2016; the concerns related to the behavior of the headrace tunnel during and after its pressurization for power generation have been surpassed.

### 5. Concluding Remarks

Some case histories are presented and discussed, trying to frame the physical behaviour(s) that lead to important gains in knowledge of geotechnical behaviour in important infrastructure projects, during detailed design and construction. Creativeness is an important aspect that guided decisions in these projects, and Prof. Victor de Mello's perspective on how to use creativeness is seen as present in all of them.

Many experienced engineers have studied and solved equivalent problems. To them these case histories may add little additional knowledge. To the younger colleagues, these examples may enlighten their decision taking process.

In all these case histories, the importance of a sound geological model to support the design studies is present; the need to have this geological model alive throughout the site investigation for the project, and also throughout the actual construction of the works, updating or even fully revising the existing geological model due to information being gathered as the works progress, is crucial for the success aimed at. In some occasions, nature as materialised in the geo-environment, excited by meteorological factors, manifests itself through a different model than that accepted and studied previously.

Difficulties in budget and time constraints sometimes add an important factor in some contract models prevailing these days in many important infrastructure projects.

Broadly speaking, why so many projects undergo significant changes after start of construction or event failures continue to happen, and so much resources and time is lost due to these situations?

It is our understanding that geo-engineering, soil and rock mechanics and geology for engineering, has developed to a point in which sound physical concepts are recognized and understood. Mathematical tools have been developed to very sophisticated levels, in which the required input parameters many times are not practically obtainable, other than in research related activities and projects.

Anticipation of a geological model is very important in order to plan and properly interpret data from a site investigation program; Fookes (1997, 2000) provides a very important contribution discussing and proposing basic geological models for different geological environments. Fookes (1998) also gives an important contribution when he clearly states "if you do not know what you are looking for in a site investigation you are not likely to find much of value". Keeping the model "open" to be re-discussed at the light of new information coming from the site, during construction work, is of fundamental importance – early stages of excavation in a major construction site provide infinitely more information than localized boreholes.

The relevance of construction methodology and its inter-relation with design hypotheses also plays an important role, especially in soil-structure interaction behaviour, and should complement aspects of the geological model during design and construction.

The constant updating of the state of knowledge or of practice is crucial when pursuing the required optimizations in the major infrastructure projects so needed by our societies. I hope that the discussion of these important geotechnical works adds to the state of practice and knowledge.

As a last tribute to Victor de Mello in this occasion, I think it is valid to share one of his most used sayings, an Arab proverb:

*He who knows not, and knows not that he knows not - He is a fool, shun him.*

*He who knows not, and knows that he knows not - He is simple, teach him.*

*He who knows, and knows not that he knows - He is asleep, wake him.*

*He who knows, and knows that he knows - He is wise, follow him.*

which was discussed, in many interactions with Prof. John Burland before his death, as meriting revision and both proposing that the last line should be re-written and a further line should be added as follows:

*He who knows, and knows that he knows – He is insufferable, use him.*

*He who knows, and knows when he knows not – He is wise, follow him.*

## Acknowledgments

I would like to share with you all my gratitude, *in memoriam*, to Prof. Victor de Mello, who taught and led me in the field of applied geomechanics, opening my mind to the myriad of facets with which nature express itself, “*always considering that there is no reason for two things being equal*”. His approach on how to tackle engineering problems, with sound concepts and wise thoughts, plays a very important part of my professional practice as well as of my private life, and is specially acknowledged.

Our gratitude has also to be extended to many colleagues, specially to Profs. Georg Sadowski and Claudio Wolle, Mr. Carlos Manoel Nieble and Dr. Werner Bilfinger, who have a continuous and important participation, as well as Construtora Odebrecht, Construtora Andrade Gutierrez and Intertechne Consultores Associados, in facing and solving some of the geotechnical challenges faced during my professional practice. In the preparation of this technical paper, and the presentation that accompanies it, the collaboration and critical review of Mr. Bruno S. Dzialoszynski was greatly appreciated.

I also have to acknowledge the fact that numerous of Victor’s friends incorporated me as their friends, sharing with me their enormous experience in life through geotechnical engineering; special gratitude is shared with Prof. Michele Jamiolkowski, Dr. David Carrier, Prof. John Burland, and Prof. Harry Poulos.

Finally, my gratitude to Dr. Purnanand Savoikar, Chairman of the IGS Goa Chapter of the Indian SSMGE, who transferred his enthusiasm in this task during the preparation of this Lecture. The gratitude is extended to all members of the Goa Chapter and to the Indian SSMGE.

## References

Barton, N.R.; Lien, R. & Lunde, J. (1974). Engineering classification of rock masses for design of tunnel support. *Rock Mechanics*, 6(4):189-239.

Benson, R.P. (1988). Design of unlined and lined pressure tunnels. *Proc. International Symposium of Tunneling*

for Water Resources and Power Projects, New Delhi, pp. 155-170.

Bjerrum, L. & Andersen, K.H. (1972). In-situ measurement of lateral pressures in clay. *Proc. Fifth European Regional Conference ISSMFE, Madrid*, pp. 11-20.

Bjerrum, L.; Nash, J.K.T.L.; Kennard, R.M. & Gibson, R.E. (1972). Hydraulic fracturing in field permeability testing. *Géotechnique*, 22(2):319-332.

Bogomolov, G.V. (1965). *Hydrogéologie*. Ed. de la Paix, Moscow.

Carlsson, A. & Olson, T. (1977). Hydraulic conductivity of swedish crystalline rocks. *The Bulletin of the Geological Institutions of the University of Uppsala*, NS7:71-84.

Dale, T.N. (1923). The Commercial Granites of New England. *U.S. Geol. Surv. Bull.*, 738:488.

de Mello, L.G.F.S. (2005). *Geotechnical Failures*. Jennings Lecture, Johannesburg. Distributed on digital format on a pendrive.

de Mello, L.G.F.S.; Sadowski, G.R. & Nieble, C.M. (1987). The foundation treatment of residual soils conditioned by canaliculae: A case historie. *Anais da Conferencia Ibero-Americana sobre Aproveitamentos Hidraulicos, Lisboa*, v. I, pp. B.01-B.012.

de Mello, L.G.F.S.; Sadowski, G.R. & Nieble, C.M. (2004). Shear resistance of biotite schists: Peak and post-peak behaviour. *Advances in Geotechnical Engineering: The Skempton Conference, ICE, London*, pp. 535-544.

de Mello, V.F.B. (1977). Reflections on design decisions of practical significance to embankment dams. *XVII Rankine Lecture. Géotechnique*, 27(3):281-355.

de Mello, V.F.B. (1972). Thoughts on soil mechanics applicable to residual soils. *Proc. III Southeast Asian Conference on Geotechnical Engineering, Hong Kong*, pp. 5-34.

de Mello, V.F.B.; Larocca, E.S.; Quintanilha, R. & Meireles, B. (2004). Reappraising historical coincidences that radically misled slope destabilization analyses of homogeneous earth dams. *Advances in Geotechnical Engineerin: The Skempton Conference, ICE, London*, v. 2, pp. 881-897.

Fookes, P.G. (1997). *Geology for engineers: The geological model, prediction and performance - 1<sup>st</sup> Glossop Lecture*. *Quarterly Journal of Engineering Geology*, 30(4):293-424.

Fookes, P.G. (1998). *Judging the Lie of the Land - Meeting Report of the First Glossop Lecture*. *Ground Engineering*, 10(8):36.

Fookes, P.G. (1997). *Tropical Residual Soils*. *Geological Society Professional Handbooks*. Geological Society, London.

Fookes, P.G.; Baynes, F.J. & Hutchinson, J.N. (2000). Total geological history: A model approach to the anticipation, observation and understanding os site consitions. *Proc. International Conference on Geotechnical*

- and Geological Engineering; GeoEng 2000, Melbourne, pp. 370-460.
- Fossen, H. (2010). Structural Geology. Cambridge University Press, Cambridge.
- Haimson, B. & Fairhurst, C. (1967). Initiation and extension of hydraulic fractures in rocks. Society of Petroleum Engineers Journal, 7(3):310-318.
- Hencher, S.R.; Carter, T.G.L.; Lee, S.R. & Richards, R. (2011). Sheeting joints: Characterisation, shear strength and engineering. Rock Mechanics and Rock Engineering, 44(1):1-22.
- Holzhausen, G.R. (1989). Origin of sheet structure, 1. Morphology and boundary conditions. Engineering Geology, 27(1-4):225-278.
- Kennard, R.M. (1970). The Measurement of Soil Permeability In-situ by the Constant Head Test. Ph.D. Thesis, University of London, London.
- Machado, A.d.B. (1983). The contribution of termites to the formation of laterites. II International Seminar on Lateritisation Process, São Paulo, pp. 261-270.
- Morgenstern, N.R. & Vaughan, P.R. (1963). Some Observations on Allowable Grouting Pressures, Grouts and Drilling Muds in Engineering Practice. Butterworths, London.
- Norwegian Geotechnical Institute (2013). Rock Mass Classification and Support Design. [Online] www.ngi.no.
- Power, M.; Chiou, B.; Abrahamson, N. & Rblee, C. (2006). The next generation of ground motion attenuation models (NGA) Project: An overview. Proc. 8<sup>th</sup> Earthquake Engineering Research Center - Draft Report, San Francisco, pp. 2022.1-2022.
- Remy, J.P.P.; Da Silva Lopes A.; De Ávila J.P. & Herkenhoff C.S. (1985). Choice of the foundation treatment of Balbina earth dam. 15<sup>th</sup> International Conference on Large Dams, Lausanne, v. 3, pp. 263-283.
- Santos, O.G.; Sathler, G.D.; Herkenhoff, C.S. & Moreira, J.E. (1985). Experimental grouting of residual soil of Balbina Earth Dam Foundation, Amazon, Brazil. Proc. 1<sup>st</sup> International Conference on Geomechanics in Tropical Lateritic and Saprolitic Soils, Brasilia, v. 2, pp. 143-154.
- Sathler, G. & Camargo, F.P. (1985). Tubular cavities in the residual soil of the foundation of Balbina earth dam - Amazon - Brazil. Proc. 15<sup>th</sup> International Conference on Large Dams, Lausanne, v. III, pp. 285-293.
- Terzaghi, K. (1962). Dam foundation on sheeted granite. Géotechnique, 12(3):199-208.



# A Method for Designing Finger Drains and Assessing Phreatic Lines for Dams

M.C.N. Araújo, T.F. de Souza Júnior, M.N.B. Trevizolli, C.A. Teixeira, S.H.C. Teixeira, V.P. Faro

**Abstract.** Finger drains are linear drains used to collect and conduct percolated water in embankment dams. They are arranged crosswise into earth dams, either permanently or as a technique to treat clogged filters. Given their easy operation, they are often applied in engineering practice, without the aid of specific dimensioning techniques in many cases. The aim of this paper is to propose a method for designing finger drains for earth dams, considering geometric and hydraulic characteristics (length, width, spacing, height and reservoir level). Moreover, the method allows estimating the phreatic line inside the dam. The method was based on data from small scale physical models and on numerical models, calibrated using the physical model results. Twenty-seven numerical models were developed by simulating seepage for different spacing between drains and lengths of drains, besides three reference numerical models with different lengths of drainage mat. The numerical modeling was validated using the results of four small-scale models processed with software Seep/W.

**Keywords:** dams, drainage, finger drains, model, small-scale.

## 1. Introduction

Internal drainage systems contribute to the stability of earth dams. An effective drainage significantly reduces the risk of accidents. Massad (2003) states that most of the accidents involving earth dams are caused by the absence of an efficient flow control system.

Typically, soils with very low permeability are chosen to build earth dams, in order to minimize water flow through the soil mass. Due to the characteristics of the used materials, seepage inevitably occurs through the dam earthfill. According to Cruz (1996), drainage systems are the main defense against concentrated and preferential flows; that is, drainage systems regulate seepage in the dam itself and in its foundation, reducing the pore-pressure and disciplining flow leakage downstream of the dam.

Finger drains are linear elements arranged side by side in the main flow direction, perpendicular to the dam axis, at specific distances from one another. These drainage devices are recommended as an alternative to drainage blankets when the cost of drainage materials is very high or when the volume of granular material required for building a drainage blanket is not available. They are also used in corrective interventions on clogged filters, for maintenance

purposes. The drains can be designed with sloped sides to allow an even distribution of ground stress.

The cross-section of finger drains must be large and/or enough permeable to support the flow that percolates without raising the pore-pressures in the earth fill dam. Therefore, it is important to assess the spacing between drains to ensure that the hydraulic heads are dissipated and pore-pressures do not interfere with the structure functioning. Drainage systems should be designed to maintain the stability of these structures and prevent phreatic levels from rising.

The shape of the three-dimensional phreatic surface inside a dam provided with linear drains, as well as the format of the flow network and the way in which pore-pressures are distributed in the earth fill are, strictly speaking, unknown. Nowadays, there are no practical methods to estimate the position of the phreatic line when using finger drains, even though it influences the variation of safety factors of the dam downstream shoulder.

Thus, this paper proposes a method for designing finger drains for earth dams, considering its geometry, such as length, width, spacing, and height, and for obtaining an outline of the phreatic line inside the dam. The method is based on small-scale physical models and numerical models calibrated by small-scale responses. Twenty-seven numerical

---

Michelle Caroline Nogueira de Araújo, M.Sc. Student, Departamento de Engenharia de Construção Civil, Universidade Federal do Paraná, Curitiba, PR, Brazil. e-mail: mcnaraújo@gmail.com.

Tennison Freire de Souza Jr., M.Sc. Student, Departamento de Engenharia de Construção Civil, Universidade Federal do Paraná, Curitiba, PR, Brazil. e-mail: tennisonfreire@outlook.com.

Marina Naim Brock Trevizolli, M.Sc. Student, Departamento de Engenharia de Construção Civil, Universidade Federal do Paraná, Curitiba, PR, Brazil. e-mail: marinatrevizolli@hotmail.com.

Celimar Azambuja Teixeira, Associate Professor, Departamento de Engenharia de Construção Civil, Universidade Tecnológica Federal do Paraná, Curitiba, PR, Brazil. e-mail: celimar@utfpr.edu.br.

Sidnei Helder Cardoso Teixeira, Associate Professor, Departamento de Engenharia de Construção Civil, Universidade Federal do Paraná, Curitiba, PR, Brazil. e-mail: sidnteix@outlook.com.

Vitor Pereira Faro, Associate Professor, Departamento de Engenharia de Construção Civil, Universidade Federal do Paraná, Curitiba, PR, Brazil. e-mail: vitorpereirafaro@hotmail.com.

Submitted on August 22, 2017; Final Acceptance on October 2, 2018; Discussion open until April 30, 2019.

DOI: 10.28927/SR.413309

models with finger drains were developed, which simulated percolation for different combinations of drain spacing and length, besides three reference models, with different lengths of drainage blanket. The results were processed and design abacuses were developed based on the studied parameters so that, once applied, the estimated behaviors were similar to those provided by the numerical and physical models results.

In general, drainage systems are made with very permeable materials, such as sand, gravel, and crushed stone. As the availability of granular materials is limited in some regions, some designers have chosen to use linear drains, also known as finger drains or stringer drains. There are two requirements regarding the efficiency of finger drains. The first requirement is that filters and drains should avoid internal erosion of soil. This is called filtration criterion. The second, and equally important requirement, refers to the discharge capacity. The drainage system should prevent pore-pressure from increasing in the dam earth fill, this is called drainage criterion.

The water that permeates through the dam earth fill must comply with the overall flow equation, based on Darcy's law. Methods based on the overall flow equation can identify the flow that percolates through the earth fill. The flow received by each finger drain depends on the spacing between drains.

Finger drains can collect percolation water and transfer it to the downstream slope toe. Figure 1a shows finger drains in a dam. The drains are usually made with surrounding transition elements with a thicker grade, forming a "sandwich" structure, as shown in Fig. 1b. The transition elements also contribute to soil drainage, although this is not frequently considered in drain capacity.

The study carried out to develop a procedure for finger drain design, based on small-scale physical models and numerical models, is described below.

## 2. Small-Scale Model

The small-scale physical models were built using medium washed clayey sand as earth fill material. The finger drains were built using gravel with a much higher perme-

ability than the sand. Laboratory tests were made to characterize the materials used in small-scale models.

The sand was submitted to particle size analysis according to NBR 7181/1984. Constant head permeability tests were subsequently done, as described in NBR 13292/1995. Furthermore, the sand was tested to obtain minimum and maximum void ratios for non-cohesive soils, as recommended in NBR 12051/1991 and NBR 12004/1990, respectively. For the actual density of the grains, the samples were tested according to the DNER - ME 093/1994 standard. The shear strength of the sand was assessed according to BS 1377-7/9 procedures. Finally, the samples were submitted to drainage column test to determine the soil water retention curve (SWRC), as described by Furlan & Dell'avanzi (2007).

The clayey sand particle-size distribution was: 79.20% of sand, 15.40% of clay, and 5.40% of silt particles.

The sand hydraulic conductivity obtained was equal to  $1 \times 10^{-2}$  cm/s. To account the drainage criteria, gravel with a particle size between 4.8 mm and 9.5 mm was used, having material had a hydraulic conductivity equal to  $1.9 \times 10^1$  cm/s.

The tests to evaluate the sand void ratios resulted in 0.73 and 0.61 for maximum and minimum void ratios, respectively. The minimum sand void ratio was used to calibrate the pluviation height and thus obtain specific gravity of sand in order to construct the small-scale models of the dam. Three samples were modeled with three different fall heights, in terms of dry specific gravity, the behavior of the material resulted in the curve shown in Fig. 2.

The adopted fall height for constructing the models was 12 cm, which is related to a specific gravity equal to  $1.60 \text{ g/cm}^3$ , as shown in Fig. 2. The particle density values for sand and gravel were  $2.50 \text{ g/cm}^3$  and  $2.43 \text{ g/cm}^3$ , respectively.

The clayey sand samples were submitted to direct shear tests. Three samples, modeled by the sand pluviation method, with a fall height of 12 cm, were tested with normal stresses of 54 kPa, 74 kPa, and 114 kPa, under saturation. Given the permeability of the material, the shear test was performed at a displacement rate equal to 0.30 mm/min, to

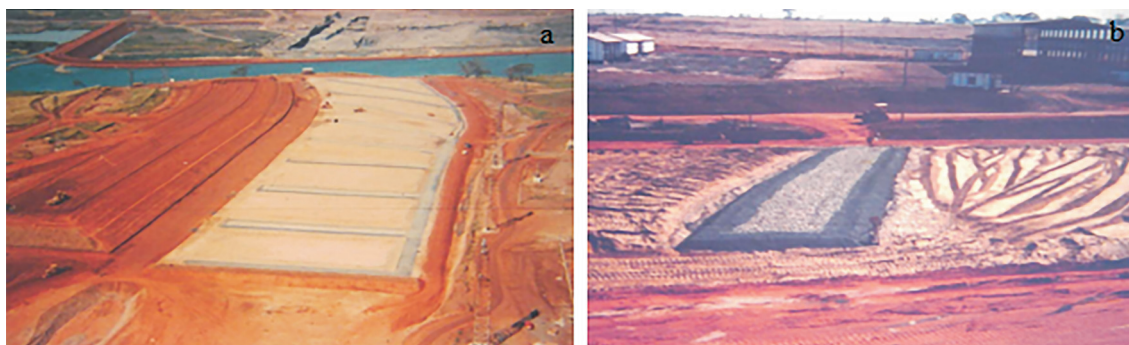


**Figure 1** - Finger drains: Use in dams (a); view of dam area (b) detail of transitions (Adapted from PUC Goiás, 2016).

ensure drained conditions during shearing. The shear test resulted in a friction angle equal to  $34^\circ$  based on the equation:  $\tau = 0.68\sigma + 5$ .

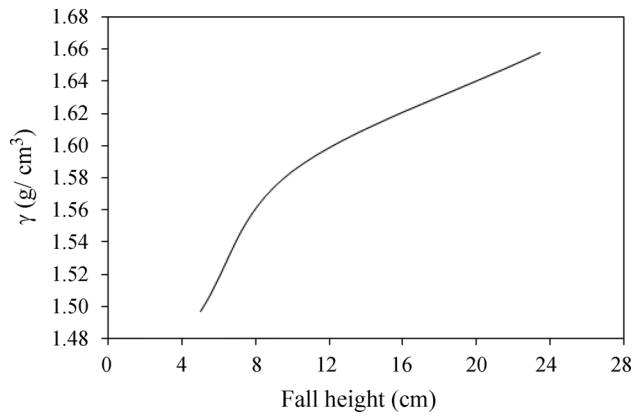


Figure 2 - Specific dry weight as a function of material fall height.

Figure 3 shows the moisture retention curve for the clayey sand soil, obtained by column test. The residual moisture content was about 16%, corresponding to 31.50 cm of capillary height.

The small-scale physical dam model was built inside a 2.50 m long, 44 cm wide, and 60 cm high metal box, with a frontal acrylic wall. The dam model was 1.90 m long, 50 cm high with a 10 cm wide crest, as shown in Fig. 4. More details about the physical models can be found in Araújo (2013).

Three longitudinal sections were used to evaluate the piezometric lines, as shown in Fig. 5. Thus, the models were split into front section (S1), middle section (S2) and rear section (S3), to obtain the pore-pressures inside the dam.

Regarding the instrumentation, some open pipe piezometers were installed to measure the pore-pressures inside the dam model. The piezometers consisted of polyethylene hoses with a 3 mm internal diameter, fixed to the

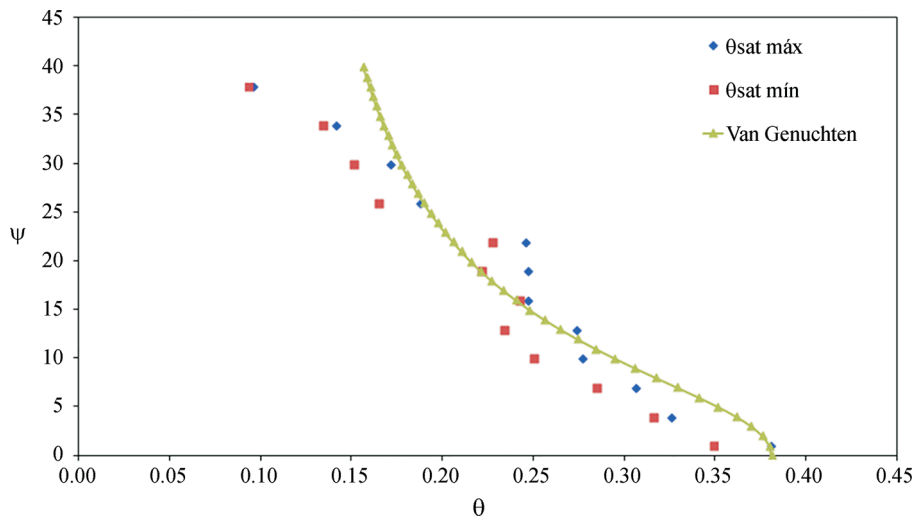


Figure 3 - Soil moisture retention curve.

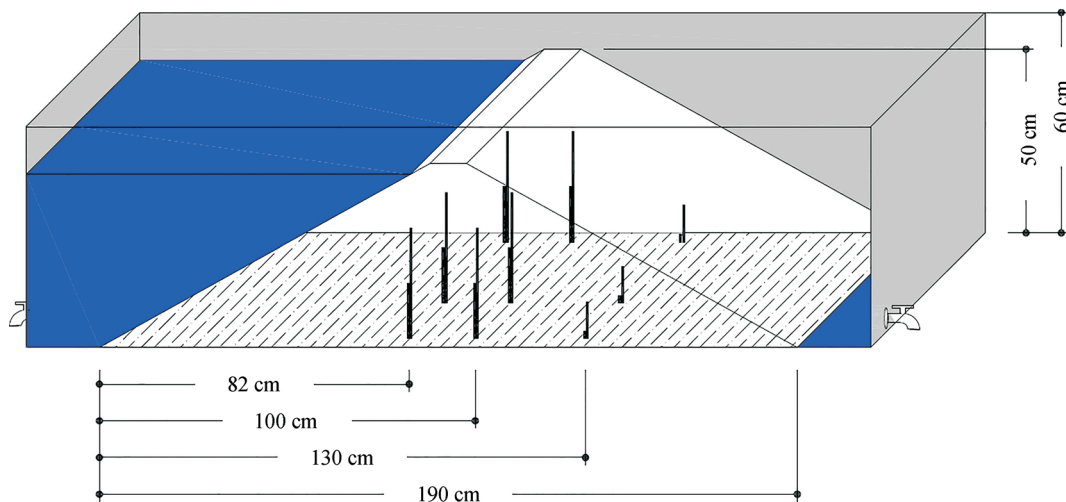


Figure 4 - Schematic of the reduced model with the piezometers location.

steel plate of the base of the box and crossing it. The inlet end of each piezometer was covered with filter paper and non-woven geotextile.

Nine pairs of piezometers were positioned on the front, middle and rear sections of the dam, in the upstream and downstream slopes and also under the crest, as shown in Figs. 4 and 5. The small-scale model allowed simulating the flow behavior in an earth fill dam where finger drains are installed.

Four small-scale models of dams were built and tested, each one simulating a specific internal drainage system. The dimensions of finger drains were: 6 cm at the base, 3 cm at the top, 3 cm high and 50 cm long. Table 1 shows the different drain types and spacing between drains for each of the 4 tested models.

The piezometers were kept saturated until the dam reservoir was filled, to facilitate construction and ensure the good performance of piezometers.

After the reservoir filling, the water tap, located downstream of the model was opened to initiate the water percolation through the earth fill. After the flow was established, the drainage of the dam was then measured during a time “t” by using a graduated cylinder, the piezometers were read and the flow rate was calculated.

In Model 1 (dam with drainage blanket), the reservoir reached the elevation 47 cm and then the water percolation started, advancing downstream through the sand. No signs of rupture or internal erosion were detected, and the flow discharged through the middle of the slope toe. The use of the drainage blanket, in this case, proved to be efficient for drainage, and the water percolated preferentially through the center of the device rather than through the side walls of the acrylic box.

**Table 1** - Tested physical model setup.

Model	Drainage device	Spacing (S) (cm)	Drainage area (cm <sup>2</sup> )
1	Drainage blanket	-	132
2	1 finger drain	88	13.5
3	2 finger drains	44	27
4	3 finger drains	22	54

In Model 2 (one finger drain, at 88 cm spacing), despite the absence of signs of rupture, a slight deformation was observed in the downstream slope. Regarding the device functionality, the simulation showed that the finger drain is efficient since the flow was mostly discharged through it. In this case, due the smaller drainage section, compared to the Model 1, some erosion (particles movement) was observed in the drain outlet.

In Model 3 (2 finger drains, at 44 cm spacing), the draining material was arranged along both sides of the dam to enable a linear flow. The functionality of devices proved highly efficient since the outflow occurred preferentially through the finger drains. Minimal erosion was observed in the outlet of both drains, as observed in Model 2.

In Model 4 (3 finger drains, at 22 cm spacing), the draining material was arranged along both sides and the middle of the downstream slope of the dam to enable a linear flow. The functionality of devices proved highly efficient, the outflow occurring initially through the middle drain, followed by the left drain and, lastly, the right drain.

The average flow rate in the four models was  $3.53 \times 10^{-6}$  m<sup>3</sup>/s. The highest value was recorded in Model 1 (with the drainage blanket) and the lowest in Model 2 (with 1 finger drain), indicating that the greater the space between the drains, the smaller the drainage area and, consequently, the lower the outflow.

Physical modeling of dams with drainage blankets and finger drains clearly demonstrated the differences in flow behavior. Analysis of cross section of each model showed that piezometric heights were fairly consistent with the situations observed in the modeling.

Section S1, in Fig. 6a, shows very similar readings in the piezometers located at the upstream side of the dam and at the crest. As the energy dissipates along the soil, the difference between the readings of piezometers increases. The head value found by the downstream piezometers is related to the total drainage area. Thus, the dam with one finger drain, which has the smaller drainage area, has shown the greater hydraulic heads. It is important to notice that the finger drains were installed along Section S1 in all four models.

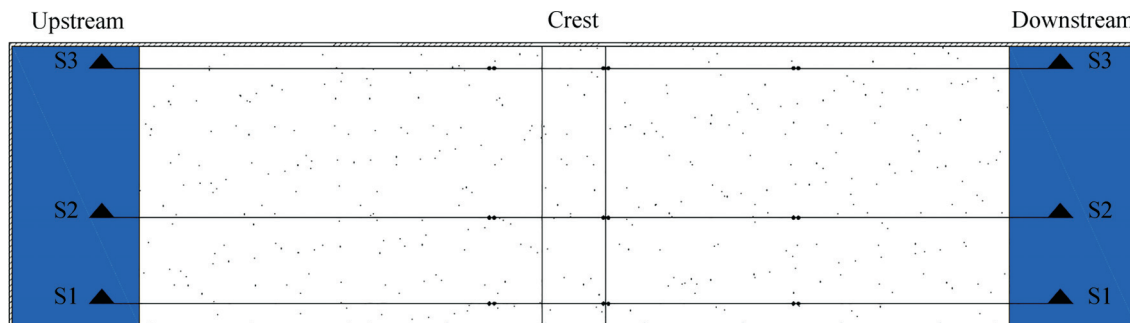


**Figure 5** - Positioning scheme of longitudinal sections.

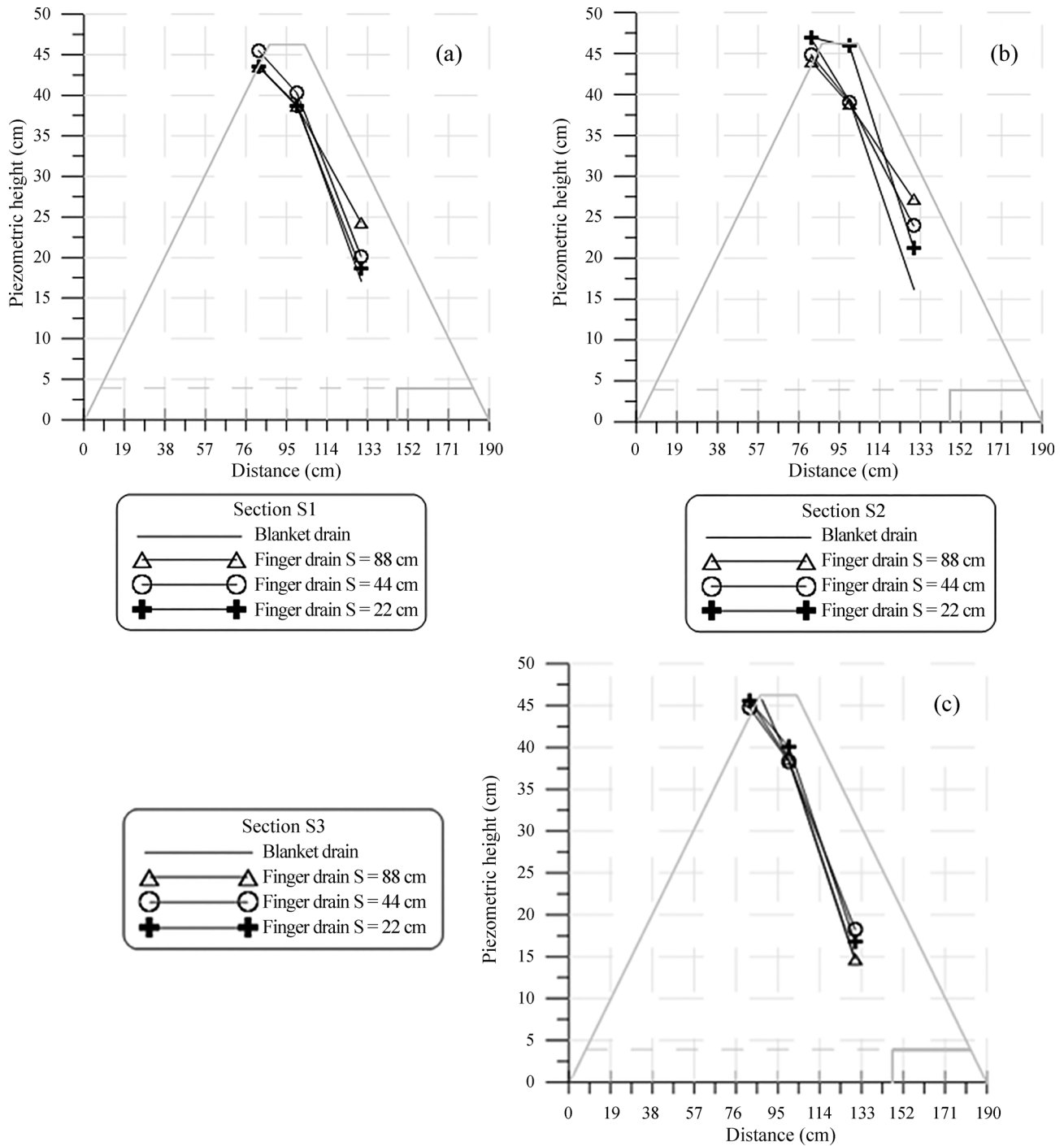


Figure 6 - Piezometric levels at sections: S1 (a); S2 (b) and S3 (c).

Results from the models with finger drains at different distances indicated that the smaller the distance between the drains, the greater the energy dissipation and the lower the hydraulic heads inside the dam. Figure 6b illustrates Section S2 that was the section where the highest piezometric levels were observed in all models.

Finally, the piezometric readings in Section S3 (Fig. 6c) were similar to those in Section S1, as both are in sections with drains - except for Model 2 (with 1 finger

drain along Section 1). In the models where drains were at 22 cm and 44 cm spacing, the water percolated from the earth fill center to the model lateral walls, resulting in very similar piezometers readings in Sections S1 and S3.

### 3. Numerical Modeling

Parametric analyses regarding the seepage behavior were conducted using numerical models with the software Seep/W. Numerical modeling is a simulation of a real phys-

ical process based on theoretical equations, allowing comparisons between different not-physically-tested scenarios. When calibrated, models reproduce the real physical process with good accuracy.

Although the employed software is not based on three-dimensional equations, it allows to model seepage in a plan. It means that gravity is considered perpendicular to modelled plan and flow can be evaluated from one side to the other side of the model by imposing convenient boundary conditions. The authors considered that using a 2D model, is the best way for modelling dams with finger drains, despite the fact that water flows in a three-dimensional way.

In 2D numerical models, the pressure head of reservoir is imposed at the upstream side of the model and zero pressure head is applied at the end of the finger drains, at the downstream side of the model, as boundary conditions. The phreatic surface elevation is, then, assumed as the values of hydraulic head obtained by computation.

The results of small-scale tests were used to calibrate seepage numerical models, which were based on the finite element method. Calibrated numerical models enabled additional analyses considering physically untested scenarios.

The parameters of materials used on numerical modelling are based in characterization tests with those materials used on small-scale models and calibration of anisotropy ratio,  $K_z/K_x$ , prior to doing parametric analyses.

For stage 1 (Numerical modelling of physical model) the procedures followed the imposition of piezometric heads found in the small-scale model as boundary condition and  $K_z/K_x = 1$ ; stage 2 (Calibration of  $K_z/K_x$  ratio for numerical modelling) was based on the assessment of piezometric heads and comparison with those obtained in small-scale models up to results are similar and stage 3 (Parametric analyses by numerical model) solved the simulation of drains with different lengths and spacing, using the  $K_z/K_x$  ratio obtained in stage 2.

Considering the geometric parameters of the model, a matrix (Table 2) of the simulation scenarios was built, by varying the drain length and spacing between drains and keeping unchanged the total head at the reservoir and the model width.

The mesh of finite elements of the numerical model is shown in Fig. 7. The model represents the horizontal section of the dam at its base. It was adopted  $K = 1.10 \times 10^2$  cm/s for earth fill material and  $K = 2.0 \times 10^0$  cm/s for drain material. As a boundary condition, the hydraulic head equal to 47 cm was adopted at the upstream side, and a null hydraulic head was adopted at the downstream side. Moreover, the application of elevation heads was considered in the entry of the piezometers.

For calibrating the  $K_z/K_x$  anisotropy ratio, two-dimensional numerical analyses were performed considering a dam with blanket drain. The  $K_z/K_x$  ratio was changed un-

**Table 2** - Matrix of modelled scenarios.

Dams	C1		
	50	70	100
1	Blanket drain		
2	88	88	88
	144	144	144
	200	200	200
3	44	44	44
	72	72	72
	100	100	100
4	22	22	22
	36	36	36
	50	50	50

C1 - Drain length; S2 - Spacing between drains.

til the found results for pore-pressure were similar to those obtained in piezometers in the small-scale test.

Figure 8 shows the phreatic line position obtained in numerical models where the piezometric readings from the small-scale model were applied as a boundary condition and the phreatic line obtained from the calibrated numerical model, considering  $K_z/K_x = 0.3$ , respectively. One can note that phreatic lines are very similar, validating the parameter calibration in the numerical method. The same comparison was made for all sections of the models and the same similarity between the physical and numerical results for piezometric lines was observed.

To carry out the parametric analysis, it was sought the  $K_z/K_x$  ratio value (0.3) that best suits the behavior of the flow in the analyzed models for the initial configuration applied in physical modeling.

#### 4. Method for Designing Finger Drains for Dams

The abacuses for designing finger drains for earth dams are shown in Fig. 9. They allow to find the relationship between the maximum total head at the upstream and downstream ends of the finger drains and the total head at the dam reservoir ( $H_{max,U}/H$  and  $H_{max,D}/H$ ), considering the datum at the dam base. The input data are the ratio  $S/H$ , where  $S$  is the spacing between the drains and  $H$  is the total head at the dam reservoir. Each abacus is associated to a  $C/H$  ratio, where  $C$  is the drain length. Abacuses were developed for the ratios  $C/H = 1$ ,  $C/H = 1.4$ , and  $C/H = 2.0$ .

Based on Fig. 10, the necessary parameters for designing the finger drains can be identified. The transverse sections of the finger drains have a width equal to  $2b$  and height equal to  $H_p$ , as shown.

In case of using drainage blanket, water flow in the finger drains can also be assessed according to two condi-

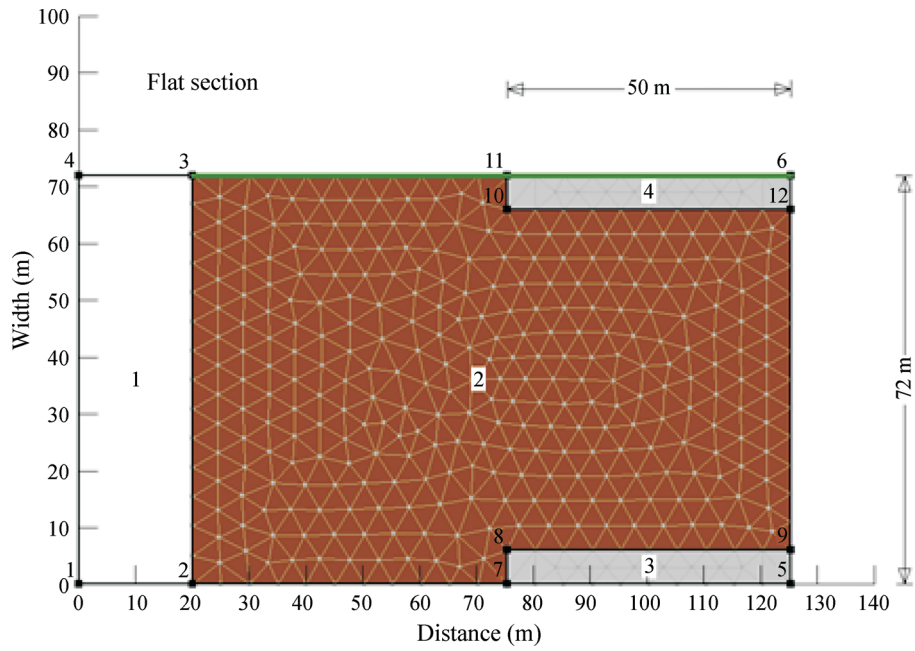


Figure 7 - Numerical model of the hypothetical dam – Plan view.

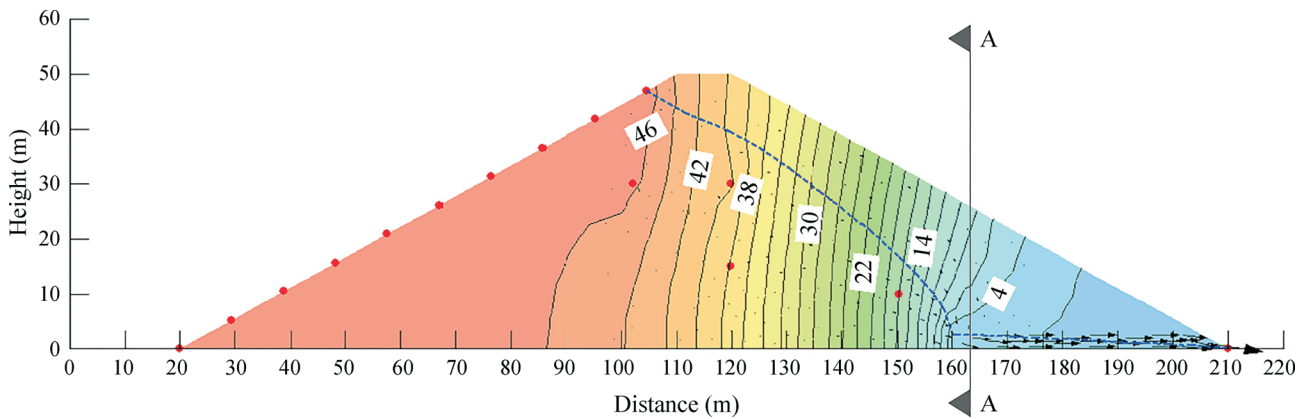


Figure 8 - Phreatic line based on the physical model piezometer readings.

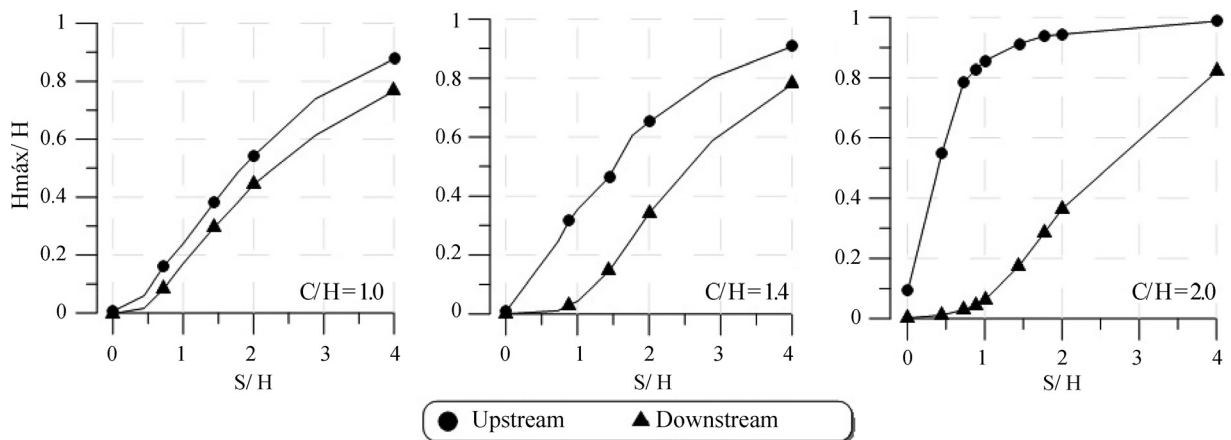
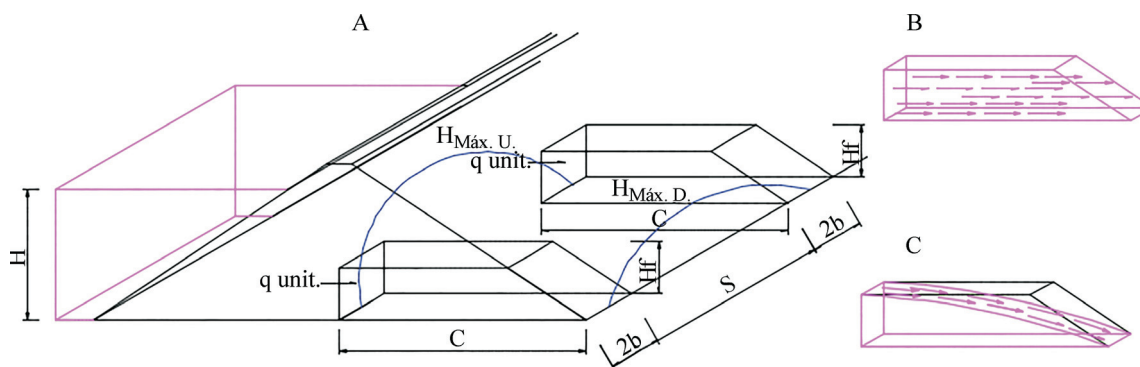


Figure 9 - Abacus to design finger drains for earth dams.



**Figure 10** - Parameters adopted in the design of the finger drain.

tions: a) phreatic line above the drain (Fig. 10b) and b) phreatic line inside the drain (Fig. 10c). Eq. 1 to Eq.3 are applied when the confined flow condition, inside the drain, is assumed (Fig. 10b). Eq. 4 is used when the unconfined flow is assumed (Fig. 10c). The designer of the drains must choose one of these two conditions in order to obtain the finger-drain height.

$$Q \cdot FS = \frac{b \cdot H_f^2}{c} K_f \quad (1)$$

Since:

$$Q = q_{unit} (S + 2b) \quad (2)$$

then:

$$H_f = \sqrt{\frac{q_{unit} (S + 2b) \cdot C \cdot FS}{K_s \cdot b}} \quad (3)$$

and:

$$H_f = \sqrt{\frac{2q_{unit} (S + 2b) \cdot C \cdot FS}{K_s \cdot b}} \quad (4)$$

where  $H_f$  - Height of finger drain (m);  $Q$  - Total flow rate for the area of influence of the drain (m<sup>3</sup>/s);  $q_{unit}$  - Unitary flow rate for the area of influence of the drain (m<sup>3</sup>/s/m);  $S$  - Spacing between finger drains (m);  $2b$  - Width of the finger drain (m);  $C$  - Length of finger drain (m);  $K_f$  - Permeability of draining material (m/s);  $FS$  - Safety factor, normally adopted equal to 10.

As mentioned, each abacus presented in Fig. 9 shows two curves featuring the relationship between the ratio  $H_{max}/H$  (maximum height of the phreatic surface between finger drains / total height of the reservoir) and the ratio  $S/H$  (spacing between finger drains/total height of the reservoir). Those abacuses are used for estimating the position of the phreatic line in dams between two finger drains.

The following step-by-step procedure can be used to estimate the piezometric heads:

- 1) Define the input data concerning drain geometry; that is, length of the drain ( $C$ ), the spacing between drains ( $S$ ), and total head of the dam ( $H$ );
- 2) Identify the abacus which best suits the condition  $C/H$  and, with the input data, calculate the ratio  $S/H$ . Project vertically up to the upstream pressure curve (curve  $H_{max,U}/H$ ) and downstream pressure curve (curve  $H_{max,D}/H$ );
- 3) With the entry point of the phreatic line in the earth fill, the head  $H_{max,U}$  at the upstream end of the drain and the head  $H_{max,D}$  at downstream the end of the drain, outline the phreatic line inside the dam.

## 5. Final Comments

Data obtained from the small-scale physical models and numerical models were analyzed to assess the behavior of finger drains in dams and better understand the three-dimensional flow in these works. Based on presented work, the following comments can be stated.

Finger drains efficiently improve internal drainage in dams, mainly because they can be built using materials with greater permeability than those used in blanket drains. However, the position of the phreatic surface when finger drains are used is higher than when blanket drains are employed.

Longer drains help to better dissipate hydraulic heads. Thus, there is an inverse relationship between the length of drains and the elevation of the phreatic line.

To improve the efficiency of finger drains, it is important to limit the space between drains or to increase its drainage area.

It is recommended that the total area of finger drains should be between 20% and 40% of the corresponding area for the solution with conventional drainage blanket and that the drainage capacity should be, at least, equal to the capacity of the drainage blanket. The increase in drainage capacity can be obtained using more permeable materials.

The recommended spacing between finger drains, in order to ensure water table inside the drains, is about 40% to 70% of the dam height.

As the length of finger drain increases, hydraulic head at the inner side of the drain increases. However, the difference in head between inner and outer ends of drain also increases.

## References

- Araújo, M.C.N (2013). Study of Equivalence between Finger Drains and Horizontal Drains in Earth Dams. M.Sc. Dissertation, Department of Civil Construction Engineering, Federal University of Paraná, Curitiba (in Portuguese).
- BSI (1990). Methods of test for soils for civil engineering purposes: Shear strength tests (total stress) - BS 1377-7. BSI British Standards, London, United Kingdom, 62 p.
- Cruz, P.T. (1996). 100 Brazilian dams: historic cases, building materials. Oficina de Textos, São Paulo, 648 p. (in Portuguese).
- DNER (1994). Determination of particles density – ME 093. DNER, São Paulo, São Paulo, Brazil, 4 p. (in Portuguese).
- Furlan, G.C. & Dell Avanzi, E. (2007). Evaluation of the influence of a contaminant hydrophobic in the characteristics of moisture retention of a sandy soil. In: VI Brazilian Congress of Environmental Geotechnics, REGEO, Recife, v.1. pp. 1-5 (in Portuguese).
- Geo-Slope International, 2012. Seep/W. Seepage and slope stability analysis. Developed by GeoStudio, 2012, version 8.15, Canada.
- Massad, F (2003). Earthworks - Basic course of geotechnics. Oficina de Textos, São Paulo, 170 p (in Portuguese).
- NBR (1984). Soil Analysis – 7181. ABNT, Rio de Janeiro, Rio de Janeiro, Brazil, 13 p (in Portuguese).
- NBR (1990). Determination of the maximum voids index of non-cohesive soils – 12004. ABNT, Rio de Janeiro, Rio de Janeiro, Brazil, 6 p (in Portuguese).
- NBR (1991). Determination of minimum voids index of non-cohesive soils - 12051. ABNT, Rio de Janeiro, Rio de Janeiro, Brazil, 14 p (in Portuguese).
- NBR (1995). Determination of the permeability coefficient of granular soils at constant load - 13292. Rio de Janeiro, Rio de Janeiro, Brazil, 9 p (in Portuguese).
- PUC Goiás (2016). Filter Sizing. Available at [http://professor.pucgoias.edu.br/SiteDocente/admin/arquivosUpload/15030/material/barragem\\_terra\\_4.pdf](http://professor.pucgoias.edu.br/SiteDocente/admin/arquivosUpload/15030/material/barragem_terra_4.pdf) and downloaded in 2018/10/20 (in Portuguese).



# Assessment of Rate Effects in Piezocone Tests from Poroelastic Cavity Expansion Analysis

G. Dienstmann, S. Maghous, F. Schnaid

**Abstract.** Cavity expansion solutions are often used in geomechanics modelling to investigate problems such as the bearing capacity of piles or interpretation of cone and pressuremeter tests. Conceived as a simplified approach to capturing the transient flow effects in the soil around an expanding cylinder, a non-linear poroelastic model is formulated in this paper based on the concept of proportional poroplasticity. The latter is used to assess rate effects and associated drainage conditions during piezocone penetration. In this context, cone tests performed in gold tailings at penetration rates ranging from 0.1 mm/s to 57 mm/s are used to validate the proposed approach. The model predictions are directly compared with in situ testing results in the space of normalized velocity  $V_h$  to cone resistance  $Q$  and to degree of drainage  $U$ , demonstrating the model capability of capturing the transitions from drained to partially drained and undrained soil regimes.

**Keywords:** cylinder expansion, finite element analysis, in situ tests, non-linear poroelasticity, transient flow.

## 1. Introduction

With the growth of the mining industry, large-scale mining operations have increased the challenge to the design of safe and economical Tailings Storage Facilities (TSF). The exploitation of minerals, such as gold, zinc, bauxite, produces large amounts of mine tailings which are often in slurry form with high water content and compressibility. Recent failures (Tonglvshan Mine, China 2017; Mariana's Dam, Brazil 2015; Mount Polley mine, Canada 2014, to cite a few) reinforce that although there has been significant improvement in the state of practice (*e.g.* Vick, 1990; Martin & McRoberts, 1999; Davies & Martin, 2000; Fahey *et al.*, 2002), available engineering technology for the design, construction, operation and closure of tailing deposits still causes important environmental impacts.

Central in the design of TSF, the geo-characterization of tailings faces difficulties coming from the heterogeneous nature of waste products, the hydraulic depositional processes and the change in the constitutive parameters during the lifetime of deposits. The experience gathered in the last 20 years (*e.g.* Schnaid *et al.*, 2013; Jamiolkowski *et al.*, 2003) shows that the deposition process often produces tailings in the so-called intermediate permeability range of  $10^{-5}$  to  $10^{-8}$  m/s (silty materials). In intermediate soils, including natural clayey and sandy-silts, tailings and other geomaterials, partially drained behavior can occur when in situ tests as cone penetration are performed at the standardized velocity (20 mm/s), introducing errors in interpretation.

For in situ tests, partially drained effects in silty soils (transient materials) can be and are usually evaluated considering a non-dimensional velocity  $V_h$  [*e.g.* Randolph & Hope, 2004]:

$$V_h = \frac{v \cdot d}{c_h} \quad (1)$$

where  $d$  is the probe diameter,  $v$  the loading rate and  $c_h$  the coefficient of horizontal consolidation.

The use of expression (1) is essentially based on experimental observation, in which normalized testing data are interpreted in a space that correlates the degree of drainage  $U$  to a non-dimensional velocity parameter  $V_h$  (House *et al.*, 2001; Schnaid *et al.*, 2004; Randolph & Hope, 2004; Chung *et al.*, 2006; DeJong *et al.*, 2013). At the same time, attempts have been made to develop a structured theoretical framework to anticipate the drained conditions in intermediate permeability soils. Most of the current developments are based on cavity expansion solutions which are recognized as useful in interpreting the response of piles (*e.g.* Soderberg, 1962; Vesic, 1972; Randolph & Wroth, 1979; Carter *et al.*, 1979; Osman & Randolph, 2012; Yu, 2000) and in in situ tests (*e.g.* Gibson & Anderson, 1961; Baligh, 1985; Teh & Houlsby, 1991; Burns & Mayne, 2002; Yu & Mitchell, 1998) with a variety of soil stress-strain models.

Following a literature review, analytical solutions for both spherical and cylindrical cavity expansion assuming a Mohr-Coulomb criterion and considering the volume change in a plastic region can be found in the work of Vesic

Gracieli Dienstmann, Ph.D., Associate Professor, Departamento de Engenharia Civil, Universidade Federal de Santa Catarina, Florianópolis, SC, Brazil. e-mail: g.dienstmann@gmail.com.

Samir Maghous, Ph.D., Full Professor, Departamento de Engenharia Civil, Universidade Federal do Rio Grande do Sul, Porto Alegre, RS, Brazil. e-mail: samir.maghous@ufrgs.br.

Fernando Schnaid, Ph.D., Full Professor, Departamento de Engenharia Civil, Universidade Federal do Rio Grande do Sul, Porto Alegre, RS, Brazil. e-mail: fschnaid@gmail.com.

Submitted on March 8, 2018; Final Acceptance on September 18, 2018; Discussion open until April 30, 2019.

DOI: 10.28927/SR.413319

(1972). In Randolph & Wroth (1979) a cavity expansion approach is used to study the pore pressure dissipation after pile installation. Semi-analytical solutions based on critical state models are reported by Yu & Houlsby (1991), Collins *et al.* (1992), Collins & Stimpson (1994), Cao *et al.* (2001), Chang *et al.* (2001) for the drained and undrained cylindrical expansion.

Finite element solutions can be used to analyse the consolidation fields in a saturated porous medium under cylindrical and spherical symmetries. One may see the studies of Jang *et al.* (2003), Silva *et al.* (2006), Zhao *et al.* (2007), LeBlanc & Randolph (2008), Xu & Lehane (2008), Wang (2000), Jaeger *et al.* (2010), Jaeger (2012), Suryasentana & Lehane (2014), modelling the soil as Tresca, Mohr Coulomb or Modified Cam-Clay under different expansion rates, capturing undrained (very fast rate) and fully drained behaviour (very slow rate).

Aiming to analyze the consolidation and rate effects induced by the expansion of a rigid cylinder embedded within an isotropic elastic medium of infinite extent, a constitutive model has been formulated in Dienstmann *et al.* (2017). The model is based on the local equivalence between the response of a perfectly plastic behavior to monotonic loading and an appropriate fictitious non-linear poroelastic behavior. Closed-form expressions for pore pressure distribution were derived according to a simplified framework, while stresses and displacements are computed numerically. The theoretical features of the model are briefly described and applied herein to the interpretation of drainage conditions during piezocone tests executed in *Fazenda Brasileiro* gold TSF.

## 2. Problem Idealization

The analytical cylindrical cavity expansion solution proposed and described in Dienstmann *et al.* (2017) is structured as a consolidation analysis of a rigid cylinder deeply embedded within an isotropic fully saturated poroelastic medium of infinite extent. The problem, idealized in Fig. 1, defines that from an initial stress and pore pressure state  $(\sigma_0, p_0)$ , a prescribed radial displacement of magnitude

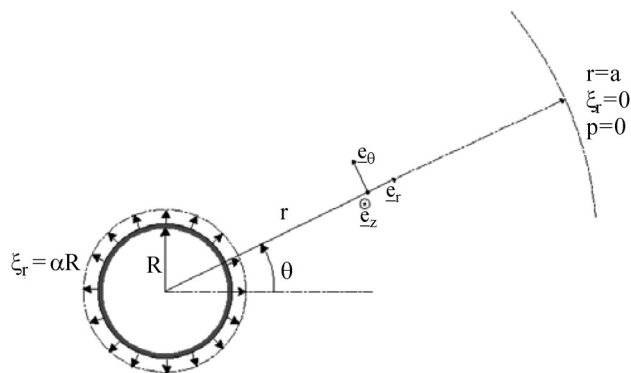


**Figure 1** - Idealized geometry and loading conditions for consolidation around an infinite expanding cylinder.

$\alpha R$  is applied at the cylinder wall  $r = R$ . The influence zone of the applied displacement is defined from  $R \leq r \leq a$  to characterize the extent of the region whose poromechanical state is no longer affected by cylinder installation and subsequent expansion (*e.g.* Blight, 1968; Randolph and Wroth, 1979; Osman and Randolph, 2012). This means in particular that displacement and excess pore pressure vanish at  $r = a$ .

The soil surrounding the cylinder is modeled as a fully saturated, isothermal poroelastic material undergoing infinitesimal strains. In all that follows, the sign convention of positive stress values for tension and negative stress values for compression will be adopted.

### 2.1. Constitutive formulation

The theoretical features of the model are based on the local equivalence between a perfectly plastic behavior response to monotonic loading and an appropriate fictitious non-linear poroelastic behavior. The non-linear behavior was considered through a secant shear modulus  $G$  which evolves with the level of strains. The model is briefly described in the sequel considering a null initial stress and pore pressure (*i.e.*,  $\sigma_0 = p_0 = 0$ ). The extension to non-zero initial state and details of the model can be found in the original work, Dienstmann *et al.* (2017).

To capture some of the non-linear features of the soil behavior, the shear modulus  $G$  was defined by a dependence law of the form  $G = G(\underline{\underline{\varepsilon}}_d, \underline{\underline{\varepsilon}}_v, p)$ , where  $\underline{\underline{\varepsilon}}_d = \sqrt{(\underline{\underline{\varepsilon}} - \frac{1}{3} \text{tr} \underline{\underline{\varepsilon}}) : (\underline{\underline{\varepsilon}} - \frac{1}{3} \text{tr} \underline{\underline{\varepsilon}})}$  and  $\underline{\underline{\varepsilon}}_v = \text{tr} \underline{\underline{\varepsilon}}$  refer respectively to equivalent deviatoric strain and volumetric strain, and  $p$  is the pore pressure.

Assuming a Drucker-Prager yield condition, the plasticity of the soil is described by

$$F(\underline{\underline{\sigma}}') = \sigma_d + T(\sigma'_m - h) \leq 0 \quad (2)$$

where  $\underline{\underline{\sigma}}' = \underline{\underline{\sigma}} + p \underline{\underline{1}}$  is the Terzaghi effective stress,  $\sigma_d = \sqrt{(\underline{\underline{\sigma}} - \frac{1}{3} \text{tr} \underline{\underline{\sigma}}) : (\underline{\underline{\sigma}} - \frac{1}{3} \text{tr} \underline{\underline{\sigma}})}$  is the equivalent deviatoric stress and  $\sigma'_m = \frac{1}{3} \text{tr} \underline{\underline{\sigma}}' = \sigma_m + p$  is the mean Terzaghi effective stress. The previous relations are defined considering a sign convention of positive stress values for tension and negative stress values for compression. Additionally, according to the classical poromechanics formulation, the pore pressure (or the fluid pressure) is defined as:  $p = u_h + u$ , where  $u_h$  refers to the hydrostatic pore pressure and  $u$  to the excess pore pressure. Parameters  $h$  and  $T$  respectively characterize the tensile strength and the friction coefficient of the Drucker-Prager yield condition, and can be derived from Mohr Coulomb parameters,  $c$  - cohesion and  $\phi$  - friction angle.

Considering that the stress associated with the secant behavior

$$\underline{\underline{\sigma}} = \underline{\underline{\sigma}}_0 + (K - \frac{2}{3}G) \text{tr} \underline{\underline{\varepsilon}} \underline{\underline{1}} + 2G \underline{\underline{\varepsilon}} - b \Delta p \underline{\underline{1}} \quad (3)$$

meets asymptotically the above yield condition (2), that is

$$\lim_{\varepsilon_d \rightarrow \infty} F(\underline{\underline{\sigma}}' = \underline{\underline{\sigma}} + p\underline{\underline{1}}) = 0 \quad (4)$$

where  $\varepsilon_{ref} \ll 1$  is a reference strain that physically represents the order of magnitude of the shear strain mobilized at yielding.

In Eq. 3  $b$  is the Biot coefficient,  $\Delta p$  defines the pore pressure variation,  $G$  is the shear modulus and  $K$  is the bulk modulus.

Adopting a constant value for the bulk modulus  $K$ , and considering an approach similar to that developed in Lemarchand *et al.* (2002) and Maghous *et al.* (2009), a simple way to meet the above condition consists in considering the following law [Maghous *et al.* (2009)].

$$G(\varepsilon_d, \varepsilon_v, p) = \frac{1}{2} [T(h - K\varepsilon_v - (1-b)p)] \times \frac{1}{1 + \frac{\varepsilon_d}{\varepsilon_{ref}}} \quad (5)$$

Figure 2 provides a non-linear poroelastic representation of the Drucker-Prager behavior as defined by Eq. 5.

Coming back to the expansion problem, the strains and pore pressures mobilized must satisfy the momentum balance equation ( $\text{div } \Delta \underline{\underline{\sigma}} = 0$ ), which should be complemented by the mechanical boundary conditions related to the displacement  $\xi$ :

$$\begin{cases} \xi = \alpha R \underline{e}_r & \text{at } r = R \\ \xi = 0 & \text{at } r = a > R \end{cases} \quad \forall t > 0 \quad (6)$$

The first condition in Eq. 6 implies that a radial displacement  $\alpha R$  is imposed at the cylinder wall, while the second condition indicates that the displacement induced by the expansion of the rigid cylinder is null at a distance  $a > R$ .

Due to problem symmetry, the displacement distribution can be sought in the form

$$\underline{\xi} = f(r) \underline{e}_r \quad (7)$$

The corresponding strain tensor reads

$$\underline{\underline{\varepsilon}} = \varepsilon_{rr} \underline{e}_r \otimes \underline{e}_r + \varepsilon_{\theta\theta} \underline{e}_\theta \otimes \underline{e}_\theta \quad (8)$$

with  $\varepsilon_{rr} = f'(r)$ ; and  $\varepsilon_{\theta\theta} = f \frac{(r)}{r}$

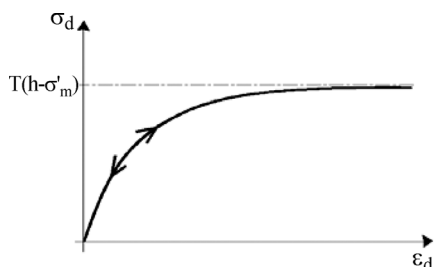


**Figure 2** - Representation of the non-linear elastic behavior associated with a Drucker-Prager yield condition.

and the stress increment associated with poroelastic law is:

$$\begin{aligned} \Delta \underline{\underline{\sigma}} = & \lambda \left( f'(r) + \frac{f(r)}{r} \right) \underline{\underline{1}} \\ & + 2G \left( f'(r) \underline{e}_r \otimes \underline{e}_r + \frac{f(r)}{r} \underline{e}_\theta \otimes \underline{e}_\theta \right) - b \Delta p \underline{\underline{1}} \end{aligned} \quad (9)$$

The displacement function  $f(r)$  is obtained by the integration of the local equilibrium equation in projection following the radial direction, observing that

$$\begin{cases} \Delta \sigma_{rr} = K \left( f'(r) + \frac{f(r)}{r} \right) + \frac{2}{3} G \left( 2f'(r) + \frac{f(r)}{r} \right) - b \Delta p \\ \Delta \sigma_{\theta\theta} = K \left( f'(r) + \frac{f(r)}{r} \right) + \frac{2}{3} G \left( 2 \frac{f(r)}{r} - f'(r) \right) - b \Delta p \end{cases} \quad (10)$$

Equation 9 can be conveniently written as

$$\begin{aligned} \frac{d}{dr} \left[ K \left( f'(r) + \frac{f(r)}{r} \right) + \frac{2}{3} G \left( 2f'(r) - \frac{f(r)}{r} \right) - b \Delta p \right] \\ + \frac{2}{r} G \left( f'(r) - \frac{f(r)}{r} \right) = 0 \end{aligned} \quad (11)$$

with  $G = G(\varepsilon_d, \varepsilon_v, p) = G(f, p)$  since

$$\begin{aligned} \varepsilon_d = & \sqrt{\frac{2}{3}} \sqrt{f'(r)^2 + \frac{f(r)^2}{r^2} - f'(r) \frac{f(r)}{r}}; \\ \varepsilon_v = & f'(r) + \frac{f(r)}{r} \end{aligned} \quad (12)$$

Equation 11 is a differential equation that couples the skeleton displacements (function  $f(r)$ ) and pore pressure ( $p$ ). The second equation for consolidation around the expanding cylinder is deduced from the solution to the fluid flow problem.

## 2.2. Pore fluid problem

To obtain the pore flow component of the problem, it is used the second poroelastic state equation

$$\Delta \Phi = b \text{tr} \underline{\underline{\varepsilon}} + \frac{1}{M} \Delta p \quad (13)$$

which relates the Lagrangian porosity change  $\Delta \Phi = \Phi - \Phi_0$  to the skeleton volumetric strain and pore pressure change Eq. 13 presents the Biot parameter  $b$  and the Biot Modulus  $M$ , and must be combined with the fluid mass balance and a flow law (Darcy law).

Neglecting the variations of fluid density, the fluid mass balance in infinitesimal skeleton strains is written as:

$$\frac{\partial \Phi}{\partial t} + \text{div} \underline{q} = 0 \quad (14)$$

where  $q$  is the filtration vector. The latter is connected to the excess pore pressure  $u$  through Darcy's law

$$\underline{q} = -\underline{k} \cdot \nabla u \quad (15)$$

where  $\underline{k}$  denotes the permeability tensor. Considering an isotropic medium,  $\underline{k} = k\underline{1}$  where  $k$  is the permeability and  $\underline{1}$  is the identity matrix.

Reporting both the second poroelastic state Eq. 13 and Darcy's law (Eq. 15) into the fluid mass balance (Eq. 14) yields:

$$b \frac{\partial \text{tr} \underline{\varepsilon}}{\partial t} + \frac{1}{M} \frac{\partial \Delta p}{\partial t} = k \nabla^2 u \quad (16)$$

where  $\nabla^2$  stands for the Laplacian operator.

From the classical reasoning for a non-linear poroelastic medium, the following generalized Navier equation can be derived (assuming irrotational displacement field)

$$\left[ K + \frac{4}{3} G \right] \nabla \text{tr} \underline{\varepsilon} + 2 \nabla G \cdot \left( \underline{\varepsilon} - \frac{1}{3} \text{tr} \underline{\varepsilon} \right) = b \nabla (\Delta p) \quad (17)$$

Equation 17, emphasizes the strong coupling between skeleton strains and pore pressure. In classical formulations, the pore pressure is only affected by the volumetric part  $\varepsilon_v$  of skeleton strains, considerably simplifying the pore fluid flow solution. However, in the adopted solution the pore pressure is also explicitly related to the deviatoric part  $\varepsilon_d$  of skeleton strains through the shear modulus  $G(\varepsilon_d, \varepsilon_v, p)$ . In this case, determination of pore pressure distribution and displacement field (function  $r \rightarrow f(r)$ ) requires solving the coupled system defined by the set of partial differential Eqs. 11, 16 and 17.

A time incremental procedure has been implemented in Dienstmann *et al.* (2017) to provide semi-analytical solutions to this problem. The basic idea consists in approximating, during the time interval  $t_n \leq t \leq t_{n+1}$ , the shear modulus  $G$  of the medium by an equivalent mean value  $G \approx G_{eq}$  that is constant in time and space. Accordingly, Eq. 17 reduces to

$$\left[ K + \frac{4}{3} G_{eq} \right] \nabla \text{tr} \underline{\varepsilon} = b \nabla (\Delta p) \quad (18)$$

which can be integrated to relate  $\text{tr} \underline{\varepsilon}$  to  $\Delta p$ .

Observing that when the hydrostatic pore pressure  $u_n$  turns to be constant  $\frac{\partial \Delta p}{\partial t} = \frac{\partial u}{\partial t}$  and following (Eq. 2) the uncoupled pressure diffusion equation can be obtained:

$$\frac{\partial u}{\partial t} = c_f \nabla^2 u \quad \text{with} \quad c_u = kM \frac{K + \frac{4}{3} G_{eq}}{Mb^2 + K + \frac{4}{3} G_{eq}} \quad (19)$$

where  $c_f$  is the fluid diffusivity coefficient. An average shear modulus is therefore introduced for each time interval  $[t_n, t_{n+1}]$  as:

$$G_{eq} = \frac{1}{a - R} \int_R^a G(\varepsilon_d(t_n), \varepsilon_v(t_n), p(t_n)) dr \quad (20)$$

The approximation  $G \approx G_{eq}$  is introduced for the diffusion equation only, while the non-linear form of the shear modulus is kept within the equilibrium equation.

The diffusion Eq. 19 together with the boundary and initial conditions (Eqs. 21-23) defines the solution of the hydraulic problem, which is characterized as a distribution of excess pore pressure over the time interval  $[t_n, t_{n+1}]$ .

$$\frac{\partial u}{\partial r} = 0 \quad \text{at} \quad r = R \quad \forall t \in [t_n, t_{n+1}] \quad (21)$$

$$u = 0 \quad \text{at} \quad r = a \quad \forall t \in [t_n, t_{n+1}] \quad (22)$$

$$u = u(r, t_n) \quad \text{at} \quad t = t_n \quad \forall r \in [R, a] \quad (23)$$

Equations 21 to 23 refer to the impermeability condition of the expanding cylinder, the negligible influence of pore pressure condition at the radius of influence, and the initial pore pressure state at time  $t_n$ , respectively. An initial pore pressure  $u_0 = u_0(r)$  at  $t = 0$  is intended to account for the excess pore pressure produced by the rigid cylinder insertion. This point will be discussed in the next section.

The general solution to the boundary value problem mentioned above is:

$$u = \sum_{i=1}^{\infty} C_i^* [\omega_i Y_0(\alpha_i r) - J_0(\alpha_i r)] e^{-c_f \alpha_i^2 (t - t_n)} \quad (24)$$

where

$$C_i^* = \frac{\int_R^a u(r, t_n) [\omega_i Y_0(\alpha r) - J_0(\alpha r)] r dr}{\int_R^a [\omega_i Y_0(\alpha r) - J_0(\alpha r)]^2 r dr} \quad (25)$$

Functions  $J_0$  and  $Y_0$  are zero-order Bessel functions of the first and second kind respectively. Scalar  $\alpha_i$  is the  $i$ -th root of the following algebraic equation with respect to variable  $x$

$$Y_1(xR)J_0(xa) - J_1(xR)Y_0(xa) = 0 \quad (26)$$

where  $J_1$  and  $Y_1$  are first-order Bessel functions referring respectively to the first and second kind. Scalar  $\omega_i$  is computed from  $\alpha_i$  as

$$\omega_i = -\frac{Y_1(\alpha_i R)}{J_1(\alpha_i R)} \quad (27)$$

From Eqs. 24 to 27 the excess pore pressure  $u$  is computed, letting the pore pressure increment be determined as  $\Delta p = u - u_0$ . The final expression of pore pressure distribution  $\Delta p$  is substituted into Eq. 11, which simplifies to be an ordinary differential equation governing the displacement function  $f(r)$  along time interval  $[t_n, t_{n+1}]$ . The latter function and the corresponding strain and stress distribution are de-

terminated using an iterative numerical procedure, which can be found in the original work, Dienstmann *et al.* (2017).

### 2.3. Initial excess pore pressure distribution

The solution developed in Dienstmann *et al.* (2017) is generalized to consider initial states of stress and pore pressure different from zero, as would be expected for problems such as pile installation and in situ tests. Expressions for initial excess of pore pressure  $u_0$  (or equivalently  $p_0$ ) generated by insertion of a rigid cylinder within the medium can be found in the literature (*e.g.* Morris & Williams, 2000; Randolph & Wroth, 1979; Poulos & Davis, 1980) and have been based on laboratory or field data. Most of collected data have shown that the pore pressure gradients are essentially radial, and that the maximum excess pore pressure  $u_{0,max}$  generated by the installation process is observed close to the cylinder (*i.e.*, at  $r = R$ ). The magnitude of the excess pore pressure appears to decrease with the radius  $r$  measured from the cylinder axis, and becomes negligibly small at a certain distance  $r = a$ , referred to as the initial radius of influence. Combining hyperbolic and logarithmic distributions, a new expression has been proposed in Dienstmann *et al.* (2017). It extends classical expressions to account for the flow restriction at the cylinder wall:

$$u_0(r) = u_{0,max} \frac{F(r)}{F(R)} \quad \text{with} \quad F(r) = 1 - \frac{a}{r} + \frac{a}{R} \ln \frac{a}{r} \quad (28)$$

for  $R \leq r \leq a$

where  $u_{0,max}$  refers to the maximum value of pore pressure generated by cylinder insertion.

Regarding  $u_{0,max}$  correlating a pile insertion into the soil with a cavity expansion problem, typical solutions derived in this context (*e.g.* Vesic, 1972; Randolph & Wroth, 1979) suggest that  $u_{0,max}$  can be evaluated from the stress paths developed in undrained triaxial tests carried out until the ultimate state (undrained strength) is attained. The excess pore pressure is thus deduced from the variation in mean and shear stresses, leading to the following estimate for normally consolidated soils (Vesic, 1972):

$$u_{0,max} = \frac{P_{c0}}{2} (1 + M_{cs}) \quad (29)$$

where  $P_{c0}$  denotes a reference initial consolidation pressure, and  $M_{cs}$  is the slope of the critical state line. It should be emphasized that expression (29) implicitly assumes that cylinder installation is fast, the elapsed time between installation and expansion is sufficiently short for pore pressures to not dissipate, thus justifying the assumption of undrained hydromechanical evolution of soil.

### 2.4. Cylindrical cavity expansion to cone resistance estimation

The cylindrical cavity expansion solution provides expressions for stress ( $\underline{\sigma}$ ), strain ( $\underline{\epsilon}$ ) and pore pressure ( $p$ )

fields. Seeking a direct comparison to in situ test as cone penetration some considerations must be drawn. In this context, the calculated cavity expansion limit pressures ( $\sigma_c$  at the cylinder wall) have been converted to cone resistance ( $q_c$ ) using an approach similar to that proposed by Rohani & Baladi (1981), and used by Silva (2005) and LeBlanc & Randolph (2008). In the approach the cone tip resistance is estimated from the vertical projections of all forces acting on the cone. The expression of the vertical resistive force  $F_z$  can be calculated from the integration of stresses over the cone tip length  $L$  (see Fig. 3):

$$F_z = \int_0^L [(\sigma'_n + u) \sin \beta + \tau \cos \beta] 2\pi r dl \quad (30)$$

Expression 30 can directly be used to determine the cone tip resistance

$$q_c = \frac{F_z}{S_c} \quad (31)$$

where  $S_c = \pi L^2 \tan^2 \beta$  denotes the piezocone cross-section area. In the context of cylindrical cavity expansion, it is more convenient to express  $q_c$  in terms of the radial stresses using  $\tau = \sigma'_n \tan \delta$  together with the equations expressing locally the horizontal and vertical force equilibrium at any point along the cone tip:

$$q_c = \sigma'_r \frac{1 + \frac{\tan \delta}{\tan \beta}}{1 - \frac{\tan \delta}{\tan \beta}} + u \quad (32)$$

where  $\beta$  is half of the angle of the cone tip (usual value  $60^\circ/2 = 30^\circ$ ),  $\delta$  is the interface friction taken as the soil friction angle  $\phi'$ ,  $\sigma'_r$  and  $u$  are respectively the radial stress and pore pressure at the expanding cylinder radius.

Figure 3 describes the idealization of stresses acting on a small portion ( $dl$ ) of the cone tip length ( $L$ ).

### 3. Gold Tailings

The present paper describes the use of a cylindrical cavity solution to assist the drainage behavior interpreta-

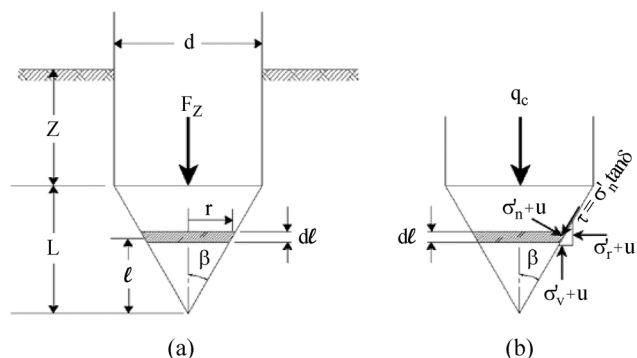


**Figure 3** - Schematic illustration of stresses acting on the cone (a) general view (b) stresses definition.

tion of experimental data from a gold TSF located in north-east Brazil (Fig. 4). The Fazenda Brasileiro Mine includes a producing gold mine and approximately 197,000 hectares of adjacent exploration properties. The site is being a subject of study for the past two decades (Bedin *et al.*, 2012, Schnaid *et al.*, 2013, Schnaid *et al.*, 2016, Dienstmann *et al.*, 2018), with a research project including site evaluation, field and laboratory tests.

A general view of Fazenda Brasileiro Mine is presented in Fig. 4, in which locations for the site investigations conducted in 2006, 2013, and 2016 are displayed. A total of eleven (11) different islands of investigation were defined, with sample collecting, and in situ tests as piezocone (conventional CPTu, and with seismic measurements SCPTu), seismic dilatometer (SDMT) and vane tests. Previous studies have shown that the material disposed is predominantly silty sand (Fig. 5) with an average in situ solids content (ratio of weights obtained before and after a drying process) of about 30%, in situ water content of 35% (ratio between water and solid weights), low to non-plastic and with high specific gravity ( $2.89 < G_s < 3.2 \text{ g/cm}^3$ ). In that respect, data referring to the gold tailings are reported in Table 1. Triaxial tests described in Bedin *et al.* (2012) and Schnaid *et al.* (2013) allowed the critical state line CSL to be established for tests carried out in compression and extension and sheared under monotonic loading. A highly-nonlinear shape of the CSL under undrained loading was observed indicating that the tailings exhibit severe strain-softening with high compressibility that at low stresses may lead to flow liquefaction.

A typical piezocone profile for tests carried out at the standard 20 mm/s penetration rate is presented in Fig. 6 and includes cone tip resistance  $q_c$ , penetration pore pressure  $u_2$ , pore pressure ratio  $B_q = (u_2 - u_h)/(q_t - \sigma_{v0})$  - where  $u_h$  is the hydrostatic pore pressure,  $q_t$  is the total cone tip resistance and  $\sigma_{v0}$  is the total vertical stress - and soil behavior index  $I_{cRW}$ , according to Robertson and Wride (1998). The soil profile identified by SCPTu and CPTu data, reveals a drained layer near the surface underlain by silty soils (from 3 m to 10 m) with  $I_{cRW}$  (soil behavior type) values typically in the 2.0 to 3.5 range, indicating clay and silt layers where excess pore pressures are relatively high, yielding  $B_q$  (pore pressure ratio) in the 0.3 to 0.6 range. Some thin drained layers were detected at different penetration depths. SCPTu data indicate thin drained layers at 5 m, 6 m and 7 m.

To evaluate the effect of drainage conditions on the piezocone (CPTu) measurements, a series of soundings were performed at the *Fazenda Brasileiro* site with the penetration rates from 0.1 mm/s to 57 mm/s. Results of adjacent (2 m spacing) soundings performed at different penetration rates are presented in Fig. 7, in which values of  $q_c$ ,  $u_2$  and  $B_q$  are plotted against depth. Steady penetration velocity profiles of 20 mm/s and 57 mm/s are compared to one profile carried out at variable penetration rates (labeled “variable”). Considerable excess pore pressure  $\Delta u$  was gen-

**Table 1** - Gold tailings characterization.

Study	Region	Physical characterization			Consolidation		Critical state		Friction angle $\phi'$	
		w (%)	$G_s$ (g/cm <sup>3</sup> )	$e_0$	$\gamma$ (kN/m <sup>3</sup> )	$\lambda$	N	$\Gamma$		$\psi$
Bedin (2010)	PZC01 to PZC05	40.1	3	1.23	18.6	0.048	2.39	2.34	0.045	33
		30	3.15	1.1	20.5	0.058	2.66	2.64	0.05	31
Klahold (2013)	PZC06 to PZC08	38.7 - 40	3 - 3.3	1.25- 1.3	19 - 19.3	0.045	2.44	2.4	0.04	30.5
	Cluster 01 and Cluster 02	32.3 - 37.8	2.85 - 2.86	0.92 - 1.08	18.94 - 19.63	-	-	-	-	-

erated over the entire depth interval in all tests (even for the slowest penetration rate of 0.1 mm/s). The pore pressure is shown to increase with increasing penetration rates, inducing maximum  $B_q$  values in the 0.6 to 0.7 range. There is no appreciable difference in measured values of  $q_c$  and  $u_2$  for tests carried out at 20 mm/s and 57 mm/s, which appears to indicate that tests are essentially undrained for these penetration rates.

For a better comparison with modeling, results of the tailings database were reinterpreted in terms of a normalized resistance  $Q = q_{cnet}/\sigma'_{v0}$  and normalized pore pressure  $U = \Delta u/\sigma'_{v0}$  plotted against a normalized velocity  $V_h$  (Eq. 1). In this analysis  $q_{cnet} = (q_c - \sigma'_{v0})$  and  $\Delta u = (u_2 - u_h)$ . Results are displayed in Fig. 8, from which it is possible to identify a region characterized by normalized velocities  $V_h$  in the range of about 0.01 to 10 where partial drainage appears to occur during cone penetration. The lowest (undrained) penetration resistance ( $Q_{UD} \approx Q_{min}$ ) is of the order of 2.0, while the drained penetration resistance ( $Q_D \approx Q_{max}$ ) is 42.0, yielding a drained to undrained ratio  $Q_D/Q_{UD}$  of about 21, which is consistent with previously reported data from Jaeger *et al.* (2010) and Lehane *et al.* (2009). When comparing results in terms of  $Q$  vs.  $V_h$  and  $U$  vs.  $V_h$  a slightly larger scatter is observed from data on the  $U$  vs.  $V_h$  space, although it is possible to identify that at fully undrained conditions the normalized pore pressure  $\Delta u/\sigma'_{v0}$  ratio is of the order of 2.2, and reduces to zero for drained penetration.

Adjusting curves in Fig. 8 are represented by empirical upper and lower limits, obtained considering a hyperbolic cosine function as suggested by Schnaid (2005):

$$Q = Q_{min} + \left( a + (1-a) \frac{1}{\cosh(bV^c)} \right) \times (Q_{max} - Q_{min}) \quad (33)$$

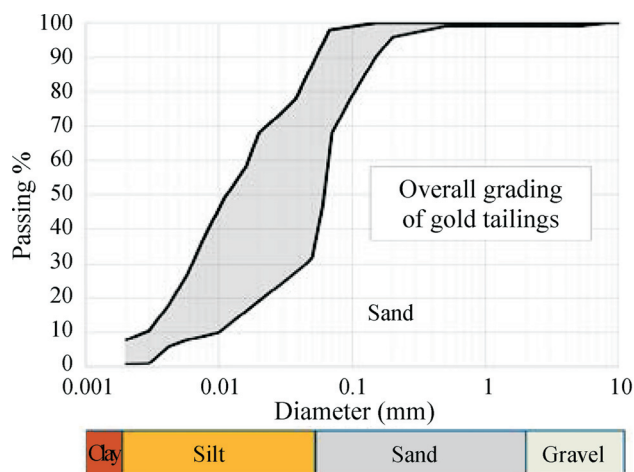


Figure 5 - Fazenda Brasileiro Mine overall grading.

$$\frac{\Delta u}{\sigma'_{v0}} = \frac{\Delta u_{max}}{\sigma'_{v0}} - \left( a + (1-a) \frac{1}{\cosh(bV^c)} \right) \times \left( \frac{\Delta u_{max}}{\sigma'_{v0}} - \frac{\Delta u_{min}}{\sigma'_{v0}} \right) \quad (34)$$

where  $a$ ,  $b$  and  $c$  are fitting parameters, and are shown in Fig. 8. From a practical point of view, parameter  $a$  embodies the difference between the undrained and the drained effective penetration, whereas  $b$  and  $c$  control the rate of change from drained to undrained. These parameters are representative of measured data in the  $Q$  vs.  $V$  space and, as an overall trend, they also cover results plotted in the  $\Delta u$  vs.  $V$  space.

### 3.1. Modelling the gold tailings

To help understand rate effects on cone measurements, properties of gold tailings were analytically mod-

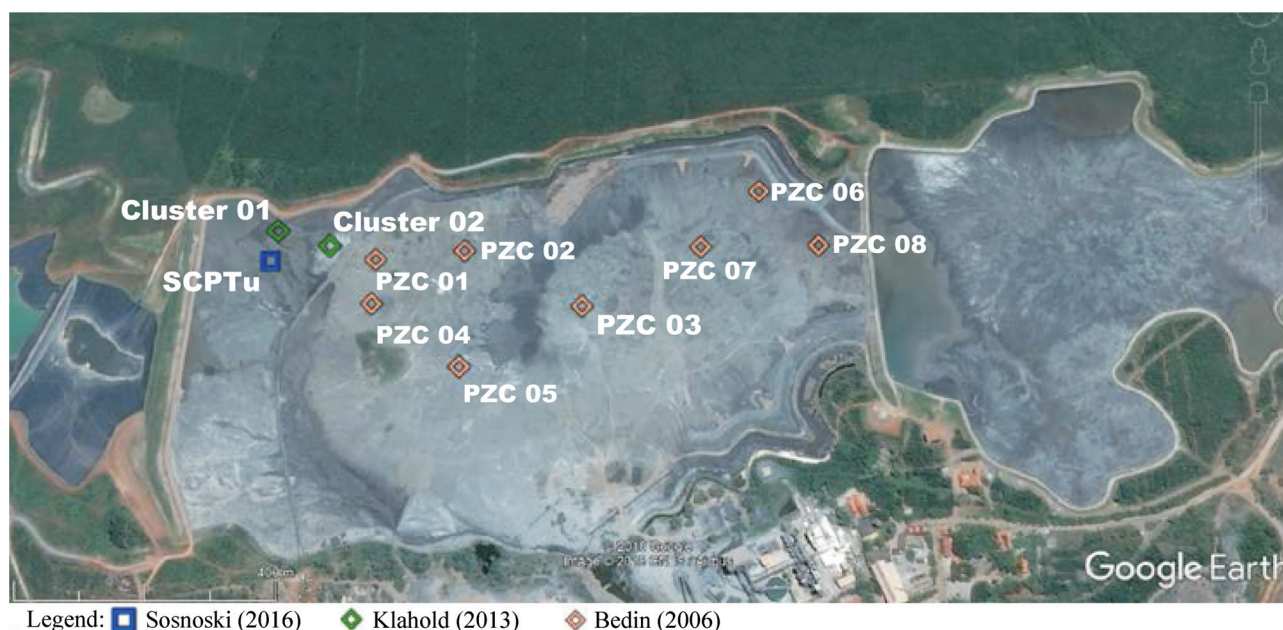


Figure 4 - Fazenda Brasileiro Mine aerial view and site investigation.

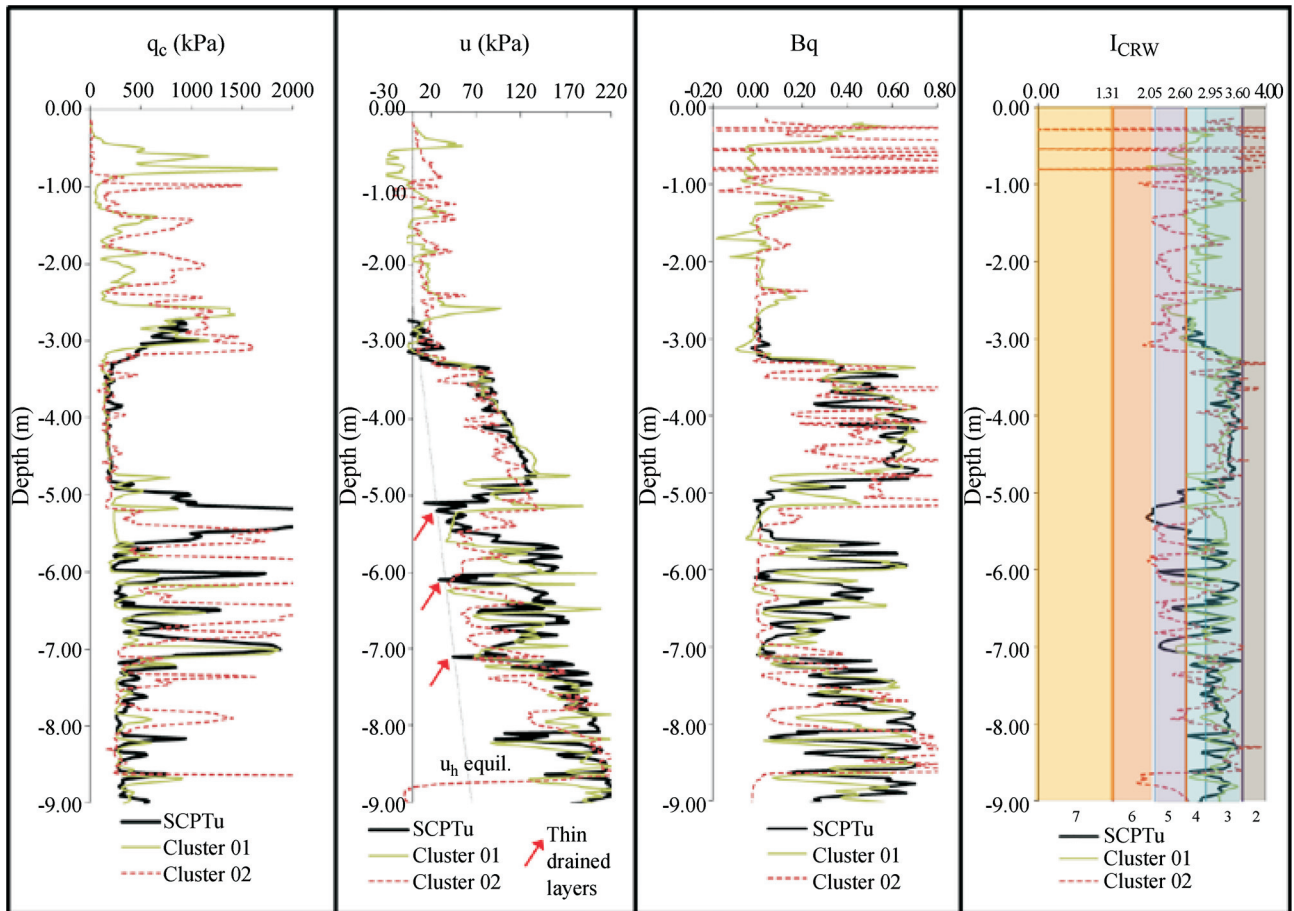


Figure 6 - Typical piezocone profile.

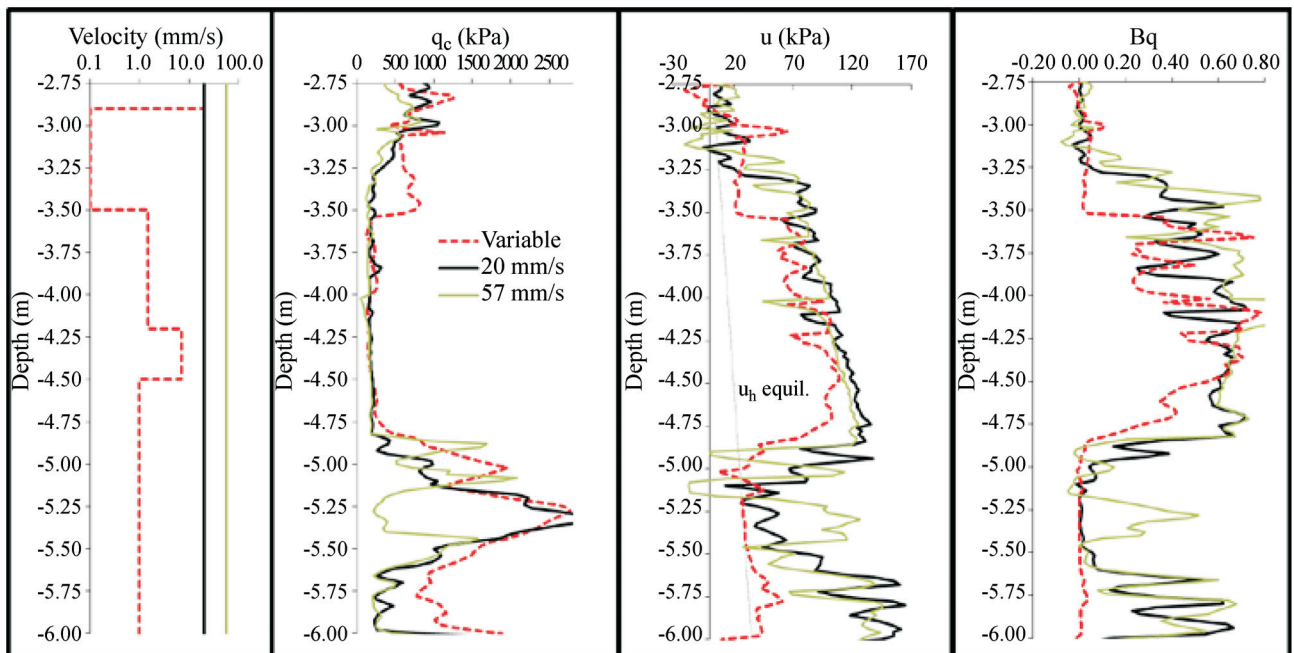


Figure 7 - Values of  $q_c$ ,  $u_2$ , and  $B_q$  measured at different penetration rates.

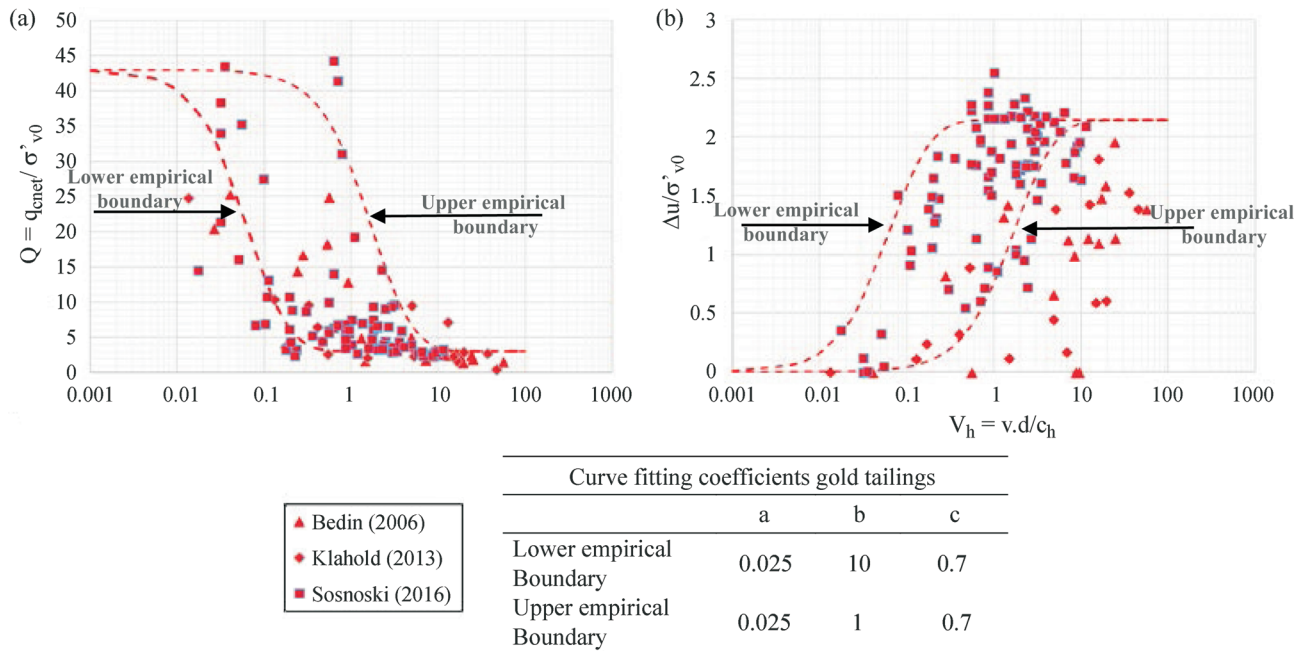


Figure 8 - Rate effects in the (a)  $Q$  vs.  $V_h$  space and (b)  $U$  vs.  $V_h$  space.

eled using the approach developed by Dienstmann *et al.* (2017). Finite Element (FE) results from a cavity expansion analysis in ABAQUS are additionally added to reinforce the applicability of the analytical model. The cavity expansion simulated in Abaqus was defined according to an axisymmetric model, with unit height and infinite extent (classical approach, see Fig. 9). The same initial and boundary conditions used in the analytical model were adopted in the finite element approach. For the constitutive model in the FE analysis, the Drucker Prager combined with linear elasticity was considered. Elements used are 8-node axisymmetric quadrilateral, biquadratic displacement, bilinear pore pressure and reduced integration (Abaqus finite element type: CAX8RP).

Parameters used in the analysis are summarized in Table 2, and were defined by the average values obtained from in situ and laboratory tests. The friction angle  $\phi'$  is  $32^\circ$

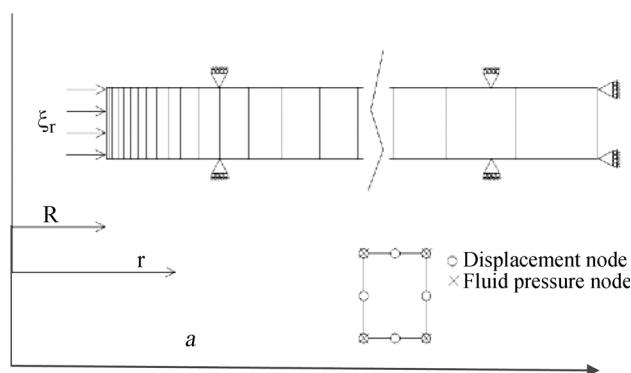


Figure 9 - Finite-element mesh detail (not in to scale).

and the  $h$  and  $T$  parameters from the Drucker Prager criterion are defined according to Mohr Coulomb yield surface condition. The initial field of excess pore pressure  $u_0(r)$  applied in both models is calculated from Eq. 28. The initial stress distribution is an isotropic and uniform (in the plane of analysis) stress field;  $\underline{\underline{\sigma}}_0 = \sigma_0 \underline{\underline{1}}$  is considered along with the subsequent simulation.

To evaluate the influence of the extension zone defined by  $a$ , the radius that defines the extension of the region affected by cylinder installation, two approaches were considered for analysis:

- $a$  as a function of the soil Rigidity Index ( $I_r$ ):  $a = \sqrt{I_r} R$  with  $I_r = 874$  (defined from triaxial results, Bedin *et al.*, 2012), corresponding to a radius of influence of about 30 times the cylinder radius ( $a = 30R$ ).
- and  $a$  defined arbitrarily as  $a = 10R$  to comply with previous studies (Vesic, 1972; Randolph & Wroth, 1979; Osman 2010, Osman & Randolph, 2012).

Applied displacements are limited to produce maximum local strains of 10% to comply with the model small strain assumptions. Although, from a practical engineering perspective, strain levels as high as 10% are often admitted for geotechnical testing interpretation. It is therefore implicitly assumed that results characterized from both the simplified model and the numerical approach are reasonable approximations for cylinder expansion, which would be more appropriately formulated by large strains.

Results in sequence are directly displayed in the normalized velocity space combined to normalized cone tip resistance  $Q/Q_{ref}$  and normalized pore pressure  $\Delta u / \Delta u_{ref}$  where  $Q_{ref}$  is the maximum value of  $Q$  ( $Q_{ref} = Q_{max}$ ) corres-

ponding to the drained penetration, and  $\Delta u_{ref}$  is the maximum value of mobilized pore pressure ( $\Delta u_{ref} = \Delta u_{max}$ ) corresponding to undrained penetration. Field measurements are directly compared to analytical and numerical predictions in Figs. 10 and 11. It is important to highlight that the goal of comparisons is not to data-fit the experimental results or to find the parameter values that most closely match the data. The analysis is performed by predicting results using the set of parameters defined from independent tests, with the aim of developing a proper understanding of the parameters controlling rate effects.

From Fig. 10 it is possible to observe that the predictions are generally able to capture the experimental trends in the  $Q$  vs.  $V_h$  and  $U$  vs.  $V_h$  spaces, with some discrepancies. Both models, analytical and numerical, capture the transition from drained to partially drained to undrained regimes, but underestimate the  $Q_D/Q_{UD}$  measured ratio of 21. Numerical and analytical prediction in the space  $U$  vs.  $V_h$  are shifted to the left with respect to pore pressure measurements, producing lower  $V_h$  for the onset of drained conditions. Typical values for the transition from undrained to partially drained behavior are in the range of 1 to 10, while predictions are underestimated by at least one log-cycle.

To assess the influence of the size of the deformable zone, in Fig. 11 results from predictions using  $a = 10R$  are displayed. It can be observed that a reduction of the influence zone has a significant effect on the variation of pore pressure with time, producing acceptable comparisons of measured and predicted rate effects.

#### 4. Conclusions

Accurate prediction and assessment of drainage conditions during geotechnical testing is a challenging issue for relevant interpretation of experimental data. For this purpose, theoretical poromechanical formulations may reveal useful in the understanding of different geotechnical problems. Cavity-expansion solutions have notably proven successful in providing valuable support for the evaluation of bearing capacity of piles or the interpretation of cone and pressuremeter tests. In this context, analytical solutions have been derived for the problem of cylinder expansion within a non-linear poroelastic medium. The fully coupled approach has been then applied to the investigation of rate effects that arise during piezocone tests performed in a gold tailing deposit. Field data are directly compared to analytical predictions as well as to finite element solutions in terms of normalized velocity vs. normalized cone tip re-

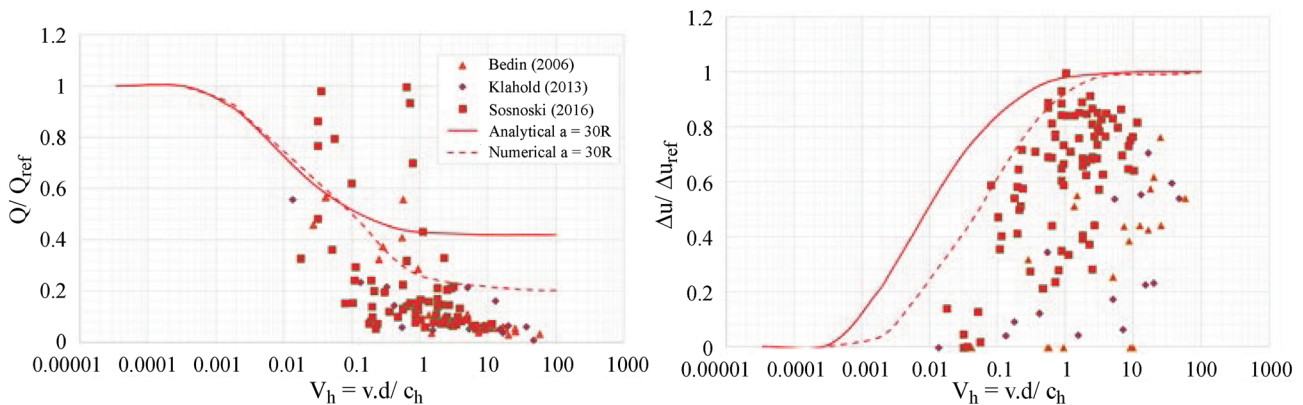


**Figure 10** - Comparisons between analytical and numerical predictions to field data in tailings for  $a/R = 30$ .

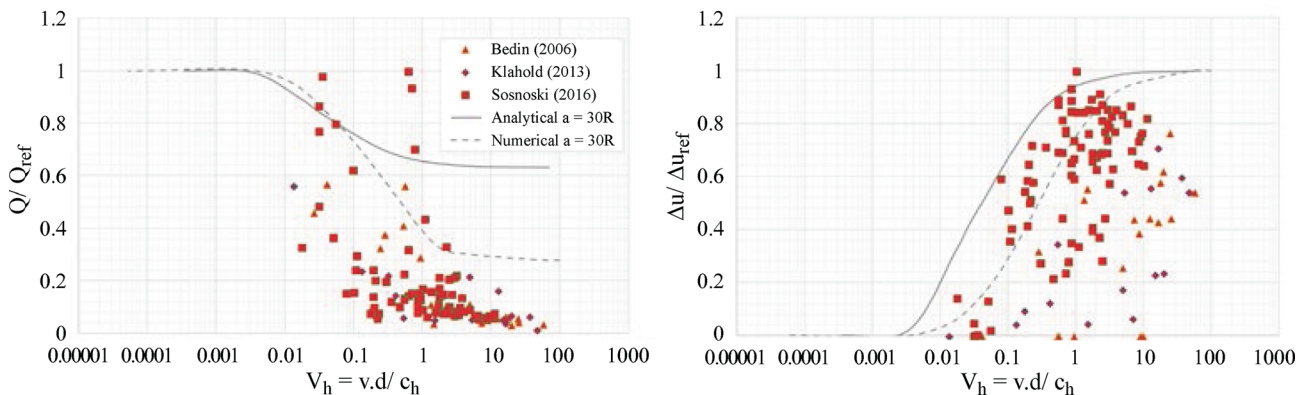


**Figure 11** - Comparisons between analytical and numerical predictions to field data in tailings for  $a/R = 10$ .

**Table 2** - Gold Tailings constitutive parameters.

Constitutive parameters	
$p_{c0}^*$	100 kPa
$\sigma_0'$	-50 kPa
$\phi; M_c^{**}; T^{***}$	32°; 0.98; 0.98
$u_{0\max} = p_{c0}(1 + M_c)/2$	100 kPa
$\sigma_0 = \sigma_0' - p$	-150 kPa
$\gamma_w$	10 kN/m <sup>3</sup>
$k$	1.00E-08 m/s
$K$	5814 kPa
$\epsilon_{ref}$	0.01
$b$	0.999
$M$	2.3 GPa
$R$	2.5 cm
$a$	10R 30R cm

\*Reference consolidation pressure used to define the maximum value of excess pore pressure  $u_{0\max}$ .

\*\* $M_c$  is the slope of the critical state line obtained directly from  $\phi$ .

\*\*\* $T$  is the frictional coefficient of the Drucker Prager model obtained directly from  $\phi$ .

sistance  $Q/Q_{ref}$  and normalized pore pressure  $\Delta u/\Delta u_{ref}$ . Although the ratio of the drained to undrained resistance  $Q_d/Q_{vd}$  is underestimated in both models, the predictions capture the experimental trends in the  $Q$  vs.  $V_h$  and  $U$  vs.  $V_h$  spaces, providing relevant estimates for the transition velocity from drained to partially drained to undrained regimes. It was observed that partially drained behavior occurs generally at normalized velocities  $V_h$  within the range of 0.01 to 10, which is in close agreement with values reported from experimental testing data.

## Acknowledgments

The authors gratefully appreciated the financial support provided by the Brazilian Research Council CNPq. We are particularly grateful to YAMANA for the permission to assess their operational facilities and to GEOFORMA for the collaboration during the field tests.

## References

- Abaqus, Version 6.9 [Computer software]. Simulia Corp., Providence, RI.
- Baligh, M.M. (1985). Strain path method. Journal of Soil Mechanics and Foundation engineering Division, ASCE, 111(GT9):1108-1136.
- Bedin, J. (2006). Interpretation of Piezocone Test in Bauxite Residues. Dissertation, Universidade Federal do Rio Grande do Sul, Porto Alegre, Brazil, 150 p. (in Portuguese).
- Bedin, J. (2010). Study of the Geomechanical Behavior of Tailings. PhD Thesis, Universidade Federal do Rio Grande do Sul, Porto Alegre, Brazil, 205 p. (in Portuguese).
- Bedin, J.; Schnaid, F.; Fonseca, A.J.P.V. & Costa Filho, L.M. (2012). Gold tailings liquefaction under critical state soil mechanics. Geotechnique, 62:263-267.
- Blight, G.E. (1968). A note on field vane testing of silty soils. Canadian Geotechnical Journal, 5(3):142-149.
- Burns, S.E. & Mayne, P.W. (2002). Analytical cavity expansion - Critical state model for dissipation in fine-grained soils. Soils and Foundations, 42(2):131-137.
- Cao, L.F.; Teh, C.I. & Chang, M.F. (2001). Undrained cavity expansion in modified Cam clay. I: Theoretical analysis. Geotechnique, 51(4):323-334.
- Carter, J.P.; Randolph, M.F. & Wroth, C.P. (1979). Stress and pore pressure changes in clay during and after the expansion of a cylindrical cavity. International Journal for Analytical and Numerical Methods in Geomechanics, 3(4):305-22.
- Chang, M.F.; Cao, L.F. & Teh, C.I. (2001). Undrained cavity expansion in modified Cam clay II: Application to the interpretation of cone penetration tests. Geotechnique, 51(4):331-346.
- Chung, S.F.; Randolph, M.F. & Schneider, J.A. (2006). Effect of penetration rate on penetrometer resistance in clay. Journal of Geotechnical and Geoenvironmental Engineering, 132(9):1188-1196.
- Collins, I.F.; Pender, M.J. & WANG, Y. (1992). Cavity expansion in sands under drained loading conditions. International Journal for Numerical and Analytical Methods in Geomechanics, 1992(16):3-23.
- Collins, I.F. & Stimpson, J.R. (1994). Similarity solutions for drained and undrained cavity expansions in soils. Geotechnique, 44(1):21-34.
- Davies, M.P. & Martin, T.E. (2000). Tailings and Mine Waste '00. Proc. 7th International Conference on Tailings and Mine Waste '00, Fort Collins, Brookfield, Rotterdam, pp. 3-15.
- DeJong, J.T.; Jaeger, R.A.; Boulanger, R.W.; Randolph, M. & Wahl, D.A.J. (2013). Variable penetration rate cone testing for characterization of intermediate soils. Proc. 4th International Conference on Site Characterization. CRC Press, London, v. 1, pp. 25-42.
- Dienstmann, G.; Maghous, S. & Schnaid, F. (2017). Theoretical analysis and finite element simulation for non-linear poroelastic behavior of cylinder expansion in infinite media under transient pore-fluid flow conditions. International Journal of Geomechanics, 17(7):04017001.
- Dienstmann, G.; Schnaid, F.; Maghous, S. & DeJong, J. (2018). Piezocone penetration rate effects in transient gold tailings. Journal of Geotechnical and Geoenvironmental Engineering, 144(2):04017116.
- Fahey, M.; Newson, T.A. & Fujiyasu, Y. (2002). Engineering with tailings. Proc. 4th International Congress

- on Environmental Geotechnics, Rio de Janeiro, Brazil. Balkema, Netherlands, v. 2, p. 947-973.
- Gibson, R.E.; & Anderson, W.F. (1961). In situ measurement of soil properties with the pressuremeter. *Civil Engineering and Public Works Review*, 56(658):615-618.
- House, A.R.; Oliveira, J.R.M.S. & Randolph, M.F. (2001). Evaluating the coefficient of consolidation using penetration tests. *International Journal of Physical Modelling in Geotechnics*, 1(3):17-25.
- Jaeger, R.A.; DeJong, J.T.; Boulanger, R.W.; Low, H.E. & Randolph, M.F. (2010). Variable penetration rate CPT in an intermediate soil. *Proc. International Symposium of Cone Penetration Testing*, Huntington Beach. Omnipress, Madison, v. 2, p. 527-534.
- Jaeger, R.A. (2012). Numerical and Experimental Study on Cone Penetration in Sands and Intermediate Soils. Ph.D. Thesis, Univ. of California, Davis.
- Jamiolkowski, M.; Lo Presti., D.C.F. & Manassero, M. (2003). Evaluation of relative density in shear strength of sands from cone penetration tests (CPT) and flat dilatometer (DMT). *Soil Behaviour and Soft Ground Construction*, ASCE, 119:201-238.
- Jang, I.S.; Chung, C.K.; Kim, M.M. & Cho, S.M. (2003). Numerical assessment on the consolidation characteristics of clays from strain holding, self-boring pressuremeter test. *Computers and Geotechnics*, 30(2):121-140.
- Klahold, P.A. (2013). Interpretation of Field Tests on Soils with Intermediate Permeability. M.Sc. Thesis, Universidade Federal do Rio Grande do Sul, Porto Alegre, Brazil, 105 p. (in Portuguese).
- LeBlanc, C. & Randolph, M.F. (2008). Interpretation of piezocones in silt, using cavity expansion and critical state methods, *Proc. 12th International Conference of International Association for Computer Methods and Advances in Geomechanics*, Goa, India, (IACMAG), Balkema, Lisse, v. 2, p. 822-829.
- Lehane, B.M.; O'Loughlin, C.D.; Gaudin, C. & Randolph, M.F. (2009). Rate effects on penetrometer resistance in kaolin. *Geotechnique*, 59(1):41-52.
- Lemarchand, E.; Ulm, F.J. & Dormieux, L. (2002). The effect of inclusions on the friction coefficient of highly-filled composite materials. *Journal of Engineering Mechanics*, 128(8):876-884.
- Maghous, S.; Dormieux, L. & Barthelemy, J. (2009). Micromechanical approach to the strength properties of frictional geomaterials. *European Journal of Mechanics A/Solids*, 28(1):179-188.
- Martin, T.E. & McRoberts, E.C. (1999). Tailings and mine waste. *Proc. 6th International Conference on Tailings and Mine Waste '99*, Fort Collins, Colorado, Balkema, Netherlands, p. 287-302.
- Morris, P.H. & Williams, D.J. (2000). A revision of Blight's model of field vane testing. *Canadian Geotechnical Journal*, 37(5):1089-1098.
- Osman, A. (2010). Comparison between coupled and uncoupled consolidation analysis of a rigid sphere in a porous elastic infinite space. *Journal of Engineering Mechanics*, 136(8):1059-1064.
- Osman, A.S. & Randolph (2012). Analytical solution for the consolidation around a laterally loaded pile. *International Journal of Geomechanics*, 12(3):199-208.
- Poulos, H.G. & Davis, E. H. (1980). *Pile Foundations Analysis and Design*. John Wiley and Sons, Inc., New York.
- Randolph, M.F. & Hope, S.N. (2004). Effect of cone velocity on cone resistance and excess pore pressure. *Proc. of the International Symposium on Engineering Practice and Performance of Soft Deposits*, Yodogawa Kogisha Co. Ltd, Osaka, p. 147-152.
- Randolph, M.F. & Wroth, C.P. (1979). An analytical solution for the consolidation around a driven pile. *International Journal for Numerical and Analytical Methods in Geomechanics*, 3(2):217-229.
- Robertson, P.K. & Wride, C.E. (1998) Evaluation cyclic liquefaction potential using the cone penetration test. *Canadian Geotechnical Journal*, 35(3):442-459.
- Rohani, B. & Baladi, G.Y. (1981). Correlation of mobility cone index with fundamental engineering properties of soil. *International Society for Terrain - Vehicle Systems*, 3:959-990.
- Schnaid, F. (2005). Geo-characterization and properties of natural soils by in situ tests. *Proc. International Conference on Soil Mechanics and Geotechnical Engineering*, Osaka, Milpress, Rotterdam, v. 1, p. 3-46.
- Schnaid, F.; Lehane, B.M. & Fahey, M. (2004). In situ test characterization of unusual geomaterials. *Proc. 2nd International Conference on Site Characterization*, Millpress, Rotterdam, Netherlands, v. 1, p. 49-74.
- Schnaid, F.; Bedin, J.; Viana da Fonseca, A.J.P. & de Moura Costa Filho, L. (2013). Stiffness and strength governing the static liquefaction of tailings. *Journal of Geotechnical and Geoenvironmental Engineering*, 139(12):2136-2144.
- Schnaid, F.; Odebrecht, E.; Sosnoski, J. & Robertson, P.K. (2016). Effects of test procedure on flat dilatometer test (DMT) results in intermediate soils. *Canadian Geotechnical Journal*, 53(8):1270-1280.
- Silva, M.F. (2005). Numerical and Physical Models of Rate Effects in Soil Penetration. Ph.D. Thesis, Cambridge University, Cambridge.
- Silva, M.F.; White, D.J. & Bolton, M.D. (2006). An analytical study of the effect of penetration rate on piezocone tests in clays. *International Journal for Analytical and Numerical Methods in Geomechanics*, 30(6):501-527.
- Soderberg, L.O. (1962). Consolidation theory applied to foundation pile time effects. *Geotechnique*, 12(3):217-225.
- Sosnoski, J. (2016). Interpretation of CPTU and DMT Tests in Intermediate Permeability Soils. MSc Thesis,

- Universidade Federal do Rio Grande do Sul, Porto Alegre, Brazil, 137 p. (in Portuguese).
- Suryasentana, S.K. & Lehane, B.M. (2014). Numerical derivation of CPT-based p-y curves for piles in sand. *Geotechnique*, 64(3):186-94.
- Teh, C.I. & Houlsby, G.T. (1991). An analytical study of the cone penetration test in clay. *Geotechnique*, 41(1):17-34.
- Vesic, A.S. (1972). Expansion of cavities in infinite soil mass. *Proc. of the American Society of Civil Engineers (ASCE)*, 98(3):265-290.
- Vick, S.G. (1990). *Planning, Design, and Analysis of Tailings Dams*, 2nd Ed., BiTech, Vancouver, 369 p.
- Wang, H. (2000). *Theory of Linear Poroelasticity with Applications to Geomechanics*. Princeton University Press, Princeton, New Jersey.
- Xu, X. & Lehane, B.M. (2008). Pile and penetrometer end bearing resistance in two-layered soil profiles. *Geotechnique*, 58(3):187-97.
- Yu, H.S. (2000). *Cavity Expansion Methods in Geomechanics*. Kluwer Academic Publishers, Dordrecht, Netherlands.
- Yu, H.S. & Houlsby, G.T. (1991). Finite cavity expansion in dilatant soils: Loading analysis. *Geotechnique*, 41(2):173-183.
- Yu, H.S. & Mitchell, J.K. (1998). Analysis of cone resistance: review of methods. *Journal of Geotechnical and Geoenvironmental Engineering*, 124(2):140-149.
- Zhao, J.; Sheng, D. & Sloan, S. (2007). Cavity expansion of a gradient-dependent solid cylinder. *International Journal of Solids Structures* 44(13):4342-4368.
- K*: Bulk Modulus  
*k*: permeability  
 $\underline{k}$ : permeability tensor  
 $\bar{L}$ : cone tip length  
*M*: Biot modulus  
 $M_{cs}$ : slope of the critical state line  
*p*: pore pressure - hydrostatic plus excess pore pressure  
 $p_0$ : initial pore pressure - hydrostatic plus excess pore pressure  
 $p_{e0}$ : reference initial consolidation pressure  
*Q*: normalized resistance  
 $Q_D$ : drained normalized resistance  
 $Q_{ref}$ : reference normalized resistance  
 $Q_{max}$ : maximum normalized resistance  
 $Q_{min}$ : minimum normalized resistance  
 $Q_{UD}$ : undrained normalized resistance  
 $\underline{q}$ : filtration vector  
 $\bar{q}_c$ : cone tip resistance  
 $q_{cnet}$ : cone tip net resistance  
 $q_t$ : total cone tip resistance  
*r*: radial distance  
*R*: cylinder radius  
 SCPTu - seismic piezocone test  
 $s_c$ : piezocone cross-section area  
 TSF: Tailings Storage Facilities  
*T*: Drucker Prager friction coefficient  
*t*: time of analysis  
 $t_n$ : time of analysis  
 $t_{n+1}$ : time of analysis  
*U*: degree of drainage  
*u*: excess pore pressure  
 $u_0$ : initial excess pore pressure  
 $u_{0,max}$ : maximum initial excess pore pressure  
 $u_2$ : penetration pore pressure (position 2)  
 $u_{ref}$ : reference penetration pore pressure  
 $u_{max}$ : maximum penetration pore pressure  
 $u_{min}$ : minimum penetration pore pressure  
 $u_h$ : hydrostatic pore pressure  
*w*: water content  
 $V_h$ : horizontal normalized penetration velocity  
*v*: loading rate  
 $Y_0$ : zero-order Bessel functions of the second kind  
 $Y_1$ : first-order Bessel functions of the second kind  
 $\alpha$ : radial displacement ratio  
 $\alpha_i$ :  $i^{th}$  root of an algebraic function  
 $\beta$ : half of the angle of the cone tip  
 $\Gamma$ : specific volume of CSL (Critical State Line) at  $p' = 1$  kPa  
 $\gamma$ : specific weight  
 $\Delta u$ : pore pressure decay  
 $\Delta u_{max}$ : maximum pore pressure decay  
 $\Delta u_{min}$ : minimum pore pressure decay  
 $\delta$ : interface friction  
 $\underline{\xi}$ : displacement vector  
 $\bar{\xi}$ : radial displacement

## List of Symbols

- a*: radius of the zone of influence  
*a*: fitting parameter for the hyperbolic cosine function  
*b*: Biot coefficient  
*b*: fitting parameter for the hyperbolic cosine function  
 $B_q$ : pore pressure ratio  
*c*: fitting parameter for the hyperbolic cosine function  
 $c_n$ : horizontal coefficient of consolidation  
 $c_n$ : fluid diffusivity coefficient  
 CPTU: piezocone test  
*d*: probe diameter size  
 $dl$ : small portion of the cone tip length  
 $e_0$ : initial void ratio  
 $F_z$ : vertical resistive force  
 $G_s$ : specific gravity  
*G*: shear modulus  
 $G_{eq}$ : equivalent shear modulus  
*h*: Drucker Prager tensile strength  
 $I_{cRW}$ : soil behaviour index according Robertson & Wride (1998)  
 $I_r$ : Rigidity Index  
 $J_0$ : zero-order Bessel functions of the first kind  
 $J_1$ : first-order Bessel functions of the first kind

$\bar{\varepsilon}_d$ : equivalent deviatoric strain

$\varepsilon_v$ : volumetric strain

$\varepsilon_{ref}$ : reference strain

$\underline{\underline{\varepsilon}}$ : strain matrix

$\bar{\varepsilon}_r$ : radial strain

$e_{qq}$ : orthogonal strain

$\underline{e}_r$ : unit vector in the radial direction

$\underline{e}_\theta$ : unit vector in the orthogonal direction

$\underline{\underline{\sigma}}$ : total stress matrix

$\underline{\underline{\sigma}}'$ : effective stress matrix

$\bar{\sigma}_d$ : equivalent deviatoric stress

$\sigma_m$ : mean total stress

$\sigma'_m$ : mean effective stress

$\sigma'_n$ : effective normal pressure

$\sigma_r$ : radial pressure

$\sigma'_r$ : effective radial pressure

$\sigma_{v0}$ : total vertical pressure

$\sigma'_{v0}$ : effective vertical pressure

$\sigma_0$ : initial pressure

N: specific volume of NCL (Normal Consolidation Line) at

$p' = 1$  kPa

$\lambda$ : slope of the NCL (Normal Consolidation Line)

$\Phi$ : Lagrangian porosity

$\phi$ : friction angle

$X$ : variable

$\varpi_i$ : scalar computed from  $\alpha_i$

$\psi$ : state parameter

$\underline{\underline{I}}$ : identity matrix

# Behavior of Geosynthetic-Encased Stone Columns in Soft Clay: Numerical and Analytical Evaluations

N.R. Alkhorshid, G.L.S. Araújo, E.M. Palmeira

**Abstract.** The type of improvement technique that will be applied to a soil beneath an embankment depends on the nature of the problematic soil existing at the site. Soft soils beneath embankments typically present high compressibilities and low shear strengths. In some cases, geosynthetic-encased stone columns (GECs) have shown advantages over other solutions to improve embankment behavior. The aim of this study is to investigate the performance of GECs by means of numerical and analytical methods. Finite Element Analyses were conducted to evaluate the behavior of ordinary and geosynthetic-encased stone columns underneath an embankment. Parametric studies were then conducted to investigate the influence of geosynthetic stiffness, column spacing, friction angle of column material and Stress Concentration Ratio (SCR) on the performance of the columns. The results obtained have shown that there are several parameters that are of paramount importance in improving the performance of GECs, such as geosynthetics stiffness, column spacing and thickness of soft soil layer.

**Keywords:** embankment, geosynthetics, settlement, soft soil, stone column, radius variation.

## 1. Introduction

In some cases, soil properties are not appropriate for supporting structures such as buildings, embankments, dams and bridges. This leads to the need for a proper method that can be effective to improve the performance of the geotechnical structure. The use of stone columns is a popular solution that has been considered when dealing with soft soils. Stone columns not only reduce settlements but also behave like vertical drains and accelerate the consolidation process (Han & Ye, 2001).

Since the performance of ordinary stone columns is highly dependent on the lateral confinement provided by surrounding soil, when it comes to very soft soils ( $S_u < 15$  kPa) the application of this solution may not be feasible. This problem can be solved by increasing lateral confinement to the column material by using geosynthetic encasement. In this context, Geosynthetic Encased Columns (GECs) have been applied successfully in several engineering works (Raithel & Kempfert, 2002; Alexiew *et al.*, 2005; Araujo *et al.*, 2009; De Mello *et al.*, 2008; Alexiew & Raithel, 2015; Schnaid *et al.*, 2017).

Considering previous studies that have provided valuable information on the performance of GECs, further studies are still needed for a better understanding of the key parameters in designing GECs. Besides experimental and analytical solutions, numerical analysis can be used as a powerful tool to investigate the performance of GECs (e.g. Khabbazian *et al.*, 2010; Kaliakin *et al.*, 2012; Keykhos-

ropur *et al.*, 2012; Alkhorshid *et al.*, 2014; Yoo, 2015; Mohapatra *et al.*, 2017).

Since most of the analytical solutions have considered unit cell idealization in their procedure, this concept and axisymmetric analyses have been adopted to assess the influence of geosynthetic encasement on the behavior of stone columns (EBGEO, 2011; Elsayw, 2013; Almeida *et al.*, 2013; Hosseinpour *et al.*, 2014; Alkhorshid, 2017).

The analytical solution presented by Barron (1948) was focused on the behavior of the foundation system reinforced by vertical drains, discussing the dissipation of excess pore water pressure and the rate of consolidation settlement. This solution was a basis for later studies on the foundation reinforced by conventional and encased stone columns (Wang, 2009; Castro & Sagaseta, 2011; Santos, 2011) considering the time-settlement behavior under consolidation process. On the other hand, some other studies (Raithel & Kempfert, 2000; Pulko *et al.*, 2011; Zhang & Zhao, 2014) were also developed to evaluate the behavior of encased stone columns and the surrounding soil which did not consider time-dependent settlement of the foundation.

In this study, the Finite Element Method (FEM) was used to investigate the effect of encasement on the column beneath an embankment. The FEM predictions were then compared with those from three analytical methods.

---

Nima Rostami Alkhorshid, D.Sc., Associate Professor, Instituto de Engenharias Integradas, Universidade Federal de Itajubá, Itajubá, MG, Brazil. e-mail: nimara@unifei.edu.br.

Gregório Luís Silva Araújo, D.Sc., Associate Professor, Departamento de Engenharia Civil e Ambiental, Universidade de Brasília, Brasília, DF, Brazil. e-mail: gregorio@unb.br.

Ennio Marques Palmeira, Ph.D., Full Professor, Departamento de Engenharia Civil e Ambiental, Universidade de Brasília, Brasília, DF, Brazil. e-mail: palmeira@unb.br.

Submitted on May 22, 2018; Final Acceptance on October 24, 2018; Discussion open until April 30, 2019.

DOI: 10.28927/SR.413333

## 2. Methods of Investigation

### 2.1. Analytical methods

#### 2.1.1. Raithel & Kempfert (2000) method

Raithel & Kempfert (2000) proposed an analytical method (hereafter referred to by the code R&K) for the design of encased stone column foundations which is adopted by the German Standard EBGEO (2011). This method was firstly proposed by Raithel (1999) and assumes identical settlements for both stone column and surrounding soil as a whole (unit cell, Fig. 1) under long-term drained condition when maximum value of radius variation and settlements are obtained. As illustrated in Fig. 1b, the load on the unit cell is shared by the column ( $\Delta\sigma_{v,c}$ ) and surrounding soil ( $\Delta\sigma_{v,s}$ ). In this method, the ring (geotextile) tensile force can be calculated by:

$$F_R = J \frac{\Delta r_{geo}}{r_{geo}} \quad (1)$$

where  $J$  is the geotextile tensile stiffness,  $\Delta r_{geo}$  and  $r_{geo}$  are geotextile casing radius variation and initial casing radius,

respectively. The settlement at the top of column can be determined by:

$$S_c = \left( 1 - \frac{r_c^2}{(r_c + \Delta r_c)^2} \right) \cdot h \quad (2)$$

where  $r_c$ ,  $\Delta r_c$  and  $h$  are column radius, column radius variation and column length, respectively.

This method uses the load redistribution factor ( $E$ ) which represents the stress concentration on the top of the column. As shown in Eq. 2, the settlement of the column is a function of the column radius variation ( $\Delta r_c$ ) which is dependent on the applied stress shared by the surrounding soil ( $\sigma_{v,B}$ ) that can be calculated by the following equation:

$$\sigma_{v,B} = \frac{\sigma_0 - E \cdot \sigma_0}{1 - a_c} \quad (3)$$

where,  $\sigma_0$ ,  $E$  and  $a_c$  are vertical stress on the unit cell, load redistribution factor and area replacement ratio, respectively. The area replacement ratio can be determined by:

$$a_c = \frac{A_c}{A_E} \quad (4)$$

where,  $A_c$  and  $A_E$  are column and unit cell area, respectively.

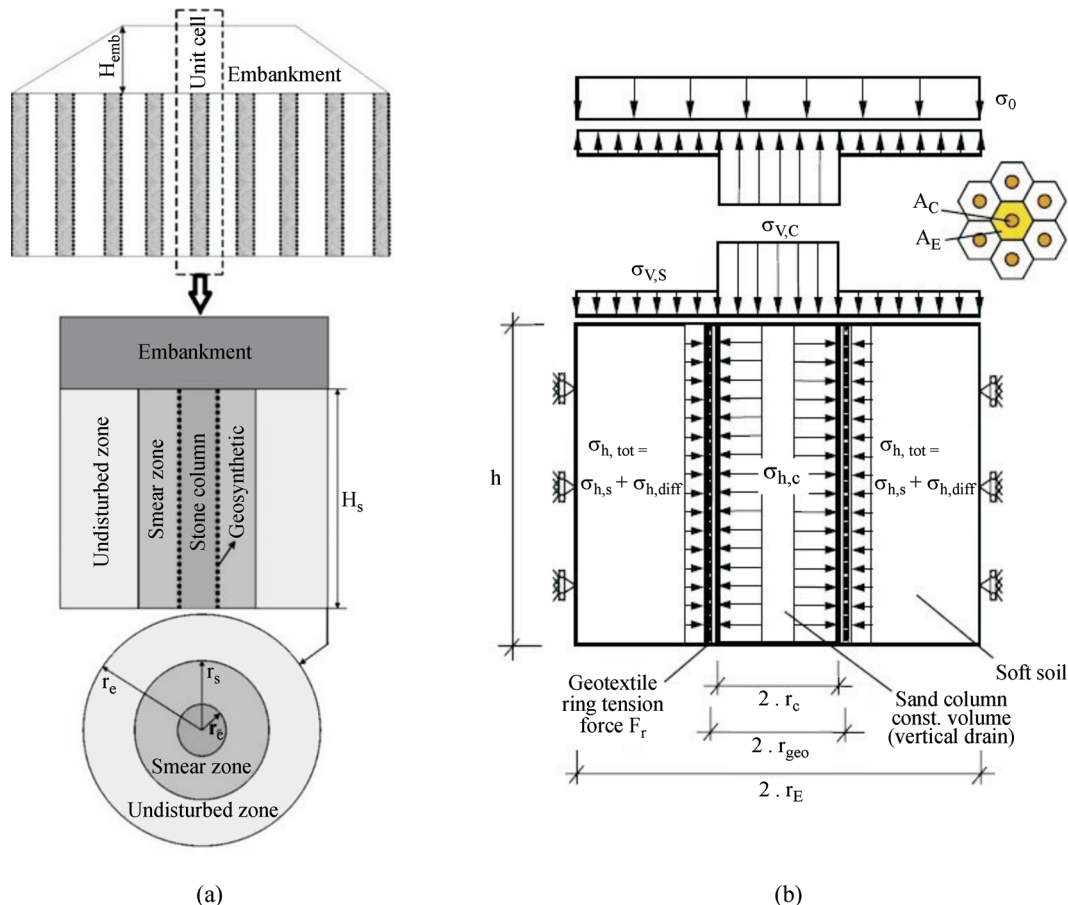


**Figure 1** - Unit cell idealization: (a) unit cell under the embankment and (b) unit cell calculation model (Raithel & Kempfert, 2000).

On the other hand, the settlement of the surrounding soil is also a function of  $\sigma_{v,B}$  and consequently dependent on  $E$ . Thus, by equalizing the settlement of the column and the surrounding soil ( $S_c = S_B$ ),  $E$  can be found by some iteration process. When  $E$  is determined, the column radius variation can be calculated.

### 2.1.2. Pulko *et al.* (2011) method

The method proposed by Pulko *et al.* (2011), (hereafter referred to by the code PEA) is an extension of the elastic analysis proposed by Balaam & Booker (1985) and Raithel & Kempfert (2000) and considers elastoplastic behavior of the column material considering confined column yielding based on the dilatancy theory presented by Rowe (1962). In this method the vertical deformations at the top of the column and the surrounding soil are also assumed to be equal. The shear stress along the column/soil interface is neglected. Furthermore, the soil is considered to remain elastic and the column is supposed to behave as a perfectly elastoplastic material satisfying the Mohr-Coulomb failure criterion. Additional information on the method is presented by Pulko *et al.* (2011).

### 2.1.3. Zhang & Zhao (2014) method

Zhang & Zhao (2014) developed an analytical method (code Z&Z) for the design of conventional and geotextile encased stone columns. The method adopts the unit cell idealization and considers the column as an elastic material. The column is divided from top to bottom into  $i$  ( $i = 1, 2, \dots, n$ ) sections. For each section there is a unique settlement and radius variation. The total settlement is the sum of the settlements obtained in each section. Comparing to Raithel & Kempfert (2000), this method takes into account the shear stress between the soil and the column considering settlement inequality at the top of the column and of the surrounding soil. More details on the method are presented by Zhang & Zhao (2014).

## 2.2. Numerical modelling (PLAXIS 2D)

### 2.2.1. Hardening Soil (HS) model

The Hardening Soil (HS) model (available in PLAXIS 2D) is a development on Mohr-Coulomb model, created by linking non-linear elastic and elastoplastic models, also known as hyperbolic elastoplastic model. HS is able to model the double stiffening performance of soil, which is not influenced by the compressive yield or shear failure. This model can simulate the stress dependency of soil stiffness but does not take into account soil secondary compression and stress relaxation. Additional information about this model is presented by Schanz *et al.* (1999).

### 2.2.2. Axisymmetric model

The behavior of GECs and soft clay unit cell under axisymmetric conditions (Fig. 2) was modeled using PLA-

XIS 2D (Brinkgreve & Vermeer, 2014). The column was entirely buried in the surrounding soil with its tip resting on a rigid layer at the bottom. The soft clay was modelled by the HS model (Gäb & Schweiger, 2008) and the embankment and the column were modelled using Mohr-Coulomb model assuming typical values of properties of these materials. The properties of the soft clay, stone column and embankment are shown in Table 1.

The geosynthetic material was modelled as a linear elastic material (the same assumption was adopted in all three analytical methods). The boundary conditions of the unit cell (Fig. 2) allow deformations along the vertical direction only. The vertical and horizontal displacements at the base of the unit cell were restrained.

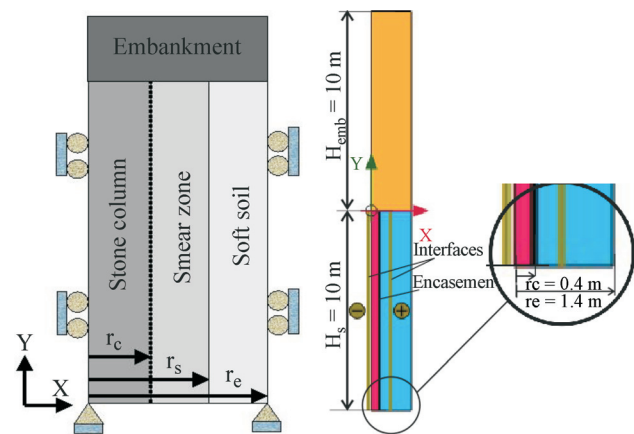


Figure 2 - Axisymmetric unit cell model and boundary condition.

Table 1 - Material parameters in FE model.

Material properties	Soft clay	Stone column	Embankment
	Hardening Soil (HS)	Mohr-Coulomb (MC)	Mohr-Coulomb (MC)
$\gamma_{sat}$ (kN/m <sup>3</sup> )	16	19	22
$E'$ (kPa)	-	45000	42000
$\phi'$ (°)	23	39	35
$\psi$ (°)	0	5	0
$c'$ (kPa)	7	0	6
$\nu'$	0.2	0.3	0.33
$E_{50}^{ref}$ (kPa)	2313	-	-
$E_{oed}^{ref}$ (kPa)	1850	-	-
$E_{ur}^{ref}$ (kPa)	6938	-	-
$K_0$	0.6	0.37	0.43
$m$ (power)	1	-	-
$P^{ref}$ (kPa)	100	-	-
OCR	1	-	-

### 3. Comparisons Between Predictions by Fem and Analytical Methods

Comparisons between results from the four cited methods (Finite element, R&K, PEA and Z&Z) were carried out for the analysis of an embankment reinforced with GECs distributed in a square pattern. In the validation model, the radius of the columns within the unit cell,  $r_c$  was equal to 0.4 m (typical for GECs, Alexiew *et al.*, 2005), radius of the influence area of the column  $r_e = 1.4$  m, diameter ratio ( $N = r_e/r_c$ ) equal to 3.5, area replacement ratio ( $\alpha = r_c^2/r_e^2$ ) equal to 8.16%, column length ( $l_c$ ) and unit cell height ( $H_s$ ) both equal to 10 m, height of embankment ( $H_{emb}$ ) equal to 10 m, and geosynthetic tensile stiffness ( $J$ ) equal to 2000 kN/m (EBGEO, 2011).

Zhang & Zhao (2014) pointed out that in case of large deformations, the method Z&Z may not provide appropriate

results. In order to minimize this issue, in the present study the calculation procedure was changed so that the column was assumed to be as a whole, not in sections. For  $i = 1$ , the maximum value of radius variation ( $\Delta r_{c,max z} = 0$ ) and then the vertical strain of the column ( $\varepsilon_{zc}$ ) were determined. Then, the  $\varepsilon_{zc}$  was multiplied by the entire length of the column ( $l_c$ ). For small level of deformation this procedure may not provide appropriate results.

As shown in Fig. 3a and Table 2, the settlements estimated by R&K and Z&Z are in good agreement with those of FEM. The maximum values of radius variation under different embankment heights estimated by R&K (Fig. 3b and Table 3) show good agreement with those of FEM. On the other hand, PEA and Z&Z led to underestimation and overestimation of the radius, respectively. The maximum values of radius variation from Z&Z, up to an embankment height of 3 m, are closer to those of FEM. For PEA, the re-

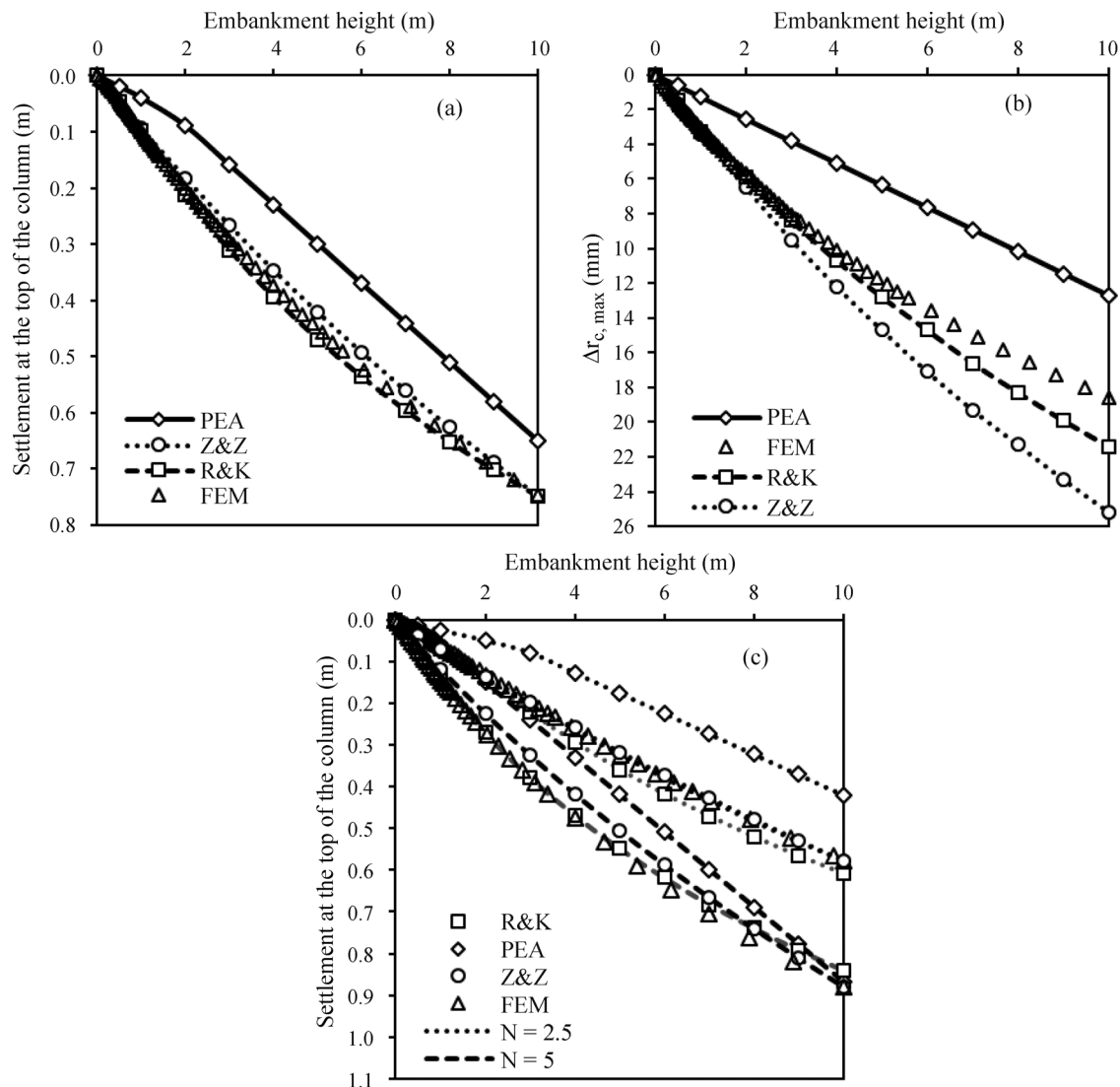


**Figure 3** - Settlement behavior of GECs under embankment loading: (a) vertical settlement of the column from FE and analytical methods; (b) variation of column radius; (c) vertical settlement of column for different values of  $N$ .

sults present significant differences for any height of embankment. Figure 3c presents settlement at the top of the column for different values of diameter ratio,  $N$ , where it can be seen that the results from R&K and Z&Z also compare better with FEM predictions than PEA.

**Table 2** - Settlement at the top of the column considering different methods (m).

Method	Embankment height (m)			
	2 m	6 m	8 m	10 m
FEM	0.2	0.515	0.637	0.747
R&K	0.213	0.536	0.652	0.749
PEA	0.089	0.37	0.51	0.65
Z&Z	0.182	0.492	0.626	0.748

### 4. Parametric Study

The effects of geosynthetic encasement, column radius of influence, unit cell heights and friction angle of the stone column material ( $\phi_c$ ) on the behavior of the column were investigated by a parametric study comparing *FEM* with analytical methods. The parameters used in parametric study are given in Table 4.

#### 4.1. Settlement and radius variation of *GECs*

Geosynthetic encasement provides a confinement around the column that reduces radius variation ( $\Delta r_c$ ). Figure 4a and Table 5 show the maximum value of radius variation versus geosynthetic tensile stiffness for the same properties and characteristics adopted in the comparison between FEM and predictions from analytical methods. Comparing the results from analytical methods with those

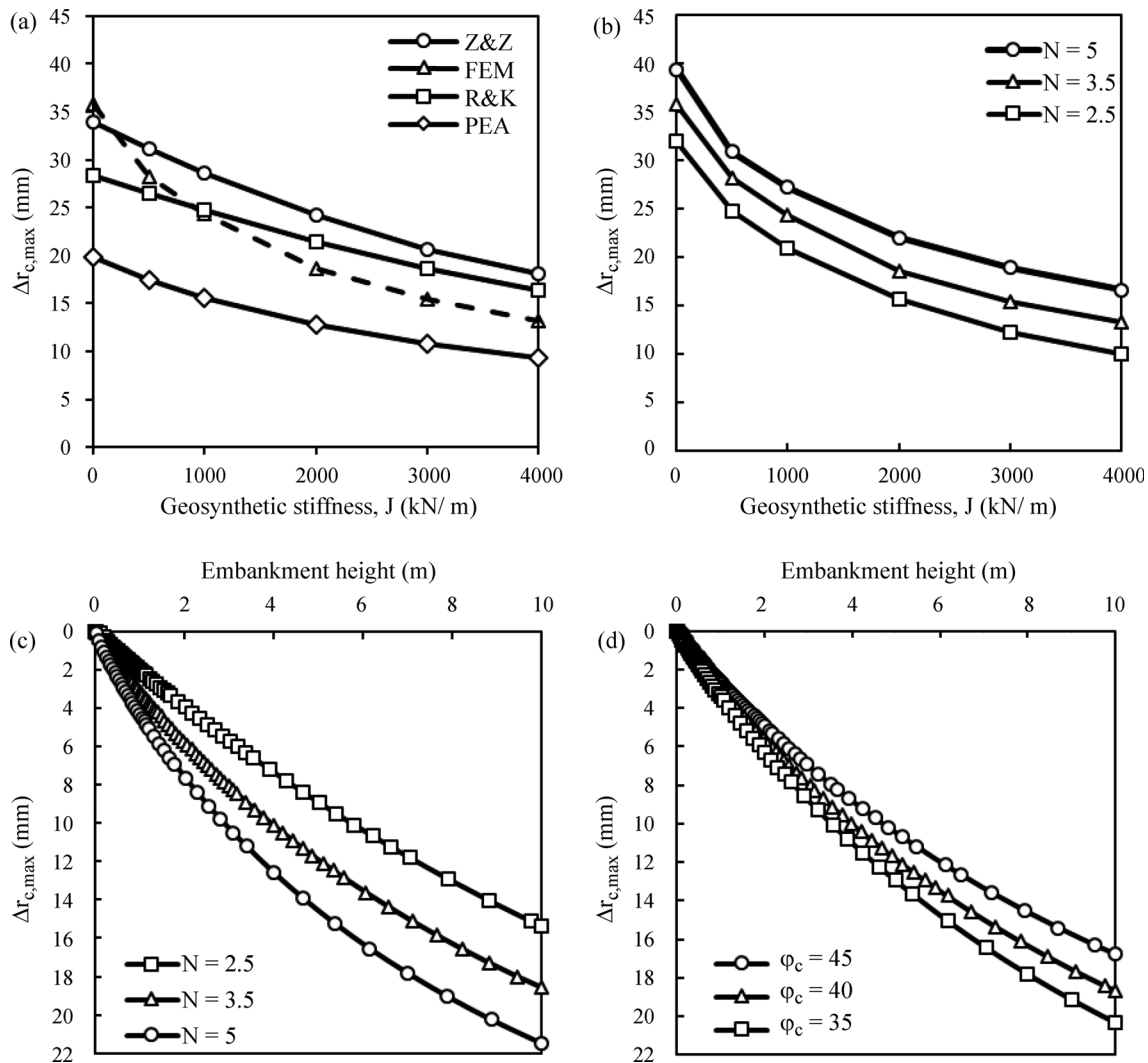


**Figure 4** - Radius variation: (a) Maximum value of radius variation versus geosynthetic stiffness by different methods (FEM, R&K, PEA, and Z&Z); (b) maximum value of radius variation versus geosynthetic stiffness using FEM for different values of  $N$ ; (c) maximum value of radius variation versus different embankment heights using FEM with different values of  $N$  and (d) maximum value of radius variation versus different embankment heights using different values of friction angle of the column.

**Table 3** - Maximum value of radius variation of the column ( $\Delta r_{c,max}$ ) considering different methods (mm).

Method	Embankment height (m)			
	2 m	6 m	8 m	10 m
FEM	5.74	13	16.15	18.6
R&K	5.9	14.7	18.3	21.4
PEA	2.55	7.64	10.18	12.73
Z&Z	6.5	17.1	21.3	25.17

from FEM (just for encased column), the overall deviations of R&K predictions are considerably less than those of PEA and Z&Z. The minimum and maximum deviations of R&K were equal to 1.5% (for  $J = 1000$  kN/m) and 24% (for  $J = 4000$  kN/m), respectively. On the other hand, PEA and Z&Z presented higher values of maximum deviations reaching 38% (for  $J = 500$  kN/m) and 36% (for  $J = 4000$  kN/m), respectively. The average deviation of Z&Z (23.8%) was less than that of PEA (33.8%). Another parameter that affects radius variation value is the diameter ratio ( $N$ ).

By increasing  $N$  for the same value of  $r_c$ , the area replacement ratio ( $\alpha$ ) decreases and the maximum value of radius variation increases. As shown in Fig. 4b, the geosynthetic tensile stiffness significantly influences column radius variation.

Figure 4c shows column radius variation versus embankment height for different values of  $N$  and  $J = 2000$  kN/m. The results also show the significant influence of  $N$  on column radius variation. In Fig. 4d the maximum value of radius variation is plotted against different embankment heights for different column soil friction angles. Radius

**Table 4** - Parameters used in the parametric studies.

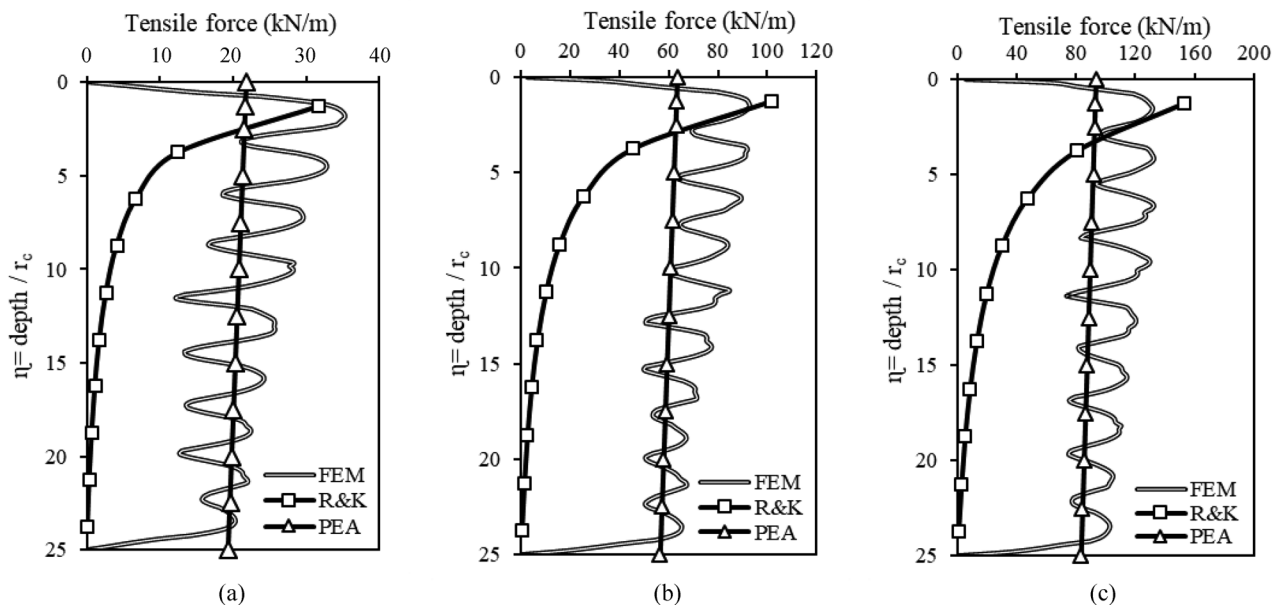
Parameters	Values
Geosynthetic stiffness, $J$ (kN/m)	0-4000
Diameter ratio, $N$ (-)	2.5, 3.5, 5
Height of unit cell, $H_s$ (m)	5, 10, 15
Friction angle of column material, $\phi_c$ ( $^\circ$ )	35, 40, 45

**Table 5** - Maximum value of column radius variation ( $\Delta r_{c,max}$ ) for different methods (mm).

Method	Tensile stiffness, $J$ (kN/m)			
	500	1000	2000	4000
FEM	28.22	24.32	18.6	13.24
R&K	26.5	24.7	21.4	16.4
PEA	17.42	15.52	12.73	9.37
Z&Z	31.19	28.65	24.2	18.1

variation increases as soil friction angles decreases. As shown in Fig. 3 and also in Figs. 4c-d, predicted values of settlement and maximum radius variation are significantly influenced by the embankment height. By increasing the vertical stress at the top of the unit cell, the settlements and column radius variations increase markedly. However, using lower values of  $N$  improves the performance of the column. Alternatively, increasing the value of the friction angle of the column, reduces deformations of the column.

Figure 5a-c show tensile force versus depth ratio for different values of geosynthetic tensile ( $\eta = \text{depth}/r_c$ ) for different values of geosynthetic tensile

**Figure 5** - Tensile force versus depth ratio for different geosynthetic stiffness; (a) Tensile force for  $J = 500$  kN/m, (b) Tensile force for  $J = 2000$  kN/m, (c) Tensile force for  $J = 4000$  kN/m.

stiffness. Predicted values of tensile force indicate that, as tensile stiffness of geosynthetic increases, radius variation reduces at any depth along the column. In addition, increments of  $J$  values do not influence significantly the depth of the maximum value of radius variation. Several studies have shown this depth varies between 1.5 to 3 column diameters (Ali *et al.*, 2012; Hong *et al.*, 2016; Alkhorshid, 2017). Comparing the results of both numerical and analytical studies indicate that R&K, from depth ratio of almost 5 and beyond underestimated the results while PEA presented better estimates. It is important to consider that R&K provides more accurate predictions of the maximum tensile force. Finally, it is possible to observe that the curves have completely different trends and this is because of the better accuracy of the Finite Element Method, whereas the analytical methods have to adopt some simplifying assumptions. Similar variations in tensile forces along the column length were also observed in other studies (Gniel & Bouazza, 2009; Pulko *et al.*, 2011; Almeida *et al.*, 2013).

The results, presented in Fig. 6a, clearly indicate the importance of the unit cell height on the column behavior. The geosynthetic tensile stiffness is also important in the reduction of column settlements. In Fig. 6b, the vertical settlement at the top of the column due to an embankment height of 10 m is plotted versus different values of  $J$ . The results indicate that at any value of  $J$ , the minimum settlement is obtained for higher friction angle. The lowest values of settlement are obtained for  $\phi_c = 45^\circ$ .

**4.2. Influence of geosynthetic stiffness on Stress Concentration Ratio (SCR)**

The stress concentration ratio (SCR) is defined as the ratio between the vertical stress supported by the column

( $q_c$ ) and that supported by surrounding soil ( $q_s$ ), ( $SCR = q_c/q_s$ ). SCR basically depends on the geosynthetic tensile stiffness, physical properties of soil, column materials and distance between adjacent columns, that may be arranged in triangular, square or hexagonal patterns. As shown in Figs. 7 and 8, the greater the geosynthetic stiffness, the higher additional confinement along the column length which results in supporting larger shares of vertical stress. This means that for higher values of  $J$ , geosynthetic encasement produces greater values of SCR, depending on tensile stiffness. Figure 7 shows the effective stress distributions as cross marks. When it comes to the conventional column, these cross marks in the surrounding soil are visibly greater than those for the encased column, which means that a higher share of vertical stress goes to surrounding soil. The SCRs predicted by means of FEM and analytical analyses show that R&K results take a different trend for higher values of  $J$ , whereas PEA and Z&Z results are closer to those of FEM (Fig. 9a). There is almost a unique agreement between PEA and Z&Z on SCR.

The influence of  $N$  values is shown in Fig. 9b. As it can be seen, higher  $N$  values lead to lower SCR values and also the difference between SCRs for higher values of  $J$  is greater. As shown in Fig. 9c, the friction angle of column ( $\phi_c$ ) can affect SCR, because higher values of  $\phi_c$  make the column capable of sustaining higher vertical stresses.

**4.3. Influence of geosynthetic stiffness on maximum tensile force**

As cited in this study, vertical stress on top of the unit cell causes settlement and radius variation of the column. The radius variation causes a ring tensile stress in the geosynthetic encasement. Tensile force is a function of geo-

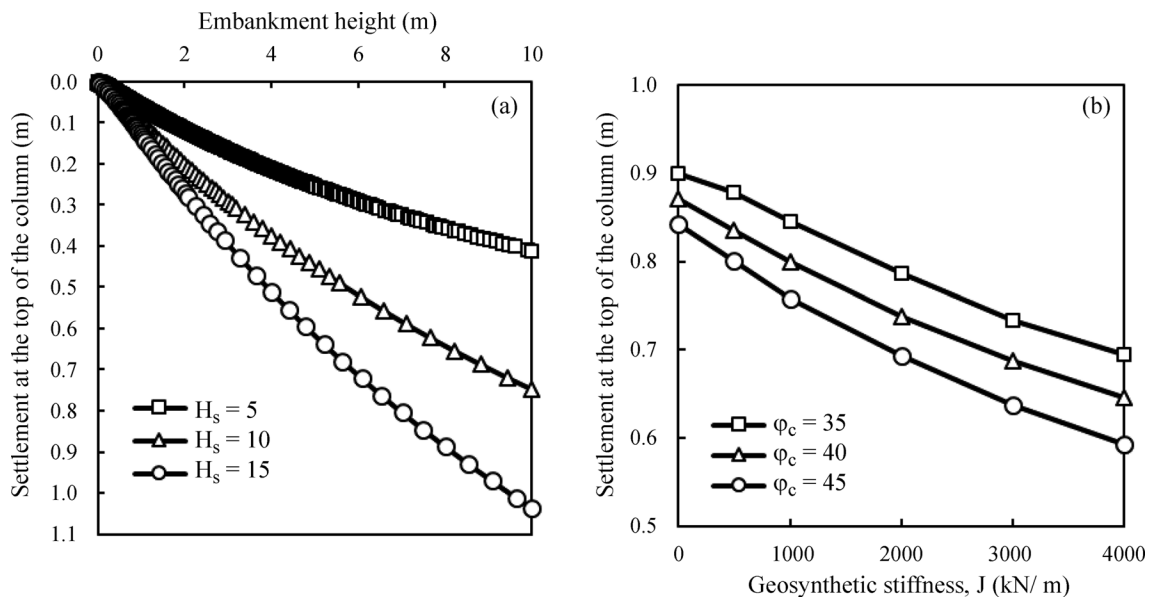


**Figure 6** - Vertical settlement at the top of the column: (a) vertical settlement versus embankment heights (b) vertical settlement versus geosynthetic stiffness.

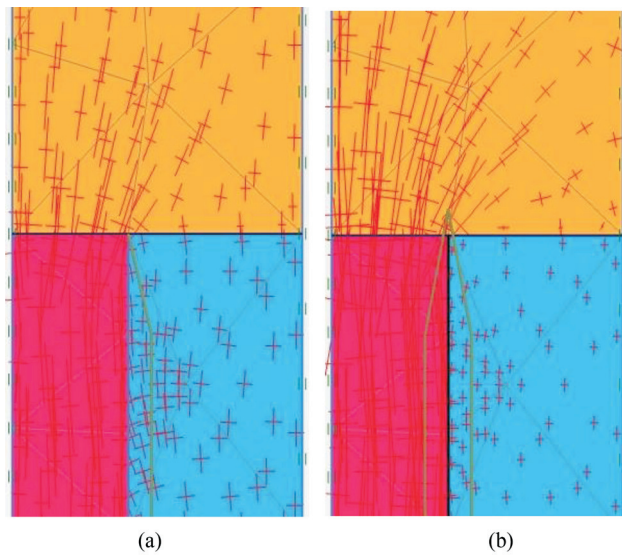


**Figure 7** - Effective stress distribution: (a) ordinary stone column; (b) encased stone column ( $J = 2000$  kN/m).

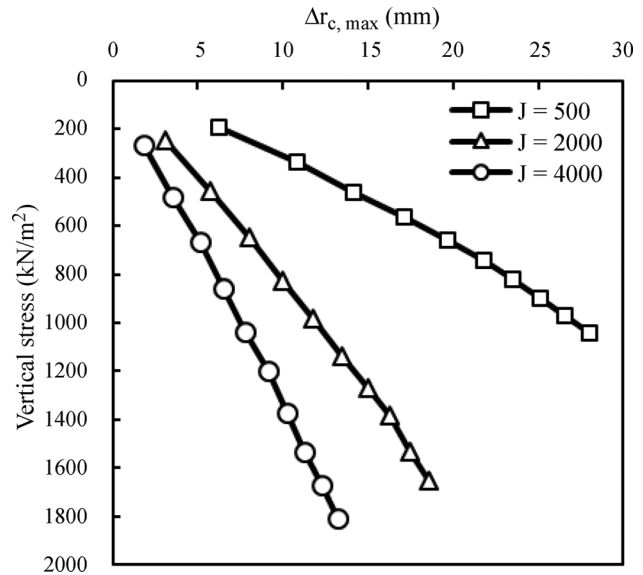


**Figure 8** - Radius variation of column versus vertical stress on column.

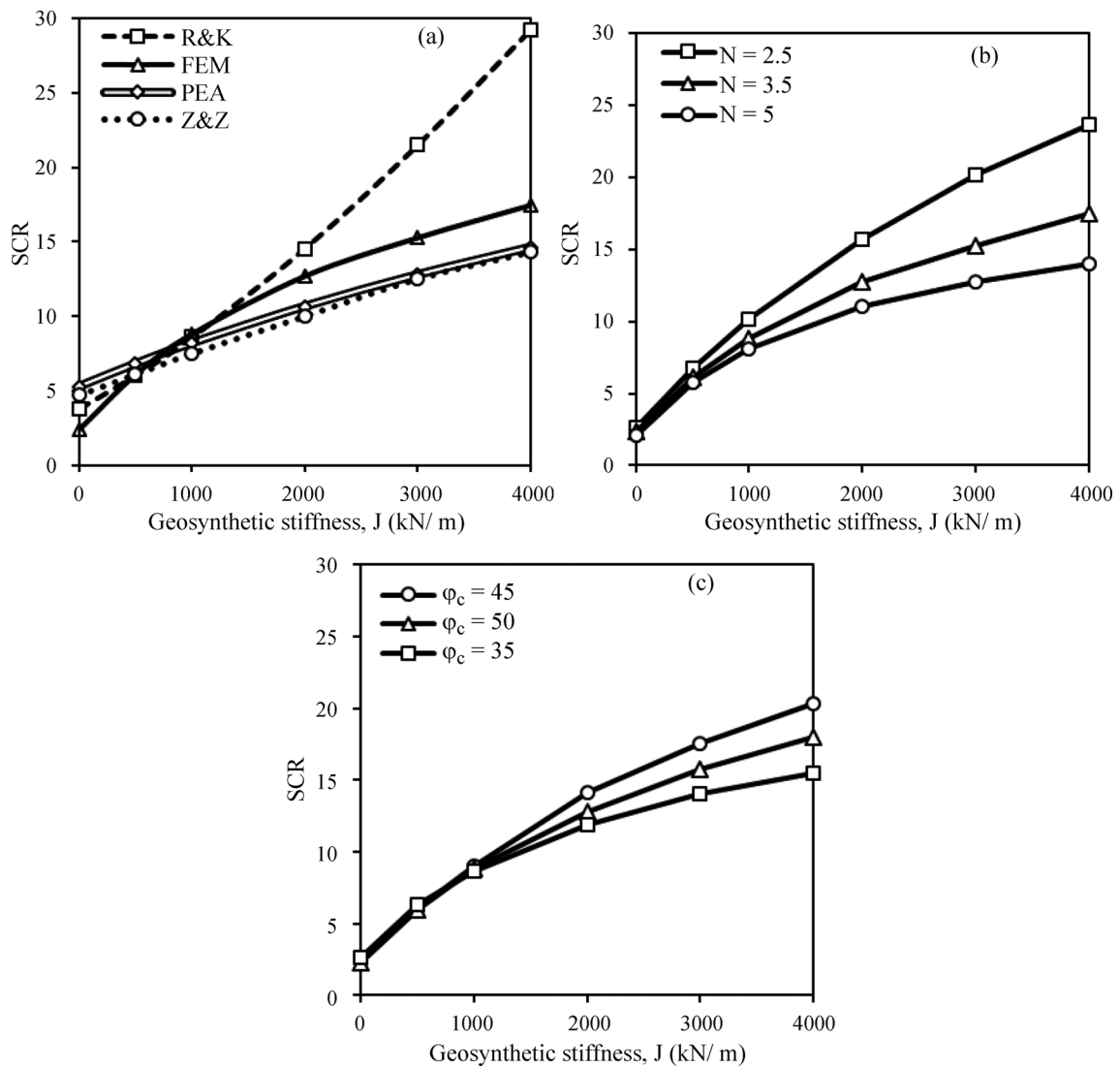


**Figure 9** - Stress Concentration ratio (SCR): (a) Predicted SCRs by means of FE and analytical methods; (b) influence of  $N$  values on SCR by FE analysis; (c) influence of  $\phi_c$  on SCR by FE analysis.

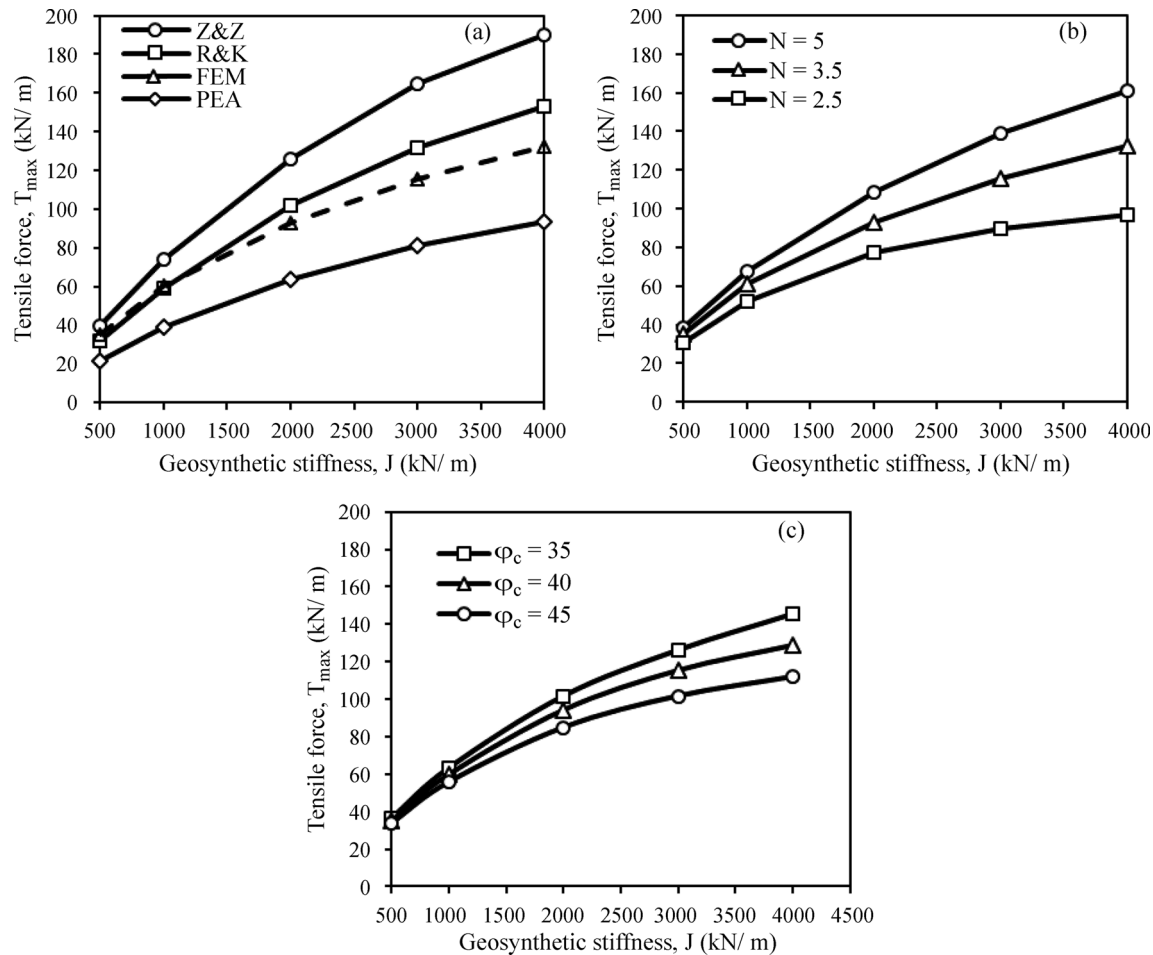


**Figure 10** - Maximum tensile force ( $T_{max}$ ): (a) predicted values of  $T_{max}$  by FE and analytical analyses; (b) effect of  $N$  values on  $T_{max}$ ; (c) effect of friction angle on  $T_{max}$ .

synthetic stiffness ( $J$ ), radius of column ( $r_c$ ) and radius variation ( $\Delta r_c$ ). Figure 10a shows predicted maximum tensile forces ( $T_{max}$ ) by FEM and by the analytical methods. The agreement between FEM and R&K is satisfactory for values of  $J$  up to 2000 kN/m. PEA and Z&Z produce higher rates of deviation from FEM results. The result of FEM analyses for different  $N$  values (Fig. 10b), shows that for lower values of  $N$ , the geosynthetic encasement presents lower values of  $T_{max}$ . As shown in Fig. 10c, friction angle of column material ( $\phi_c$ ) may cause slight differences in the values of  $T_{max}$ .

## 5. Conclusions

In this study a series of finite element and analytical analyses for evaluating the performance of GECs was carried out. In addition, the results of FEM and analytical methods were compared in order to investigate the capability of the analytical methods to predict the behavior of geosynthetic-encased column. The following conclusions were developed:

- Among the three methods analyzed, the results of R&K generally show a better agreement with those of FEM, comparing with PEA and Z&Z;
- The greater the values of geosynthetic tensile stiffness ( $J$ ), the smaller the value of radius variation along the column length. However, greater values of  $J$  do not affect the depth of the maximum value of radius variation;
- The settlements at the top of the column with higher values of  $J$ , are evidently less than those for lower values of tensile stiffness;
- By decreasing diameter ratio ( $N$ ), the settlement, radius variation and tensile force of the column decrease and alternatively SCR increases.
- Friction angle of column material ( $\phi_c$ ) can play an important role in the performance of GECs. At identical  $J$ , higher values of  $\phi_c$  increase SCR and, then again, higher values of  $\phi_c$  decrease settlement and tensile forces in the column.
- Except at the depth of maximum tensile force, the predicted values of tensile force along the column indicate that PEA is in closer agreement with those from FEM.

However, R&K underestimated the results at some depths.

## Acknowledgments

The authors would like to thank the following institutions for their support in the research activities described in this paper: Brazilian National Council for Scientific and Technological Development (CNPq), CAPES - Brazilian Ministry of Education, Universidade de Brasília and Universidade Federal de Itajubá.

## References

- Alexiew, D. & Raithel, M. (2015). Geotextile-Encased Columns: Case Studies over Twenty Years. In: B. Indraratna, J. Chu, & C. Rujikiatkamjorn (eds) *Ground Improvement Case Histories*. Elsevier, Oxford, pp. 451-477.
- Alexiew, D.; Brokemper, D. & Lothspeich, S. (2005). Geotextile Encased Columns (GEC): Load capacity, geotextile selection and pre-design graphs. *Geo-Frontiers Congress 2005*. January 24-26, Austin, Texas, United States: ASCE.
- Ali, K.; Shahu, J.T. & Sharma, K.G. (2012). Model tests on geosynthetic-reinforced stone columns: a comparative study. *Geosynthetics International*, 19(4):433-451.
- Alkhorshid, N.R. (2017). *Analysis of Geosynthetic Encased Columns in Very Soft Soil*. PhD Thesis, Departamento de Engenharia Civil e Ambiental, Universidade de Brasília, 128 p.
- Alkhorshid, N.R.; Nalbantoglu, Z. & Araujo, G.L. (2014). 3D analysis of full scale stone column reinforced soft clay: Numerical Evaluation. *Proc. XVII Congresso Brasileiro de Mecânica dos Solos - Cobramseg, Goiânia, Brasil*.
- Almeida, M.S.S.; Hosseinpour, I. & Riccio, M. (2013). Performance of a geosynthetic-encased column (GEC) in soft ground: Numerical and analytical studies. *Geosynthetics International*, 20(4):252-262.
- Araujo, G.L.; Palmeira, E.M. & Cunha, R.P. (2009). Behaviour of geosynthetic-encased granular columns in porous collapsible soil. *Geosynthetics International*, 16(6):433-451.
- Balaam, N.P. & Booker, J.R. (1985). Effect of stone column yield on settlement of rigid foundations in stabilized clay. *International journal for Numerical and Analytical Methods in Geomechanics*, 9(4):331-351.
- Barron, R.A. (1948). Consolidation of fine-grained soils by drain wells. *Trans. Am. Soc. Civ. Engrg*, 113:718-742.
- Brinkgreve, R.B. & Vermeer, P.A. (2014). *PLAXIS: Finite Element Code for Soil and Rock Analysis*. Balkema, Rotterdam.
- Castro, J. & Sagasetta, C. (2011). Deformation and consolidation around encased stone columns. *Geotextiles and Geomembranes*, 29(3):268-276.
- De Mello, L.G.; Mondolfo, M.; Montez, F.; Tsukahara, C.N. & Bilfinger, W. (2008). First use of geosynthetic encased sand columns in South America. *Proc. 1st Pan-American Geosynthetics Conference*, pp. 1332-1341.
- EBGEO. (2011). *Recommendations for Design and Analysis of Earth Structures Using Geosynthetic Reinforcements*. Essen-Berlin: Germany: Geotechnical Society (DGGT), Ernst & Sohn.
- Elsawy, M.B. (2013). Behaviour of soft ground improved by conventional and geogrid-encased stone columns, based on FEM study. *Geosynthetics International*, 20(4):276-285.
- Gäb, M. & Schweiger, H.F. (2008). Numerical analysis of a floating stone column foundation using different constitutive models. *Second International Workshop on Geotechnics of Soft Soils*, CRC Press, pp. 137-142.
- Gniel, J. & Bouazza, A. (2009). Improvement of soft soils using geogrid encased stone columns. *Geotextiles and Geomembranes*, 27(3):167-175.
- Han, J. & Ye, S.L. (2001). Simplified method for consolidation rate of stone column reinforced foundations. *Journal of Geotechnical and Geoenvironmental Engineering*, 127(7):597-603.
- Hong, Y.S.; Wu, C.-S. & Yu, Y.-S. (2016). Model tests on geotextile-encased granular columns under 1-g and undrained conditions. *Geotextiles and Geomembranes*, 44(1):13-27.
- Hosseinpour, I.; Riccio, M. & Almeida, M.S.S. (2014). Numerical evaluation of a granular column reinforced by geosynthetics using encasement and laminated disks. *Geotextile and Geomembrane*, 42(4):363-373.
- Kaliakin, V.N.; Khabbazian, M. & Meehan, C.L. (2012). Modelling the behavior of geosynthetic encased columns: Influence of granular soil constitutive model. *International Journal of Geomechanics*, 12(4):357-369.
- Keykhosropur, L.; Soroush, A. & Imam, R. (2012). 3D numerical analyses of geosynthetic encased stone columns. *Geotextile and Geomembrane*, 35:61-68.
- Khabbazian, M.; Kaliakin, V.N. & Meehan, C.L. (2010). Numerical study of the effect of geosynthetic encasement on the behaviour of granular columns. *Geosynthetics International*, 17(3):132-143.
- Mohapatra, S.R.; Rajagopal, R. & Sharma, J. (2017). 3-Dimensional numerical modeling of geosynthetic-encased granular columns. *Geotextiles and Geomembranes*, 45(3):131-141.
- Pulko, B.; Majes, B. & Logar, J. (2011). Geosynthetic-encased stone columns: Analytical calculation model. *Geotextiles and geomembranes*, 29(1):29-39.
- Raithel, M. (1999). Zum Trag- und Verformungsverhalten von geokunststoffummantelten Sandsäulen. Kassel, Germany, Heft 6.: In: *Schriftenreihe Geotechnik*. Universität Gesamthochschule Kassel.

- Raithel, M. & Kempfert, H.G. (2000). Calculation models for dam foundations with geotextile coated sand columns. Proc. International Conference on Geotechnical and Geological Engineering, Melbourne.
- Raithel, M.; Kempfert, H.G. & Kirchner, A. (2002). Geotextile-Encased Columns (GEC) for foundation of a dyke on very soft soils. Proc. Seventh International Conference on Geosynthetics, pp. 1025-1028.
- Rowe, P.W. (1962). The stress-dilatancy relation for static equilibrium of an assembly of particles in contact. Proceedings of the Royal Society, pp. 500-527.
- Santos, C.T. (2011). Rational Analysis of Consolidation in Geosynthetic Encased Columns Foundation System. PhD Thesis, Instituto Tecnológico de Aeronáutica, 304 p.
- Schanz, T.; Vermeer, P.A. & Bonnier, P.G. (1999). The hardening soil model: Formulation and verification. Beyond 2000 in computational geotechnics. In: 10 years of PLAXIS. Balkema, Rotterdam, pp. 1-16.
- Schnaid, F.; Winter, D.; Silva, A.E.; Alexiew, D. & Kuster, V. (2017). Geotextile encased columns (GEC) used as pressure-relief system. Instrumented bridge abutment case study on soft soil. Geotextiles and Geomembranes, 45(3):227-236.
- Wang, G. (2009). Consolidation of soft clay foundations reinforced by stone columns under time-dependent loadings. Journal of Geotechnical and Geoenvironmental Engineering, 135(12): 1922-1931.
- Yoo, C. (2015). Settlement behavior of embankment on geosynthetic-encased stone column installed soft ground - A numerical investigation. Geotextiles and Geomembranes, 43(6):484-492.
- Zhang, L. & Zhao, M. (2014). Deformation analysis of geotextile-encased stone columns. Int. J. Geomech, 15(3):1-10.

### List of Symbols

- $H_{emb}$  = height of embankment  
 $H_s$  = length of unit cell  
 $J$  = tensile modulus of geotextile  
 SCR = stress concentration ratio  
 $q$  = total applied stress  
 $q_c$  = applied stress shared by column  
 $q_s$  = applied stress shared by soil  
 $r_c$  = radius of column  
 $r_e$  = radius of zone of influence of column cylinder  
 $\alpha$  = area replacement ratio  
 $\Delta r_c$  = lateral bulging of column  
 $\varepsilon_{rc}$  = radial strain of column  
 $\gamma_{sat}$  = saturated unit weight  
 $E'$  = drained elastic modulus  
 $E_{oed}^{ref}$  = oedometric modulus of soft soil  
 $E_{50}^{ref}$  = secant modulus/triaxial modulus of soft soil  
 $E_{ur}^{ref}$  = unload-reload modulus of soft soil  
 $c'$  = effective cohesion  
 $\phi'$  = drained frictional angle  
 $m$  = power of stress dependency of stiffness  
 $\psi$  = dilatancy angle  
 $\nu'$  = effective Poisson's ratio  
 $K_0$  = lateral earth pressure coefficient  
 OCR = overconsolidation ratio  
 $P^{ref}$  = reference mean stress



# On the Compatibility and Theoretical Equations for Mixtures of Tropical Soils and Bentonite for Barrier Purposes

T.L.C. Morandini, A.L. Leite

**Abstract.** Vast regions of the globe are covered by tropical soils, increasing the perspective of using them for barrier design at solid/liquid disposal facilities. They comprise diverse pedological taxonomies, but have common features, specially the dominant mineral composition of quartz, kaolinite clay and Fe-Al-Mn oxides/hydroxides. Despite the vast occurrence, sometimes tropical soil samples may not be suitable for barrier purposes, which can be overcome using bentonite as additive, provide that technical evaluations are adopted. An important technical issue to be addressed is the compatibility between the barrier materials and the liquids to be disposed. Compatibility studies usually involve laboratory testing using direct and indirect methods, which were involved in this research. The indirect studies involved modified Atterberg limits and the direct approach was developed using direct permeation. The tropical soil samples were selected to be in different weathering stages, considering the laterization degree. The chosen bentonite content to compose the mixtures was 3, 6, 9 and 12% on a dry weight basis. The elected chemical solutions for these studies were: calcium chloride ( $\text{CaCl}_2$ ), nitric acid ( $\text{HNO}_3$ ), sodium hydroxide ( $\text{NaOH}$ ), ethanol ( $\text{C}_2\text{H}_5\text{OH}$ ) and tap water. As a summary, the main research objectives were: (1) comparison between direct and indirect methods for compatibility evaluation; (2) assessment of the influence of the bentonite content on the compatibility of tropical soil samples; (3) investigation of the influence of the laterization degree on compatibility and (4) evaluation of theoretical equations to predict the compatibility of these samples through back analysis. The results indicate that: indirect and direct methods are similar from a qualitative point of view; bentonite is more sensitive to chemicals than the natural soil components; the laterization degree is not so influential on the compatibility and good compatibility predictions were obtained with the proposed theoretical equations.

**Keywords:** bentonite, clayey barriers, compatibility predictions, modified Atterberg limits, theoretical equations, tropical soils.

## 1. Introduction

Tropical soils cover approximately 2.5 billion hectares on the globe (IBGE, 2005), a number that alone demonstrates the great potential of these materials for civil construction. They result from intensive weathering and pedological processes, mainly laterization, driven by the hot and humid climate of the tropics (Van Breemen & Buurman, 2003). Laterization leads to peculiar mineralogy, mainly composed of quartz, kaolinite and Fe-Al-Mn oxides/hydroxides, standing on a very loose and porous structure.

The similarity in terms of mineralogical composition of tropical soil samples is not reflected by their variety of pedological classifications, as showed by the taxonomies presented on Table 1. Since these terms are not familiar to the geotechnical community, precious information is often neglected in the engineering practice.

Nogami & Vilibor (1995) have drawn the attention of the geotechnical community to the potentiality of the pedologic taxonomies for used in pavement works. Having the laterization degree and grain size distribution as the main attributes, they proposed the MCT (Miniature, Compacted,

Tropical) Classification SystemP for pavement purposes, which has been successfully applied in Brazil for decades.

This system is based on the results of the laboratory compaction test Mini-MCV (Moisture Condition Value) and the weight loss by immersion in water. The main soil orders of the MCT system refers to sandy, clayey, lateritic and non-lateritic soil specimens. Usually, the lateritic character is favorable for compaction. Later, Vertamatti (1998) introduced a transitional order between the lateritic and non-lateritic soils, calling the new system MCT-M, which will be used later in this study.

Sometimes, however, the decrease in hydraulic conductivity ( $k$ ) induced by compaction may not be sufficient for barriers, as pointed out by Lukiantchuki & Esquivel (2010). In these cases, the use of bentonite as admixture is interesting, considering the well-known ability of this clay to reduce hydraulic conductivity and increase sorption (*e.g.* Ebina *et al.*, 2004; Akbulut & Saglamer, 2004; Osinubi & Nwaiwu, 2006; Osinubi *et al.*, 2009; Morandini & Leite, 2013; Akcanca & Aytakin, 2014; Morandini & Leite, 2015a).

Thiago Luiz Coelho Morandini, Ph.D., Associate Professor, Departamento de Engenharia Civil, Centro Federal de Educação Tecnológica de Minas Gerais, Belo Horizonte, MG, Brazil. e-mail: thiagomorandini@des.cefetmg.br.

Adilson do Lago Leite, Ph.D., Associate Professor, Departamento de Engenharia Civil, Universidade Federal de Ouro Preto, Ouro Preto, MG, Brazil. e-mail: adilsonlagoleite@gmail.com.

Submitted on August 8, 2018; Final Acceptance on November 9, 2018; Discussion open until April 30, 2019.

DOI: 10.28927/SR.413345

**Table 1** - Pedologic orders of tropical soils according to different taxonomies (Source: Morandini & Leite, 2015a).

Brazilian Soil Classification System	WRB/FAO	U.S. Taxonomy
Latosols	Ferralsols	Oxisols
Claysols	Lixisols	Ultisols
	Acrisols	
	Alisols	Oxisols / Ultisols
Nitisols	Nitisols	Oxisols / Ultisols
Plintosols	Plinthosols	Oxisols

Another important issue for barrier design is the capacity of the compacted clay liner (CCL) to maintain its properties after contacting with the different contaminant fluids to be disposed. For instance, these contaminant solutions may involve municipal solid waste leachate, urban sewage, effluents from industrial and mining activities and others. This capacity is called “liner compatibility”, which is very important for the long term performance of the barrier.

It is clear that compatibility depends upon complex soil-fluid interactions, which are not easy to identify and understand. So, most of the methods for investigating compatibility aim to recognize the changes in the mechanical properties of the soil specimens, instead of identifying specific “solid-fluid” reactions that take place mainly at the microscopic scale.

Laboratory works on compatibility are often classified as “indirect” and “direct” methods (Shackelford, 1994). The indirect methods investigate the changes in soil index properties, such as Atterberg Limits, for instance, after contact with the aggressive fluids that will be disposed. It only gives a perspective of the soil compatibility, once the “direct properties” of the soil that are involved in the barrier performance are not directly evaluated, such as hydraulic conductivity, swelling potential, shear strength and others.

Examples of the application of indirect methods for clays (bentonite and kaolinite) and tropical soils, using different chemical solutions (organic, saline, acid and alkaline), can be found on Bowders & Daniel (1987), Budhu *et al.* (1990), Egloffstein (2001), Farnezi & Leite (2007), Bouazza *et al.* (2007) and Katsumi *et al.* (2008). These authors have used modified Atterberg limits and/or free swelling tests for evaluating compatibility, finding a reduction in the plasticity as well as in the swelling potential of the clays, particularly when saline solutions and concentrated organic solutions with low dielectric constant were percolated. They have also concluded that the liquid limit was more sensitive than the plastic limit, and divalent ions had preference over monovalent ions. Most of these conclusions were consistent with the expected effect of the reduction in the double-layer thickness of clay particules, as pointed out by Mitchell (1993).

Direct studies, in turn, evaluate the changes induced by the contaminant liquids in properties that will be directly involved in the barrier performance. They certainly provide a more realistic scenario of what the barrier will face in the field, as pointed out by Budhu *et al.* (1990), Shackelford (1994), Shackelford *et al.* (2000) & Kinsela *et al.* (2010). Nevertheless, percolating soil with chemical solutions is not always feasible, since the laboratory testing apparatus must resist corrosion and other possible damage caused by the chemicals from the contaminant solutions. As most of the ordinary equipment found in conventional geotechnical laboratories may not support these solutions, direct percolation sometimes is restricted.

Interesting reports on the direct percolation of chemical solutions on clayey soil samples can be found in Stewart *et al.* (2003), Sunil *et al.* (2006 & 2009), Nayak *et al.* (2007), Katsumi *et al.* (2008) and Kinsela *et al.* (2010). Those papers have demonstrated that organic and salty solutions, as well as actual and synthetic leachates have reduced the plasticity and increased the hydraulic conductivity of the studied soil samples.

Morandini & Leite (2015a,b) describe the modifications imposed to tropical soils, a result of the bentonite addition, in terms of hydraulic conductivity and shear strength, respectively. The studied soil samples were lateritic, transitional and non-lateritic specimens of tropical soils according to the MCT-M system (Vertamatti, 1998), using bentonite proportions of 0, 3, 6, 9 and 12% (dry weight basis) to compose mixtures. Laboratory works have included: 1) mineralogical, geotechnical and chemical characterization; 2) estimation of hydraulic conductivity (flexible-wall permeameter); 3) shear strength and 4) direct and indirect compatibility. The findings of the items 1 through 3 have been described by Morandini & Leite (2015a,b), while compatibility (item 4) is treated in the present paper.

So, direct and indirect compatibility studies were performed using the following chemical solutions: calcium chloride ( $\text{CaCl}_2$ ), nitric acid ( $\text{HNO}_3$ ), sodium hydroxide ( $\text{NaOH}$ ), ethanol ( $\text{C}_2\text{H}_5\text{OH}$ ) and tap water. As a summary, the research objectives of this specific study were: (1) comparison between direct and indirect methods for compatibility evaluation; (2) assessment of the influence of the bentonite content on the compatibility of tropical soil sam-

ples; (3) investigation of the influence of the laterization degree on the compatibility and (4) evaluation of theoretical equations to predict the compatibility of these samples through back analysis.

## 2. Theoretical Propositions

As mentioned before, in spite of the variety of the pedological orders of the tropical soils showed on Table 1, their mineralogical composition is dominated by quartz, kaolinite and Fe-Al-Mn oxides/hydroxides. The concentration of oxides/hydroxides can be part of the parental rock heritage, but it is also related to the stage of the weathering process (mainly hydrolysis) and pedological evolution.

In terms of electrical charges, the clay fraction of tropical soils is a mix of permanent charged minerals mainly provided by the kaolinite clay, with variable charged solids, such as Fe-Al-Mn oxide/hydroxide (Yong *et al.*, 1992 and Yu, 1997). Most of the permanent charges of the kaolinite are negative and result from isomorphous substitution and lattice breaking at the mineral genesis (Yong *et al.*, 1992). The variable charges, in turn, are related to the specific sorption of the radicals  $H^+$  and  $OH^-$  from the water molecule breaking, mainly controlled by the pH conditions of the soil solution (Grim, 1968 and Yu, 1997).

The constant charge density ( $\sigma_p$ ) at the midpoint distance between two clay particles on the clay-electrolyte system can be modeled by Eq. 1 (Mitchell, 1993), where  $c_{i0}$  is the ionic concentration (ions/m<sup>3</sup>),  $z_i$  the ionic valence,  $e$  the electric charge ( $1.602 \times 10^{-19}$  Coulomb),  $\psi$  the electric potential,  $k$  the Boltzmann constant ( $1.38 \times 10^{-23}$  JK<sup>-1</sup>) and  $T$  the absolute temperature (in Kelvins). Equation 1 is usually referred as the Guy-Chapman model (Mitchell, 1993) and can be used also on the estimation of variable charge density of variable charge soils ( $\sigma_v$ ), but in this case the electric potential ( $\psi$ ) is constant (Yu, 1997).

As pointed out by Mitchell (1993), two equations were used to compose Eq. 1: (1) the potential function ( $\psi_0$ ), expressed by Eq. 2, being  $x$  a dimensional quantity equivalent to  $1 \text{ \AA}$ ,  $e$  the electronic charge, and (2)  $(1/\lambda)$  the distance function which is related to the electric permittivity ( $\epsilon$ ), as can be seen in Eq. 3.

$$\sigma_p = \sqrt{8c_{i0}\epsilon kT} \sinh \frac{z_i e \Psi}{2kT} \quad (1)$$

$$\Psi_0 = \frac{z_i e \Psi}{kT} \quad (2)$$

$$\frac{1}{\lambda^2} = \frac{2c_{i0}z_i^2 e^2}{\epsilon kT} \quad (3)$$

The quantity  $\lambda$  expresses the physical space of the gravity centroid between two charged particles and represents the ionic double layer thickness, which can be calculated using Eq. 4, where  $\epsilon_0$  is the vacuum permittivity

( $8.85 \times 10^{-12} \text{ C}^2\text{J}^{-1}\text{m}^{-1}$ ) and  $D$  is the dielectric constant of the pore solution.

$$\lambda = \sqrt{\frac{\epsilon_0 D k T}{2c_{i0}z_i^2 e^2}} \quad (4)$$

Equations 1 through 4 show that the compatibility of clay can be influenced by the differences in the chemical composition of the pore solution, since the ionic double layer thickness and the plasticity and hydraulic properties of the soils are closely related.

The ionic double layer thickness is estimated using the ionic strength ( $I = 0.5\sum c_i z_i^2$ ) and the dielectric constant ( $D$ ) of the pore solution for constant temperature conditions (Bouazza *et al.*, 2007 and Katsumi *et al.*, 2008). Therefore, a theoretical compatibility index ( $R_{CB}$ ) was formulated to estimate the compatibility of pure bentonite samples by the correlation of the water ionic strength ( $I_0$ ) and dielectric constant ( $D_w$ ) to the pore solution parameters ( $I_{eq}$  and  $D_s$ ), as presented in Eq. 5. When the  $R_{CB}$  is one, full compatibility exists of the pore solution relative to water, while  $R_{CB}$  values smaller or greater than one indicate incompatibility.

$$R_{CB} = \sqrt{\frac{I_0 D_s}{I_{eq} D_w}} \quad (5)$$

As suggested by Bolt (1955),  $I_0 = 0.25 \text{ M}$  for pure sodium bentonite clay; in turn,  $I_{eq}$  can be estimated by the geometric mean between the ionic strength of the water ( $I_0$ ) and pore solution ( $I_s$ ), multiplied by the cation activity ( $\alpha$ ), as presented in Eq. 6 (Langmuir, 1997).

$$I_{eq} = \sqrt{\alpha I_0 I_s} \quad (6)$$

As mentioned before, calcium chloride ( $\text{CaCl}_2$ ) 1 M and ethanol ( $\text{C}_2\text{H}_5\text{OH}$ ) solutions were used in the indirect and direct compatibility tests of this research, so the  $R_{CB}$  values for these solutions were estimated as follows.

Considering the  $\text{CaCl}_2$  1 M solution:  $I_s = 2.0 \text{ M}$ ;  $\alpha_{Ca} = 0.293$ ;  $\alpha_{Na} = 0.734$ , which leads to  $I_{eq} = 0.607$  and  $R_{CB} = 0.64$ . For the ethanol solution, the dielectric constant ( $D$ ) is 24.3, resulting in  $R_{CB} = 0.55$ . In these cases, the theoretical compatibility for both solutions is smaller than one, which indicates loss of plasticity, being the ethanol solution more "incompatible" to the bentonite sample than the  $\text{CaCl}_2$  1 M solution.

Since the premises adopted for calculating the  $R_{CB}$  by Eq. 5 cannot be directly applied to the mixtures (bentonite + tropical soil), an expedite model ( $R_{CM}$ ) was formulated using the proportion of bentonite clay (%B) of the mixture and also its natural clay content, which is almost exclusively composed of kaolinite. As this last clay presents an interlayer expansion length in the order of 7 to 12  $\text{\AA}$ , while for the bentonite it is 80  $\text{\AA}$ , it is reasonable to think that the effect of any pore solution to the kaolinite clay is only 15%

(12 Å/80 Å) compared to the bentonite, as presented by Eq. 7.

### 3. Materials and Methods

#### 3.1. Summary of the sample properties

The bentonite clay used in the tests is commercially available in Brazil with the denomination Brasgel PA<sup>®</sup>. The soil samples of lateritic, transitional and non-lateritic behavior, according to the abacus of Vertamatti (1998), were collected in the vicinities of Ouro Preto, state of Minas Gerais, Brazil.

Mixtures using these soils and the commercial bentonite were manually composed. The sampling locations and preparation, as well as the mixing and characterization methods and results are fully reported by Morandini & Leite (2015a). Table 2 presents only the sample designations, including the bentonite proportions of the mixtures (dry weight basis), and Table 3 reprints a summary of the geotechnical and physicochemical properties as presented by Morandini & Leite (2015a).

#### 3.2. Indirect compatibility tests

Modified plastic ( $\omega_p$ ) and liquid ( $\omega_L$ ) limits were determined in the laboratory using the solutions and concentrations described next, as they represent the classes of organic and inorganic liquids miscible in water presented by Shackelford (1994). The test procedures followed the Brazilian standards NBR 6459 (ABNT, 2016) for the laterite and NBR 7180 (ABNT, 2016) for the former. Special care was taken for handling these solutions because of their aggressive nature.

- Water: tap water
- Salt: CaCl<sub>2</sub> at the concentration of 1 M (ionic strength = 2 M = 40.1 mg/L),
- Organic: Ethanol (C<sub>2</sub>H<sub>5</sub>OH), PA (dielectric constant = 24.3)
- Acid: HNO<sub>3</sub> diluted to pH = 3
- Base: NaOH diluted to pH = 11

Besides measuring  $k$  in the laboratory with different permeation fluids, this parameter was also estimated theoretically ( $k_M$ ) through the proposition of Morandini & Leite (2015a) shown in Eq. 10. It is a variation of the well-known

Kozeny-Carman (KC) equation that includes the mesoplastic point (MP), the  $C_{KC}$  coefficient (a shape factor related to the geometry of the soil pores);  $\gamma/\mu_f$ , respectively for the unit weight and dynamic viscosity of the percolating fluid;  $e$  the soil void ratio and  $a$  and  $b$ , the linearization parameters for these soil samples as referred in Morandini & Leite (2015a). The characteristic equations that resulted from Eq. 10 are described by the equations 11, 12 and 13 for the samples SL, ST and SN, respectively.

$$k_M = C_{KC} \frac{\gamma_f e^3}{\mu_f 1+e} aMP^b \quad (10)$$

$$k_M = C_{KC} \frac{\gamma}{\mu} \frac{e^3}{1+e} 8.32 \times 10^{-4} MP^{-4.48} \quad (11)$$

$$k_M = C_{KC} \frac{\gamma}{\mu} \frac{e^3}{1+e} 2.95 \times 10^2 MP^{-7.56} \quad (12)$$

$$k_M = C_{KC} \frac{\gamma}{\mu} \frac{e^3}{1+e} 4.68 \times 10^1 MP^{-7.26} \quad (13)$$

#### 3.3. Direct compatibility tests

##### 3.3.1. Sample preparation

Compacted soil specimens of the mixtures were prepared under Normal Proctor energy at 2% wet of optimum moisture content using the tested chemical solutions and tap water. These compaction effort and moisture content are ordinary for landfill liner construction in Brazil and many other countries. The specimens were 5 cm in diameter and 10 cm high. Their bentonite content (dry weight basis) was chosen according to the criterion that they must show a minimum  $k$ -value of  $5 \times 10^{-8}$  cm/s under an effective confining stress of 40 kPa. This  $k$ -value meets most of the international standards for barrier design (Koch, 2002), and the confining stress of 40 kPa is ordinary for municipal solid waste landfills. So, according to Fig. 1, the proportions that meet these criterion on a dry weight basis, called here as “optimum bentonite content”, were: SL<sub>OT</sub> = 9%; ST<sub>OT</sub> = 4% and SN<sub>OT</sub> = 2%.

**Table 2** - Sample designation and bentonite proportions (dry weight basis).

Lateritic samples		Transitional samples		Non-lateritic samples	
Designation	Bentonite (%)	Designation	Bentonite (%)	Designation	Bentonite (%)
SL	0.0	ST	0.0	SN	0.0
SL03	3.0	ST03	3.0	SN03	3.0
SL06	6.0	ST06	6.0	SN06	6.0
SL09	9.0	ST09	9.0	SN09	9.0
SL12	12.0	ST12	12.0	SN12	12.0

**Table 3** - Summary of the geotechnical and physicochemical properties of the samples (Reprinted from Morandini & Leite, 2015a).

Property	Sample															
	SL	SL03	SL06	SL09	SL12	ST	ST03	ST06	ST09	ST12	SN	SN03	SN06	SN09	SN12	BENT
Liquid limit $\omega_L$ (%)	23	42	57	72	87	52	78	96	117	156	56	76	96	117	136	683
Plastic limit $\omega_p$ (%)	12	21	23	26	27	30	28	29	27	28	31	34	37	40	44	91
Plasticity index $PI$ (%)	11	21	33	47	60	22	50	67	90	128	25	42	59	76	92	592
Mesoplastic point $MP$ (%)	17	32	40	49	57	41	53	62	72	92	44	55	67	79	90	387
Density of solids $\rho_s$ (g/cm <sup>3</sup> )	2.90	2.89	2.88	2.86	2.84	2.84	2.83	2.82	2.80	2.79	2.76	2.75	2.74	2.73	2.72	2.45
Grain size (%)																
Clay	29	29	30	30	31	41	39	41	41	42	36	38	42	44	46	91
Silt	16	18	17	20	17	9	10	9	9	8	10	11	11	11	12	9
Fine sand	35	34	34	29	28	36	17	17	18	19	23	20	20	19	20	0
Medium sand	16	15	15	15	17	8	27	26	25	24	18	19	19	17	14	0
Coarse sand	3	3	4	5	7	5	6	6	6	6	10	9	6	6	6	0
Gravel	1	1	0	1	0	1	1	1	1	1	3	3	2	3	2	0
USCS classification	CL	CL	CH	CH	CH	MH	CH	CH	CH	CH	MH	CH	CH	CH	CH	CH
Activity (Skempton)	0.38	0.71	1.11	1.55	1.94	0.54	1.28	1.63	2.19	3.05	0.68	1.10	1.39	1.73	2.01	6.50
Normal proctor compaction																
$\rho_{dmax}$ (g/cm <sup>3</sup> )	1.82	1.81	1.79	1.78	1.76	1.62	1.66	1.62	1.60	1.59	1.62	1.61	1.60	1.59	1.58	*NR
$w_{or}$ (%)	12.5	14.5	16.2	17.8	19.1	21.5	22.5	23.3	24.0	24.8	22.2	23	23.6	24.4	25.1	*NR
Saturation at $w_{or}$ (%)	61.0	70.5	77.0	83.8	88.6	88.4	89.8	88.8	89.7	91.4	87.1	89.2	90.3	92.5	94.3	*NR
Cation exchange capacity (cmol/kg)	3.6	6.2	9.8	12.9	15.7	6.9	13.5	18.6	25.3	36.0	7.9	11.6	16.0	20.3	24.8	99.4
pH at 1:2.5 soil:solution $H_2O$ v( $H_2O$ )	5.35	6.19	7.14	8.03	8.79	5.15	7.76	8.24	8.63	8.96	4.84	5.65	6.68	7.47	8.24	9.92
pH at 1:2.5 soil:solution KCl (KCl)	6.16	6.44	6.86	7.54	7.93	5.21	5.94	6.58	7.06	7.33	4.60	5.03	5.43	6.00	6.39	8.77
$\Delta$ pH	0.81	0.25	-0.28	-0.49	-0.86	0.06	-1.82	-1.66	-1.57	-1.63	-0.24	-0.62	-1.25	-1.47	-1.85	-1.15
Electrical cond. (mS/cm)	0.09	0.28	0.5	0.67	0.84	0.05	0.43	0.68	0.87	0.97	0.08	0.44	0.78	1.02	1.35	1.3
Specific Ssrface - $S_s$ (m <sup>2</sup> /g)	28.2	48.4	76.3	100.4	122.3	53.8	105.3	145.6	197.3	281.3	61.3	90.5	124.7	158.7	193.6	775.9

\*NR - Not Rated.

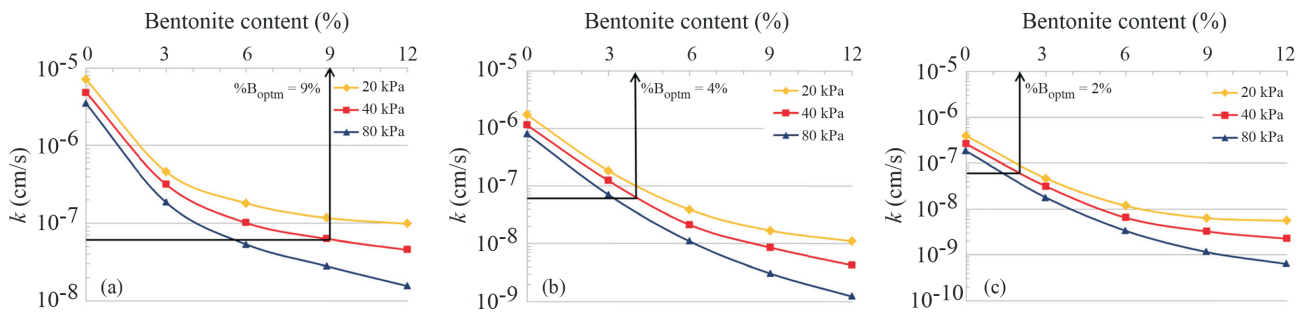


**Figure 1** - Bentonite content necessary to achieve a hydraulic conductivity of  $5 \times 10^{-8}$  cm/s under a confining stress of 40 kPa, called “optimum bentonite content”: (a)  $SL_{OT}$  sample; (b)  $ST_{OT}$  sample and (c)  $SN_{OT}$  sample (Morandini & Leite, 2015a).

3.3.2. Inert permeability cells

Flexible wall permeability tests under constant head conditions were applied to determine the  $k_w$  and  $k_f$  of the samples. Usually these cells are an adaptation from the conventional triaxial cells, that usually have many metallic parts vulnerable to corrosion when chemical solutions are percolated. To avoid corrosion, two “inert” triaxial cells were designed using only plastic materials, one for permeability determination and the other as a solution reservoir (Fig. 2). The parts of this new equipment are described next:

- Not welded walls made of acrylic (polymethyl-methacrylate);
- Base and top made of high density nylon;
- 0.5” low density polyethylene tubes;
- Stainless steel connections.

3.3.3. Test conditions

The schematic of the test apparatus used in soil percolation is depicted in Fig. 3. Pressure application systems were installed at the base ( $p_1$ ) and over the top ( $p_2$ ) of the soil specimens, along with the confining pressure system ( $\sigma_3$ ). A transducer for pore pressure ( $u$ ) monitoring and an elec-

tronic gage for flow measurement were also coupled to the triaxial cell.

The test method followed the recommendations of Head (1986) and Morandini & Leite (2013), including backpressure saturation and pre-consolidation of the samples using the chemical solutions and tap water as permeation fluid. The backpressure saturation was limited to 300 kPa and full saturation was considered when the Skempton  $B$  parameter reached a minimum of 0.94. In turn, pre-consolidation was induced by applying a total confining stress ( $\sigma_3$ ) of 323 kPa, leading to a constant effective confining stress ( $\sigma'_3$ ) of 40 kPa, used for pre-consolidation as well as for percolation.

Once these procedures were terminated, percolation was imposed to the soil specimens by the application of a  $p_1$  of 300 kPa, while  $p_2$  was kept constant at 250 kPa. These conditions have produced a porepressure ( $u$ ) of 283 kPa, a hydraulic head of 50 kPa and a hydraulic gradient ( $i$ ) in the order of 50. So,  $k$  values were determined using Darcy’s Law under constant head conditions.

Some aspects of these tests must be highlighted, as pointed out in Morandini & Leite (2013): (1) because of op-

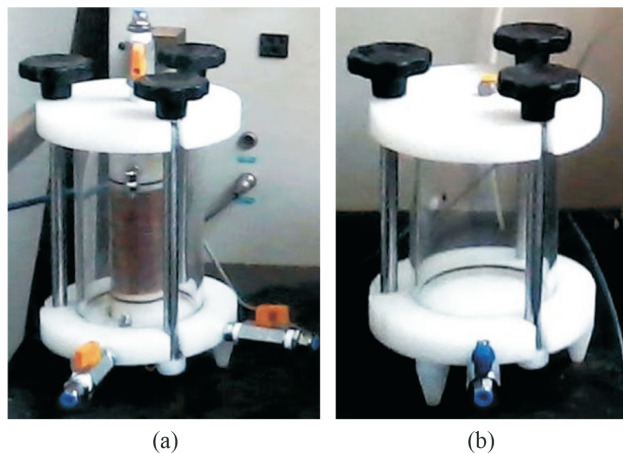


**Figure 2** - Inert triaxial chambers: (a) triaxial chamber and (b) solution reservoir.

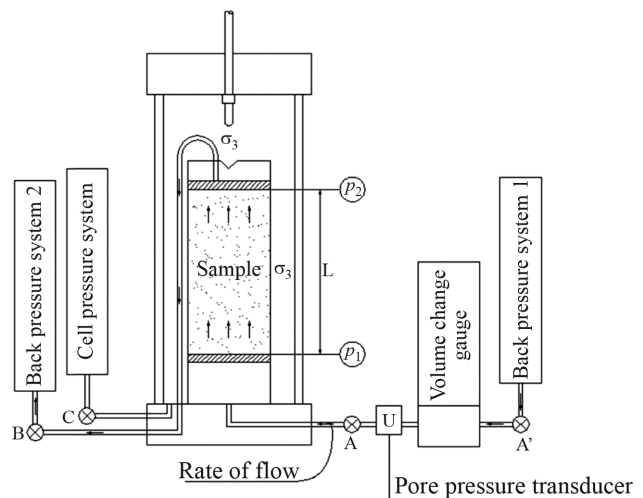


**Figure 3** - Schematic of the apparatus used in the percolation tests (Reprinted from Morandini & Leite, 2013).

erational reasons, including difficulties in soil compaction, moulding, saturation and consolidation, the hydraulic conductivity of the pure bentonite samples was not measured; (2) the rule  $\sigma_3 > p_1 > p_2$  has been complied with to avoid soil liquefaction induced by excessive pore pressure increase; (3) the reported  $k_w$  and  $k_f$  values are the arithmetic average of 3 measures.

## 4. Results and Discussion

### 4.1. Indirect compatibility

Some of the bentonite properties are presented in Table 4, including the conventional and modified Atterberg limits, the mesoplastic point (MP), the indirect compatibility index ( $R_c$ ) and the bentonite theoretical compatibility index ( $R_{CB}$ ). As the pH variation induced by the acid and alkaline solutions was not incorporated into the compatibility model of Eq. 7, the  $R_{CB}$  was not calculated for the  $HNO_3$  and NaOH solutions.

It is clear from Table 4 that the ethanol ( $C_2H_5OH$ ) and calcium chloride ( $CaCl_2$ ) solutions had the major influence on the plasticity of the bentonite sample relative to the other solutions, as demonstrated by the variation of the  $R_c$  and  $R_{CB}$  values. It must be also pointed out the similarity between the theoretical compatibility index ( $R_{CB}$ ) and the laboratory mesoplastic-point-based compatibility index ( $R_c$ ) for these last solutions.

As can be seen in Fig. 4, the influence of the solutions on the bentonite properties was more accentuated for the

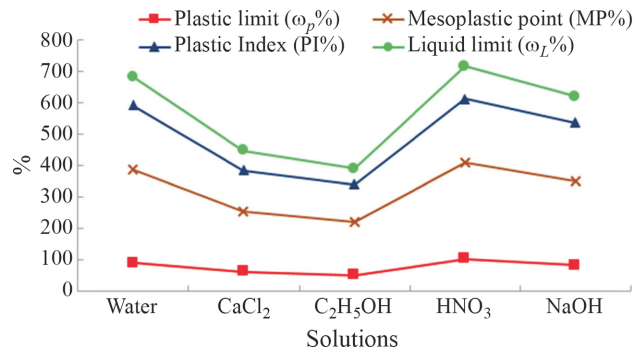


Figure 4 - Bentonite properties with different chemical solutions.

liquid limit compared to the plastic limit, which has reflected also in the shape of the PI and MP curves. This result was consistent with the literature, as mentioned in the Introduction section.

Table 5 and Fig. 5 present the conventional and modified Atterberg limits as well as the  $R_c$  values for the tropical soilsamples and their mixtures.

Figure 5 illustrates that the use of water as the molding fluid for the natural soilsamples (SL, ST and SN) resulted in a small variation between the modified and conventional Atterberg limits, so it is concluded that the bentonite clay content was the main responsible for the increase in their incompatibility.

Figure 6 depicts the relation  $R_c$  vs. bentonite content of the soil samples and some excerpts of these diagrams are

Table 4 - Bentonite properties.

Properties	Chemical solutions				
	Water	CaCl <sub>2</sub>	C <sub>2</sub> H <sub>5</sub> OH	HNO <sub>3</sub>	NaOH
Liquid limit ( $\omega_L$ %)	683	447	391	715	620
Plastic limit ( $\omega_p$ ) (%)	91	63	52	103	83
Plasticity Index (PI) (%)	592	384	340	612	537
Mesoplastic Point (MP) (%)	387	255	221	409	352
Indirect compatibility Index ( $R_c$ )	1.00	0.66	0.57	1.06	0.91
Theoretical compatibility Index ( $R_{CB}$ )	1.00	0.64	0.55	-	-

Table 5 - Conventional and modified Atterberg limits for the tropical soils and their mixtures with bentonite.

Solution	Soil samples														
	SL	SL03	SL06	SL09	SL12	ST	ST03	ST06	ST09	ST12	SN	SN03	SN06	SN09	SN12
	$\omega_L$ (%)														
Water	23	42	57	72	87	52	78	96	117	156	56	76	96	117	136
CaCl <sub>2</sub>	22	39	53	66	80	51	75	90	107	137	55	74	89	106	120
C <sub>2</sub> H <sub>5</sub> OH	21	38	52	65	77	50	74	89	105	134	54	73	88	104	118
HNO <sub>3</sub>	22	42	56	74	88	52	79	96	118	158	56	75	95	108	138
NaOH	22	41	55	69	83	51	76	94	113	150	55	75	93	114	130

Table 5 - cont.

Solution	Soil samples														
	SL	SL03	SL06	SL09	SL12	ST	ST03	ST06	ST09	ST12	SN	SN03	SN06	SN09	SN12
$\omega_p$ (%)															
Water	12	21	23	26	27	30	28	29	27	28	31	34	37	40	44
CaCl <sub>2</sub>	11	21	22	24	25	29	27	27	25	24	30	33	35	36	39
C <sub>2</sub> H <sub>5</sub> OH	12	20	21	23	24	29	26	27	25	24	30	33	34	36	38
HNO <sub>3</sub>	12	21	23	26	28	29	28	29	28	29	32	34	37	41	45
NaOH	12	21	23	25	26	29	27	28	28	26	31	34	36	39	42
PI (%)															
Water	11	21	33	47	60	22	50	67	90	128	25	42	59	76	92
CaCl <sub>2</sub>	12	19	31	43	55	22	48	63	82	113	24	41	55	70	81
C <sub>2</sub> H <sub>5</sub> OH	9	18	31	42	53	21	47	62	80	110	24	40	54	68	80
HNO <sub>3</sub>	11	21	33	47	61	23	51	67	91	129	24	41	58	67	93
NaOH	11	20	32	44	57	22	49	66	86	124	24	41	57	75	88
$R_c$															
Water	1.0	1.0	1.0	1.0	1.0	1.0	1.0	1.0	1.0	1.0	1.0	1.0	1.0	1.0	1.0
CaCl <sub>2</sub>	0.95	0.95	0.93	0.92	0.91	0.98	0.96	0.94	0.92	0.88	0.97	0.97	0.97	0.91	0.88
C <sub>2</sub> H <sub>5</sub> OH	0.93	0.92	0.91	0.90	0.88	0.97	0.95	0.93	0.90	0.86	0.97	0.97	0.96	0.89	0.87
HNO <sub>3</sub>	0.98	1.00	0.99	1.02	1.01	0.99	1.01	1.01	1.02	1.01	1.01	1.01	0.98	0.95	1.02
NaOH	0.97	0.99	0.97	0.96	0.95	0.99	0.98	0.98	0.97	0.96	0.99	0.99	0.98	0.97	0.96

worth mentioning: (1) the addition of bentonite has led to an increase in the incompatibility of the soil samples denoted by the linear decrease of the  $R_c$  values, which corroborates the above analysis of Fig. 5; (2) a decrease in the  $R_c$  value indicates loss of plasticity relative to water, which was the case presented by the ethanol, calcium chloride and sodium hydroxide solutions; (3) the acidic solution resulted in a slight increase in the plasticity for the SL and ST samples, while it was oscillatory for the SN mixtures; (4) of all natural soil samples (without any bentonite addition), the SL sample had the greatest incompatibility denoted by the lowest  $R_c$  values along the ordinate axis; (5) in spite of the variability of the  $R_c$  values of the natural soils (0% of bentonite), as shown in Fig. 6(a), the similarity among all diagrams indicates that the laterization stage had little influence on the general compatibility.

Satisfactory correlations between laboratory  $R_c$  (Eq. 8) and theoretical  $R_{cM}$  (Eq. 7) for ethanol and calcium chloride solutions can be observed in Fig. 7, since differences of no more than 4% between these two variables were found. It is also observed that the best fit was reached for the SL sample (Figs. 7a and 7b).

In general terms, the  $R_c$  values for all soil samples and chemical solutions are in the range from 0.93 to 1.01, meaning more compatibility for these samples when compared with the pure bentonite clay values, whose values varied

from 0.57 (C<sub>2</sub>H<sub>5</sub>OH), 0.66 (CaCl<sub>2</sub>), 0.91 (NaOH) to 1.06 (HNO<sub>3</sub>).

The influence of the weathering stage of the natural soil samples on the compatibility was analyzed by plotting the weathering index  $K_i$  vs.  $R_c$  (Fig. 8).  $K_i$  is defined as  $1.7 \times \text{SiO}_2/\text{Al}_2\text{O}_3$  (IBGE, 2005), so a small  $K_i$  value refers to advanced weathering and vice versa. The  $K_i = 2.0$  of the kaolinite clays is taken as a reference.

The  $K_i$  index values for the samples SL, ST and SN are respectively 1.72, 2.36 and 3.08 (Morandini & Leite, 2015a), and no clear dependence of the  $R_c$  on  $K_i$  is observed since the curves for ST and SN are very similar.

#### 4.2. Direct compatibility

The laboratory hydraulic conductivity ( $k$ ) and the relative hydraulic conductivity measured with chemical solutions ( $k_r$ ) for the samples compacted at the "optimum bentonite content" are presented on Table 6. It is clear from this table that the permeation with the other chemical solutions increased  $k$  relative to water, as confirmed by their  $k_r$  values greater than one. An exception is made for the lateritic soil (SL<sub>OT</sub> sample), since its permeation with HNO<sub>3</sub> slightly reduced  $k$  relative to water ( $k_r < 1 = 0.87$ ).

The  $k_r$  values from Table 6 denote a significant increase (from 2.3 to 6.1) in  $k$  when the ethanol solution was permeated. Daniel & Liljestrand (1984), Fernandez & Quigley (1985), Daniel *et al.* (1993) and Shackelford (1994)

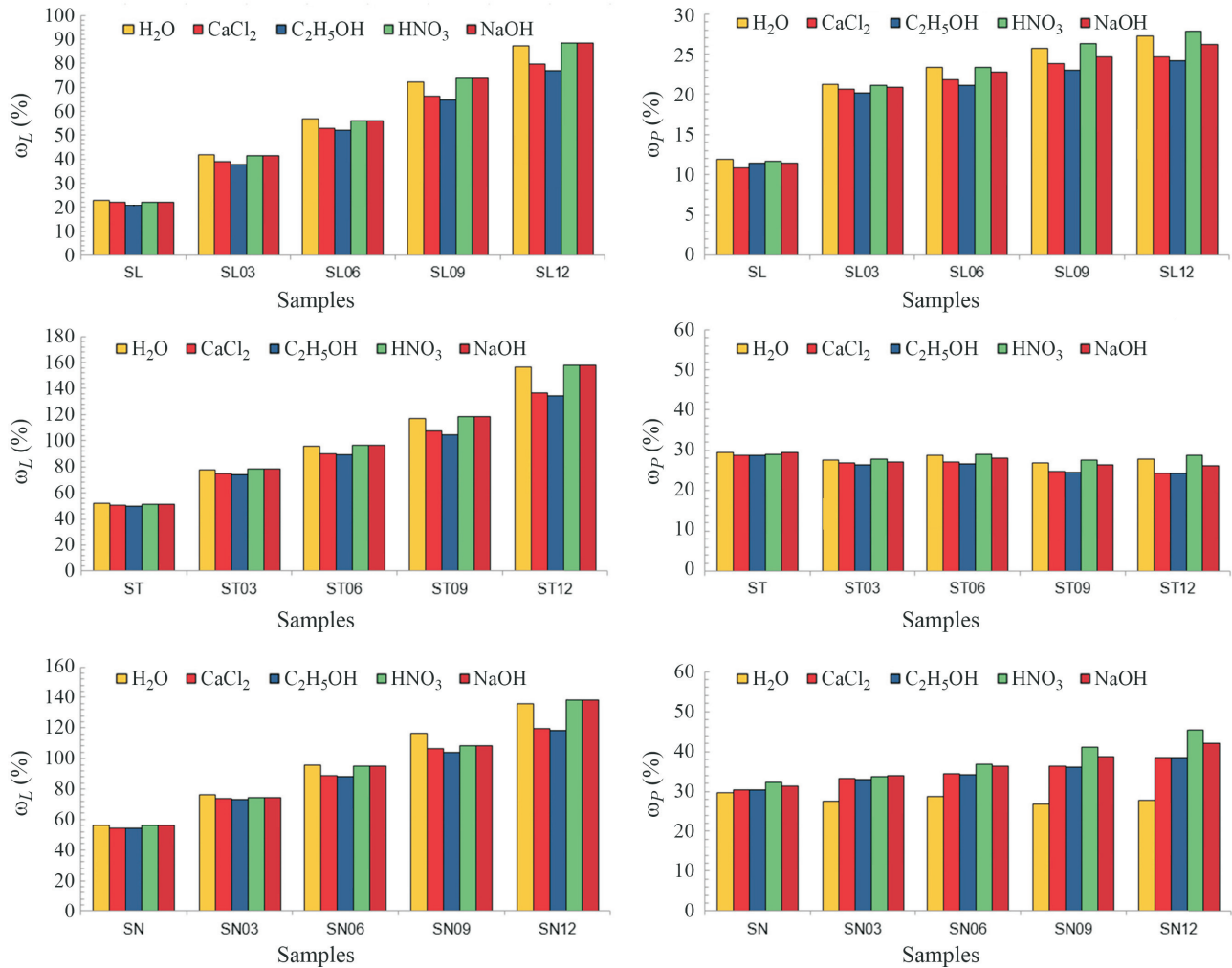


Figure 5 - Liquid limit ( $\omega_L$ ) and plastic limit ( $\omega_P$ ) for the tropical soils and their mixtures using water and other chemical solutions.

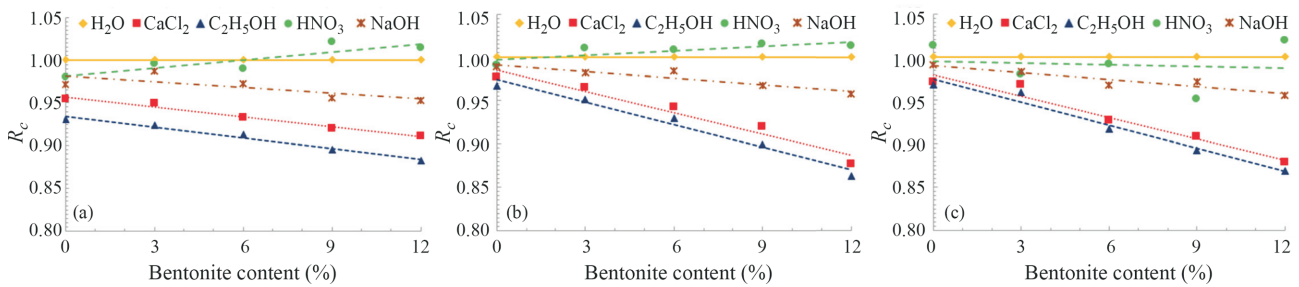


Figure 6 -  $R_c$  vs. bentonite content: (a) SL sample and its mixtures; (b) ST sample and its mixtures (c) SN sample and its mixtures.

also reported on the increase of  $k$  for different clays due to contact and percolation with organic solutions of low dielectric constant, as is the case of the ethanol PA reagent (24.3) used in this research.

A simple comparison between  $k_c$  values from Table 6 (direct compatibility) and  $R_c$  values from Table 5 and Fig. 5 (indirect compatibility) reveals the same order of incompatibility for all the samples and solutions, as follows:

$C_2H_5OH > CaCl_2 > NaOH > HNO_3$ . This fact increases the perspective of using the modified Atterberg limits as a preliminary tool for evaluating the compatibility of soils for barrier purposes.

Table 7 summarizes the soil parameters used estimate  $k_M$  values according to Eq. 11. A value  $C_{KC} = 0.2$  was applied as suggested by Chapuis & Albertin (2003) when dealing with clayey soils. Table 8 presents the mesoplastic point

(MP) values, the fluid parameters ( $\gamma/\mu$ ) and the resultant  $k_M$ . These MP values were calculated from Eqs. 5 through 7 for

the  $\text{CaCl}_2$  and  $\text{C}_2\text{H}_5\text{OH}$  solutions; laboratory MP values were used for  $\text{HNO}_3$  and  $\text{NaOH}$  solutions.

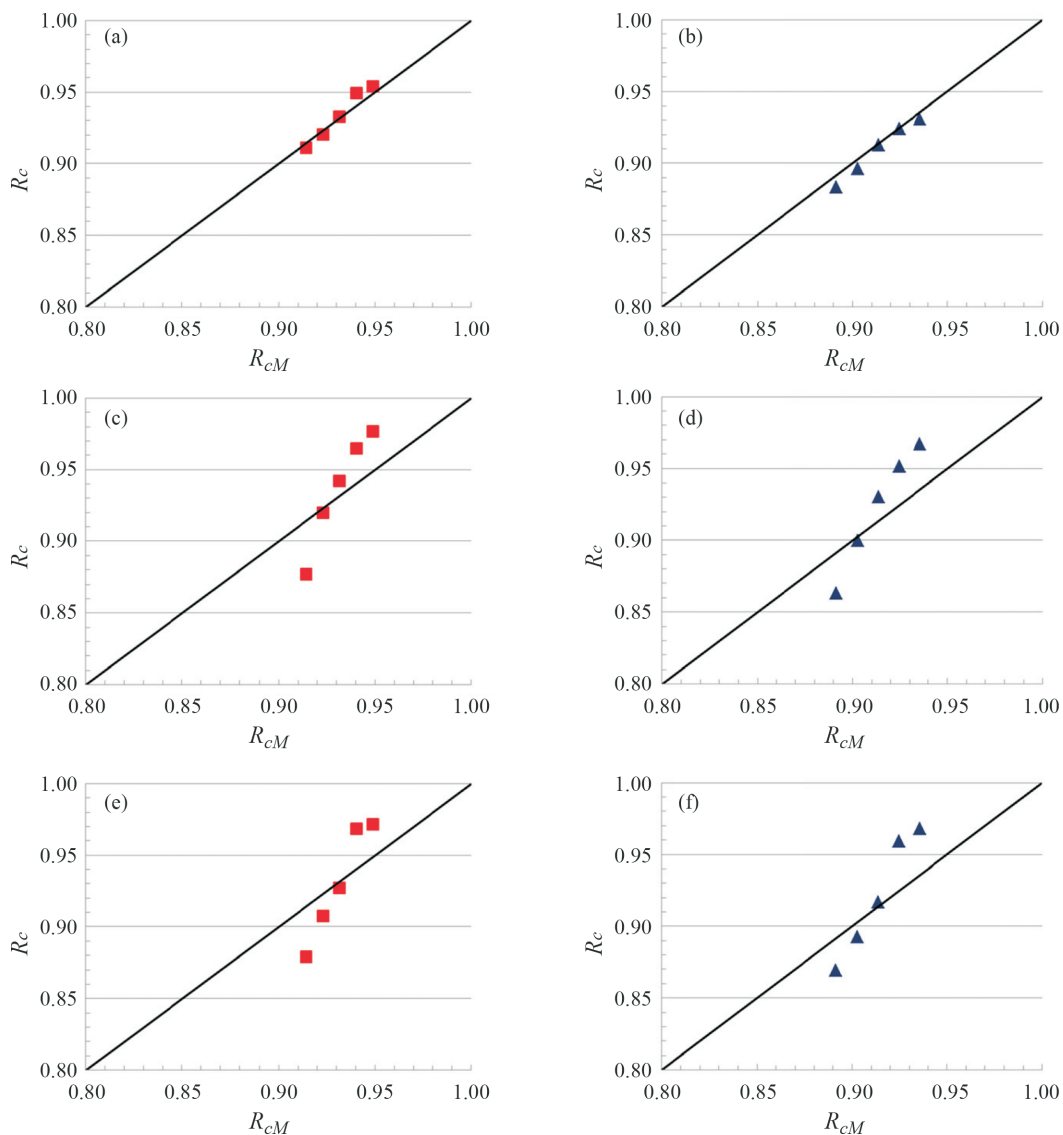


**Figure 7** - Correlation between the  $R_c$  and  $R_{cM}$  values: (a) SL sample/ $\text{CaCl}_2$ ; (b) SL sample/ $\text{C}_2\text{H}_5\text{OH}$ ; (c) ST sample/ $\text{CaCl}_2$ ; (d) ST sample/ $\text{C}_2\text{H}_5\text{OH}$ ; (e) SN sample/ $\text{CaCl}_2$  and (f) SN sample/ $\text{C}_2\text{H}_5\text{OH}$ .

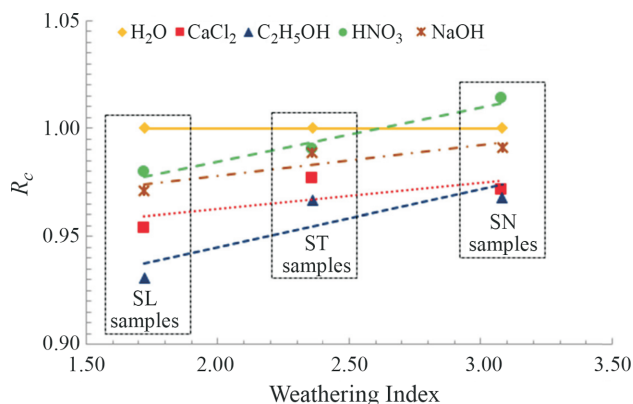


**Figure 8** - Weathering index  $K_i$  vs.  $R_c$  for all the natural soil samples and chemical solutions.

**Table 6** - Hydraulic conductivity ( $k$ ) and relative hydraulic conductivity ( $k_r$ ) for the “optimum bentonite content” samples with different solutions.

Sample	Chemical solutions				
	Water ( $k_r$ )	CaCl <sub>2</sub> ( $k_r$ )	C <sub>2</sub> H <sub>5</sub> OH ( $k_r$ )	HNO <sub>3</sub> ( $k_r$ )	NaOH ( $k_r$ )
SL <sub>OT</sub>	6.3 x 10 <sup>-8</sup> cm/s (1.00)	1.1 x 10 <sup>-7</sup> cm/s (1.74)	3.8 x 10 <sup>-7</sup> cm/s (6.10)	5.5 x 10 <sup>-8</sup> cm/s (0.87)	7.5 x 10 <sup>-8</sup> cm/s (1.19)
ST <sub>OT</sub>	6.3 x 10 <sup>-8</sup> cm/s (1.00)	1.0 x 10 <sup>-7</sup> cm/s (1.61)	3.5 x 10 <sup>-7</sup> cm/s (5.60)	6.4 x 10 <sup>-8</sup> cm/s (1.01)	8.2 x 10 <sup>-8</sup> cm/s (1.31)
SN <sub>OT</sub>	5.9 x 10 <sup>-8</sup> cm/s (1.00)	8.4 x 10 <sup>-8</sup> cm/s (1.43)	1.4 x 10 <sup>-7</sup> cm/s (2.34)	7.5 x 10 <sup>-8</sup> cm/s (1.27)	8.1 x 10 <sup>-8</sup> cm/s (1.37)

The correlation between the  $k$  measured in the laboratory and the theoretical  $k_M$  from Table 8 is depicted in Fig. 9(a) as function of the soil samples, and 9(b) as a function of the chemical solutions. Good fits

were observed for all samples and solutions, exception made for the SN<sub>OT</sub> sample (pointed in Fig. 9a) and the C<sub>2</sub>H<sub>5</sub>OH solution (see Fig. 9b), whose measured  $k$  is smaller than  $k_M$ , but remaining in the same order of magnitude.

**Table 7** - Soil parameters used to estimate  $k_M$ .

Soil sample	$e$	$a$	$b$	$C_{kc}$
SL <sub>OT</sub>	0.608	0.00083	-4.48	0.2
ST <sub>OT</sub>	0.735	295.12092	-7.56	0.2
SN <sub>OT</sub>	0.665	46.77351	-7.26	0.2

If the theoretical propositions presented here are directly connected to the double layer theory in which bentonite clay is clearly inserted, it is reasonable to think that the  $k_M$  values estimated for the mixtures with greater bentonite content should give better fit to the models, as was the case of the samples SL<sub>OT</sub> (9%) and ST<sub>OT</sub> (4%) compared to the sample SN<sub>OT</sub> (2%).

**Table 8** - Solution parameters, mesoplastic point (MP) and the resultant  $k_M$  values.

	Solutions				
	Water	CaCl <sub>2</sub>	C <sub>2</sub> H <sub>5</sub> OH	HNO <sub>3</sub>	NaOH
$\gamma/\mu$ (cm <sup>-1</sup> s <sup>-1</sup> )	99300	99300	402165	99300	99300
Sample	MP(%)				
SL <sub>OT</sub>	49.0	45.1	43.9	50.0	46.8
ST <sub>OT</sub>	55.8	53.4	52.7	56.4	54.9
SN <sub>OT</sub>	51.4	49.9	49.5	50.9	50.7
Sample	$k_M$ (cm s <sup>-1</sup> )				
SL <sub>OT</sub>	6.21E-08	9.01E-08	4.12E-07	5.65E-08	7.60E-08
ST <sub>OT</sub>	8.34E-08	1.17E-07	5.24E-07	7.76E-08	9.51E-08
SN <sub>OT</sub>	6.19E-08	7.76E-08	3.32E-07	6.67E-08	6.90E-08

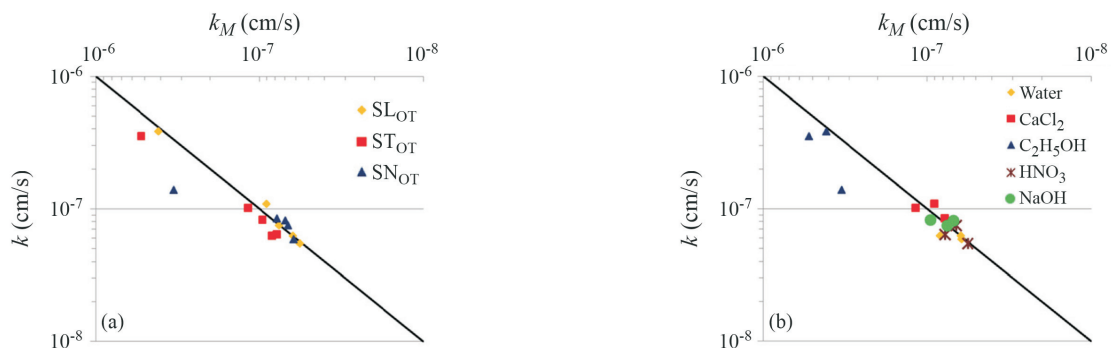


**Figure 9** - (a) Laboratory  $k$  vs. theoretical  $k_M$  for the “optimum bentonite content” samples; (b) Laboratory  $k$  vs.  $k_M$  as a function of the chemical solutions.

## 5. Conclusions

Four research objectives were stated in the Introduction section, and the next conclusions will be presented in the same order, as follows:

- (1) "A comparison between laboratory direct and indirect methods for compatibility evaluation". The incompatibility order was the same for both direct and indirect methods, considering all solutions and soil samples:  $C_2H_5OH > CaCl_2 > NaOH > HNO_3$ . This fact corroborates the perspective of using indirect methods as a preliminary tool for comparing different candidate soils for barrier purposes from a qualitative point of view. Small laboratory effort is needed for this last approach.
- (2) "An assessment of the influence of the bentonite content on the compatibility of tropical soil samples". It was demonstrated by Figs. 5 and 6 that the bentonite content had major influence on the decrease of the compatibility of the tropical soils for all solutions. However, exception made for the ethanol PA reagent, the compatibility indexes  $R_c$  and  $k_r$  close to 1 demonstrate that small proportions of bentonite, up to 12% (dry weight basis) as in this research, do not affect the soil so much.
- (3) "An investigation of the influence of the laterization degree on the compatibility". Figure 8 demonstrates that the weathering stage (laterization degree) of the tropical soil samples had minor influence on the compatibility results.
- (4) "An evaluation of theoretical equations to predict the compatibility of these samples through back analysis". In general terms, good predictions were obtained both for direct or indirect methods relative to the laboratory tests results. For indirect compatibility, these comparisons were presented in Table 4 for the bentonite sample and in Fig. 7 for the natural soil samples and mixtures considering the ethanol and calcium chloride solutions. In turn, direct compatibility comparisons were presented on Fig. 9 for all soil samples and solutions.

The issues to be addressed in future research must involve the use of other tropical soil samples comprising the many pedological taxonomies of Table 1, as well as the use of real liquids from actual disposal sites. Additionally, as the results of the present research were obtained by means of an "instantaneous" contact of the soil with the contaminant solutions, a long term analysis is suggested to evaluate possible changes on the composition and/or mechanical behavior of the compacted tropical soils.

## Acknowledgments

The authors give special Acknowledgments to Fundação de Amparo à Pesquisa do Estado de Minas Gerais (FAPEMIG) for supporting this research (grant number

TEC-APQ02502-12) and for providing a full scholarship to the first author during his Ph.D. course. The company Bentonit União Nordeste Ltda gently donated the bentonite samples used in laboratory tests.

## References

- ABNT (2016). Soil: Determination of the Liquid Limit - NBR 6459. Associação Brasileira de Normas Técnicas, Rio de Janeiro, 5 p. (In Portuguese).
- ABNT (2016). Soil: Determination of Plastic Limit - NBR 7180. Associação Brasileira de Normas Técnicas, Rio de Janeiro, 3 p. (In Portuguese).
- Akcanca, F. & Aytakin, M. (2014). Impact of wetting-drying cycles on the hydraulic conductivity of liners made of lime-stabilized sand-bentonite mixtures for sanitary landfills. *Environ. Earth. Sci.*, 72(1):56-69.
- Akbulut, S. & Saglamer, A. (2004). Modification of hydraulic conductivity in granular soils using waste materials. *Waste Manag.*, 24(5):491-499.
- Bolt, G.H. (1955). Analysis of the validity of the Gouy-Chapman theory of the electric double layer. *J. Colloid Sc.*, 10(2):206-218.
- Bouazza, A.; Stephan, J. & Thaveesak, V. (2007). Investigation of the effects and degree of calcium exchange on the Atterberg limits and swelling of geosynthetic clay liners when subjected to wet-dry cycles. *Geotext. Geomembr.*, 25(1):170-185.
- Bowders, J.J. & Daniel, D.E. (1987). Hydraulic conductivity of compacted clay to dilute organic chemicals. *J. Geotech. Eng.*, 113(12):1432-1448.
- Budhu, M.; Giese, R.F.; Campbell, G. & Baumgrass, L. (1990). The permeability of soils with organic fluids. *Can. Geotech. J.* 28(1), 140-147.
- Chapuis & Albertin (2003). On the use of the Kozeny-Carman equation to predict the hydraulic conductivity of soils. *Can. Geotech. J.*, 40(1):616-628.
- Daniel D.E. & Liljestrand H.M. (1984). Effects of Landfill Leachates on Natural Linear Systems Chemical Manufacturers. Association Report, The University of Texas, Geotechnical Engineering Center, Austin, Texas, 86 pp.
- Daniel, D.E.; Shan, H.Y. & Anderson, J.D. (1993). Effects of partial wetting on the performance of the bentonite component of a geosynthetic clay liner. *Geosynthetics*, 3(1):1482-1496.
- Ebina, T.; Minja, R.J.A.; Nagase, T.; Onodera, Y. & Chatterjee, A. (2004). Correlation of hydraulic conductivity of clay-sand compacted specimens with clay properties. *Appl. Clay Sci.*, 26(1):3-12.
- Egloffstein, T.A. (2001). Natural bentonites: influence of the ion exchange and partial desiccation on permeability and self-healing capacity of bentonites used in GCLs. *Geotext. Geomembr.*, 19(1):427-444.
- Farnezi, M.K. & Leite, A.L.L. (2007). Lateritic soil and bentonite mixtures assessment for liner usage purpose. *Soils and Rocks*, 30(2):103-112.

- Fernandez, F. & Quigley, R.M. (1988). Viscosity and dielectric constant controls on the hydraulic conductivity of clayey soils permeated with simple liquid hydrocarbons. *Can. Geotech. J.*, 25(1):582-589.
- Grim, R.E. (1968). *Clay Mineralogy*, 2<sup>nd</sup> ed. McGraw-Hill Co, New York, 596 p.
- Head, K.H. (1986). *Manual of Soil Laboratory Testing: Effective Stress Tests*, 3<sup>rd</sup> ed. John Wiley and Sons, London, 422 p.
- IBGE (2005). *Pedology technical manual*, 2<sup>nd</sup> ed. Technical Manuals in Geosciences. Brazilian Institute of Geography and Statistics, Rio de Janeiro, 316 p. (In Portuguese).
- Katsumi, T.; Ishimori, H.; Onikata, M. & Fukagawa, R. (2008). Long-term barrier performance of modified bentonite materials against sodium and calcium permeant solutions. *Geotext. Geomembr.* 26(1):14-30.
- Kinsela, A.S.; Tjitradjaja, A.; Collins, R.N.; Waite, T.D.; Payne, T.E.; Macdonald, B.C.T. & White, I. (2010). Influence of calcium and silica on hydraulic properties of sodium montmorillonite assemblages under alkaline conditions. *J. Colloid Interface Sci.* 343(1):366-373.
- Koch, D. (2002). Bentonites as a basic material for technical base liners and site encapsulation cut-off walls. *Appl. Clay Sci.* 21(1):1-11.
- Langmuir, D. (1997). *Aqueous Environmental Geochemistry*, 1<sup>st</sup> ed. Prentice, New Jersey, 600 p.
- Lukiantchuki, J.A. & Esquivel, E.R. (2010). Hydraulic conductivity and shear strength behavior of compacted lateritic soil bentonite mixtures used for sanitary landfill liners. *Soils Rocks* 33(2):69-79.
- Mitchell, J. K. (1993). *Fundamentals of Soil Behaviour*, 2<sup>nd</sup> ed. John Wiley e Sons, New York, 437 p.
- Morandini, T.L.C. & Leite. A.L. (2013). Characterization, hydraulic conductivity and compatibility of mixtures of tropical soil and bentonite for barrier usage purpose. *Soils and Rocks*, 35(3):267-278.
- Morandini, T.L.C. & Leite. A.L., (2015a). Characterization and Hydraulic Conductivity of some Tropical Soils Samples and Bentonite Mixtures for CCL Purposes. *Eng. Geol.* 196(1): 533-564.
- Morandini, T.L.C. & Leite. A.L. (2015b). Mixtures of non-lateritic tropical soils and bentonite for purposes of flow barriers. *Proc. VIII Brazilian Congress of Environmental Geotechnics, REGEO, Brasília*, pp. 1-9. (In Portuguese).
- Nayak, S.; Sunil, B.M. & Shrihari, S. (2007). Hydraulic and compaction characteristics of leachate-contaminated lateritic soil. *Eng. Geol.* 94(3):137-144.
- Nogami, J.S. & Villibor, D.F. (1995). *Pavement of low cost with lateritic soils*, 1<sup>st</sup> ed., Villibor, São Paulo, 213 p. (In Portuguese).
- Osinubi, K.J. & Nwaiwu, C.M. (2006). Design of compacted lateritic soil liners and covers. *J. Geotech. and Geoenviron. Eng.* 132(2):203-213.
- Osinubi, K.J.; Eberemu, A.O. & Amadi, A.A. (2009). Compacted lateritic soil treated with blast furnaces slag as hydraulic barriers in waste containment. *Intern. J. Risk Assessm. Manag.* 13(2):177-188.
- Shackelford, C.D. (1994). *Hydraulic Conductivity and Waste Contaminant Transport in Soil*. David E. Daniel and Stephen J. Trautwein (eds), American Society for Testing and Materials - STP 1142, Philadelphia, 611 p.
- Shackelford, C.D.; Benson, C.H.; Katsumi, T.; Edil, T.B. & Lin, L. (2000). Evaluating the hydraulic conductivity of GCLs permeated with non-standard liquids. *Geotext. Geomembr.* 18(2):133-161.
- Stewart, D.I.; Studds, P.G. & Cousens, T.W. (2003). The factors controlling the engineering properties of bentonite-enhanced sand. *Appl. Clay Sci.* 23(1):97-110.
- Sunil, B.M.; Nayak, S. & Shrihari, S. (2006). Effect of pH on the geotechnical properties of laterite. *Eng. Geol.* 85(1):197-203.
- Sunil, B.M.; Nayak, S. & Shrihari, S. (2009). Shear strength characteristics and chemical characteristics of leachate-contaminated lateritic soil. *Eng. Geol.* 106(1):20-25.
- Van Breemen, N. & Buurman, P. (2003). *Soil Formation*, 1<sup>st</sup> ed. Kluwer Academic Publishers, New York, Boston, Dordrecht, London, Moscow, 385 p.
- Vertamatti, E. (1998). New geotechnical considerations on Amazon tropical soils of fine texture. *Proc. XXIII Annual Meeting of Paving, RAPv, Florianópolis*, pp. 533-564. (In Portuguese).
- Yong, R.N.; Mohamed, A.M.O. & Warkentin, B.P. (1992). *Principles of Contaminant Transport in Soils*, 1<sup>st</sup> ed. Elsevier, Amsterdam, 342 p.
- Yu, T.R. (1997). *Chemistry of Variable Charge Soils*, 1<sup>st</sup> ed. Oxford University Press, New York, 448 p.



## ***Technical Notes***

***Soils and Rocks***  
**v. 41, n. 3**



# The Performance of a Sand Reinforced with Coconut Fibers Through Plate Load Tests on a True Scale Physical Model

J.M.G. Sotomayor, M.D.T. Casagrande

**Abstract.** The use of recycled materials has experienced a growing global interest in the last decades. Products like natural fibers are being studied to replace synthetic fibers in some applications because they are renewable resources that have a lower cost. Fibers can be used as reinforcement for covers of landfill sites, landfilling over soft soils, and evapotranspiration covers. The use of coconut fibers represent an opportunity to reduce the environmental issue waste of this fruit in tropical countries. The main objective of this research is to evaluate the load-settlement behavior of non-reinforced and reinforced sand with coconut fibers using either a random or a layered distribution. In that sense, plate load tests with both non-reinforced and reinforced sand were performed fixing the moisture content and percentage of fibers for all tests. The results show that the greatest settlement reduction is obtained with layered distribution. Conversely, random distribution provides more ductility and, consequently, the mixture can resist a highest load than layered distribution.

**Keywords:** coconut fiber, layered distribution, plate load test, random distribution.

## 1. Introduction

In the literature, one of the firsts investigations about the influence of root reinforcement on soil strength has been conducted by Endo & Tsuruta (1969) who showed that the shear strength of soil with tree root system could be expressed by the same forms as Coulomb law. The growing interest led researchers to study the effect of discrete fibers on soil shear strength. In that sense, researchers as Gray & Ohashi (1983) began to develop models based on force equilibrium to correctly predict the influence of various soil-fiber parameters. The better characteristics of synthetic fibers than natural fibers attracted the attention of researchers. Studies carried out on reinforced soil with synthetic fibers have demonstrated that the principal parameters on the shear strength are soil particle size and shape (Maher & Gray, 1990; Al-Refeai, 1991; Sadek *et al.*, 2010; Pino & Baudet, 2015), sand relative density (Consoli *et al.*, 2009a; Sharma & Kumar, 2017), fiber orientation (Gray & Al-Refeai, 1986; Michawloski & Cermak, 2002), fiber percentage and length (Maher & Ho, 1994; Yetimoglu & Salbas, 2003; Consoli *et al.*, 2007b; Li & Zornberg, 2012) and fiber aspect ratio (Maher & Woods, 1990; Ranjan *et al.*, 1994; Chou *et al.*, 2016). The understanding of the soil-fiber mechanism has led researchers to study ecofriendly materials as Tolêdo Filho *et al.* (1997), Ahmad *et al.* (2010) and Estabragh *et al.* (2013) developed studies using natural fibers to reinforce silty sand, clays and mortar, respectively. A review study about synthetic (PP, PE, PET, Nylon, Glass, PVA; and steel) and natural (coir, sisal,

palm, jute, flax, straw, bamboo; and cane) fibers was carried out by Hejazi *et al.* (2012) showing that, in all cases, fibers help to reduce the brittleness of the composite soil. The literature concludes that the use of natural-synthetic fibers in geotechnical engineering is feasible in embankments and road construction (Santoni *et al.*, 2001; Tingle *et al.*, 2002; Chauhan *et al.*, 2008), retaining walls (Arenicz & Chowdhury, 1988; Park & Tan, 2005), earthquake engineering (Leflaive, 1988; Amir-Faryar & Aggour, 2016), slope protection (Zornberg, 2002; Bhardwaj & Mandal, 2008), and foundation engineering (Sharma & Kumar, 2017; Wasti & Bütün, 1996).

The Brazilian Institute for Geography and Statistics (IBGE) revealed that, in Brazil, the coconut production has grown from 1,300,000 to 2,000,000 tons in ten years. According to the Brazilian Agricultural Research Corporation, the coconut shells represent between 80% and 85% of weight of the fruit and about 70% of the waste generated in Brazilian beaches, thus becoming a serious environmental issue, particularly in tropical countries, however, the coconut fiber applications are reduced to evapotranspiration coverage. Researchers have shown interest in using coconut fiber as concrete reinforcement (Majid *et al.*, 2011; Ramli *et al.*, 2013), nevertheless few studies are carried out for uses in soil reinforcement. The main objective of this research is the applicability of coconut fibers as reinforcement of soil embankments, soil foundation and other engineering applications. A secondary objective is to compare random with layered reinforcement distribution fixing

---

Juan Manuel Girao Sotomayor, D.Sc., Departamento de Engenharia Civil, Pontifícia Universidade Católica do Rio de Janeiro, Rio de Janeiro, RJ, Brazil. e-mail: girao.sotomayor@aluno.puc-rio.br.

Michèle Dal Toé Casagrande, D.Sc., Full Professor, Departamento de Engenharia Civil e Ambiental, Universidade de Brasília, Campus Darcy Ribeiro, Brasília, DF, Brazil. e-mail: mdtcasagrande@unb.br.

Submitted on March 29, 2018; Final Acceptance on September 18, 2018; Discussion open until April 30, 2019.

DOI: 10.28927/SR.413361

the moisture content and percentage of fibers. Static and dynamic plate load tests are often used for bearing capacity evaluation of shallow foundations (Moraes *et al.*, 2007). No studies have used the plate load test to evaluate reinforced soil with coconut fiber. This paper reports static plate load test results under controlled conditions on non reinforced and reinforced sand evaluating the load-settlement behavior and compares a random with a layered reinforcement distribution. The use of coconut fiber represents an opportunity to reduce the environmental issue of waste. One of the study limitations is that there was no analysis of resistance to fiber degradation, however, Hejazi *et al.* (2012) showed that the high lignin content of coconut fibers makes the degradation slower compared to other vegetable fibers.

## 2. Materials

### 2.1. Coconut fiber

Coconut fibers were collected by a partnership between the municipal company of urban cleaning and the department of public services conservation. The fibers were received in sacks, subsequently going through shredding, cleaning of all solid residues, manually cut, and stored into bags (Fig. 1). The fiber average dimensions were 50 mm in length and the content used was 0.5% by dry weight of soil. Previous studies have demonstrated that a fiber content of 0.5% is an upper limit considering workability and homogeneity (Consoli *et al.*, 2003a; Consoli *et al.*, 2009b; Consoli *et al.*, 2007a; Anagnostopoulos *et al.*, 2013).

### 2.2. Soil matrix

The Unified Soil Classification System (USCS) classifies the sand, obtained from the region of Santa Cruz in southern Brazil, as non plastic poorly graded SP. The sand has a mean diameter of 0.89 mm and non-uniformity and curvature coefficients of 5.08 and 1.01, respectively. The specific gravity of the solids was 2.642, the maximum and minimum void ratios were 0.70 and 0.50, respectively. The fines content was 2.2% with no organic matter. The layers

were compacted to a relative density of 50% because, in practice, covers and landfill sites do not possess high compaction values. The moisture content was 10.0% and dry unit weight 16.5 kN/m<sup>3</sup>.

## 3. Preparation of Layers

First was placed half of the sand into mixer of 20 L, a bit of water was spread over the surface to avoid dust, fibers were manually placed covering all surface, then the other sand half was added. The mixer was turned on, while the water was added to reach the moisture content calculated. The fibers were added as a replacement of sand using Eqs. 1 and 2.

$$W_R = V \times \gamma_R \quad (1)$$

$$W_R = W_S + W_F = P_S \times W_R + P_F \times W_R \quad (2)$$

where,  $W_R$ ,  $W_S$ , and are dry weight of reinforced layer, sand and fibers, respectively;  $\gamma_R$  is dry unit weight of reinforced layer;  $V$  is the total volume of reinforced layer to be placed;  $P_S$  and  $P_F$  are the percentages of sand and fibers in reinforced layer, respectively.

In layered distribution did not mixture the sand with the fiber, the fiber percentage was placed between each layer of sand.

A wooden box, 1.4 m x 1.4 m in plan dimensions, and 1.5 m high was used as test box. The mixture thickness is 1.2 m which is equivalent to 4 times the plate diameter. The test box was filled with 12 consecutive layers with a 0.1 m thickness.

## 4. Equipment Setup

A load transmission/reaction system was developed by the Materials and Structures Laboratory of Pontifícia Universidade Católica do Rio de Janeiro to conducted the plate load test. It was built on a steel gantry with a 1000 kN workload (Fig. 2). The load was applied by a hydraulic jack with a 600 kN maximum load connected to a hand pump and one load transducer with a 20 kN capacity was placed below the jack. A circular steel plate with 0.3 m in diameter and one inch in thickness was used. Displacement transducers TD1, TD2, and TD3 were radially placed over the plate at every 120°. Transducers TD4 and TD5 were placed off the plate at 0.05-0.10 m distance in order to register the settlements around the plate (Fig. 3). The displacement transducers were fixed to a reference beam and held by external supports to ensure a stable reference. The main scale limitation of the plate loading test is found in the dimensions of the test box, which, although it was 4 times the diameter of the plate in depth, did not support the greater range of stresses permitted by the addition of fibers to the sand. This large increase in deformation energy was not previously considered in the determination of the dimensions of the test box.



Figure 1 - Coconut fibers 50 mm in length.

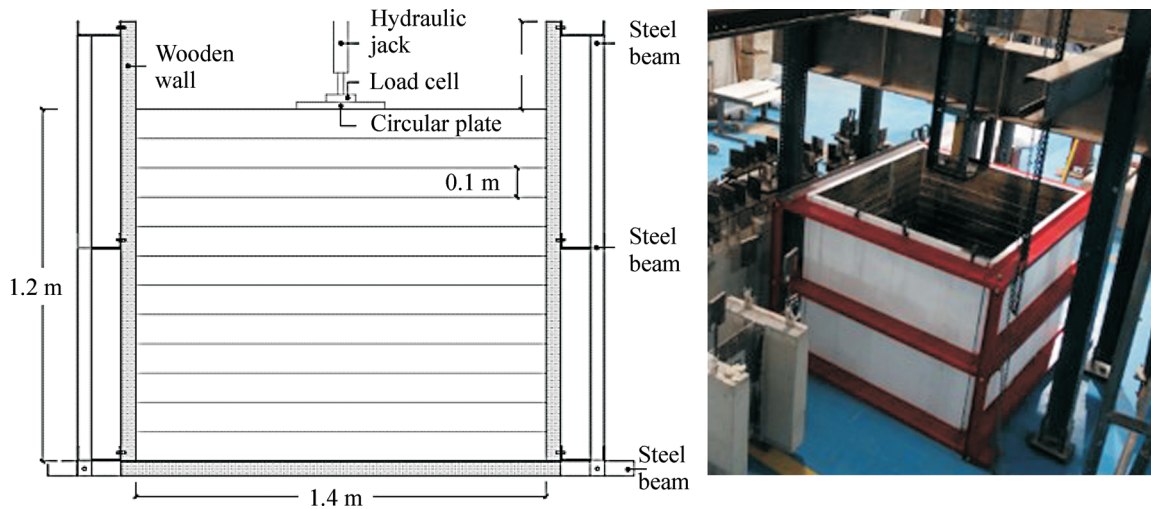


Figure 2 - Test box.

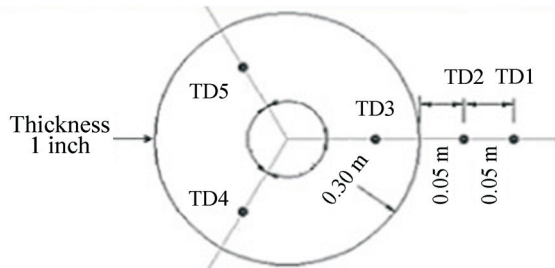
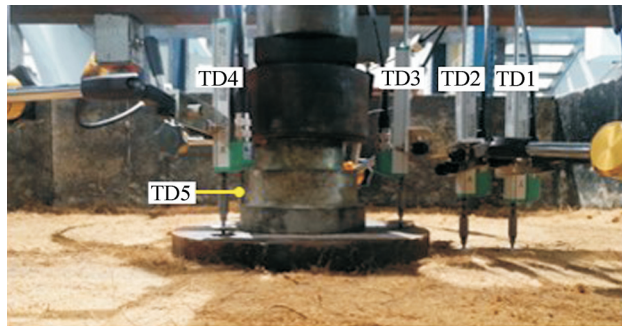


Figure 3 - Displacement transducers locations.

## 5. Results and Analyses

Non-reinforced sand was tested in order to determine the material basic behavior. Sand was then reinforced with randomly distributed fibers to observe the fiber influence on the load-settlement behavior. Finally, reinforced sand with layered distributed fibers was tested to compare the influence of fiber distribution layout, by maintaining the same fiber content in each layer.

The tests ended when the plate presented rotations over its axis. During test, sand becomes stiff beneath the plate and does not allow larger settlements.

### 5.1. Load-settlement behavior

The non reinforced sand fails at the point where the load-settlement relation changes its inclination; this point is defined as bearing capacity of the foundation,  $q_{ult}$ . This change occurs for random distribution in low settlements while for the layered distribution in large settlements.

Most methods to estimate  $q_{ult}$  have been developed based on the expression proposed by Terzaghi (1951). The expression adapted for a plate load test on cohesionless soils using a circular footing is defined as

$$q_{ult} = 0.3\gamma \times B \times N_{\gamma} \quad (3)$$

where  $\gamma$  is the sand unit weight;  $B$  is the plate diameter and  $N_{\gamma}$  is a bearing capacity factor which depends of the sand friction angle,  $\phi$ . There are many methods to define  $N_{\gamma}$ , the lack of consensus in the methods being due to complexity in obtaining  $q_{ult}$  by experimental tests. Sixty methods to determine the bearing capacity factor  $N_{\gamma}$  presented by Diaz-Segura (2013), were used to calculate  $q_{ult}$  using the Eq. 3. Triaxial tests with the non reinforced sand obtained an angle of friction of  $32.5^{\circ}$ . Figures 4(a) and 4(b) show the variation range of  $q_{ult}$  calculated, and the  $q_{rest}$  obtained in the test, respectively. The physical model is validated by the numerical methods because  $q_{ult} = 40$  kPa is inside the values range calculated (35-40 kPa).

Load-settlement curves in large deformations are presented in Fig. 5. Initially, non-reinforced sand shows a parabolic curve and then a linear tendency. This linearity is typical of granular soils: the grains keep rearranging themselves, and therefore, the mass of soil does not have a well-defined shear failure.

Normally, plate load tests on granular soils achieved a proportionality between load and settlements, therefore, the results in large deformations are compatible. The strain hardening response shows the reinforced sand as more duc-

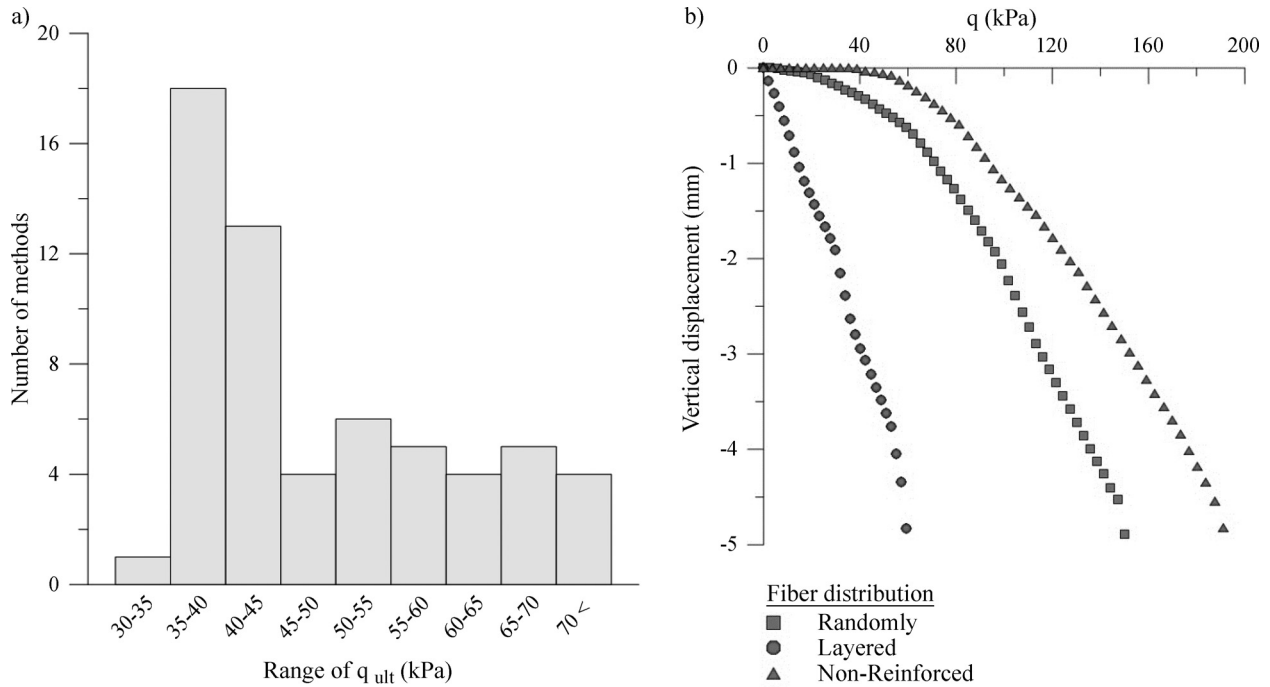


**Figure 4** - Bearing capacity of the non reinforced sand: (a) Numerical (b) Experimental.

tile. At the 400 kPa value there is an intersection between the three curves: at this stress level the fibers have occupied most of the void spaces increasing interaction with the sand grains and activating the development of the fiber tensile strength that produces the strain hardening behavior.

The reinforced (random distribution) and the non reinforced curves are almost parallel until 400 kPa: after the reinforced curve shows a continuous stress increase, while stress in non reinforced sand decreases. In this range, the layered distributed reinforced curve presents a lower settle-

ment resistance than the non reinforced sand, however, after 400 kPa this distribution presents the best settlement resistance.

Lateral movement of the grains is produced by the stress transfer from plate to sand which affects the grains stability. Fibers distributed in layers act as a restraint against this movement (Fig. 6), however, generate a major layer stiffness, consequently, the layered reinforcement test endure a minor load than randomly reinforcement test. Consoli *et al.* (2003b) also observed a stiffer response due to a combined effect between the continued increase in the material strength at large deformations and the increase in the horizontal stresses below the plate.

The transducers TD1 and TD2, in Figs. 7(a) and 7(b), placed 0.05 and 0.10 m from the plate border showed that non-reinforced sand has a vertical upward expansion while in the reinforced case the sand is pulled down in the direction of the plate, this mechanism also having been observed

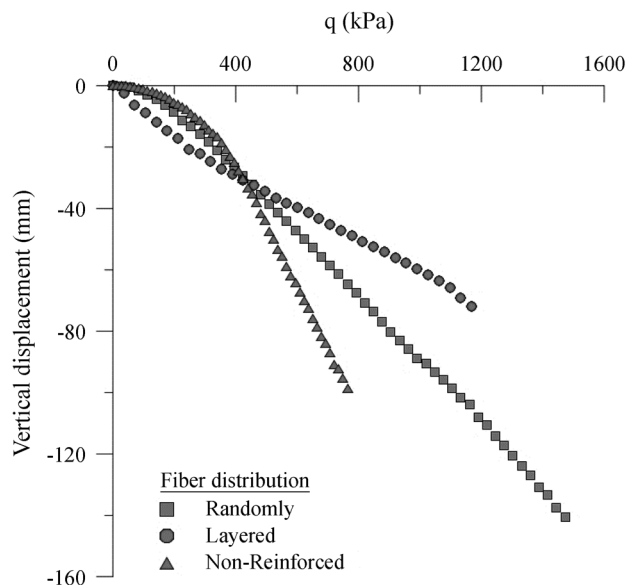


**Figure 5** - Load-settlement curves in large deformations.

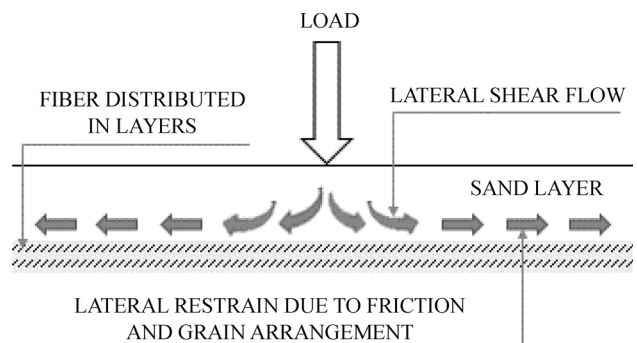


**Figure 6** - Lateral restraining capability.

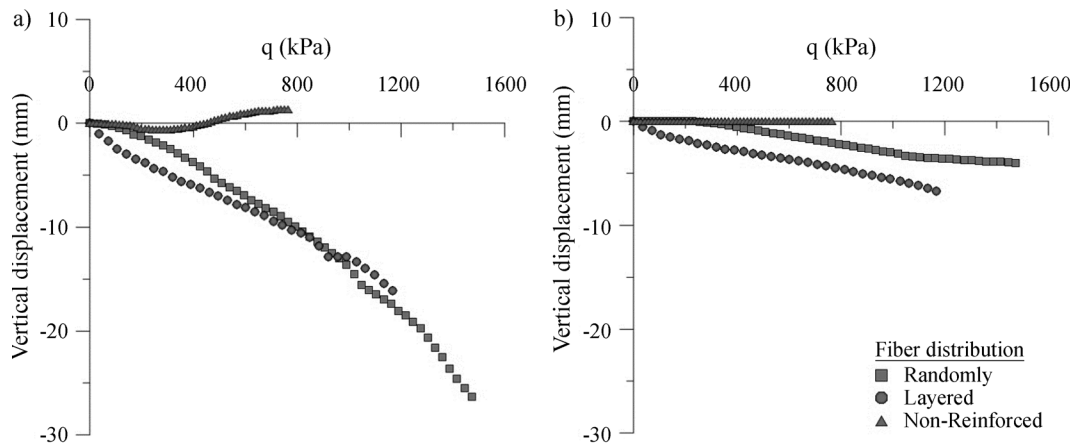


**Figure 7** - Load-settlements curves around the plate. (a) 0.05 m (b) 0.10 m.

by Consoli *et al.* (2009a). Fibers generate an additional confinement effect around the sand grains, the restriction for grains movement and the fiber capacity to work in tension reduces the sand dilative behavior. According to Consoli *et al.* (2003b), fibers reduce the movement of sand due to the transfer mechanism by the fiber-sand friction distributing the energy over a larger area.

The overall evaluation of the results shows that the fiber addition initially restricts the natural rearrangement of sand grains as the displacement increases to a certain limit. Once this limit is reached, the grains have no direction to move without strongly interacting with the randomly distributed fibers or the fibers distributed in layers, which start to contribute to the displacement resistance as shown in the Fig. 5.

### 5.2. Shear failure mechanism

Figure 8 shows the exhumation after the tests. The change in the shear mechanism showed by the transducers TD1 and TD2 was verified. Vesic (1975) explained that the failure characterized by the vertical upward expansion presented by the non reinforced sand corresponds to local shear failure. However, the reinforced cases presented a

punching shear failure. In Fig. 9 the maximum stress reached in non reinforced sand was 770 kPa, while layered and randomly reinforced sand reached 1200 and 1500 kPa, respectively.

The size and shape of fissures indicate stress release, if the sand does not have enough tenacity to keep absorbing energy the affected area will be bigger. In non reinforced sand, the Fig. 10(a) shows radial cracks appearing normal to the circumference of the plate. The concentration of stresses was dissipated from the layer base to the surface, superficially cracks appeared perpendicular to the radial crack trying to propagate in all directions. In the reinforced cases, cracks were concentric with the plate and there were no perpendicular cracks, therefore, fibers improve the sand behavior avoiding the appearance of cracks.

### 6. Conclusions

The performance of a medium density compacted sand reinforced with coconut fibers was studied through plate load test in true scale with an equipment setup detailed in this paper. The following conclusions were based in the obtained results.



**Figure 8** - Shear mechanism: (a) local shear (non-reinforced sand), (b) punching shear (randomly and layered reinforced sand).

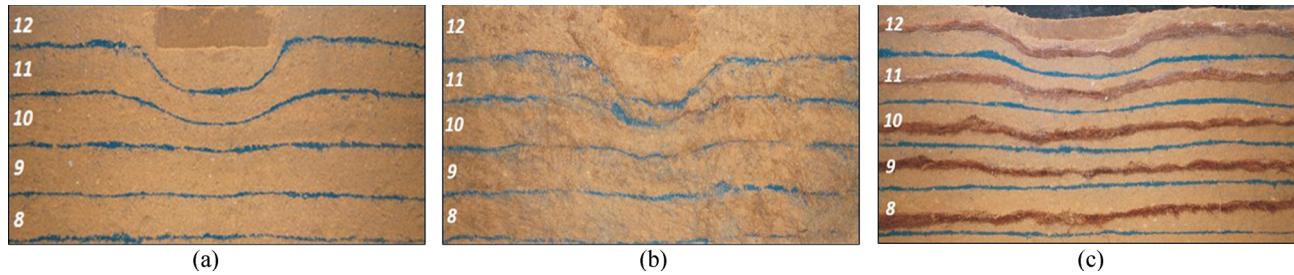


**Figure 9** - Settlement: (a) non-reinforced (770 kPa), (b) randomly reinforcement (1500 kPa), (c) layered reinforcement (1200 kPa).

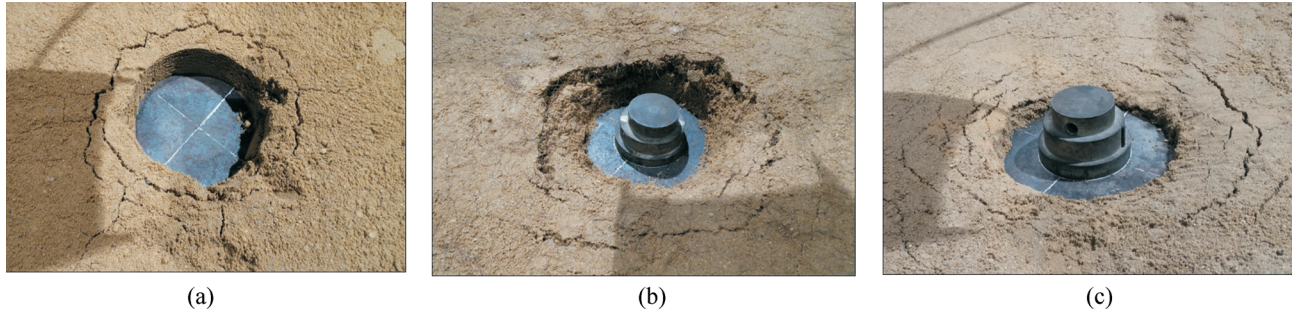


**Figure 10** - Cracks: (a) non-reinforced (770 kPa), (b) randomly reinforcement (1500 kPa), (c) layer reinforcement (1200 kPa).

In low stresses, fibers add voids around themselves reducing the normal rearrangement of grains and the bearing capacity. In large stresses, grains occupy the voids around the fibers improving the fiber-sand interaction, coconut fibers activate the tensile resistance significantly improve the load-settlement behavior and influence the change of shear mechanism.

The non reinforced sand showed a vertical shear from a bottom layer to surface, displaying a stress concentration in the loading area, whereas the reinforced sand presented shear failures that propagated off the loading area around the plate, showing that the fibers distribute the stresses over a larger area.

The membrane effect generated under the layered distribution got the higher settlement reduction due to restraint of grains lateral movement, however, this stiffens the layer and creates potential planes of weakness. This effect does not happen with the random distribution.

It is recommended a combination to provide the advantages of each one. In superficial layers can be used the random distribution to reduce the cracks while in the intermediate layers can be used the layered distribution. The use of recycled coconut fiber is an opportunity to reduce the environmental problem in tropical countries.

## Acknowledgments

The authors manifest their acknowledgement to the CNPq (Brazilian Council of Scientific Technological Research) for the financial support, and to Municipal Government of Rio de Janeiro for providing the fibers.

## References

- Ahmad, F.; Bateni, F. & Azmi, M. (2010). Performance evaluation of silty sand reinforced with fibres. *Geotextiles and Geomembranes*, 28(1):93-99.
- Al-Refeai, T.O. (1991). Behavior of granular soils reinforced with discrete randomly oriented inclusions. *Geotextiles and Geomembranes*, 10(4):319-333.
- Amir-Faryar, B. & Aggour, M.S. (2016). Effect of fibre inclusion on dynamic properties of clay. *Geomechanics and Geoengineering*, 11(2):104-113.
- Anagnostopoulos, C.A.; Papaliangas, T.T.; Konstantinidis, D. & Patronis, C. (2013). Shear strength of sands reinforced with polypropylene fibers. *Geotechnical and Geological Engineering*, 31(2):401-423.
- Arenicz, R.M. & Chowdhury, R.N. (1988). Laboratory investigation of earth walls simultaneously reinforced by strips and random reinforcement. *Geotechnical Testing Journal*, 11(4):241-247.
- Bhardwaj, D.K. & Mandal, J.N. (2008). Study on polypropylene fiber reinforced fly ash slopes. *Proc. 12th Int. Conf. of Int. Assoc. for Comp. Meth. and Advan. in Geomech. (IACMAG)*, Goa, India.
- Chauhan, M.S.; Mittal, S. & Mohanty, B. (2008). Performance evaluation of silty sand subgrade reinforced with fly ash and fibre. *Geotextiles and Geomembranes*, 26(5):429-435.
- Chou, J.S.; Yang, K.H. & Lin, J.Y. (2016). Peak shear strength of discrete fiber-reinforced soils computed by machine learning and metaensemble methods. *Journal of Computing in Civil Engineering*, 30(6):04016036.

- Consoli, N.C.; Vendruscolo, M.A. & Prietto, P.D.M. (2003a). Behavior of plate load tests on soil layers improved with cement and fiber. *Journal of Geotechnical and Geoenvironmental Engineering*, 129(1):96-101.
- Consoli, N.C.; Casagrande, M.D.T.; Prietto, P.D. & Thomé, A.N. (2003b). Plate load test on fiber-reinforced soil. *Journal of Geotechnical and Geoenvironmental Engineering*, 129(10):951-955.
- Consoli, N.C.; Casagrande, M.D.T. & Coop, M.R. (2007a). Performance of a fibre-reinforced sand at large shear strains. *Géotechnique*, 57(9):751-756.
- Consoli, N.C.; Heineck, K.S.; Casagrande, M.D.T. & Coop, M.R. (2007b). Shear strength behavior of fiber-reinforced sand considering triaxial tests under distinct stress paths. *Journal of Geotechnical and Geoenvironmental Engineering*, 133(11):1466-1469.
- Consoli, N.C.; Casagrande, M.D.T.; Thomé, A.; Dalla Rosa, F. & Fahey, M. (2009a). Effect of relative density on plate loading tests on fibre-reinforced sand. *Géotechnique*, 59(5):471-476.
- Consoli, N.C.; Vendruscolo, M.A.; Fonini, A. & Dalla Rosa, F. (2009b). Fiber reinforcement effects on sand considering a wide cementation range. *Geotextiles and Geomembranes*, 27(3):196-203.
- Diaz-Segura, E.G. (2013). Assessment of the range of variation of  $N_{\gamma}$  from 60 estimation methods for footings on sand. *Canadian Geotechnical Journal*, 50(7):793-800.
- Endo, T. & Tsuruta, T. (1969). The effect of tree roots upon the shearing strength of soil. Annual Report No. 18 of the Hokkaido Branch, Tokyo Forest Experiment Station, Tokyo, Japan, p. 168-179.
- Estabragh, A.R.; Bordbar, A.T. & Javadi, A.A. (2013). A study on the mechanical behavior of a fiber-clay composite with natural fiber. *Geotechnical and Geological Engineering*, 31(2):501-510.
- Gray, D.H. & Al-Refeai, T. (1986). Behavior of fabric-vs. fiber-reinforced sand. *Journal of Geotechnical Engineering*, 112(8):804-820.
- Gray, D.H. & Ohashi, H. (1983). Mechanics of fiber reinforcement in sand. *Journal of Geotechnical Engineering*, 109(3):335-353.
- Hejazi, S.M.; Sheikhzadeh, M.; Abtahi, S.M. & Zadhoush, A. (2012). A simple review of soil reinforcement by using natural and synthetic fibers. *Construction and Building Materials*, 30:100-116.
- Leflaive, E. (1988). Texsol: Already more than 50 Successful Applications. Proc. International Symposium on Theory and Practice of Earth Reinforcement. Balkema, Fukuoka, Japan, 5-7 October, 1988.
- Li, C. & Zornberg, J.G. (2012). Mobilization of reinforcement forces in fiber-reinforced soil. *Journal of Geotechnical and Geoenvironmental Engineering*, 139(1):107-115.
- Maher, M.H. & Gray, D.H. (1990). Static response of sands reinforced with randomly distributed fibers. *Journal of Geotechnical Engineering*, 116(11):1661-1677.
- Maher, M.H. & Ho, Y.C. (1994). Mechanical properties of kaolinite/fiber soil composite. *Journal of Geotechnical Engineering*, 120(8):1381-1393.
- Maher, M.H. & Woods, R.D. (1990). Dynamic response of sand reinforced with randomly distributed fibers. *Journal of Geotechnical Engineering*, 116(7):1116-1131.
- Majid A.; Liu A.; Hou, S. & Nawawi, C. (2011). Mechanical and dynamic properties of coconut fibre reinforced concrete. *Construction and Building Materials*, 30:814-825.
- Michalowski, R.L. & Cermak, J. (2002). Strength anisotropy of fiber-reinforced sand. *Computers and Geotechnics*, 29(4):279-299.
- Moraes L.S.; Cintra J.C. & Aoki N. (2007). Dynamic plate load tests. *Soils & Rocks*, 30(2):113-122.
- Park, T. & Tan, S.A. (2005). Enhanced performance of reinforced soil walls by the inclusion of short fiber. *Geotextiles and Geomembranes*, 23(4):348-361.
- Pino, L.F.M. & Baudet, B.A. (2015). The effect of the particle size distribution on the mechanics of fibre-reinforced sands under one-dimensional compression. *Geotextiles and Geomembranes*, 43(3):250-258.
- Ramli, M.; Kwan, W.H. & Abas, N.F. (2013). Strength and durability of coconut-fiber-reinforced concrete in aggressive environments. *Construction and Building Materials*, 38:554-566.
- Ranjan, G.; Vasan, R.M. & Charan, H.D. (1994). Behavior of plastic fiber-reinforced sand. *Geotextiles and Geomembranes*, 13:555-565.
- Sadek, S.; Najjar, S.S. & Freiha, F. (2010). Shear strength of fiber-reinforced sands. *Journal of Geotechnical and Geoenvironmental Engineering*, 136(3):490-499.
- Santoni, R.L.; Tingle, J.S. & Webster, S.L. (2001). Engineering properties of sand-fiber mixtures for road construction. *Journal of Geotechnical and Geoenvironmental Engineering*, 127(3):258-268.
- Sharma, V. & Kumar, A. (2017). Influence of relative density of soil on performance of fiber-reinforced soil foundations. *Geotextiles and Geomembranes*, 45(5):499-507.
- Terzaghi, K. (1951). *Theoretical Soil Mechanics*. Chapman and Hall, Limited., London.
- Tingle, J.S.; Santoni, R.L. & Webster, S.L. (2002). Full-scale field tests of discrete fiber-reinforced sand. *Journal of Transportation Engineering*, 128(1):9-16.
- Tolêdo Filho, R.D.; England, G.L. & Ghavami, K. (1997). Comportamento em compressão de argamassas reforçadas com fibras naturais. *Revista Brasileira de Engenharia Agrícola Ambiental*, 1:79-88.
- Vesic, A.S. (1975). Bearing capacity of shallow foundations. *Foundation Engineering Handbook*, 3:121-147.

- Wasti, Y. & Bütün, M.D. (1996). Behaviour of model footings on sand reinforced with discrete inclusions. *Geotextiles and Geomembranes*, 14(10):575-584.
- Yetimoglu, T. & Salbas, O. (2003). A study on shear strength of sands reinforced with randomly distributed discrete fibers. *Geotextiles and Geomembranes*, 21(2):103-110.
- Zornberg, J.G. (2002). Discrete framework for limit equilibrium analysis of fibre-reinforced soil. *Géotechnique*, 52(8):593-604.

### List of Symbols

mm : millimeters  
 m: meters  
 °: degree

kPa: kilopascal  
 $\phi$ : friction angle  
 $W_R$ : dry weight of reinforced layer  
 $W_S$ : dry weight of sand  
 $W_F$ : dry weight of fibers  
 $\gamma_R$ : dry unit weight of reinforced layer  
 $V$ : total volume of reinforced layer  
 $P_s$ : percentage of sand  
 $P_f$ : percentage of fiber  
 kN: kilonewton  
 $q_{ult}$ : bearing capacity  
 $B$ : plate diameter  
 $N\gamma$ : bearing capacity factor  
 TD: displacement transducers

# Porosity Changes of Compacted Soil Percolated with Acidic Leachate

E.P. Korf, P.D.M. Prietto, A.A. Silveira, C. Ulsen, L. Bragagnolo

**Abstract.** This paper evaluates porosity changes in compacted soil subjected to acidic leachate percolation through different dry unit weights. The porosity of compacted soil is presented in different nominal porosities or dry unit weights (41.9% and 15.5 kN/m<sup>3</sup>, 43.8% and 15.0 kN/m<sup>3</sup>, and 45.7% and 14.5 kN/m<sup>3</sup>) percolated with a sulfuric acid solution under a constant vertical stress of 280 kPa. Porosity was evaluated via X-ray microtomography ( $\mu$ -CT) and mercury intrusion porosimetry (MIP). The results demonstrated that percolation by a 2% sulfuric acid solution in compacted clay soil caused changes in pore size distribution, increased the pore diameter in all specimens' layers, and increased the porosity in specimens' upper layers due to acidic attack on the soil's microstructure. The porosity assessed by mercury intrusion showed a good correlation with the macroscopically measured porosity. The same behavior was not observed via  $\mu$ -CT due to the limited resolution of the images and the inability to characterize the micropores.

**Keywords:** compacted soil, containment barriers, mercury intrusion porosimetry (MIP), soil percolation, X-ray microtomography ( $\mu$ -CT).

## 1. Introduction

Compacted clay soils percolated by aggressive chemical agents, such as leachate from industrial waste, can be affected in the soil structure, resulting in an increase of hydraulic conductivity and a consequent reduction of reactivity, harming the ability of the soil to retain and attenuate contaminants (Broderick & Daniel, 1990; Favaretti *et al.*, 1994; Hueckel *et al.*, 1997; Knop *et al.*, 2008). According to Francisca and Glatstein (2010), the hydraulic behavior of fine or recently compacted soils is mainly influenced by interactions between percolated liquid and mineral particles. Thus, acid attack in clay soils can result in their chemical alteration and release of ions; it can also influence several physical, biological, and chemical processes (Agbenyeku *et al.*, 2016).

To understand the phenomena resulting from interaction between acid leachate and compacted soil particles, it is essential to evaluate the microstructure of the soil, since acid leachate has a substantial influence on the mechanical behavior of both natural and compacted soils (Burton *et al.*, 2015). Therefore, one of the essential parameters for microstructure alteration studies under different geotechnical conditions is porosity. Two porosity scales should be considered: microporosity, which can be defined as the saturated pores space; and macroporosity, considered as a two-phase system, which may contain both liquid and steam (Sedighi & Thomas, 2014).

Many studies have evaluated porosity in clayey, sandy, or cemented soils via image analysis from scanning electron microscopy (Rozenbaum *et al.*, 2007; Schoonderbeek *et al.*, 1983), 2D/3D X-ray tomography (Lima *et al.*, 2007; Luo *et al.*, 2008; Pires *et al.*, 2010; Trong *et al.*, 2008) or a combination of techniques, such as mercury intrusion porosimetry (MIP) with image analysis (Amirtharaj *et al.*, 2010; Gribble *et al.*, 2011; Labus, 2001; Marcelino *et al.*, 2007; Roels *et al.*, 2001; Rouquerol *et al.*, 2012; Tovey & Houslow, 1995). However, only a few studies have explored the performance of compacted materials in containing acid solutions due to difficulties in obtaining data at the micropore scale. In addition, the performance of compacted materials is continuously monitored at a macrostructural scale by settlement observation, which does not guarantee efficiency in blocking the percolation of contaminants. Therefore, determining the porosity and pore size distribution of compacted clayey soils is an essential complementary study.

The goal of this study is to evaluate variations in the porosity of compacted soil submitted to sulfuric acid (H<sub>2</sub>SO<sub>4</sub>) leachate percolation in different conditions (percolated with water and with 2% H<sub>2</sub>SO<sub>4</sub>). Sulfuric acid was chosen because it has high acidic characteristics similar to those of the leachate generated by most industrial and mining residues. Two different porosity quantification techniques were used: X-ray microtomography ( $\mu$ -CT) and

---

Eduardo Pavan Korf, Ph.D., Associate Professor, Programa de Pós-Graduação em Ciência e Tecnologia Ambiental, Universidade Federal da Fronteira Sul, Erechim, RS, Brazil. e-mail: eduardo.korf@uffs.edu.br.

Pedro Domingos Marques Prietto, Ph.D., Associate Professor, Faculdade de Engenharia, Universidade de Passo Fundo, Passo Fundo, RS, Brazil. e-mail: pdmp@upf.br.

Adriana Augustin Silveira, Ph.D., Associate Professor, Faculdade de Engenharia, Universidade de Passo Fundo, Passo Fundo, RS, Brazil. e-mail: aas@upf.br.

Carina Ulsen, Ph.D., Associate Professor, Laboratório de Caracterização Tecnológica, Departamento de Engenharia de Minas e Petróleo, Universidade de São Paulo, São Paulo, SP, Brazil. e-mail: carina@lct.poli.usp.br.

Lucimara Bragagnolo, Researcher, Universidade Federal da Fronteira Sul, Erechim, RS, Brazil. e-mail: lucimarabragagnolo@hotmail.com.

Submitted on April 24, 2018; Final Acceptance on October 2, 2018; Discussion open until April 30, 2019.

DOI: 10.28927/SR.413369

MIP. Examining the porosity and pore size distribution of the compacted clay soils was necessary to explain changes at the microstructural scale. Additionally, the examination may contribute to prediction studies and to the technological development of new materials that could ensure the effectiveness of compacted clay soils as an impermeable containment barrier.

## 2. Experimental Procedures

The studied soil samples were obtained from the University of Passo Fundo's Geotechnical Experimental Site in southern Brazil. The samples were characterized by their chemical and mineralogical compositions, content of organic matter, pH, and particle size distribution.

The chemical composition of the soil samples was determined for both pulverized and compacted samples (then compared to reference materials from approximately 290 national and international analytical standards - NIST) using a PANalytical® Axios Advanced X-ray fluorescence spectrometer (XRF) with a 4-kV rhodium X-ray tube, a detection capacity above 0.1%, and a scan time of approximately 6 min. Loss on ignition (LOI) was carried out at 1000 °C for 2 h.

The mineralogical composition of the samples was assessed by X-ray powder diffraction (XRD) with a PANalytical® Empyrean X-ray diffractometer. The analytical conditions were as follows:  $2\theta$  angle, ranging from 3° to 70°, and 10-second time steps. The identification of the crystalline phases was performed by comparing the sample diffractogram with the PDF-2 reference database from the International Centre for Diffraction Data (n.d.) and the PAN-ICSD - PANalytical Inorganic Crystal Structure Database (PANalytical, 2007).

Organic matter content was determined via the organic matter oxidation method using a sulfochromic solution, as presented by Tedesco *et al.* (1995). The pH was measured in H<sub>2</sub>O (Tedesco *et al.*, 1995). The particle size distribution was determined by sedimentation according to standard procedures (ABNT, 1984, 2005).

To define the variables for the percolation tests, different nominal porosities and dry unit-specific weights were evaluated according to the normal and modified compaction energy values of the soil, which were 41.9% (15.5 kN/m<sup>3</sup>) and 45.7% (14.5 kN/m<sup>3</sup>), respectively, with 26% moisture in both cases. Only one value was used for moisture because it is the optimum value for both normal energy and modified energy (plus 2%) typically used in engineering projects. The tests were carried out in 2 blocks, with each block comprising 2 repetitions for the adopted nominal porosities. In addition, 4 repetitions were performed in each block for a central point (43.8% - 15 kN/m<sup>3</sup>) in order to evaluate the experimental error for mean comparison (identified by "CP" 1 to 8). In one of the experimental blocks, percolation was conducted with distilled water; in the other, 2% sulfuric acid (H<sub>2</sub>SO<sub>4</sub>) was used.

The percolation tests were conducted over an extended period of time: 30 to 70 days. The tests included specimens 7 cm in diameter and 6 cm in height, and percolation was performed with a hydraulic gradient of 8.33 m/m under the application of a constant vertical stress of 280 kPa to simulate a 15-m height of waste mining over the barrier, with a total specific weight of 18.6 kN/m<sup>3</sup> based on literature data (Bedin, 2010; Schnaid *et al.*, 2006).

After acidic percolation, the specimens were cut into three layers (top, middle, and bottom layers, considering downward flow). Samples from each layer were cut into prismatic shapes with approximate dimensions of 2.0 cm x 0.7 cm x 0.7 cm and were identified by layer (T = top, M = middle, B = bottom). After the samples were leached, they were dried. For each layer, the macroscopically measured porosity was determined by theoretical relation to dry unit-specific weights. Porosity was also determined by high-resolution  $\mu$ -CT with a Bruker® Skyscan 1172 and by MIP with Micrometrics Autopore IV equipment according to the procedure described in ISO 15901-1 (ISO, 2016). With the  $\mu$ -CT and MIP techniques, the average cumulative distribution curve of the pores and variations in the pore size distributions in the specimens' layers were determined.

The characterization by microtomography comprised three phases: (1) data acquisition via rotation of the sample in 0.4° steps, resulting in a minimum pixel size of 5  $\mu$ m; (2) 3D image reconstruction; and (3) binarization of the generated images (Fig. 1) and grayscale segmentation corresponding to voids and solids to determine the void volume (porosity). The segmentation was performed using a numerical algorithm (LI method) available in the Image J® software. Comparatively speaking, this method best represents the magnitude of values of porosity evaluated.

Regarding image processing, the collection and magnification conditions used in  $\mu$ -CT define the image resolution and, therefore, its constituents. In this study, the detected pixel size was 5  $\mu$ m (each pixel). For segmentation, to define a pore, at least 2 pixels were considered, so it was possible to characterize only pores larger than 10  $\mu$ m (10 000 nm).

MIP was performed in the following operating conditions: contact angle of 130°, mercury pressure from 0.5 psi to 40 000 psi, equilibrium time of 10 s, and mercury surface tension of 485 dynes/cm. The pore diameter ( $d_p$ ) accessible to mercury depends on the applied pressure, mercury surface tension, and contact angle with the studied material, as described by the Washburn equation:  $d_p = -4 \cdot \gamma \cdot \cos\theta / \text{Pressure}$  (Washburn, 1921). In the adopted operating conditions, considering an intrusion pressure up to 40 000 psi, it is possible to characterize the pores down to 4.5 nm.

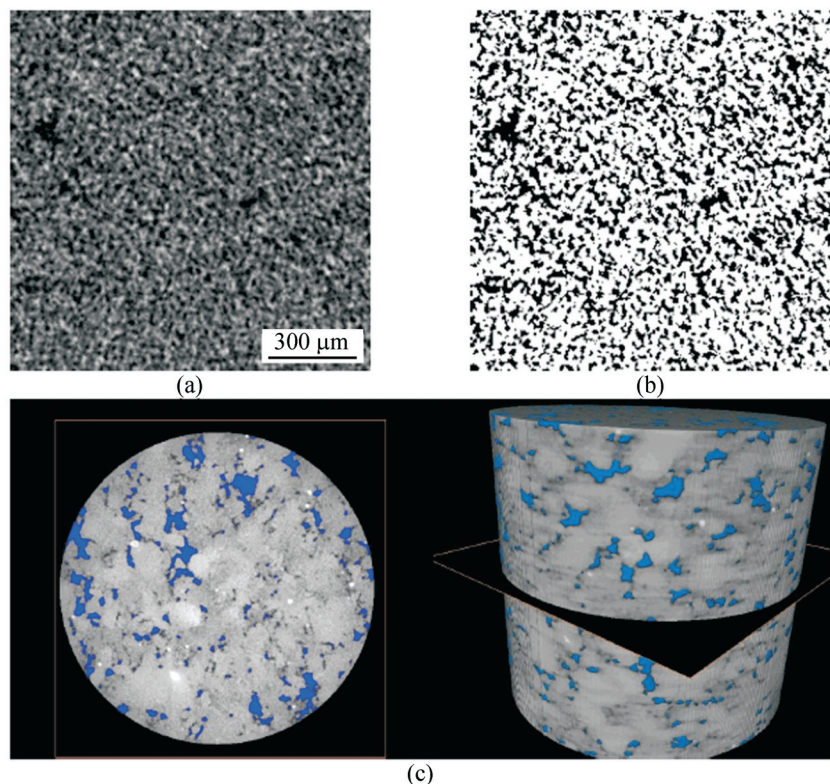


**Figure 1** - Example of visualization of the analyzed samples: (a) in 2D; (b) after 2D segmentation; (c) a view of a circular cross-section from a reconstructed solid in 3D, with solid material indicated in gray and voids represented in blue.

### 3. Results

The sampled soil possessed a low organic matter content (< 0.8%), a high clay-size particle content (68%), and an acidic pH (pH = 5.5). According to X-ray diffraction analysis (Fig. 2) and chemical composition (Table 1), the soil was a kaolinite-based clay with a significant presence of hematite (Fe<sub>2</sub>O<sub>3</sub> content of 11.7% - Table 1), quartz (SiO<sub>2</sub> content of 47.9%) and aluminum oxide (AlO<sub>3</sub> content of

26.6%). These characteristics represent promising conditions for use as a base material for containment barriers.

Table 2 shows the porosity results obtained from the macroscopically measured value determination, via MIP and μ-CT, for specimens tested by percolation with a 0% and 2% sulfuric acid solution. The specimens were presented according to their central and factorial points, both of which were related to the nominal porosity values - P (nominal). Moreover, the median pore diameter (D50) was

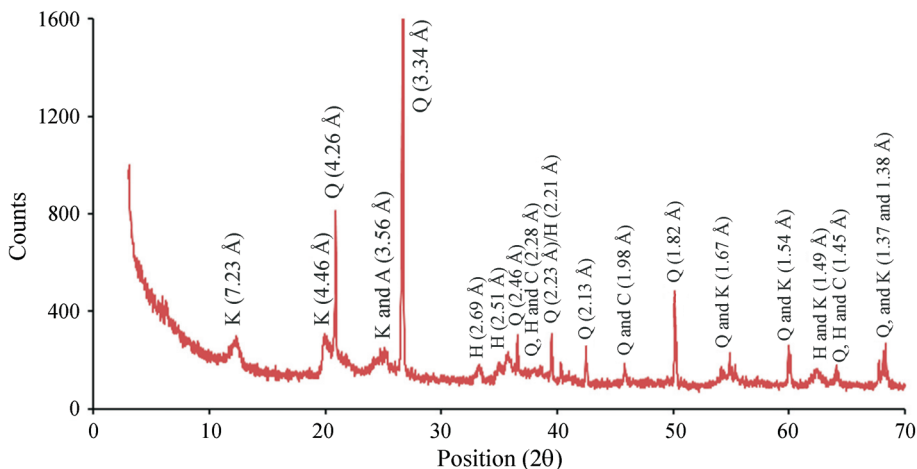


**Figure 2** - Mineralogical identification of the sampled soil (C - Kaolinite, Q - Quartz, H - Hematite, Ca - Calcite) by DRX.

**Table 1** - Chemical composition (XRF) and loss on ignition (LOI).

Oxide	Content (%)	Element	Content (%)
SiO <sub>2</sub>	47.9	Si	22.4
Fe <sub>2</sub> O <sub>3</sub>	11.7	Fe	8.2
Al <sub>2</sub> O <sub>3</sub>	26.6	Al	14.1
CaO	< 0.1	Ca	< 0.1
TiO <sub>2</sub>	1.7	Ti	1.0
K <sub>2</sub> O	0.4	K	0.3
ZrO <sub>2</sub>	0.1	Zr	< 0.1
SO <sub>3</sub>	< 0.1	S	< 0.1
MgO	0.4	Mg	0.2
P <sub>2</sub> O <sub>5</sub>	0.1	P	< 0.1
MnO	< 0.1	Mn	< 0.1
Na <sub>2</sub> O	< 0.1	Na	< 0.1
V <sub>2</sub> O <sub>5</sub>	< 0.1	V	< 0.1
Loss on ignition	10.9	O	50.6
C	3.0		

presented. Comparative data are shown in Fig. 3. Figure 3 also illustrates the average porosity of 8 specimens from the top, middle, and bottom layers, percolated with water (Fig. 3a) and 2% sulfuric acid solution (Fig. 3b) and assessed by MIP,  $\mu$ CT, and macroscopically measured.

Figure 4 shows the average porosity assessed by MIP for the nominal initial porosity of each specimen's layers percolated with water (Fig. 4a) and 2% sulfuric acid solution (Fig. 4b).

In Fig. 5, the top row shows the average cumulative distribution curve of the pores of the top, middle, and bottom layers, assessed by MIP and  $\mu$ -CT, of specimens subjected to percolation with 0% and 2% sulfuric acid solution. The variations in the specimen layers' pore size distributions, measured by MIP and  $\mu$ CT after leaching with water (Fig. 5b) and 2% sulfuric acid (Fig. 5c), are also shown.

Figure 6 shows the correlation between the porosity obtained from MIP (Fig. 6a) and  $\mu$ -CT (Fig. 6b) and the macroscopically measured values for samples percolated with water and 2% sulfuric acid in different layers.

#### 4. Discussion

The average porosity of the samples percolated with 2% sulfuric acid solution (Table 2, Fig. 3b) was higher in the upper layers than in the middle and lower layers, with the exception of samples with a value of 41.9 for nominal porosity, which had similar porosity values for all layers. In this case, more efficient compaction may have promoted more homogeneous percolation of the acid solution in the samples, besides reducing the transport of particles to the lower layers.

**Table 2** - Porosity obtained by the different methods used on specimens percolated with water and 2% sulfuric acid solution.

Tests Specimens	0% H <sub>2</sub> SO <sub>4</sub>								2% H <sub>2</sub> SO <sub>4</sub>							
	CP1	CP6	CP2	CP3	CP5	CP7	CP4	CP8	CP1	CP6	CP2	CP3	CP5	CP7	CP4	CP8
P (nominal porosity)	41.9								43.8							
Top	45.7								45.7							
P (Macroscopically measured)	35.6	36.8	41.2	37.3	39.4	40.2	39.4	39.2	38.1	41.1	42.0	40.9	40.4	38.2	40.6	40.7
P ( $\mu$ -CT)	37.4	33.5	37.7	34.8	35.6	32.0	29.4	30.5	33.0	42.2	39.4	31.6	32.8	36.4	37.3	37.0
D50 ( $\mu$ -CT)	21.7	n.d.	25.9	28.1	25.3	29.5	22.7	21.3	29.0	25.7	29.3	34.1	31.2	27.0	28.4	28.4
P (MIP)	34.1	38.5	42.4	35.8	39.3	38.2	40.8	38.3	37.6	38.4	42.0	40.6	39.7	39.5	41.3	41.9
D50 (MIP)	14.5	17.4	29.7	14.2	20.9	21.0	20.8	19.9	15.9	19.3	20.6	18.9	17.9	19.3	21.7	20.3
P (Macroscopically measured)	36.7	36.6	39.0	41.2	36.9	41.3	41.1	36.6	33.1	39.7	36.9	36.4	38.2	37.8	40.1	44.2
P ( $\mu$ -CT)	36.7	33.6	34.4	29.2	42.6	27.1	32.2	38.4	27.7	28.2	34.2	34.5	33.3	32.6	34.6	25.6
D50 ( $\mu$ -CT)	18.0	17.1	26.7	31.5	24.2	32.4	21.4	22.3	31.1	32.0	29.2	29.1	28.7	30.6	27.5	38.6
P (MIP)	35.6	36.6	37.8	42.8	38.6	39.6	40.4	38.6	36.1	39	37.6	36.4	38.4	39.2	37.9	41.7
D50 (MIP)	15.2	16.1	18.5	36.5	16.5	23.0	18.1	18.0	15.4	34.1	16.6	16.2	17.2	20.6	19.1	22.3
P (Macroscopically measured)	38.9	37.4	38.1	38.1	37.6	39.4	39.4	42.6	41.3	33.9	37.3	41.6	42.4	35.2	35.2	40.4
P ( $\mu$ -CT)	31.8	32.6	30.4	40.3	45.6	44.0	27.7	31.8	34.6	38.0	27.8	28.1	35.4	31.1	31.4	26.2
D50 ( $\mu$ -CT)	17.4	17.1	30.8	24.6	23.2	23.8	25.9	21.9	26.5	25.3	34.3	35.1	27.4	30.7	28.3	37.5
P (MIP)	38.7	38.2	41.1	36.7	36.6	37.3	35.9	40.9	39.9	36.0	35.5	38.3	30.7	38.4	36.4	45.2
D50 (MIP)	18.1	17.0	21.0	16.7	16.0	18.0	nd	30.8	18.3	20.4	16.8	23.0	16.9	24.5	15.4	24.3

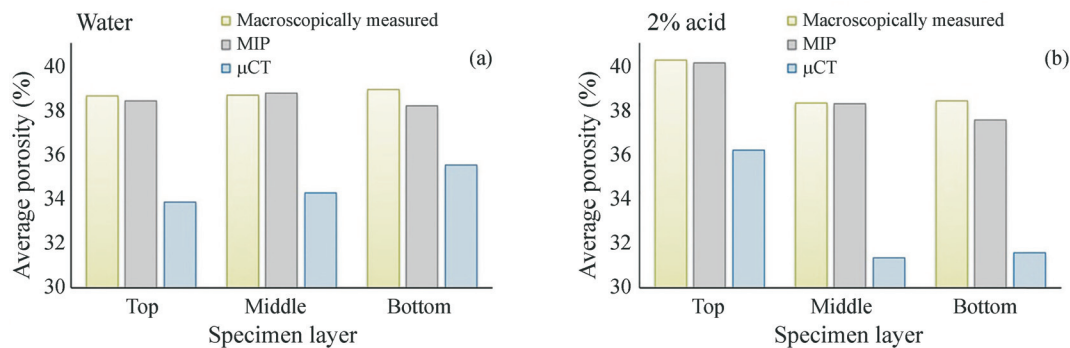


**Figure 3** - Average porosity of the top, middle, and bottom layers of the 8 (CP1 to CP8) specimens subjected to percolation with (a) water and (b) 2% sulfuric acid.

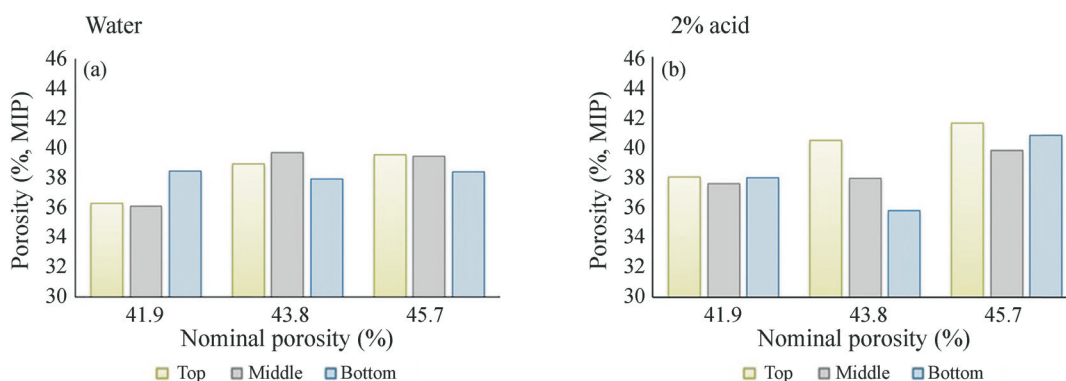


**Figure 4** - Average porosity variation in different layers for each nominal initial porosity in specimens subjected to percolation by (a) water and (b) 2% sulfuric acid as assessed by MIP.

This behavior, *i.e.*, higher average porosity values for samples percolated with 2% sulfuric acid solution in upper layers, might represent evidence for acidic attack on soil structure, since this result was not observed in samples percolated with aqueous solution, in which the porosity tended to be similar across layers (0% acid, Fig. 3a). The lower porosities observed in the lower layers after acid percolation may possibly be due to both the filling of voids in these layers by products from the chemical attack and the closure of micropores caused by the impact of the applied load of the upper layers under compression.

Regarding nominal porosity, a total average porosity reduction of 12% occurred for samples treated with water and 2% acid when compared with nominal porosity values (41.9, 43.8, and 45.7). This effect may have been caused by the vertical load application, not acid percolation.

The disparity in results between MIP and  $\mu$ CT occurred due to the different resolutions of each technique, *i.e.*,  $\mu$ -CT does not detect micropores. Therefore, the total porosity assessed by  $\mu$ CT was noticeably lower when compared to MIP and macroscopically measured porosity (Table 2, Fig. 3a,b) (10 to 20% lower). Additionally, the median pore diameter ( $D_{50}$ ) (Table 2) demonstrated a large difference between the applied techniques: The pore diam-

eter in MIP measurements was up to 50% larger than in  $\mu$ CT; this difference is even more evident in samples percolated with acid solution. Thus, MIP showed smaller  $D_{50}$  values, reflecting a range of smaller-diameter pores and enabling the identification of micropores (< 2 nm) and mesopores (between 2 and 50 nm) according to the classification proposed by IUPAC (Rouquerol *et al.*, 1994);  $\mu$ -CT, on the other hand, only allowed the identification of macropores (> 50 nm).

The pores' cumulative distribution curve (Fig. 5) clearly demonstrates differences in terms of range between the techniques (MIP and  $\mu$ CT). The minimum pore size evaluated by  $\mu$ CT was 10 000 nm (10  $\mu$ m), whereas MIP detected pores as small as approximately 4 nm (0.004  $\mu$ m). Regarding pore size distribution, percolated samples of 2% sulfuric acid (Fig. 5a) demonstrated clear changes in microstructure from the point of view of increasing pore diameter. Moreover, it was observed that percolation with 2% sulfuric acid equalized the pores' size distribution, especially in the upper layers (Fig. 5c).

The modification of pore size distribution among the layers can be explained by the acidic attack on the structure, which caused an increase in both pore diameter and total porosity, especially in the upper layers of the tested speci-

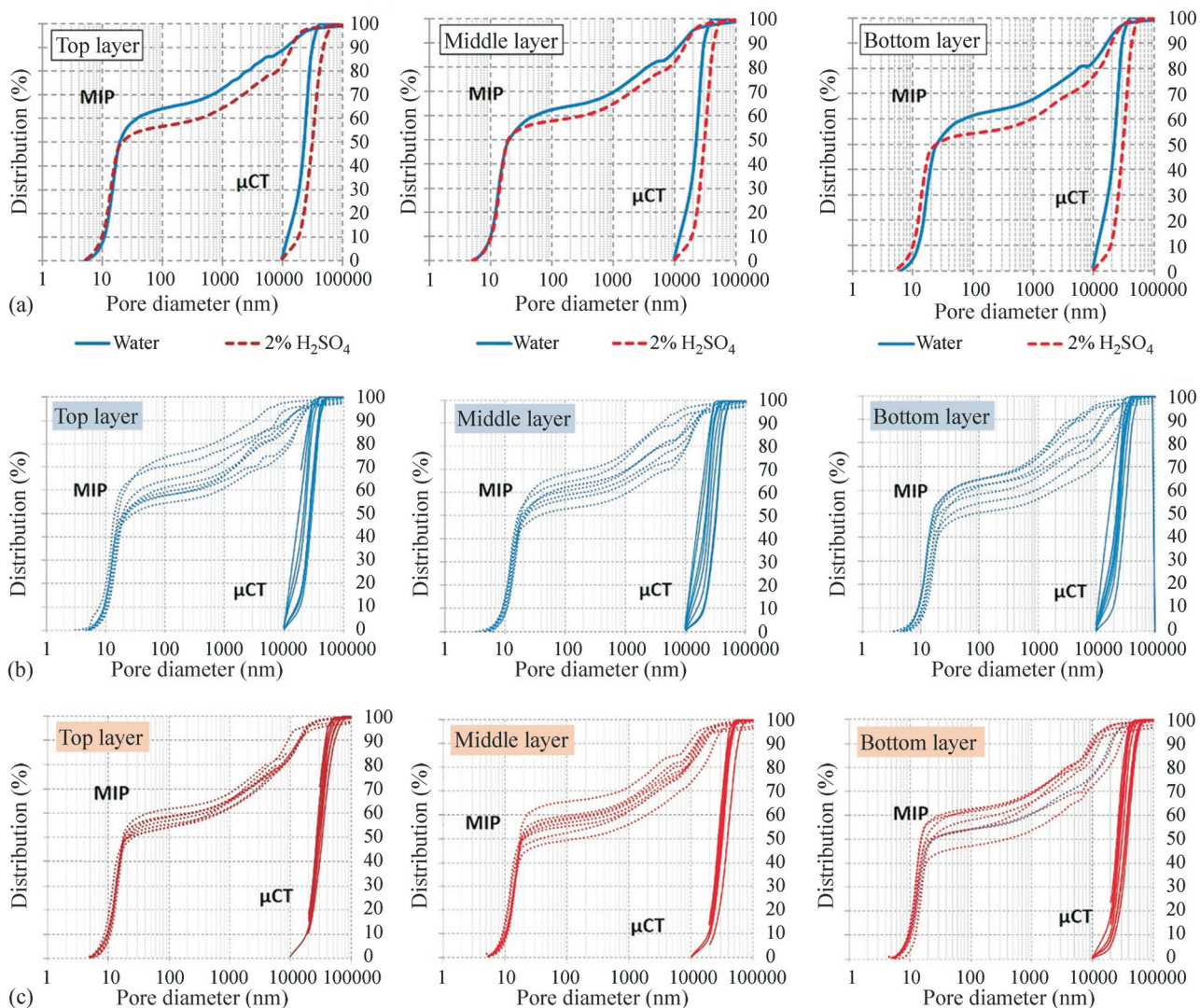


**Figure 5** - Pore size distribution of average specimen's layers by MIP and  $\mu$ CT when leached with: a) water and 2% sulfuric acid; b) water; c) 2% sulfuric acid.

mens. This evidence would not have been obtainable had only a macrostructural analysis of compacted barriers been performed, in which changes in hydraulic conductivity and mechanical behavior would have been observed without knowing their cause being known. Knowledge about the impact of pores on soil microstructures can also provide a better understanding of, for example, which contaminant transport process is most relevant to the study of subsurface contamination vulnerability and how to better predict performance with greater certainty and reliability.

In regard to the analytical determination of porosity, the best correlation was found between the MIP results and the macroscopically measured porosity (Fig. 6a and Table 2). On the other hand, the porosity determined by  $\mu$ -CT had a low correlation with the macroscopically measured porosity (Fig. 6b) because the detection limit of the technique does not allow the quantification of micropores. Al-

though the micropores contributed little to the total porosity of the specimens when compared to the volume of macropores, they did significantly influence the calculation of the median diameter.

It should be noted that the maximum possible resolution from the  $\mu$ -CT technique is equivalent to 1  $\mu$ m, which is far weaker than the resolution obtainable by MIP (4.5 nm for 40 000 psi of intrusion pressure). To reach a similar resolution in  $\mu$ -CT, the sample size would have to be reduced to about 1 mm, which would lead to the loss of the sample's representativeness.

Analyses by  $\mu$ -CT are often mentioned in the literature because the method is non-destructive and allows the pore structure to be viewed. Several researchers have successfully used  $\mu$ -CT to quantify porosity, but only for materials with larger particle diameters than clay fractions; besides, these researchers were more interested in macroporous

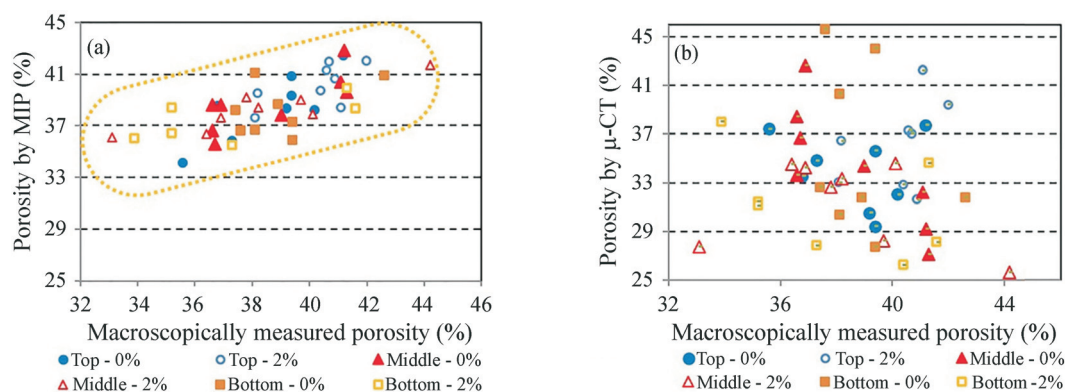


**Figure 6** - Porosity obtained from (a) MIP and (b)  $\mu$ -CT regarding the macroscopically measured values for samples percolated with water (0%) and 2% sulfuric acid in different layers.

characterization (Lima *et al.*, 2007; Luo *et al.*, 2008; Neto *et al.*, 2011; Pires *et al.*, 2005). For the study of compacted soils,  $\mu$ -CT is only partially effective due to the presence of microporosity.

The use of mercury intrusion under high pressure can erroneously quantify the porosity of a sample due to the effects of compression or structural changes (Giesche, 2006; With & Glass, 1997) - this factor should be carefully considered. In addition, ordinary calculations consider pores as cylinders, which may not represent their actual sizes and dimensions. Despite these disadvantages, this study noted that mercury intrusion showed the best correlation with the macroscopically measured porosity as well as the best sensitivity for micropore characterization. The intrusion, which curved up to 40 000 psi, did not indicate structural changes in the samples.

In this sense, limitations can be overcome, and the most satisfactory and conclusive results can be obtained by using a combination of different techniques. Some studies in the literature have used a combination of MIP with tomography and other techniques to assess the porosity of porous materials (Abel *et al.*, 1999; Gribble *et al.*, 2011; Roels *et al.*, 2001); this approach was also considered in this study and allowed for the characterization of porosity and pore size distribution.

## 5. Conclusions

Samples percolated with a solution of 2% sulfuric acid in compacted clay soil samples suffered changes in the pore size distribution and an increase in pore diameter in the specimens; a greater increase in porosity in the specimens' upper layers was observed due to acidic attack on the soil microstructure. The porosity assessed by mercury intrusion porosimetry (MIP) showed the best correlation with the macroscopically measured porosity. The same behavior was not observed for  $\mu$ -CT results due to limited image resolution, which precluded the identification of micropores.

## Acknowledgments

The authors wish to express their gratitude to CNPq, FAPERGS (Universal/CNPq 486340/2011-2 e PRONEM/FAPERGS/CNPq 11/2041-4) and CAPES for financial support to the research group.

## References

- Abel, A.B.; Willis, K.L. & Lange, D.A. (1999). Mercury intrusion porosimetry and image analysis of cement-based materials. *Journal of Colloid and Interface Science*, 211(1):39-44.
- ABNT, Associação Brasileira de Normas Técnicas (1984). NBR 7181: Soil - Granulometric Analysis. ABNT, Rio de Janeiro.
- ABNT, Associação Brasileira de Normas Técnicas (2005). NBR ISO 15901-1: Pore size distribution and porosity of solid materials by mercury porosimetry and gas adsorption. ABNT, Rio de Janeiro.
- Agbenyeku, E.E.; Muzenda, E. & Msibi, M.I. (2016). Chemical alterations in three clayey soils from percolation and interaction with acid mine drainage (AMD). *South African Journal of Chemical Engineering*, 21(1):28-36.
- Amirtharaj, E.; Ioannidis, M.A.; Parker, B. & Tsakiroglou, C.D. (2010). Statistical synthesis of imaging and porosimetry data for the characterization of microstructure and transport properties of sandstones. *Transport in Porous Media*, 86(1):135-154.
- Bedin, J. (2010). Estudo do Comportamento Geomecânico de Resíduos de Mineração. Thesis, Escola de Engenharia, Universidade Federal do Rio Grande do Sul, Porto Alegre, 207 p.
- Broderick, G.P. & Daniel, D.E. (1990). Stabilizing compacted clay against chemical attack. *J. Geotech. Engrg.*, 116(10):1549-1567.
- Burton, G.J.; Pineda, J.A.; Sheng, D. & Airey, D. (2015). Microstructural changes of an undisturbed, reconsti-

- tuted and compacted high plasticity clay subjected to wetting and drying. *Engineering Geology*, 193(1):363-373.
- Favaretti, M.; Moraci, N. & Previatello, P. (1994). Effects of Leachate on the hydraulic and Mechanical Behavior of Clay Liners. 1 st Congress on Environmental Geotechnics, Alberta, Canada, p. 221-226.
- Francisca, F.M. & Glatstein, D.A. (2010). Long term hydraulic conductivity of compacted soils permeated with landfill leachate. *Applied Clay Science*, 49(3):187-193.
- Giesche, H. (2006). Mercury porosimetry: a general (practical) overview. *Particle & Particle Systems Characterization*, 23(1):1-11.
- Gribble, C.M.; Matthews, G.P.; Laudone, G.M.; Turner, A.; Ridgway, C.J.; Schoelkopf, J. & Gane, P.A.C. (2011). Porometry, porosimetry, image analysis and void network modeling in the study of the pore-level properties of filters. *Chemical Engineering Science*, 66(16):3701-3709.
- Hueckel, T.; Kaczmarek, M. & Caramuscio, P. (1997). Theoretical assessment of fabric and permeability changes in clays affected by organic contaminants. *Canadian Geotechnical Journal*, 34(4):588-603.
- International Centre for Diffraction Data. (n.d.). It provides information on mission, research, developed products, etc.
- ISO, International Standards Organisation (2016). ISO 15901-1:2016: Evaluation of pore size distribution and porosity of solid materials by mercury porosimetry and gas adsorption - Part 1: Mercury porosimetry.
- Knop, A.; VanGulck, J.; Heineck, K.S. & Consoli, N.C. (2008). Compacted artificially cemented soil-acid leachate contaminant interactions: Breakthrough curves and transport parameters. *Journal of Hazardous Materials*, 155(1-2):269-276.
- Labus, M. (2001). Comparison of computer image analysis with mercury porosimetry in sandstone porosity measurement. *Geological Quarterly*, 45(1):75-79.
- Lima, I.; Appoloni, C.; Oliveira, L. & Lopes, R.T. (2007). Characterization of ceramic materials through computerized 3D microtomography. *Revista Brasileira de Arqueometria, Restauração e Conservação*, 1(2):22-27.
- Luo, L.; Lin, H. & Halleck, P. (2008). Quantifying soil structure and preferential flow in intact soil using x-ray computed tomography. *Soil Science Society of America*, 72(4):1058-1069.
- Marcelino, V.; Cnudde, V.; Vansteelandt, S. & Caro, F. (2007). An evaluation of 2D-image analysis techniques for measuring soil microporosity. *European Journal of Soil Science*, 58(1):133-140.
- PANalytical. (2007). PANalytical Inorganic Crystal Structure Database.
- Pires, L.F.; Borges, J.A.R.; Bacchi, O.O.S. & Reichardt, K. (2010). Twenty-five years of computed tomography in soil physics: a literature review of the Brazilian contribution. *Soil & Tillage Research*, 110(2):197-210.
- Pires, L.F.; Pilotto, J.E.; Timm, L.C.; Bacchi, O.O.S. & Reichardt, K. (2005). Qualitative and quantitative analysis of soil samples by computerized tomography. *Ciências Exatas e da Terra, Ciências Agrárias e Engenharias*, 11(2):7-15.
- Reis Neto, J.M.; Fiori, A.P.; Lopes, A.P.; Marchese, C.; Coelho, C.V.P.; Vasconcellos, E.M.G.; Silva, G.F. & Secchi, R. (2011). A Computed X-ray microtomography integrated into petrography in three-dimensional study of porosity in rocks. *Revista Brasileira de Geociências*, 41(3):498-508.
- Roels, S.; Elesen, J.; Carmeliet, J. & Hems, H. (2001). Characterisation of pore structure by combining mercury porosimetry and micrography. *Materials and Structures*, 34(2):76-82.
- Rouquerol, J.; Avnir, D.; Fairbridge, W.; Everett, D.H.; Haynes, J.H.; Pernicone, N.; Ramsay, J.D.F.; Sing, K.S.W. & Unger, K.K. (1994). Recommendations for the characterization of porous solids. *Pure and Applied Chemistry*, 66(8):1739-1758.
- Rouquerol, J.; Baron, G.; Denoyel, R.; Giesche, H.; Groen, J.; Klobes, P.; Levitz, P.; Neimark, A. V.; Rigby, S.; Skudas, R.; Sing, K.; Thommes, M. & Unger, K. (2012). Liquid intrusion and alternative methods for the characterization of macroporous materials. *Pure and Applied Chemistry*, 84(1):107-136.
- Rozenbaum, O.; Le Trong, E.; Rouet, J.L. & Bruand, A. (2007). 2D-image analysis: A complementary tool for characterizing quarry and weathered building limestones. *Journal of Cultural Heritage*, 8(2):151-159.
- Schnaid, F.; Bedin, J. & Corte, C. (2006). Avaliação do comportamento geotécnico de barragens de rejeito de minério de ferro através de ensaios de piezocone. *Solos e Rochas*, 29:391-394.
- Schoonderbeek, D.; Thiel, F. & Bisdorn, E.B.A. (1983). Quantimet 720 analysis of porosities in backscattered electron scanning images made with different photo-techniques. *Geoderma*, 30(1-4):271-275.
- Sedighi, M. & Thomas, H.R. (2014). Micro porosity evolution in compacted swelling clays - A chemical approach. *Applied Clay Science*, 101(1):608-618.
- Tedesco, M.J.; Gianello, C.; Bissani, C.A.; Bohnen, H. & Volkweiss, S.J. (1995). Análises de Solo, Plantas e Outros Materiais. Embrapa, Porto Alegre.
- Tovey, N.K. & Houslow, M.W. (1995). Quantitative micro-porosity and orientation analysis in soils and sediments. *Journal of the Geological Society*, 152(1):119-129.

- Trong, E.L.; Rozenbaum, O.; Rouet, J. & Bruan, A. (2008). A simple methodology to segment X-ray tomographic images of a multiphasic building stone. *Image Analysis & Stereology*, 27(1):175-182.
- Washburn, E.W. (1921). Note on a method of determining the distribution of pore sizes in a porous material. *Proceedings National Academy of Sciences*, 7(4):115-116.
- With, G. de. & Glass, H.J. (1997). Reliability and reproducibility of mercury intrusion porosimetry. *Journal of the European Ceramic Society*, 17(6):753-757.



## **Case Study**

***Soils and Rocks***  
**v. 41, n. 3**



# Effects of Spatial Variability on Slope Reliability: A Hypothetical Case Study

E. Muñoz, M.P. Cordão Neto, A. Ochoa

**Abstract.** Due to the complexity and uncertainty involved in mass movements, it is not possible to predict their occurrence with accuracy. This uncertainty is due to the space-time variability of physical soil parameters and processes, which determine the boundary conditions of the problem. In this study, we analyzed the influence of spatial variability of the parameters that determine soil resistance, the water retention curve and the unsaturated hydraulic conductivity function on the Factor of Safety of a hypothetical slope. To determine the parameters to which the slope is more sensitive, we carried out a sensitivity analysis using the First-Order Second-Moment Method. We assumed that spatial variability follows normal and lognormal distribution, by using a methodology based on Monte Carlo Simulations and a Kriging process. The water flow equation is solved using numerical methods and the Factor of Safety was found with the Limit Equilibrium Method. According to the sensitivity analysis, the parameters that most affect the stability of the slope analyzed are cohesion, friction angle, air-entry value, and saturated hydraulic conductivity. When varying the air-entry value and cohesion, the probability distributions have very low dispersion, and mode has values similar to the deterministic values of Factor of Safety. The hydraulic conductivity variation results in that the values of mode move further away from the deterministic Factor of Safety as time progresses, increasing at the same time the dispersion. When all parameters are varied simultaneously, the behavior of the Factor of Safety is highly influenced by the hydraulic conductivity.

**Keywords:** factor of safety (*FS*), hydrology, landslides, uncertainty, unsaturated soil.

## 1. Introduction

Landslides are among the most frequent natural disasters in the world, especially in tropical regions, which are characterized by having deep and weathered soil profiles, steep slopes, and high precipitation (Cho, 2014). Understanding the mechanical behavior of soil-water system becomes relevant since landslides cause significant human and economic losses (Tarolli *et al.*, 2011; Legorreta Paulin *et al.*, 2016).

Due to the complexity and uncertainty surrounding the landslide phenomenon, it is not possible to accurately predict its occurrence (Metya & Bhattacharya, 2015). Uncertainty could be the result of many factors, such as, the natural spatial and temporal variability of geotechnical and hydrological parameters (Cho, 2007; Casagli *et al.*, 2009; Imaizumi *et al.*, 2009), limitations of in-situ research, and imperfections in the applied model (Lacasse, 2013; Raia *et al.*, 2013; Athapaththu *et al.*, 2015). However, estimations of slope safety level are often based upon deterministic values that result in unrealistic hazard assessments, being necessary to develop tools that allow the inclusion of the effects of probability.

The most common probabilistic approaches used in geotechnical engineering are namely: Point Estimate Method, *PEM*, First-Order Second-Moment Method, *FOSM*, and Monte-Carlo Simulation Method, *MSM*, (*e.g.*

Chowdhury 1986; Christian *et al.*, 1992; Chowdhury 1992; Duncan 2000; Griffiths & Fenton 2004; Chok 2008; Griffiths *et al.*, 2009).

The spatial variability of soil properties has been stochastically studied since Alonso (1976), who showed the uncertainty level of the parameters involved and the degree of correlation of soil properties. Li & Lumb (1987), Cho (2007), Wang *et al.* (2011), and Li *et al.* (2013) studied spatial variability under the framework of the Limit Equilibrium Method, *LEM*, and the Finite Element Method, *FEM*. Li & Lumb (1987) discussed some improvements on the *FOSM* probabilistic approach to slope design. Cho (2007) and Wang *et al.* (2011) presented a numerical procedure for a probabilistic slope stability analysis based on *MSM*. Other methods used to study the spatial variability of soil parameters are the Random Element Method, *RFEM*, (*e.g.*, Griffiths & Fenton 2004; Chok 2008; Griffiths *et al.*, 2009; Hue Le *et al.*, 2015), and the Stochastic Finite Element Method, *SFEM*, (*e.g.*, Farah *et al.*, 2011; Jiang *et al.*, 2014).

Among parameters frequently studied are: hydraulic conductivity (*e.g.*, Griffiths & Fenton 1993; Gui *et al.*, 2000; Srivastava *et al.*, 2010; Santoso *et al.*, 2011; Otálvaro & Cordão-Neto 2013), cohesion (*e.g.*, Li & Lumb 1987; Cho 2007; Li *et al.*, 2013; Tietje *et al.*, 2014), friction angle (*e.g.*, Cho 2007; Griffiths *et al.*, 2009; Jiang *et al.*, 2014;

Estefanía Muñoz, Ph.D. Student, Universidad Nacional de Colombia, Medellín, Colombia, e-mail: emunozh@unal.edu.co.

Manoel P. Cordão Neto, Ph.D., Associate Professor, Universidade de Brasília, Brasília, DF, Brazil, e-mail: porfirio@unb.br.

Andrés Ochoa, Associate Professor, Ph.D., Universidad Nacional de Colombia, Medellín, Colombia, e-mail: aochoaj@unal.edu.co.

Submitted on September 8, 2017; Final Acceptance on September 18, 2018; Discussion open until April 30, 2019.

DOI: 10.28927/SR.413381

Metya & Bhattacharya 2015), Young’s modulus (*e.g.*, Farah *et al.*, 2011; Griffiths & Fenton, 2009), Poisson’s ratio (*e.g.*, Farah *et al.*, 2011), unit weight (*e.g.*, Griffiths *et al.*, 2011; Wang *et al.*, 2011), air-entry value (*e.g.*, Otálvaro & Cordão-Neto 2013), void ratio (*e.g.*, Hue Le *et al.*, 2015), and undrained shear strength (*e.g.*, Griffiths & Fenton 2004; Wang *et al.*, 2011; Li *et al.*, 2013).

In this analysis, we propose a methodology to assess the influence of spatial variability on unsaturated slope stability based on the *MSM* and a Kriging process. The Kriging process is used to interpolate the values of each parameter in the nodes and calculate the value in the element, while the *MSM* is employed to find the probability density function of Factor of Safety, *FS*.

We use the Finite Elements Method, *FEM*, and Finite Difference Method, *FDM*, to solve the water flow equation numerically, and the *LEM* to find the Factor of Safety, *FS*. The varied parameters are determined through a sensitivity analysis with the *FOSM*. This methodology allows the varying of soil parameters using the same equations to solve in space the flow equation numerically, *i.e.*, the shape functions.

## 2. Flow and Stability Analysis

When assessing slope stability, the processes occurring within the soil mass due to changes in water content must be simulated, which is possible by solving the unsaturated soil flow equation. In this analysis, the spatial and temporal solutions are determined using the *FEM* and *FDM*, respectively.

As the flow equation solution is a function of the hydraulic head, *h*, it is necessary to define constitutive models of hydraulic conductivity and water content volume involving *h*. As water content constitutive relation, we use the Soil Water Retention Curve, *SWRC*, by Van Genuchten (1980), expressed by

$$\Theta = \left[ \frac{1}{1 + (ah)^n} \right]^m, \quad m = 1 - \frac{1}{n} \quad (1)$$

where *a* is the inverse of air-entry value, *m* and *n* are shape parameters, and  $\Theta$  is the normalized volumetric moisture content, defined as

$$\Theta = \frac{\theta_w - \theta_r}{\theta_s - \theta_r} \quad (2)$$

where  $\theta_r$  and  $\theta_s$  are the residual and saturation volumetric contents, respectively. This constitutive relation allows to obtain the term  $\beta_w = \partial\theta_w/\partial h$ , which is a measure of the facility of water entering or leaving a soil element due to suction variations.

As a constitutive relation for the hydraulic conductivity,  $k_w$ , and the degree of saturation,  $S_r$ , it is used the power law model by Campbell (1974), expressed as

$$k_w(S_r) = k_s S_r^d \quad (3)$$

where  $d = 2b + 3$ , *b* is a soil empirical exponent, and  $k_s$  is the coefficient of saturated hydraulic conductivity.

The pore water pressure, *pwp*, field obtained from the flow analysis, and Bishop’s Method are used to calculate *FS*. It is noted that we assume a fixed failure surface, corresponding to the most probable surface for the stationary case. This surface represents the condition with the lowest *FS*, *i.e.*, the most conservative condition.

## 3. Geometry, Initial Conditions and Soil Properties

The geometry of the analyzed slope is the hypothetical case presented by Otálvaro & Cordão-Neto (2013). The slope is divided into a mesh of 900 rectangular elements (approximately 1 m x 1 m). Slope inclination is 1.5 H: 1.0 V, width is 45 m, and height is 10 m. The water table level is that resulting from the stationary analysis, by imposing *pwp* equal to zero at the slope foot, and a steady flow of  $7 \times 10^{-7}$  m/s entering on the left side. Figure 1 shows the water table position, and slope geometry.

Table 1 shows the values of the soil parameters used in the modelling. Mean,  $\mu$ , coefficient of variation, *CV*, and air-entry values are those estimated by Oliveira (2004) using the “Three-Sigma rule”.

The values of the soil water retention curve parameters are those by Oliveira (2004) and Otálvaro & Cordão-Neto (2013), shown in Table 2. The *CV* of *n* is determined

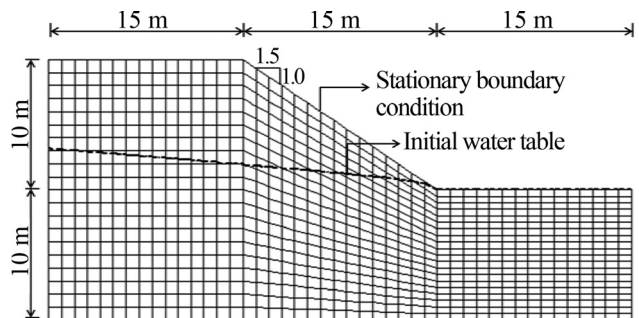


Figure 1 - Geometry and initial conditions of the problem.

Table 1 - Soil parameters.

Parameter	$\mu$	CV [%]
Unit weight $\gamma$ [kN/m <sup>3</sup> ]	18.1	4.2
Effective cohesion $c'$ [kPa]	2	20
Effective friction angle $\phi$ [°]	30	6
$k_s$ [m/s]	$1 \times 10^{-5}$	90
$*\phi^b$ [°]	30	15

\*Angle indicating the shear strength change with matric suction change.

**Table 2** - Parameters of the water retention curve according to Van Genuchten model.

Parameter	$\mu$	CV [%]
$m$ [-]	0.06	0.6
$n$ [-]	2	0.6
$a$ [-]	8	30
$\theta_s$ [-]	0.463	17
$\theta_r$ [-]	0.04	12

by Simota & Mayr (1996), and the CV of  $\theta_s$  and  $\theta_r$  are those found by Gitirana Jr. & Fredlund (2005). Table 3 shows the values of hydraulic conductivity curve parameters, where the mean of  $b$  is obtained from Rueda (2008), and the CV from the information published by Clapp & Hornberger (1978). Figures 2a and 2b show the SWRC and the unsaturated hydraulic curve, respectively.

#### 4. Sensitivity Analysis

In order to understand the general influence of mechanical and hydraulic parameters on  $FS$ , we perform a sensitivity analysis using FOSM. This method is used because it has a simple mathematical formulation and permits to quantify the influence of each variable independently, without requiring great computational efforts. Mechanical soil parameters considered as independent variables are: unit weight,  $\gamma$ , cohesion,  $c$ , friction angle,  $\phi$ , and rate of increase in shear strength with suction,  $\phi^b$ . Hydraulic parameters are those defining the water retention and unsaturated hydraulic conductivity curves, *i.e.*,  $n$ ,  $b$ ,  $a$ ,  $k_s$  and  $\theta_s$ .

**Table 3** - Parameters of unsaturated hydraulic conductivity curve.

Parameter	$\mu$	CV [%]
$b$ [-]	4.6	33
$d$ [-]	12.2	33

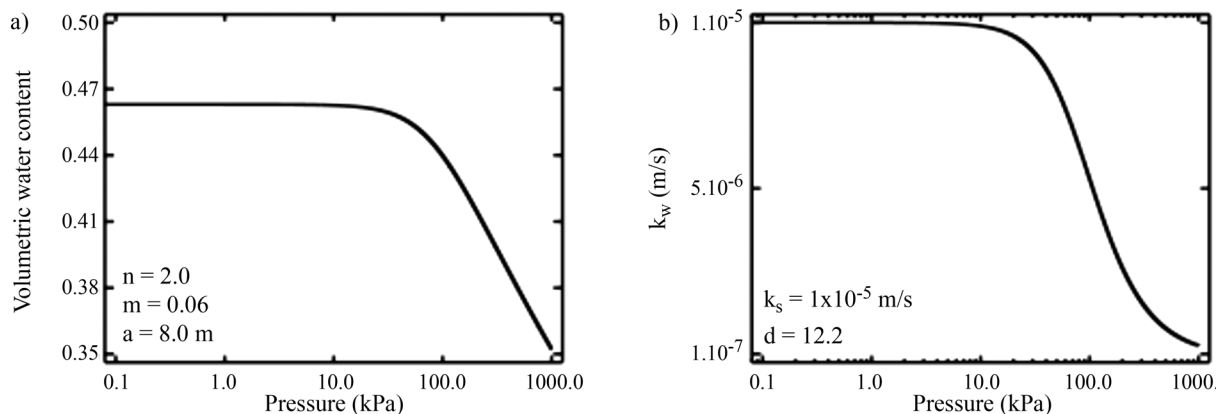
**Figure 2** - Curves of (a) soil water retention, and (b) unsaturated hydraulic conductivity.

Figure 3 shows the percent variance of  $FS$ ,  $V[FS]$ , of each parameter at 0, 8, 24 and 40 h, indicating that mechanical parameters have stronger influence on the variance at initial time, whereas hydraulic parameters become more important as time increases. For times greater than 24 h,  $FS$  is dominated by hydraulic conductivity. The shape parameters of water retention and hydraulic conductivity curves have irrelevant influence when compared to  $k_s$  and  $\phi$ . It is noted that hydraulic parameters have no influence at time zero, because the mass matrix, representing the pore pressure variation with changes to the amount of water, is zero at that time.

#### 5. Parameter Spatial Variation

According to the results obtained in the sensitivity analysis, the most influential mechanical parameters in  $FS$  behavior are  $c$  and  $\phi$ , and the hydraulic parameters are  $a$  and  $k_s$ , hence we focus on variations within these parameters. We assume that there is no correlation between any of the parameters.

To perform the variation, we assign random values of parameter to each node of the mesh. Then, the values of the four nodes composing each element are interpolated to obtain the variable value in each element. This interpolation is carried out with the same shape functions used to solve the flow equation at spatial dimension

$$P_{elem_m} = \sum_{i=1}^{i=4} p_i N_i(0,0) \quad (4)$$

where  $P_{elem_m}$  is the parameter value in the element  $m$ ,  $p_i$  is the parameter value designated in node  $i$  composing the element  $m$ , and  $N_i$  is the shape functions of node  $i$  evaluated in the local coordinate (0,0). By using the shape function, a correlation between the parameter values attributed to the elements is maintained, avoiding abrupt changes among adjacent elements. Shape functions interpolate values for each one of the four nodes of the element, and each node belongs to several elements simultaneously. In other words, we performed a *Kriging* process. This process is

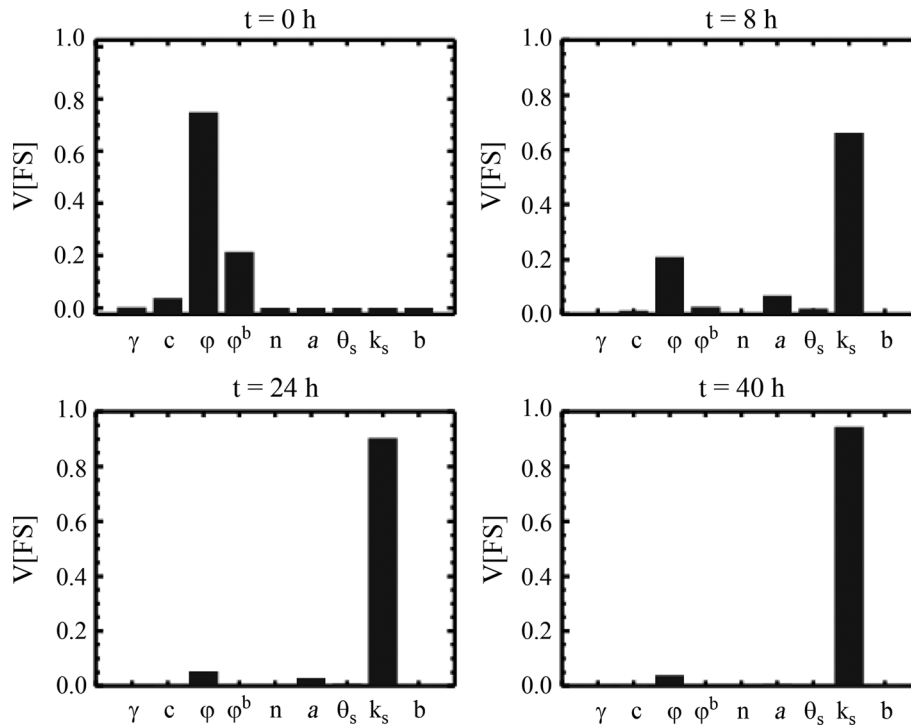


**Figure 3** - Percent variance of *FS* of each parameter.

based on the basic idea that the value of a function at a given point can be calculated as a weighted average of the known values of the same function in the vicinity of the point (Oliver & Webster, 1999; Stein, 2012). In this case, the weights are given by the shape functions.

The node values for each parameter are assigned following normal and lognormal distributions, with mean and standard deviation shown in Table 2 and Table 3. In order to avoid negative or very small values leading to unrealistic values of *FS*, we truncate the normal distribution at zero for all the parameters except for  $k_s$ , which is truncated at  $1 \times 10^{-9}$  m/s. The probability of negative values is spread within all the possible values.

Figure 4 shows the fields resulting from interpolation of the values of the friction angle, indicating that there is a correlation between the adjacent elements. Fig. 5 shows the correlograms exhibiting that an important correlation between elements is preserved to a distance of approximately 2 m. These results are similar for both normal and lognormal distributions, and using the Pearson and Spearman correlations.

Figure 6 summarizes the methodology used to vary spatially each parameter. After generating the parameter random field and keeping all other parameters and boundary conditions constant, we carried out a short-term flow analysis (a 24-h rainfall event). *FS* is found with *pwp* field and Bishop’s Method. Following the Monte Carlo Method, we perform the same procedure  $n_c$  times for each parameter finding  $n_c$  values of *FS*.  $n_c$  is the number of necessary iterations required for Probability Density Functions, *pdfs*, of

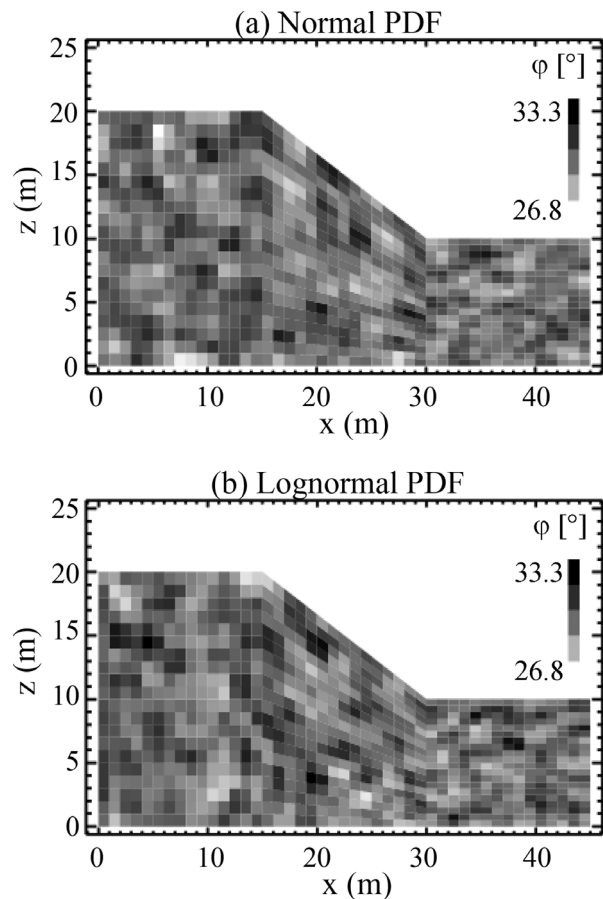


**Figure 4** - The field of value for friction angle assuming (a) a normal distribution, and (b) a lognormal distribution.

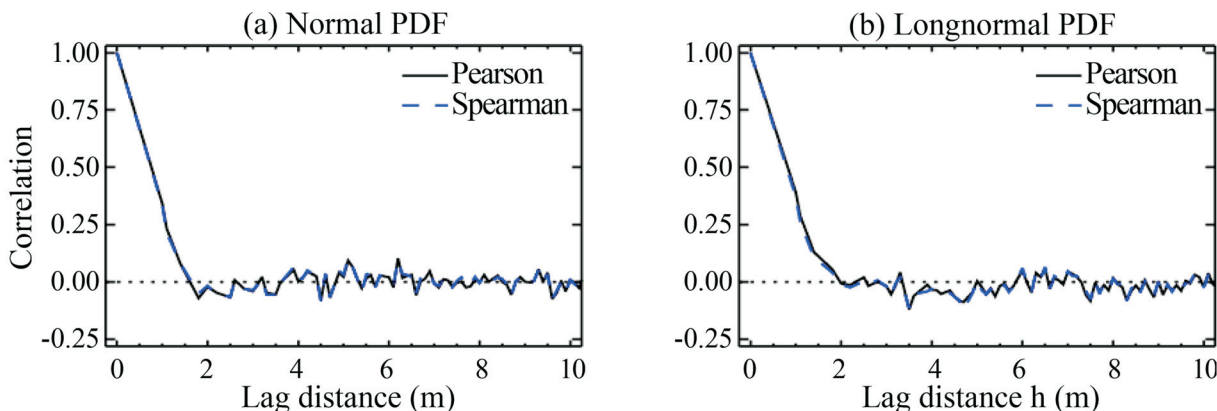


Figure 5 - Correlogram of friction angle following (a) a normal distribution, and (b) a lognormal distribution.

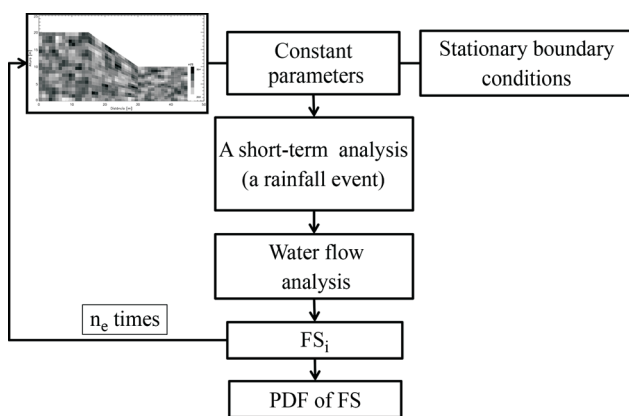


Figure 6 - Methodology to analyze the influence of spatial variability.

$FS$  to reach a constant shape. Each parameter is individually varied and then all simultaneously so that  $FS$  probability functions are determined for different times. By varying a single parameter, the minimum number of iterations is 1000, and by varying all parameters simultaneously,  $n_e$  is 5000.

Figures 7 to 11 show the  $pdfs$  of  $FS$  by varying the parameters for different times. The horizontal axis is  $\Delta FS$ , i.e.,

the difference at each time between the generated  $FS$  (for each relative frequency) and the deterministic  $FS$  value. When  $\Delta FS$  is zero, the  $FS$  of the  $pdf$  generated is equal to the deterministic  $FS$ . When  $\Delta FS$  is negative, the  $FS$  value obtained is less than the deterministic  $FS$ ; and when  $\Delta FS$  is positive, the  $FS$  generated is greater than deterministic  $FS$ .

Figure 7 shows the  $pdfs$  of  $FS$  obtained by varying the cohesion parameter. The  $pdfs$  following both distributions have a mode similar to the deterministic  $FS$ , and a very low dispersion, indicating that variations of  $c'$  are irrelevant for all the times analyzed. Although the cohesion value varies along the surface of rupture, when performing  $n_e$  iterations, the values tend towards the mean.

Figure 8 shows the  $pdfs$  of  $FS$  when the friction angle is varied. The  $pdfs$  have a similar mode to the deterministic  $FS$  value, but their dispersion is greater than that obtained by varying  $c'$ . Similarly, the value of the friction angle tends towards the mean after many iterations, but as  $\phi$  is multiplied by the effective stress from the stability model, which varies with time, the dispersion is greater.

Figure 9 shows the  $pdfs$  of  $FS$  by varying the air-entry value. When it is assumed a normal distribution, the  $pdfs$  of  $FS$  are similar to the ones obtained by varying  $c'$ , indicating a low relevance in the slope stability. However, when it is

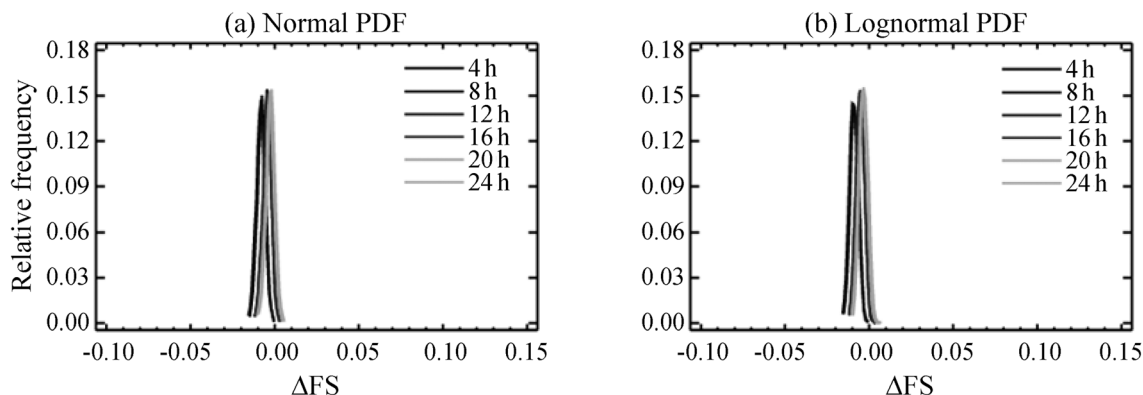
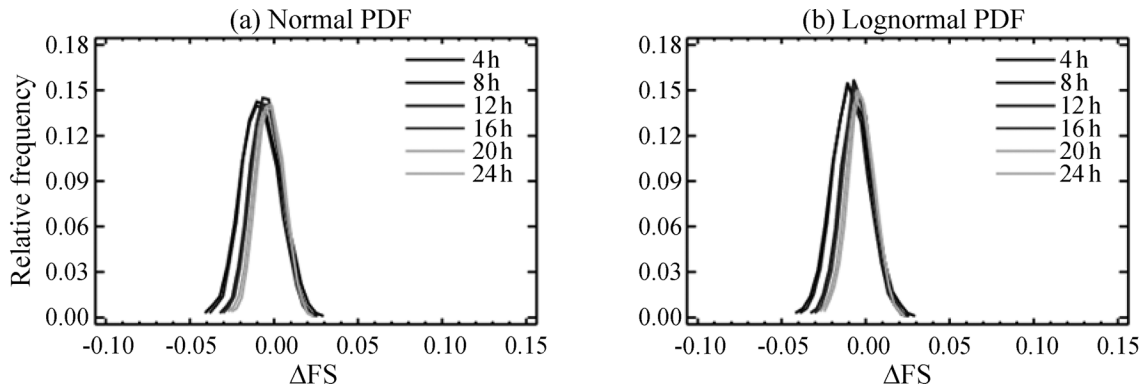
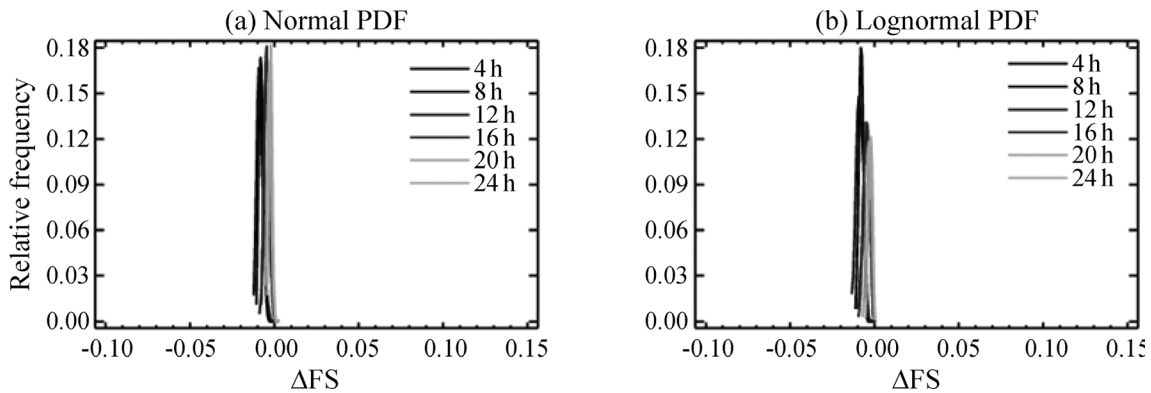


Figure 7 -  $pdf$  of  $FS$  by spatially varying the cohesion following (a) normal distribution and (b) lognormal distribution.



**Figure 8** - *pdf* of *FS* by spatially varying the friction angle following (a) normal distribution and (b) lognormal distribution.



**Figure 9** - *pdf* of *FS* by spatially varying the air-entry value following (a) normal distribution and (b) lognormal distribution.

assumed a lognormal distribution, the mode decreases as time increases.

The low dispersion of the *pdfs* of *FS* is due to the time when suction begins is controlled by the air-entry value, resulting in a null effect of *a* variation when the suction has greater values. The same happens in the soil below the water table level because it is saturated. Consequently, the influence of *a* is only important at points near the water table in the unsaturated zone.

Figure 10 shows the influence of variations in saturated hydraulic conductivity. When  $k_s$  follows a normal distribution the mode and dispersion of *pdfs* of *FS* increase ( $\Delta FS > 0$ ) when time increases, decreasing the relative frequency of the mode.

When  $k_s$  follows a lognormal distribution, the dispersion also increases as time increases, but the mode decreases ( $\Delta FS < 0$ ), and the relative frequency of the mode increases. These differences are due to *FS* for the slope

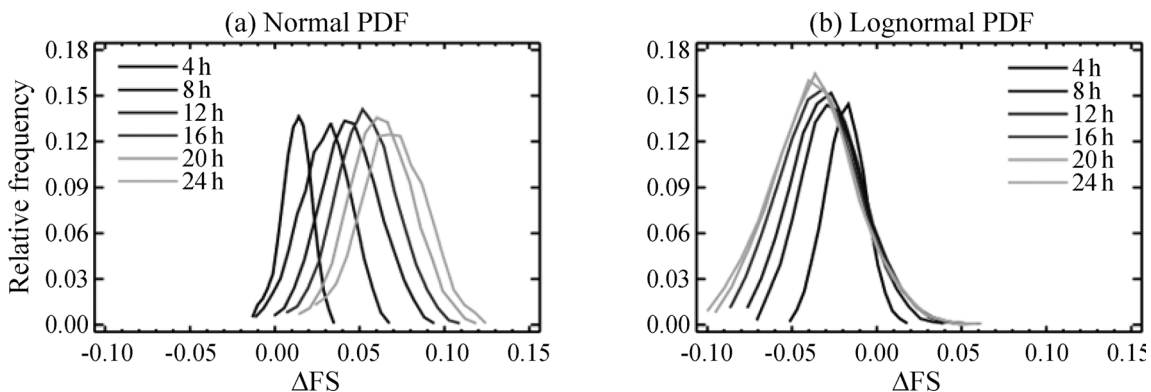


**Figure 10** - *pdf* of *FS* by spatially varying the saturated hydraulic conductivity following (a) normal distribution and (b) lognormal distribution.

studied being greater when hydraulic conductivity coefficient values are high and normal distributions assign higher probabilities to these values than lognormal distributions. The *pdfs* obtained by varying  $k_s$  for both distributions show a strong influence on slope stability, since the dispersion is high and modes do not match the deterministic *FS* values.

Figure 11 shows that by varying all parameters simultaneously, the *pdfs* of *FS* have a similar behavior to the *pdfs* resulting from  $k_s$  variation, confirming the strong influence of this parameter on slope stability. By assuming normal distributions for varying these parameters, dispersion is greater.

Figures 12 and 13 show the relative and cumulative frequencies and probabilities of failure,  $P_f$ , for each time assuming normal and lognormal distributions, respectively. Although the variability of air-entry value has little influence on stability, the *pdfs* of *FS* generated by its variation move rapidly to the left, reaching high probabilities of failure (100% at 16 h) in a short time.

At 12 h, varying all the parameters simultaneously and following a normal distribution, the  $P_f$  is less than the  $P_f$  obtained by varying the air-entry value, cohesion coefficient, and friction angle, but it is greater than the  $P_f$  obtained by varying  $k_s$ . This suggests that the  $P_f$  decreases when hydraulic conductivity increases.

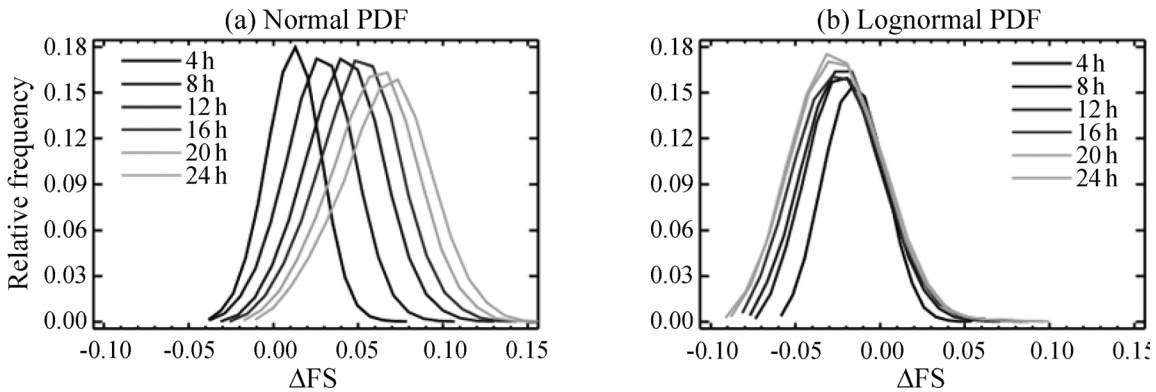


**Figure 11** - *pdf* of *FS* by spatially varying simultaneously all parameters following (a) normal distribution and (b) lognormal distribution.

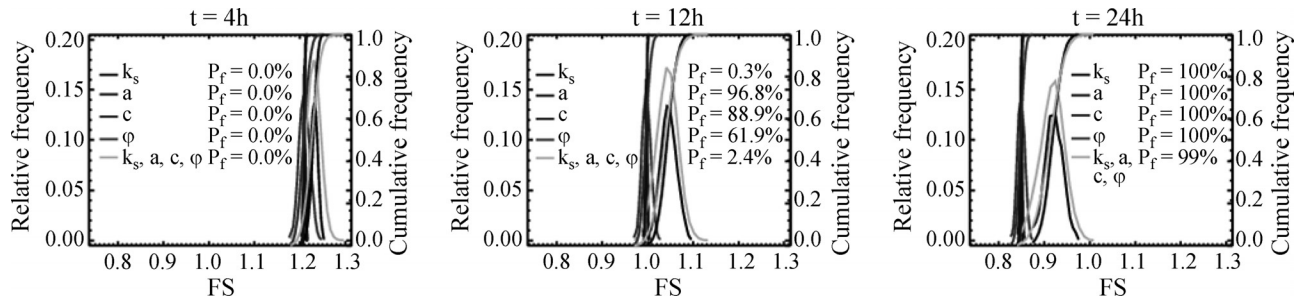


**Figure 12** - *FS* distributions and failure probabilities by spatially varying the parameters for 4, 12 and 24 h, following normal distributions.

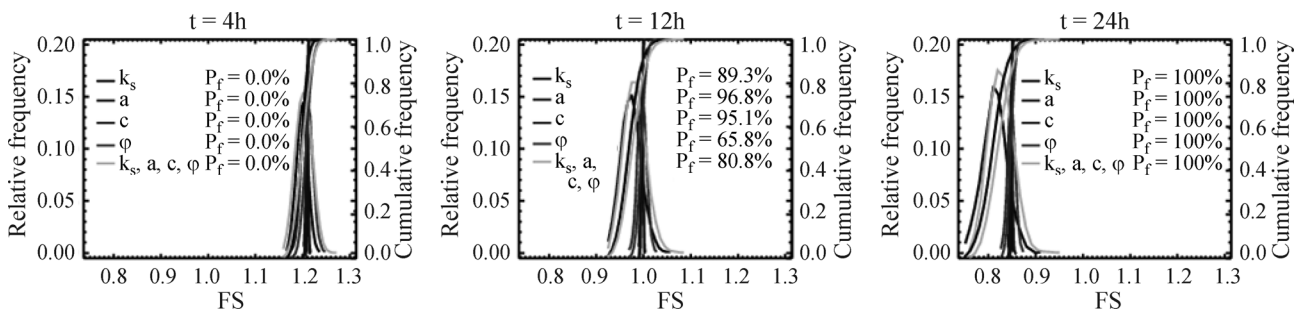


**Figure 13** - *FS* distributions and failure probabilities by spatially varying the parameters for 4, 12 and 24 h, following lognormal distributions.

**Table 4** - Time required to reach a  $P_f$  equal to 100%.

Parameter	$T_{pf} = 100\% \text{ [h]}$	
	Normal <i>pdf</i>	Lognormal <i>pdf</i>
$k_s$	20	16
$a$	16	16
$c$	16	16
$\varphi$	16	16
$k_s, a, c$ and $\varphi$	24	20

When varying simultaneously all the parameters following a lognormal distribution, the  $P_f$  is less than  $P_f$  obtained by varying  $k_s$ ,  $a$  and  $c$ , but it is greater than  $P_f$  obtained by varying  $\varphi$ . It suggests that spatial variability in the friction angle throughout the slope decreases failure probability. Varying the hydraulic conductivity and following a lognormal distribution, the *pdf* of  $FS$  moves more rapidly to the left than when following normal distributions. This can be explained by higher probabilities being assigned to low coefficients by lognormal distributions.

As the conditions of the slope analyzed are very unfavorable, the failure probability,  $T_{pf}$ , is equal to 100% for all cases at a specific time during the rainfall event. Table 4 shows the times when  $P_f$  is 100%, indicating that the slope reaches this probability after 16 h when are varied  $a$ ,  $c$  and  $\varphi$ , while when it is varied  $k_s$  and all the parameters simultaneously, the time is greater and depends on the distribution assumed.

## 6. Conclusions

We used different approaches to analyze the influence of spatial parameter variability on slope stability. According to the sensitivity analysis based on FOSM the  $FS$  of the analyzed slope is most sensitive to friction angle and saturated hydraulic conductivity. The influence of mechanical parameters is greater for short times (< 8 h), and it decreases over time, increasing the influence of the hydraulic parameters. For times close to 24 h, the  $FS$  value depends almost entirely on the saturated hydraulic conductivity, because the location of the water table plays an important role in the analyzed slope stability, and it varies considerably with this parameter.

By assuming both normal and lognormal distributions to assign the values in each node, the influence of cohesion and air-entry values is irrelevant, while the influence of saturated hydraulic conductivity and all parameters simultaneously is very significant. The *pdf* of  $FS$  obtained by varying all the parameters simultaneously is highly related to the *pdf* obtained by varying  $k_s$ , showing the importance of conductivity in  $FS$ .

For the slope analyzed here, the higher the hydraulic conductivity coefficient, the greater the  $FS$ . This explains the contradictory *pdf* behavior of  $FS$  by assuming normal

and lognormal distributions. In the first case, the curves move to the right over time ( $\Delta FS > 0$ ), indicating a lower probability of failure, while in the case of lognormal distributions, which are considered more realistic, curves move to the left ( $\Delta FS < 0$ ) as time increases. This is because lognormal distribution gives higher probabilities to lower values of  $k_s$  than normal distribution.

We note that these results are valid only for the hypothetical case analyzed, but the methodology can be easily implemented to evaluate the spatial variability of soil parameters when the finite elements method is used to solve the flow equation.

## Acknowledgments

The authors thank COLCIENCIAS (Colombia), CNPq (Brazil) and CAPES (Brazil) for their financial support.

## References

- Alonso, E.E. (1976). Risk analysis of slopes and its application to slopes in canadian sensitive clays. *Géotechnique*, 26(3):453-472.
- Athapaththu, A.M.R.G.; Tsuchida, T. & Kano, S. (2015). A new geotechnical method for natural slope exploration and analysis. *Nat. Hazards*, 75(2):1327-1348.
- Campbell, G.S. (1974). A simple method for determining unsaturated conductivity from moisture retention data. *Soil Sci.*, 117(6):311-314.
- Casagli, N.; Tofani, V. & Adler, R.F. (2009). A look from space. K. Sassa & P. Canuti (eds.), *Landslides - Disaster Risk Reduction*. Springer, Berlin, Heidelberg, pp. 287-319.
- Cho, S.E. (2007). Effects of spatial variability of soil properties on slope stability. *Eng. Geol.*, 92(3-4):97-109.
- Cho, S.E. (2014). Probabilistic stability analysis of rainfall-induced landslides considering spatial variability of permeability. *Eng. Geol.*, 171:11-20.
- Chok, Y.H. (2008). Modelling the Effects of Soil Variability and Vegetation on the Stability of Natural Slopes. PhD Thesis, School of Civil, Environmental and Mining Engineering, The University of Adelaide, Australia, 226 p.
- Chowdhury, R.N. (1986). Geomechanics risk model for multiple failures along rock discontinuities. *Int. J. Rock Mech. Min. Sci. Geomech. Abstr.*, 23(5):337-346.
- Chowdhury, R.N. (1992). Simulation of risk of progressive slope failure. *Can. Geotech. J.*, 29(1):94-102.
- Christian, J.T.; Ladd, C.C. & Baecher, G.B. (1992). Reliability and probability in stability analysis. *Stability and Performance of Slopes and Embankments II*, Geotechnical Special Publication No. 31, . ASCE, New York, USA, 1071-1111.
- Clapp, R.B. & Hornberger, G.M. (1978). Empirical equations for some soil hydraulic properties. *Water Resour. Res.*, 14(4):601-604.

- Duncan, J. (2000). Factors of safety and reliability in geotechnical engineering. *J. Geotech. Geoenvironmental Eng.*, 126(April):307-316.
- Farah, K.; Ltifi, M. & Hassis, H. (2011). Reliability analysis of slope stability using stochastic finite element method. *Procedia Eng.*, 10:1402-1407.
- Gitirana Jr., G. & Fredlund, D.G. (2005). Evaluation of the variability of unsaturated soil properties. Proceedings of the 58th Canadian Geotechnical Conference, Canada, 128-135.
- Griffiths, D.V & Fenton, G.A. (2009). Probabilistic settlement analysis by stochastic and random finite-element methods. *J. Geotech. Geoenvironmental Eng.*, 135(11):1629-1637.
- Griffiths, D.V. & Fenton, G.A. (1993). Seepage beneath water retaining structures founded on spatially random soil. *Géotechnique*, 43(4):577-587.
- Griffiths, D.V.; Huang, J. & Fenton, G.A. (2011). Probabilistic infinite slope analysis. *Comput. Geotech.*, 38(4):577-584.
- Griffiths, D.V. & Fenton, G.A. (2004). Probabilistic slope stability analysis by finite elements. *J. Geotech. Geoenvironmental Eng.*, 130(5):507-518.
- Griffiths, D.V.; Huang, J. & Fenton, G.A. (2009). Influence of spatial variability on slope reliability using 2-d random fields. *J. Geotech. Geoenvironmental Eng.*, 135(10):1367-1378.
- Gui, S.; Zhang, R.; Turner, J.P. & Xue, X. (2000). Probabilistic slope stability analysis with stochastic soil hydraulic conductivity. *J. Geotech. Geoenvironmental Eng.*, 126(1):1-9.
- Hue Le, T.; Gallipoli, D.; Sanchez, M. & Wheeler, S. (2015). Stability and failure mass of unsaturated heterogeneous slopes. *Can. Geotech. J.*, 52(11):1747-1761.
- Imaizumi, F.; Maita, H. & Miyamoto, K. (2009). Dimensionless parameters controlling occurrence of shallow landslides. *J. Japan Soc. Eros. Control Eng.*, 62(2):13-20.
- Jiang, S.H.; Li, D.Q.; Zhang, L.M. & Zhou, C.-B. (2014). Slope reliability analysis considering spatially variable shear strength parameters using a non-intrusive stochastic finite element method. *Eng. Geol.*, 168(86):120-128.
- Lacasse, S. (2013). Protecting society from landslides - The role of the geotechnical engineer. 8<sup>th</sup> Terzaghi Oration. Proc. 18<sup>th</sup> International Conference on Soil Mechanics and Geotechnical Engineering, France, p. 1-21.
- Legorreta Paulin, G.; Pouget, S.; Bursik, M.; Quesada, F.A. & Contreras, T. (2016). Comparing landslide susceptibility models in the rio el estado watershed on the sw flank of pico de Orizaba volcano, Mexico. *Nat. Hazards*, 80(1):127-139.
- Li, K.S. & Lumb, P. (1987). Probabilistic design of slopes. *Can. Geotech. J.*, 24:520-535.
- Li, L.; Wang, Y.; Cao, Z. & Chu, X. (2013). Risk de-aggregation and system reliability analysis of slope stability using representative slip surfaces. *Comput. Geotech.*, 53:95-105.
- Metya, S. & Bhattacharya, G. (2015). Reliability analysis of earth slopes considering spatial variability. *Geotech. Geol. Eng.*, 34:103-123.
- Oliveira, O.M. (2004). Estudo Sobre a Resistência ao Cisalhamento de um Solo Residual Compactado Não Saturado. PhD Dissertation, Escola Politécnica da Universidade de São Paulo, Brazil, 330 p.
- Oliver, M.A. & Webster, R. (1999). Kriging: A method of interpolation for geographical information systems. *Int. J. Geogr. Inf. Syst.*, 4(3):313-332.
- Otálvaro, I. & Cordão-Neto, M. (2013). Probabilistic analyses of slope stability under infiltration conditions. Cacedo, B.; Murillo, C.; Hoyos, L.; Colmenares, J. & Berdugo, I. (eds.), *Advances in Unsaturated Soils*, Taylor & Francis, pp. 539-543.
- Raia, S.; Alvioli, M.; Rossi, M.; Baum, R.L.; Godt, J.W. & Guzzetti, F. (2013). Improving predictive power of physically based rainfall-induced shallow landslide models: a probabilistic approach. *Geosci. Model Dev. Discuss.*, 6(1):1367-1426.
- Rueda, O.A. (2008). Modelamiento de la Humedad del Suelo en la Región Cafetera de Colombia Bajo Diferentes Coberturas Vegetales. MSc Dissertation, Departamento de Geociencias y Medio Ambiente, Universidad Nacional de Colombia, Colombia, 104 p.
- Santoso, A.M.; Phoon, K.-K. & Quek, S.T. (2011). Effects of soil spatial variability on rainfall-induced landslides. *Comput. Struct.*, 89(11-12):893-900.
- Simota, C. & Mayr, T. (1996). Predicting the soil water retention curve from readily-available data obtained during soil surveys. *Int. Agrophysics*, 10: 185-188.
- Srivastava, A.; Babu, G.L.S. & Haldar, S. (2010). Influence of spatial variability of permeability property on steady state seepage flow and slope stability analysis. *Eng. Geol.*, 110(3-4):93-101.
- Stein, M.L. (2012). Interpolation of spatial data: some theory for kriging. Springer Science & Business Media, New York, 156 p.
- Tarolli, P.; Borga, M.; Chang, K.T. & Chiang, S.H. (2011). Modeling shallow landsliding susceptibility by incorporating heavy rainfall statistical properties. *Geomorphology*, 133(3-4):199-211.
- Tietje, O.; Fitze, P. & Schneider, H.R. (2014). Slope stability analysis based on autocorrelated shear strength parameters. *Geotech. Geol. Eng.*, 32(6):1477-1483.
- van Genuchten, M. (1980). A closed-form equation for predicting the hydraulic conductivity of unsaturated soils. *Soil Sci.*, 44:892-898.
- Wang, Y.; Cao, Z. & Au, S.K. (2011). Practical reliability analysis of slope stability by advanced Monte Carlo

simulations in a spreadsheet. *Can. Geotech. J.*, 48(1):162-172.

### List of Symbols

$a$ : inverse of air-entry value.  
 $b$ : hydraulic conductivity soil empirical exponent.  
 $c$ : soil effective cohesion.  
 CV: coefficient of variation.  
 FEM: Finite Element Method.  
 FOSM: First Order Second Moment.  
 FS: factor of safety.  
 $h$ : hydraulic head.  
 $k_s$ : coefficient of saturated hydraulic conductivity.  
 $k_w$ : coefficient of hydraulic conductivity.  
 LEM: Limit Equilibrium Method.  
 MSM: Monte-Carlo Simulation Method.  
 $m$ : shape parameter of Van-Genuchten equation.

$n$ : shape parameter of Van-Genuchten equation.  
 $n_i$ : number of iterations.  
 $n_j$ : shape functions.  
 $P_{elem_m}$ : parameter value evaluated in each element.  
 $P_i$ : parameter value in each node.  
 $P_f$ : probability of failure.  
 $pwp$ : pore water pressure.  
 SWRC: Soil Water Retention Curve.  
 $S_r$ : degree of saturation.  
 $t$ : time.  
 VAR[.]: variance.  
 $\gamma$ : soil unit weight.  
 $\theta_r$ : residual volumetric moisture content.  
 $\theta_s$ : saturated volumetric moisture content.  
 $\Theta$ : normalized volumetric moisture content.  
 $\mu$ : mean.  
 $\phi$ : friction angle.  
 $\phi^b$ : rate of increase in shear strength with suction.

# *SOILS and ROCKS*

An International Journal of Geotechnical and Geoenvironmental Engineering

## **Publication of**

**ABMS - Brazilian Association for Soil Mechanics and Geotechnical Engineering**

**SPG - Portuguese Geotechnical Society**

**Volume 41, N. 3, September-December 2018**

## **Author index**

Aghamolaie, I.	193	Massad, F.	75, 217
Alkhorshid, N.R.	333	Matos, T.H.C.	157
Araújo, G.L.S.	333	Moghaddas, N.H.	193
Araújo, M.C.N.	309	Morandini, T.L.C.	345
Assis, A.P.	203	Morgenstern, N.R.	107
Barbosa, M.G.T.	17	Muñoz, E.	381
Bim, R.	61	Nascimento, P.N.C.	3
Bragagnolo, L.	369	Nunes, G.B.	61
Caldeira, L.	237	Ochoa, A.	381
Carraro, J.A.H.	149	Odebrecht, E.	179
Casagrande, M.D.T.	361	Oliveira, O.M.	61
Cavalcante, A.L.B.	17	Pacheco, M.P.	171
Chagas, J.V.R.	157	Palmeira, E.M.	333
Consoli, N.C.	149	Passini, L.B.	103
Cordão Neto, M.P.	157, 381	Pedrini, R.A.A.	133
Cunha, R.P.	91	Poulos, H.G.	91
Curado, T.S.	49	Póvoa, L.M.M.	3
Danziger, B.R.	171	Prietto, P.D.M.	369
de Mello, L.G.F.S.	267	Rezende, L.R.	157
Dienstmann, G.	319	Rocha, B.P.	133
Etemadifar, M.	193	Rosenbach, C.M.D.C.	149
Faro, V.P.	309	Sales, M.M.	49
Figueiredo, L.T.	203	Santa Maria, F.C.M.	33
Garcia, R.S.	17	Santa Maria, P.E.L.	33
Giacheti, H.L.	133	Scheuermann Filho, H.C.	149
Godoy, V.B.	149	Schnaid, F.	179, 319
González, A.A.M.	103	Silveira, A.A.	369
Higashi, R.A.R.	61	Sotomayor, J.M.G.	361
Korf, E.P.	369	Souza Júnior, T.F.	309
Kormann, A.C.M.	103	Teixeira, C.A.	309
Lashkaripour, G.R.	193	Teixeira, S.H.C.	309
Leão, M.F.	171	Trevizolli, M.N.B.	309
Leite, A.L.	345	Ulsen, C.	369
Ludemann, S.M.	17	Valverde, R.M.	75
Maghous, S.	319	Vaziri, N.S.	193
Maia, P.C.A.	3	Yanez, D.G.	217
Mascarenha, M.M.A.	157		



- > **Prospecção Geotécnica**  
*Site Investigation*
- > **Consultoria Geotécnica**  
*Geotechnical Consultancy*
- > **Obras Geotécnicas**  
*Ground Treatment-Construction Services*
- > **Controlo e Observação**  
*Field Instrumentation Services and Monitoring Services*
- > **Laboratório de Mecânica de Solos**  
*Soil and Rock Mechanics Laboratory*

Certificada ISO 9001 por



# Geocontrole



Parque Oriente, Bloco 4, EN10  
2699-501 Bobadela LRS  
Tel. 21 995 80 00  
Fax. 21 995 80 01  
e.mail: mail@geocontrole.pt  
www.geocontrole.pt

  
**Geocontrole**  
Geotecnia e Estruturas de Fundação SA



**COBA**

**GEOLOGY AND GEOTECHNICS**

Hydrogeology • Engineering Geology • Rock Mechanics • Soil Mechanics • Foundations and Retaining Structures • Underground Works • Embankments and Slope Stability  
Environmental Geotechnics • Geotechnical Mapping



- Water Resources Planning and Management
- Hydraulic Undertakings
- Electrical Power Generation and Transmission
- Water Supply Systems and Pluvial and Wastewater Systems
- Agriculture and Rural Development
- Road, Railway and Airway Infrastructures
- Environment
- Geotechnical Structures
- Cartography and Cadastre
- Safety Control and Work Rehabilitation
- Project Management and Construction Supervision



**PORTUGAL**

CENTER AND SOUTH REGION  
Av. 5 de Outubro, 323  
1649-011 LISBOA  
Tel.: (351) 210125000, (351) 217925000  
Fax: (351) 217970348  
E-mail: coba@coba.pt  
www.coba.pt

Av. Marquês de Tomar, 9, 6.º.  
1050-152 LISBOA  
Tel.: (351) 217925000  
Fax: (351) 213537492

**NORTH REGION**

Rua Mouzinho de Albuquerque, 744, 1.º.  
4450-203 MATOSINHOS  
Tel.: (351) 229380421  
Fax: (351) 229373648  
E-mail: engico@engico.pt

**ANGOLA**

Praceta Farinha Leitão, edifício nº 27, 27-A - 2.º Dto  
Bairro do Maculusso, LUANDA  
Tel./Fax: (244) 222338 513  
Cell: (244) 923317541  
E-mail: coba-angola@netcabo.co.ao

**MOZAMBIQUE**

Pestana Rovuma Hotel. Centro de Escritórios.  
Rua da Sé nº114. Piso 3, MAPUTO  
Tel./Fax: (258) 21 328 813  
Cell: (258) 82 409 9605  
E-mail: coba.mz@tdm.co.mz

**ALGERIA**

09, Rue des Frères Hocine  
El Biar - 16606, ARGEL  
Tel.: (213) 21 922802  
Fax: (213) 21 922802  
E-mail: coba.alger@gmail.com

**BRAZIL**

**Rio de Janeiro**  
COBA Ltd. - Rua Bela 1128  
São Cristóvão  
20930-380 Rio de Janeiro RJ  
Tel.: (55 21) 351 50 101  
Fax: (55 21) 258 01 026

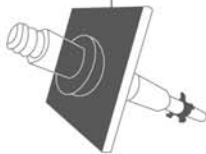
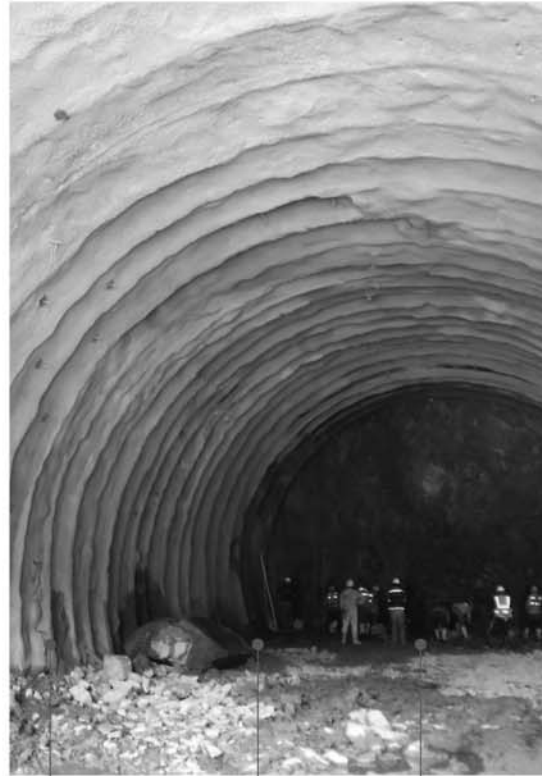
**Fortaleza**

Av. Senador Virgílio Távora 1701, Sala 403  
Aldeota - Fortaleza CEP 60170 - 251  
Tel.: (55 85) 3261 17 38  
Fax: (55 85) 3261 50 83  
E-mail: coba@esc-te.com.br

**UNITED ARAB EMIRATES**

Corniche Road - Corniche Tower - 5th Floor - 5B  
P. O. Box 38360 ABU DHABI  
Tel.: (971) 2 627 0088  
Fax: (971) 2 627 0087

Much more support  
to your business.



**Incotep - Anchoring Systems**

Incotep anchoring Systems is a division of Açotubo Group, which engaged in the development of Anchoring Systems, used in geotechnical and structural applications where high quality prestressing systems are designed to meet diverse needs.

**Know our solutions for your processes**

- Self Drilling Injection Hollow Bar
- Cold Rolled Thread Bars and Micropiles
- Hot Rolled Thread Bars
- Incotep Tie Rods (Port and Dike Construction)

- Umbrella Tubes Drilling System
- Pipes for Root Piles, among others

[www.incotep.com.br](http://www.incotep.com.br)  
+55 11 2413-2000

**INCOTEP**  
Sistemas de Ancoragem

A company Açotubo Group





Conheça mais:  
[www.geobrugg.com/pt/taludes](http://www.geobrugg.com/pt/taludes)



Safety is our nature

**TECCO® SYSTEM<sup>3</sup> com fio de aço de alta resistência**

**SISTEMA ECOLOGICAMENTE  
CORRETO PARA ESTABILIZAÇÃO  
DE TALUDES**

# Reliable solutions with **technology, quality,** and **innovation** for Civil Engineering proposes



## MACCAFERRI POLIMAC

New polymeric coating with high performance  
**PoliMac™**



Long-life galvanising  
**GalMac® 4R**

Intermetallic coating

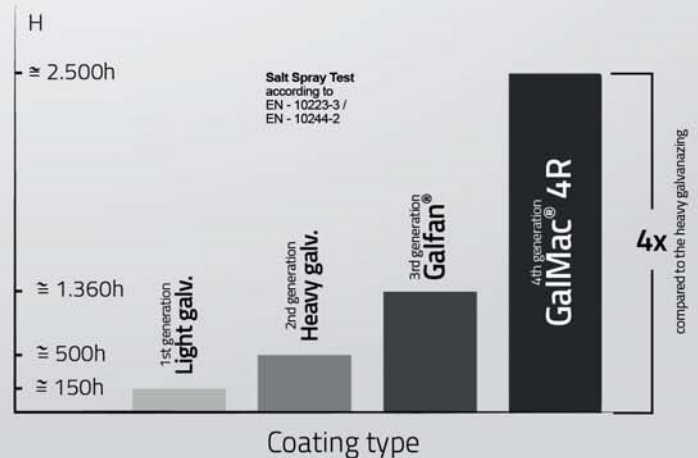
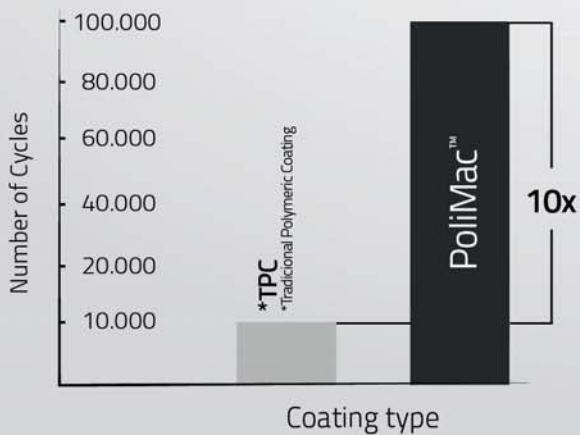
Steel wire LCC\*  
\*Low Carbon Content



The **PoliMac™** in controlled abrasion resistance tests, it showed its excellent performance by resisting up to 100,000 cycles in the standard tests **ABNT NBR 7577** and **EN 10223-3**; about **10x more** than the traditional coating.



The **GalMac® 4R** coating complies with the main national and international standards such as: **EN 10223-3: 2013, ASTM B860** and **NBR 8964**.



Follow us on our **social media**



/maccaferri



/maccaferriatriz



@Maccaferri\_BR



+MaccaferriWorld



/maccaferriworld



**MACCAFERRI**

[www.maccaferri.com/br](http://www.maccaferri.com/br)

# SPECIALISTS IN GEOTECHNICAL IN-SITU TESTS AND INSTRUMENTATION

## GEOTECHNICAL SERVICES (onshore and offshore)

### IN-SITU TESTS

Seismic CPT  
Cone Penetration Testing Undrained-CPTu (cordless system)  
Vane Shear Testing (electrical apparatus)  
Pressuremeter Testing (Menard)  
Flat Dilatometer Test-DMT (Machetti)  
Standard Penetration Test-SPT-T

### INSTRUMENTATION

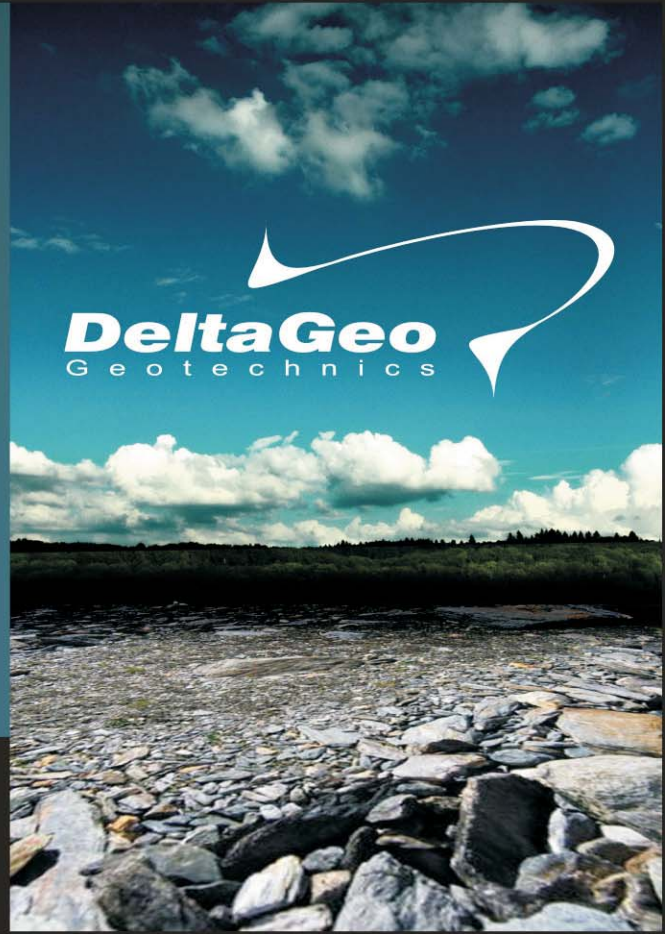
Instrumentation, installation and direct import  
Routine Monitoring  
Operation and Maintenance  
Engineering analyses  
Consultancy, design & geotechnical engineering services

### SAMPLING

Soil sampling and monitoring  
Groundwater sampling and monitoring  
Field and laboratory testing

### ENVIRONMENTAL

Environmental Services  
Soil and groundwater sampling and monitoring  
Field and laboratory testing

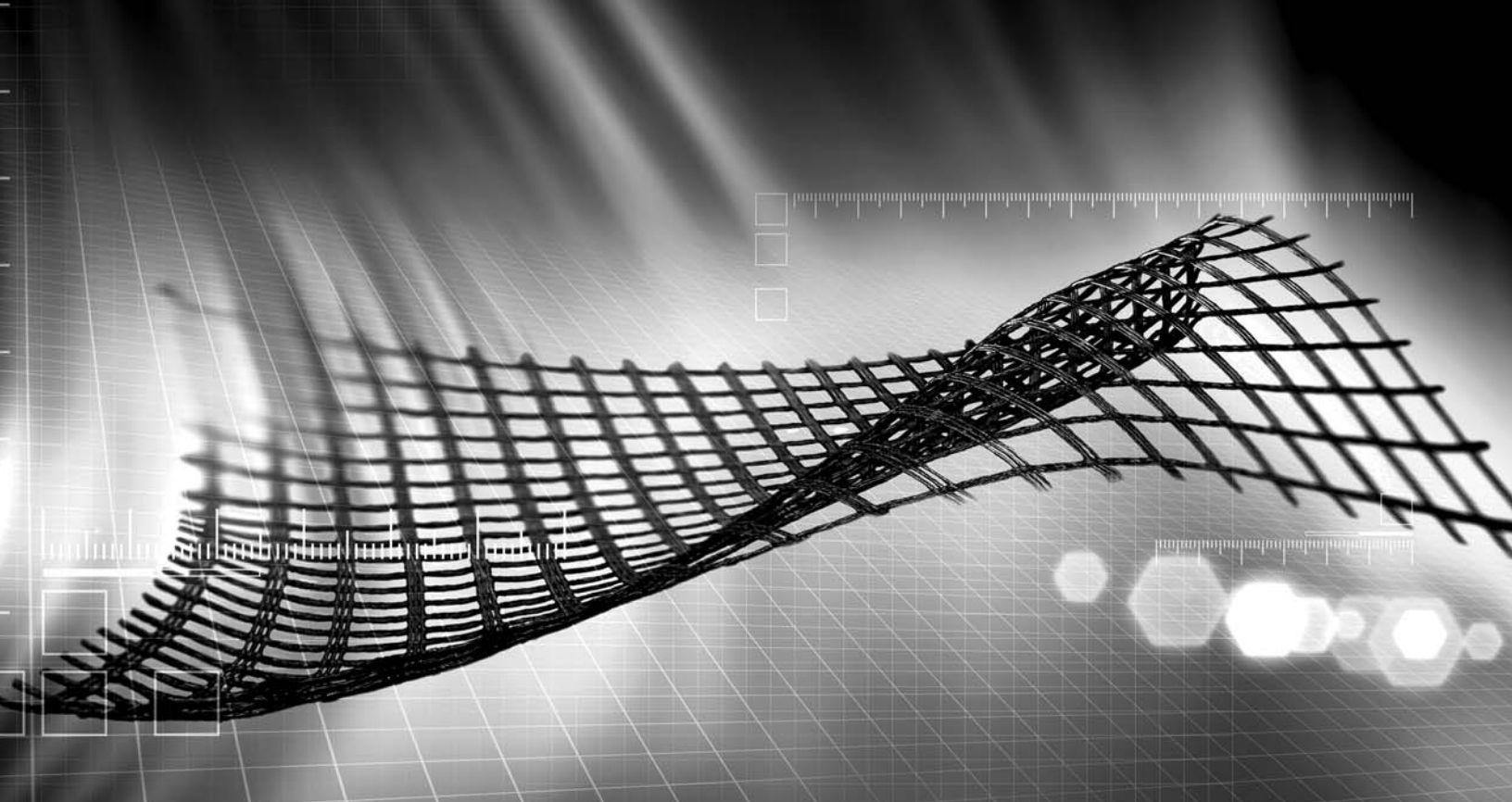


**0800 979 3436**

**São Paulo: +55 11 8133 6030**

**Minas Gerais: +55 31 8563 2520 / 8619 6469**

**[www.deltageo.com.br](http://www.deltageo.com.br) [deltageo@deltageo.com.br](mailto:deltageo@deltageo.com.br)**



# A strong, lasting connection.

With a history of over 150 years of pioneering in geosynthetics, we strive to create solutions for the most diverse engineering challenges.

Our business areas:



**Earthworks and  
Foundations**



**Environmental  
Engineering**



**Roads and Pavements**



**Hydraulic Engineering**

Talk to HUESKER Brasil:  
[www.HUESKER.com.br](http://www.HUESKER.com.br)  
[HUESKER@HUESKER.com.br](mailto:HUESKER@HUESKER.com.br)  
+55 (12) 3903 9300

Follow HUESKER Brasil in social media:



**# HUESKER**  
Ideen. Ingenieure. Innovationen.



Geotechnic and Rehabilitation

**TEIXEIRA DUARTE**  
ENGENHARIA E CONSTRUÇÕES, S.A.

• Head Office  
Lagoas Park - Edifício 2  
2740-265 Porto Salvo - Portugal  
Tel.: [+351] 217 912 300  
Fax: [+351] 217 941 120/21/26

• Angola  
Alameda Manuel Van Dunen 316/320 - A  
Caixa Postal 2857 - Luanda  
Tel.: [+34] 915 550 903  
Fax: [+34] 915 972 834

• Algeria  
Parc Miremont - Rua A, Nº136 - Bouzareah  
16000 Alger  
Tel.: [+213] 219 362 83  
Fax: [+213] 219 365 66

• Brazil  
Rua Iguatemi, nº488 - 14° - Conj. 1401  
CEP 01451 - 010 - Itaim Bibi - São Paulo  
Tel.: [+55] 112 144 5700  
Fax: [+55] 112 144 5704

• Spain  
Avenida Alberto Alcocer, nº24 - 7° C  
28036 Madrid  
Tel.: [+34] 915 550 903  
Fax: [+34] 915 972 834

• Mozambique  
Avenida Julyus Nyerere, 130 - R/C  
Maputo  
Tel.: [+258] 214 914 01  
Fax: [+258] 214 914 00

**BUILDING A BETTER WORLD**



**TPF**

PLANEGE CENOR



## Engineering and Architectural Consultancy

Geology, Geotechnics, Supervision of Geotechnical Works  
Embankment Dams, Underground Works, Retaining Structures  
Special Foundations, Soil Improvement, Geomaterials



[www.tpfplanegecenor.pt](http://www.tpfplanegecenor.pt)

# Instructions for Submission of Manuscripts

## Category of the Papers

Soils and Rocks is the international scientific journal edited by the Brazilian Association for Soil Mechanics and Geotechnical Engineering (ABMS) and the Portuguese Geotechnical Society (SPG). The aim of the journal is to publish (in English) original research and technical works on all geotechnical branches.

According to its content the accepted paper is classified in one of the following categories: Article paper, Technical Note, Case Study or Discussion. An article paper is an extensive and conclusive dissertation about a geotechnical topic. A paper is considered as a technical note if it gives a short description of ongoing studies, comprising partial results and/or particular aspects of the investigation. A case study is a report of unusual problems found during the design, construction or the performance of geotechnical projects. A case study is also considered as the report of an unusual solution given to an ordinary problem. The discussions about published papers, case studies and technical notes are made in the Discussions Section.

When submitting a manuscript for review, the authors should indicate the category of the manuscript, and is also understood that they:

- assume full responsibility for the contents and accuracy of the information in the paper;
- assure that the paper has not been previously published, and is not being submitted to any other periodical for publication.

## Manuscript Instructions

Manuscripts must be written in English. The text is to be typed in a word processor (preferably MS Word), **single column**, using ISO A4 page size, left, right, top, and bottom margins of 25 mm, Times New Roman 12 font, and line spacing of 1.5. All lines and pages should be numbered. The text should be written in the third person.

The first page of the manuscript must include the title of the paper followed by the names of the authors with the abbreviation of the most relevant academic title. The affiliation, address and e-mail must appear below each author's name. An abstract of 200 words follows after the author's names. A list with up to six keywords at the end of the abstract is required.

Although variations on the sequence and title of each section are possible, it is suggested that the text contains the following sections: Introduction, Material and Methods, Results, Discussions, Conclusions, Acknowledgements, References and List of Symbols. A brief description of each section is given next.

**Introduction:** This section should indicate the state of the art of the problem under evaluation, a description of the problem and the methods undertaken. The objective of the work should be clearly presented at the end of the section.

**Materials and Methods:** This section should include all information needed to the reproduction of the presented work by other researchers.

**Results:** In this section the data of the investigation should be presented in a clear and concise way. Figures and tables should not repeat the same information.

**Discussion:** The analyses of the results should be described in this section.

**Conclusions:** The content of this section should be based on the data and on the discussions presented.

**Acknowledgements:** If necessary, concise acknowledgements should be presented in this section.

**References:** References to other published sources must be made in the text by the last name(s) of the author(s), followed by the year of publication, similarly to one of the two possibilities below:

...while Silva & Pereira (1987) observed that resistance depended on soil density... or It was observed that resistance depended on soil density (Silva & Pereira, 1987).

In the case of three or more authors, the reduced format must be used, e.g.: Silva *et al.* (1982) or (Silva *et al.*, 1982). Two or more citations belonging to the same author(s) and published in the same year are to be distinguished with small letters, e.g.: (Silva, 1975a, b, c.). Standards must be cited in the text by the initials of the entity and the year of publication, e.g.: ABNT (1996), ASTM (2003).

Full references shall be listed alphabetically at the end of the text by the first author's last name. Several references belonging to the same author shall be cited chronologically. Some examples are listed next:

Papers: Bishop, A.W. & Blight, G.E. (1963). Some aspects of effective stress in saturated and unsaturated soils. *Geotechnique*, 13(2):177-197.

Books: Lambe, T.W. & Whitman, R.V. (1979). *Soil Mechanics*, SI Version. John Wiley & Sons, New York, 553 p.

Book with editors: Sharma, H.D.; Dukes, M.T. & Olsen, D.M. (1990). Field measurements of dynamic moduli and Poisson's ratios of refuse and underlying soils at a landfill site. Landva, A. & Knowles, G.D. (eds), *Geotechnics of Waste Fills - Theory and Practice*, American Society for Testing and Materials - STP 1070, Philadelphia, pp. 57-70.

Proceedings (printed matter or CD-ROM): Jamiolkowski, M.; Ladd, C.C.; Germaine, J.T. & Lancellotta, R. (1985). New developments in field and laboratory testing of soils. Proc. 11th Int. Conf. on Soil Mech. and Found. Engn., ISSMFE, San Francisco, v. 1, pp. 57-153. (specify if CD ROM).

Thesis and dissertations: Lee, K.L. (1965). *Triaxial Compressive Strength of Saturated Sands Under Seismic Loading Conditions*. PhD Dissertation, Department of Civil Engineering, University of California, Berkeley, 521 p.

Standards: ASTM (2003). *Standard Test Method for Particle Size Analysis of Soils - D 422-63*. ASTM International, West Conshohocken, Pennsylvania, USA, 8 p.

Internet references: Soils and Rocks available at <http://www.abms.com.br> and downloaded on August 6th 2003.

On line first publications must also bring the digital object identifier (DOI) at the end.

Figures shall be either computer generated or drawn with India ink on tracing paper. Computer generated figures must be accompanied by the corresponding digital file (.tif, .jpg, .pcx, etc.). All figures (graphs, line drawings, photographs, etc.) shall be numbered consecutively and have a caption consisting of the figure number and a brief title or description of the figure. This number should be used when referring to the figure in text. Photographs should be black and white, sharp, high contrasted and printed on glossy paper.

Tables shall be numbered consecutively in Arabic and have a caption consisting of the table number and a brief title. This number should be used when referring to the table in the text. Units should be indicated in the first line of the table, below the title of each column. Acronyms should be avoided. When applicable, the units should come right below the corresponding column heading. Additional comments can be placed as footnotes.

Equations shall appear isolated in a single line of the text. Numbers identifying equations must be flushed with the right margin. International System (SI) units must be used. The definitions of the symbols used in the

equations must appear in the List of Symbols. It is recommended that the symbols used are in accordance with Lexicon in 8 Languages, ISSMFE (1981) and the ISRM List of Symbols.

The text of the submitted manuscript (including figures, tables and references) intended to be published as an article paper or a case history should not contain more than 30 pages, formatted according to the instructions mentioned above. Technical notes and discussions should have no more than 15 and 8 pages, respectively. Longer manuscripts may be exceptionally accepted if the authors provide proper explanation for the need of the required extra space in a cover letter.

### **Discussion**

Discussions must be written in English. The first page of a discussion should contain:

The title of the paper under discussion;

Name of the author(s) of the discussion, followed by their position, affiliation, address and e-mail. The author(s) of the discussion should refer to himself (herself/themselves) as the reader(s) and to the author(s) of the paper as the author(s).

Figures, tables and equations should be numbered following the same sequence of the original paper. All instructions previously mentioned for the preparation of article papers, case studies and technical notes also apply to the preparation of discussions.

### **Editorial Review**

Each paper will be evaluated by reviewers selected by the editors according to the subject of the paper. The authors will be informed about the results of the review process. If the paper is accepted, the authors will be required to submit a version of the revised manuscript with the suggested modifications. If the manuscript is rejected for publication, the authors will be informed about the reasons for rejection. In any situation comprising modification of the original text, classification of the manuscript in a category different from that proposed by the authors, or rejection, the authors can reply presenting their reasons for disagreeing with the reviewer comments.

### **Submission**

The author(s) must upload a digital file of the manuscript to the Soils and Rocks website.

### **Follow Up**

The online management system will provide a password to the corresponding author, which will enable him/her to follow the reviewing process of the submitted manuscript at the Soils and Rocks website.

**Volume 41, N. 3, September-December 2018****Table of Contents***XXXV MANUEL ROCHA LECTURE**Internal Erosion in Dams*

L. Caldeira 237

*ARTICLES**Some Case Histories with Lessons to Learn in Dam Engineering (2<sup>nd</sup> Dr. Victor de Mello Goa Lecture)*

L.G.F.S. de Mello 267

*A Method for Designing Finger Drains and Assessing Phreatic Lines for Dams*

M.C.N. Araújo, T.F. de Souza Júnior, M.N.B. Trevizolli, C.A. Teixeira, S.H.C. Teixeira, V.P. Faro 309

*Assessment of Rate Effects in Piezocone Tests from Poroelastic Cavity Expansion Analysis*

G. Dienstmann, S. Maghous, F. Schnaid 319

*Behavior of Geosynthetic-Encased Stone Columns in Soft Clay: Numerical and Analytical Evaluations*

N.R. Alkhorshid, G.L.S. Araújo, E.M. Palmeira 333

*On the Compatibility and Theoretical Equations for Mixtures of Tropical Soils and Bentonite for Barrier Purposes*

T.L.C. Morandini, A.L. Leite 345

*TECHNICAL NOTES**The Performance of a Sand Reinforced with Coconut Fibers Through Plate Load Tests on a True Scale Physical Model*

J.M.G. Sotomayor, M.D.T. Casagrande 361

*Porosity Changes of Compacted Soil Percolated with Acidic Leachate*

E.P. Korf, P.D.M. Prietto, A.A. Silveira, C. Ulsen, L. Bragagnolo 369

*CASE STUDY**Effects of Spatial Variability on Slope Reliability: A Hypothetical Case Study*

E. Muñoz, M.P. Cordão Neto, A. Ochoa 381